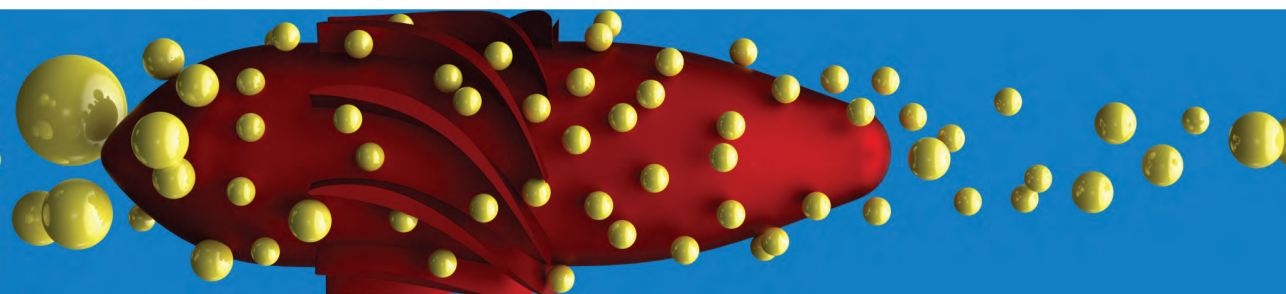


Bulk Dynamics of Droplets in Liquid-Liquid Axial Cyclones



Laurens van Campen

Propositions

accompanying the thesis

Bulk Dynamics of Droplets in Liquid-Liquid Axial Cyclones

Laurens van Campen

1. In the optimization process of a liquid-liquid cyclone, aiming at a too high azimuthal velocity will turn the cyclone into a mixer instead of a phase separator, despite the other design efforts (chapter 7 of this thesis).
2. Without adequate representation of turbulent dispersion in the droplet equation of motion, it is not possible to predict accurately a liquid-liquid cyclone phase separation efficiency operating at industrial conditions (chapter 6 of this thesis).
3. Liquid-liquid axial cyclones perform best when the swirl element is sized such that in the swirl element the maximum droplet size based on the critical Weber number for the flow is equal to the average size of droplets found upstream of the swirl element (chapter 8 of this thesis).
4. Electric measurements of the phase distribution in media with a high conductance should use the free charge carriers instead of a limit on the electric current.
5. The ever-increasing possibilities of numerical simulations of turbulent liquid-liquid flows will not make experimental validation redundant.
6. Designing an experimental facility with strict budget constraints results in the total investigation being more expensive than in case of a design aiming at best performance.
7. The quality of scientific research is inversely proportional to the measure of the business-like look of the university office.
8. Communication between researchers is like a potential barrier: it keeps the researchers apart, while the passage of the barrier leads to more creative and more fruitful interactions.
9. Liberty of choice in the Dutch educational system limits the efficient distribution of labor forces in the Dutch economy.
10. Cognitive understanding of centrifugal acceleration does not lead to successful application of these forces during speed skating.

These propositions are regarded as opposable and defensible, and have been approved as such by the supervisors Prof. dr. R.F. Mudde and Prof. dr. ir. H.W.M. Hoeijmakers.

Stellingen

behorende bij het proefschrift

Bulk Dynamics of Droplets in Liquid-Liquid Axial Cyclones

Laurens van Campen

1. Bij het optimaliseren van een vloeistof-vloeistof cycloon verandert het streven naar een te hoge azimuthale snelheid de cycloon van een fasescheider in een mixer, ongeacht de andere ontwerpspanningen. (hoofdstuk 7 van dit proefschrift)
2. Zonder toereikende representatie van de turbulente dispersie in de bewegingsvergelijking van de druppel is het niet mogelijk om nauwkeurig de fasescheiding van een vloeistof-vloeistof cycloon opererend onder industriële omstandigheden te voorspellen. (hoofdstuk 6 van dit proefschrift)
3. Vloeistof-vloeistof axiaal cyclonen presteren het beste wanneer het swirlelement zodanig ontworpen is dat in het swirlelement de maximale druppelgrootte gebaseerd op het kritische Weber-getal voor vloeistofstroming gelijk is aan de gemiddelde druppelgrootte stroomopwaarts van het swirlelement. (hoofdstuk 8 van dit proefschrift)
4. Elektrische metingen van de faseverdeling in media met hoge geleidbaarheid kunnen beter de vrije ladingen gebruiken dan de maximale stroom beperken.
5. De immer toenemende mogelijkheden van numeriek onderzoek aan turbulente vloeistof-vloeistof stromingen zullen de validatie met resultaten van experimenteel onderzoek nooit overbodig maken.
6. Het ontwerpen van een experimentele opstelling voor een beperkt budget maakt de kosten van het totale onderzoek hoger dan wanneer het ontwerp gebaseerd is op een optimale werking.
7. De kwaliteit van wetenschappelijk onderzoek is omgekeerd evenredig met de mate van zakelijke uitstraling van het universitaire kantoor.
8. Communicatie tussen wetenschappers is als een energiebarrière: van nature zoekt men elkaar niet op, terwijl het doorbreken van de barrière leidt tot creatievere en meer vruchtbare interacties.
9. De keuzevrijheid in het Nederlandse onderwijs belemmert een efficiënte allocatie van arbeidskrachten in onze economie.
10. Het begrip van centrifugale versnelling leidt niet tot het succesvol toepassen van de betreffende krachten bij het schaatsen van bochten.

Deze stellingen worden opponeerbaar en verdedigbaar geacht en zijn als zodanig goedgekeurd door de promotoren Prof. dr. R.F. Mudde en Prof. dr. ir. H.W.M. Hoeijmakers.

Bulk Dynamics of Droplets in Liquid-Liquid Axial Cyclones

Bulk Dynamics of Droplets in Liquid-Liquid Axial Cyclones

PROEFSCHRIFT

ter verkrijging van de graad van doctor
aan de Technische Universiteit Delft,
op gezag van de Rector Magnificus prof. ir. K.C.A.M. Luyben,
voorzitter van het College van Promoties,
in het openbaar te verdedigen op woensdag 8 januari 2014 om 15:00 uur

door

Laurens Joseph Arnold Marie van Campen

natuurkundig ingenieur
geboren te Nijmegen

Dit proefschrift is goedgekeurd door de promotoren:

Prof. dr. R.F. Mudde

Prof. dr. ir. H.W.M. Hoeijmakers

Samenstelling promotiecommissie:

Rector Magnificus

voorzitter

Prof. dr. R.F. Mudde

Technische Universiteit Delft, promotor

Prof. dr. ir. H.W.M. Hoeijmakers

Universiteit Twente, promotor

Prof. dr. J.G.M. Kuerten

Technische Universiteit Eindhoven

Prof. dr. O.J. Nydal

Norwegian University of Science and Technology

Prof. dr. ir. B.J. Boersma

Technische Universiteit Delft

Prof. dr. ir. H.E.A. van den Akker

Technische Universiteit Delft

ir. P.H.J. Verbeek

FMC Technologies

Prof. dr. ir. C.R. Kleijn

Technische Universiteit Delft, reservelid

The work in this thesis is part of project OG-00-004 *Development of an Ω^2R separator focusing on oil/water separation* of the Institute for Sustainable Process Technology (ISPT).

Printed by: GVO drukkers & vormgevers B.V. | Ponsen & Looijen, Ede

ISBN 978-90-6464-736-9

Copyright ©2014 by L.J.A.M. van Campen

All rights reserved. No part of the material protected by this copyright notice may be reproduced or utilized in any form or by any means, electronic or mechanical, including photocopying, recording, or by any information storage and retrieval system, without written permission from the author.

Is the Moon there when nobody looks?
David Mermin, 1985

Abstract

Separation of oil and water is an essential step in the treatment of the production streams from fossil oil wells. Settling by gravity is a robust though voluminous process and therewith expensive method at remote locations, leading to a need for smaller separation equipment. In this thesis, we describe the research performed on the development of an inline axial cyclone for oil/water separation.

This work is part of ISPT project OG-00-004 and has an experimental nature: a flow rig has been constructed to test different cyclones at flow rates up to 60 m³/h in a 10 cm diameter tube in which brine and low-viscosity lubricant oil can be mixed in almost any proportion. Results are compared with numerical datasets resulting from the same ISPT project.

Three different swirl elements have been developed for this project: a strong swirl element and a weak swirl element with 10 cm diameter, and one element with a 26 cm diameter in combination with a tapered tube section. For all three swirl elements, the velocity profile of water has been measured with Laser Doppler Anemometry (LDA). The strong swirl element has a swirl number of 3.7, the weak of 2.3 and the large diameter element of 3.9. The axial velocity profile normalized with the bulk velocity shows vortex breakdown (upstream flow in the center), where the severeness of the breakdown normalized with the upstream bulk velocity shows proportionality with the swirl number. For the azimuthal velocity, the velocity profile was proportional to the bulk velocity. The non-dimensional azimuthal velocity was similar for all three swirl elements in the region $|r/D| < 0.2$. Outside that region the relative velocity is strongly influenced by the swirl element.

Time series obtained with single phase LDA studies were used to estimate the effect of turbulent dispersion on droplet trajectories. A simplified equation of motion based on centrifugal buoyancy, drag and turbulent dispersion was solved for many fictitious droplet paths. The measured, chaotic axial velocity time series was used to mimic the radial component of the velocity fluctuations. With this model, we can predict the smallest droplet size that can be separated with a certain cyclone and the largest droplet size before it is broken by the flow. Model results show good agreement with overall bulk data obtained in the experimental flow rig.

With an intrusive endoscope technique, we measured the droplet size distribution at various positions in the axial cyclone. From this, Hinze's theory for the droplet size in turbulent pipe flow is confirmed. Furthermore, the inverse correlation between azimuthal velocity and median droplet size is shown and quantified: a lower velocity allows larger droplets to survive.

Different designs were tested to understand which parameters have a large influence on the industrially relevant parameter of separation performance. This question is answered by variation of the swirl element, swirl tube length, pickup tube diameter, flow rate and droplet size. Changes that affect the droplet size have a severe effect on separation, these are the swirl element and flow rate. Changes that increase the droplet size lead to better phase separation. The other geometrical changes can be used to optimize performance, but are not identified as parameters leading to breakthrough improvements.

Two non-dimensional numbers can be used to explain the behavior of the cyclone: the Weber number (We) based on the droplet size upstream of the swirl element and the maximum velocity obtained in the gaps of the swirl element, and the Reynolds number (Re_θ) for the droplets downstream of the swirl element based on their median diameter and the azimuthal liquid velocity. Separation is better for a smaller We number, because droplets are less vulnerable for breakup under that condition. A large Re_θ number is beneficial since the droplets then experience a large centrifugal acceleration which is larger than turbulent dispersion. Both trends are confirmed with experimental data obtained in this project. We propose that there is a function for the maximum possible separation efficiency based on both non-dimensional numbers. The inverse coupling between We and Re_θ via the azimuthal velocity makes optimization of separation efficiency difficult. Application of a large diameter swirl element (low velocity and therefore limited droplet breakup) in combination with a gradual tapering of the tube (increasing the azimuthal velocity) is a possibility to obtain both a large We and Re_θ number. Another option is to place multiple axial cyclones in series, with a stepwise increase of the swirl strength in each subsequent cyclone. In such a configuration, each step is capable of separating smaller droplets than the previous step, without immediate breakup of large droplets. This method should increase the overall quality of the phase separation.

Samenvatting

De scheiding van olie en water is een noodzakelijke stap in de behandeling van de vloeistofstroom uit een fossiele oliebron. Scheiding gebaseerd op het uitzakken van de gedispergeerde fase in een zwaartekrachtsveld is een robuust, maar volumineus proces en daardoor duur bij toepassing in installaties op afgelegen locaties zoals oceanen. Er is daarom behoefte aan kleinere apparatuur voor olie/waterscheiding. In dit proefschrift beschrijven we onderzoek dat we hebben verricht naar de ontwikkeling van een axiaal cycloon in lijn voor olie/waterscheiding. Dit onderzoek maakt deel uit van ISPT project OG-00-004 en is experimenteel van aard. Een proefopstelling is gebouwd om verschillende cyclonen te testen bij debieten oplopend tot $60 \text{ m}^3/\text{u}$ in een buis met 10 cm doorsnede. Als werkvloeistoffen werden pekewater en laag viskeuze smeerolie gebruikt, die in vrijwel elke onderlinge verhouding gemengd konden worden. De experimentele resultaten zijn vergeleken met numerieke data die verkregen waren binnen hetzelfde ISPT project.

Drie verschillende swirlelementen zijn ontwikkeld voor dit project: een sterk en zwak element, met elk 10 cm diameter en een groot element met een diameter van 26 cm. Dit laatste element werd gecombineerd met een toelopend buisdeel om het aan te sluiten op de 10 cm buis met roterende stroming. Voor alle drie de elementen hebben we het snelheidsprofiel gemeten met Laser Doppler Anemometrie (LDA). Het sterke swirlelement heeft een swirlgetal van 3,7, het zwakke van 2,3 en het grote van 3,9. Alle drie de snelheidsprofielen vertonen het vortex breakdown verschijnsel. De met de bulksnelheid genormaliseerde snelheidsprofielen vertonen evenredigheid met het swirlgetal. De azimuthale snelheid is voor elk swirlelement recht evenredig met de bulksnelheid stroomopwaarts van het swirlelement. Het azimuthale snelheidsprofiel gedeeld op de bulksnelheid was voor elk van de drie swirlelementen gelijk in het gebied $|r/D| < 0.2$. Buiten dat gebied heeft het swirl-element sterke invloed op de azimuthale snelheid.

Op basis van de met LDA verkregen lokale snelheid als functie van de tijd hebben we het effect bekeken van turbulente dispersie. We gebruikten een versimpelde bewegingsvergelijking, gebaseerd op de centrifugaal opwaartse kracht, wrijving en turbulente dispersie, om druppelpaden op te lossen voor veel fictieve druppels. De middels metingen verkregen tijdseries van de axiale snelheid, met een turbulent karakter, werden gebruikt om de snelheidsfluctuaties in de radiële richting na te bootsen. Het model voorspelt de grootte van de kleinste druppels die afgescheiden kunnen worden met een bepaald type cycloon en ook de maximale grootte van

druppels voordat ze door de vloeistofstroming zullen worden opgebroken. De resultaten van het model komen goed overeen met de rendementsdata gemeten in de experimentele opstelling.

De druppelgrootteverdeling is gemeten met een endoscoop welke op verschillende plaatsen in de buis met de roterende stroming is gestoken. De theorie van Hinze, die de druppelgrootte voorspelt voor een turbulente pijpstroming, is hiermee gevalideerd voor onze opstelling. Verder tonen de metingen de inverse relatie aan tussen de azimuthale snelheid en de mediaan van de druppelgrootte, waarvoor we een kwantitatief voorspellend model voorstellen: een lage snelheid laat grote druppels overleven.

Verschiedende ontwerpen zijn getest om grip te krijgen op de grootheden die van belang zijn bij het ontwerpen van cyclonen voor toepassing in de industrie. Gevarieerde parameters zijn: het swirlelement, lengte van de swirlbuis, diameter van de opvangbuis voor de lichte fase, debiet en druppelgrootte. Elke verandering die de druppelgrootte beïnvloedt, heeft een groot effect op het scheidingsrendement: veranderingen die leiden tot grotere druppels leiden tot een betere fasescheiding. De andere geometrieveranderingen hebben wel invloed op het scheidingsrendement, maar zullen niet tot schokkende verbeteringen leiden in de fasescheiding.

Het gedrag van onze cycloon kan ook worden gevat in twee niet-dimensionele kentallen: het Webergetal (We), gekozen voor druppels met de grootte stroomopwaarts van het swirlelement met de snelheid die ze zullen halen ter hoogte van het swirlelement, en het Reynoldsgetal (Re_θ) gedefinieerd voor druppels stroomafwaarts van het swirlelement met hun azimuthale snelheid en de mediaan van hun druppelgrootte. Een kleiner We -getal leidt tot betere scheiding, omdat druppels dan minder gevoelig zijn voor opbreking. Een groter Re_θ -getal is gunstig: de druppels ervaren dan een centrifugale versnelling die de turbulente dispersieve effecten beter overwint. Beide trends worden bevestigd met experimentele data verkregen in dit project, en we stellen voor dat elk getal de afhankelijke is van een functie die de maximaal haalbare scheiding begrenst. Vanwege de inverse koppeling tussen het Weber- en Reynoldsgetal via de azimuthale snelheid, is het maximaliseren van het scheidingsrendement erg moeilijk. Het toepassen van een swirlelement met grote diameter (lage snelheid en dus druppelafbreking), gevolgd door een geleidelijke vernauwing van de swirlbuis (verhoogt de azimuthale snelheid) is een mogelijkheid om zowel het We - als het Re_θ -getal groot te maken. Een andere optie is om cyclonen in serie te zetten met in elke opvolgende stap een toenemende swirlsterkte. Zo scheid je steeds kleinere druppeltjes af, zonder in de eerste stap de grote druppels direct kapot te breken.

Contents

Abstract	vii
Samenvatting	ix
Nomenclature	xv
1 Introduction	1
1.1 Need for cyclones	1
1.1.1 Crude oil production	1
1.1.2 Oil extraction	1
1.1.3 Cyclones are compact	2
1.2 Characterization of cyclones	3
1.3 Previous work	4
1.4 Project organization	4
1.5 Present work	5
2 Experimental facility for oil/water flow	7
2.1 Dimensions and scaling	7
2.2 Description of the parts	8
2.3 Operating procedures	14
2.3.1 Startup	15
2.3.2 Operating window	15
2.3.3 Shutdown	15
2.3.4 Maintenance operations	18
2.4 Consistency of results	18
2.4.1 Reproducibility	18
2.5 Durability of the process liquids	22
2.5.1 Possible causes	23
2.6 Facility for rotating swirl element	28
2.7 Conclusion	28
3 Experimental methods	31
3.1 Laser Doppler Anemometry	31
3.1.1 LDA apparatus	31
3.1.2 Measurement volume	32
3.1.3 Tracer particles	32

3.1.4	Traversing system	34
3.1.5	Void kernel	35
3.2	Numerical method	35
3.2.1	Single Phase	36
3.2.2	Two Phase Flow	36
3.3	Efficiency measurements	37
3.4	Droplet sizing	37
3.4.1	Direct photography with an endoscope	38
3.4.2	Liquid sampling and off-line analysis	42
3.4.3	Glass fiber sensor	45
3.4.4	Comparison of methods	47
3.5	A novel capacitance based wiremesh technique	47
3.5.1	Introduction	47
3.5.2	Geometry	49
3.5.3	Electric fields	49
3.5.4	Measurement circuit	52
3.5.5	Fluid-sensor interaction	55
3.5.6	Visualization of an oil kernel	55
3.5.7	Discussion and Conclusion	56
4	Strength of generated swirl	59
4.1	Theory	59
4.1.1	Force balances	59
4.1.2	Droplet elongation	62
4.1.3	Time scales	62
4.2	Swirl element design	65
4.2.1	Strong swirl element	65
4.2.2	Weak swirl element	71
4.2.3	Large swirl element	72
4.2.4	Tapered tube section	74
4.3	Profile of the swirling flow	75
4.3.1	Experimental conditions	77
4.3.2	Strong swirl element	77
4.4	Properties of swirling flow	79
4.4.1	Vortex decay	79
4.4.2	Precessing Vortex Core	80
4.4.3	Detail at the pick-up tube	81
4.5	Influence of operational parameters	84
4.5.1	Flow split effect	84
4.5.2	Effect of flow rate	87
4.6	Conclusion	88
4.6.1	Prediction of the velocity profile	89
4.6.2	Operational effects on phase separation	91
5	Dispersed droplets in dilute swirling flow	93
5.1	Theory	93
5.2	Droplet model	98

5.2.1	Equation of motion	98
5.2.2	Experimental input to the model	99
5.2.3	Numerical implementation	101
5.2.4	Droplet break-up	103
5.3	Dilute droplets simulation results	104
5.3.1	Smallest separated droplets	106
5.3.2	Droplet break-up	106
5.3.3	Separation window	110
5.4	Conclusions	111
5.5	Outlook	113
6	Droplet break-up and coalescence	115
6.1	Droplet size upstream of the swirl element	115
6.1.1	Turbulent liquid-liquid pipe flow	115
6.1.2	Droplet size reduction with valves	117
6.2	Droplet size reduction with a swirl element	117
6.2.1	Model of the break-up in a swirl element	117
6.2.2	Experimental results	120
6.3	Droplet coalescence inside the cyclone	123
6.4	Conclusion	125
7	Analysis of swirl separation performance	127
7.1	Geometric optimization	127
7.1.1	Swirl element type	127
7.1.2	Swirl tube length	128
7.1.3	Pick-up tube diameter	130
7.2	Operational optimization	132
7.2.1	Flow split	132
7.2.2	Flow rate	135
7.2.3	Droplet size	141
7.2.4	Phase inversion	141
7.3	Static versus Rotating element	144
7.4	Conclusion	144
8	Design considerations for Liquid-Liquid Cyclones	147
8.1	Scaling parameters	147
8.1.1	Reynolds number	147
8.1.2	Weber number	148
8.2	Prediction of current swirl elements	149
8.2.1	Method	149
8.2.2	Reynolds depends on Weber	149
8.2.3	Optimal point of operation	151
8.2.4	Dependence on droplet size	151
8.3	Guide on cyclone design	151
8.3.1	Input parameters	153
8.3.2	Single cyclone design	153
8.3.3	Multi-stage cyclone design	154

8.3.4	Sizing	156
8.3.5	Process control	159
8.3.6	Swirl element design	159
8.4	Concluding remarks	159

Bibliography	161
---------------------	------------

A Description of swirling flow	165
A.1 Governing equations	165
A.2 Empirical description of swirling flow	166
A.3 Swirl number	167
A.4 Advanced concepts	168
A.4.1 Vortex Breakdown and flow reversal	168
A.4.2 Time-independent instabilities	168

B Estimation of turbulence parameters	171
B.1 Turbulence	171
B.2 Method	172
B.3 Result	173

C Uncertainty analysis	175
C.1 Accuracy of the measurement equipment	175
C.2 Oil Concentration in outputs	176

D Drag relation for a sphere	179
-------------------------------------	------------

List of publications	181
-----------------------------	------------

Acknowledgements	183
-------------------------	------------

Curriculum Vitae	187
-------------------------	------------

Nomenclature

Roman Symbols

Symbol	Description	S.I. units
A	Area	(m ²)
B	Magnetic induction	(N/Am)
C	Electrical capacity	(C/V)
D	Electric displacement	(C/m ²)
C_d	Empirical swirl decay parameter	(-)
C_D	Drag coefficient	(-)
D	Tube diameter	(-)
D_d	Droplet diameter	(m)
D_f	Diameter of flow area	(m)
E	Electric field	(V/m)
F_b	Buoyancy force	(N)
F_c	Centrifugal force	(N)
F_d	Drag force	(N)
I	Electrical current	(A)
J	Bessel function	(-)
J	Impulse	(Ns)
J_d	Displacement current	(A/m ²)
L	Angular momentum	(kg m ² /s)
L	Length	(m)
R	Electrical Resistance	(Ω)
U	Electric potential	(V)
V	Electrical potential difference	(V)
V_d	Droplet Volume	(m ³)
a	Sphere radius for light scattering	(m)
c	Volumetric oil Concentration	(-)
d	Inter-plane distance	(m)
$d_{e^{-2}}$	Diameter of incoming laser beam	(m)
f	Focal length	(m)
g	Gravity constant	(m/s ²)
k	Wave Number	(1/m)

Roman Symbols (continued)

Symbol	Description	S.I. units
k_g	Geometry factor	(m)
ℓ	Turbulent eddy size	(m)
m_d	Droplet mass	(kg)
n	Refractive index	(-)
	Particle size distribution	(-)
p	Pressure	(Pa)
p	Momentum	(kg m/s)
r	Radial position	(m)
r_p	Radial position of a droplet	(m)
t	Shear	(N/m ²)
u	continuous phase velocity	(m/s)
u_θ	azimuthal component of the continuous phase	(m/s)
u_r	radial component of the continuous phase	(m/s)
u_z	axial component of the continuous phase	(m/s)
v	Particle velocity	(m/s)
v_θ	Tangential component of the particle velocity	(m/s)
v_r	Radial component of the particle velocity	(m/s)
v_z	Axial component of the particle velocity	(m/s)
v_r	radial velocity	(m/s)
v_θ	azimuthal velocity	(m/s)
v_{term}	terminal velocity	(m/s)
v_z	axial velocity	(m/s)
w	Wire distance	(m)

Greek symbols

Symbol	Description	S.I. units
Φ	Flowrate	(m ³ /s)
α	Angle	(°)
λ	Wavelength	(m)
ϵ	Electric permittivity	(F/m)
ϵ	Turbulent dissipation rate	(m ² /s ³)
ϵ_0	Vacuum permittivity, $1/\mu_0 c^2$	(F/m)
η	Efficiency	(-)
$\dot{\gamma}$	Strain rate	(1/s)
μ_c	Dynamic viscosity of the continuous phase	(Pa s)
μ_d	Dynamic viscosity of the dispersed phase	(Pa s)
μ_0	Vacuum permeability, $4\pi \cdot 10^{-7}$	(kg m/(As) ²)
ν	Kinematic viscosity	(m ² /s)
ρ_c	Density of the continuous phase	(kg/m ³)
ρ_d	Density of the dispersed phase	(kg/m ³)
$\Delta\rho$	Density difference	(kg/m ³)
σ	Interfacial tension	(N/m)
τ	Characteristic time scale	(s)
τ_p	Particle relaxation time	(s)
θ	Angle	(°)
ω	Frequency	(1/s)

Dimensionless groups

Group	Formula	Description
Azimuthal Reynolds	$\text{Re}_\theta = \frac{v_\theta D}{\nu}$	Intertial forces in the azimuthal direction over viscous forces
Capillary	$\text{Ca} = \frac{\mu v_f}{\sigma}$	Viscous forces over interfacial tension forces
Reynolds	$\text{Re} = \frac{u_b D}{\nu}$	Intertial forces over viscous forces
Shear Reynolds number	$\text{Re}_G = \frac{D^2}{\nu_c} \frac{du}{dy}$	Intertial force due to shear over the viscous force
Strouhal	$\text{St} = \frac{fD}{v}$	Frequency of oscillations in the wake of a cylinder
Swirl	$\Omega = \frac{2 \int_0^R u_z u_\theta r'^2 dr'}{R^3 u_b^2}$	Angular momentum flux per unit of mass flux
Weber	$\text{We} = \frac{t D_d}{\sigma}$	Shear force over interfacial tension force

Abbreviations

Name	Description
AISI	American Iron and Steel Institute
CFD	Computational Fluid Dynamics
CFX	Commercial CFD solver
DC	Direct Current
EPDM	Ethylene Propylene Diene Monomer
FS	Flow Split
GC	Gas Chromatogram
HPO	Heavy Phase Outlet
HZDR	Helmholtz Zentrum Dresden Rossendorf
ISPT	Institute for Sustainable Process Technology
LDA	Laser Doppler Anemometry
LPO	Light Phase Outlet
MSDS	Material Safety Data Sheet
NaCl	Sodium Chloride (table salt)
NBR	Nitrile Butadiene Rubber
PMMA	Poly Methyl MethAcrylate (polymer)
PP	Poly Propylene (polymer)
PTFE	Poly Tetra Fluoro Ethylene (Teflon)
PVC	Poly Vinyl Chloride (polymer)
RSM	Reynolds Stress Model
SDS	Sodium Dodecyl Sulfate (surfactant)

CHAPTER 1

Introduction

1.1 Need for cyclones

1.1.1 Crude oil production

Since the modern age discovery of fossil oil as illumination fluid by Edwin Drake in 1859 [1], both production and consumption of fossil fuels have grown to a level at which present day society cannot exist without. The extensive exploration of oil fields first focussed on “easy oil”, being shallow fields that are onshore and which are pressurized enough to produce liquids without additional aid. Nowadays, crude production has shifted to remote onshore locations and mainly off shore deep-water locations, where advanced techniques are deployed to retrieve as much crude as possible from the fields.

1.1.2 Oil extraction

Oil is formed in the subsurface by conversion of organic material under anaerobic conditions. Due to its low density compared with soil material as well as water, buoyancy moves the oil to the surface. Only if an impermeable material is present in a dome shape that can capture the rising liquid, the oil is trapped underneath. Water present in the soil is in general also less dense compared with its surroundings, and rises as well. Due to the density difference between oil and water, we typically find oil underneath an impermeable salt formation with water below the oil. Figure 1.1 depicts such a geological system. The regions indicated with “oil” and “water” are porous rocks containing the liquids.

To produce oil from a field as in figure 1.1, a well is drilled. Due to the overpressure, oil flows into the vertical tube. Mature fields, which are at lower pressure, are often mechanically assisted, for example using pumpjacks. Due to the viscosity difference of oil and water, water is more mobile as a result of which water ‘fingers’ around the oil and flows into the wellbore before all oil is produced. Due to this phenomenon, most of the time a mixture of oil and water is produced from the oil

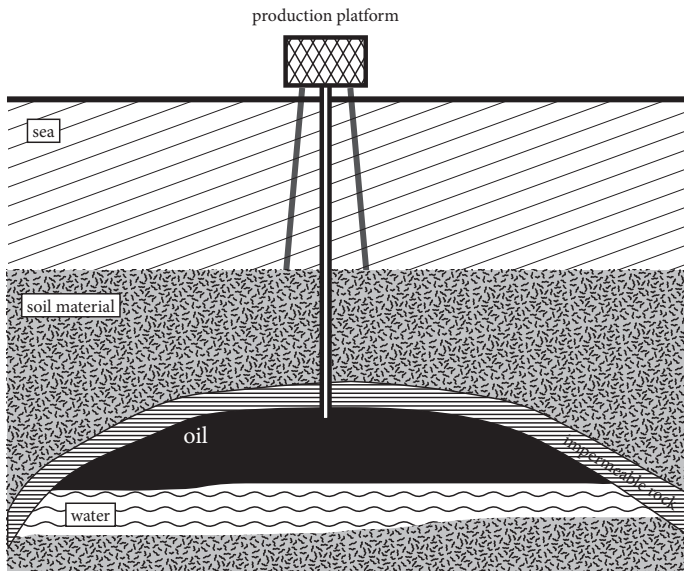


Figure 1.1: Schematic of a sub-sea oil field.

well, which requires separation in downstream process equipment.

Two current developments in the production of crude oil lead to a demand for new separation equipment: (i) an increasing amount of fossil fuels is produced offshore, with a high constructional cost of the platform and (ii) fields are produced for a longer period of time, leading to higher water concentrations (water cuts). From an economical perspective, it is desirable to separate the oil and water flow close to the well to avoid costs for transportation of non-commercial water. Typical requirements for the downstream side of the separation process is to have less than 30 ppm oil in water (legal limit to dump it overboard) and to have less than 0.5 % vol. water in oil (acceptable limit for a refinery).

1.1.3 Cyclones are compact

For bulk separation, the density difference between oil and water is a suitable physical property to exploit. The conventional way is to employ a large vessel, in which the residence time under continuous operation is long enough to allow separation of phases by gravity. The required large size to meet the requirements discussed in the preceding section leads to high investments in offshore separation equipment. Cyclones use centrifugal acceleration to separate phases with a different density, in which the acceleration can be orders of magnitude larger than that of gravity. Cyclones are therefore a promising alternative for the bulky gravity-based separation equipment.

1.2 Characterization of cyclones

Cyclones are used in many different fields for various combinations of phases. The research on cyclones typically focuses on a specific combination of phases:

- gas/solid;
- gas/liquid;
- liquid/solid;
- liquid/liquid.

Although the underlying physics is similar for all of these combinations, there are differences. A liquid cyclone is less turbulent due to the higher viscous forces, though the interfacial chemistry between the phases can cause liquid-liquid emulsions. A gas cyclone typically has the advantage of a large density difference, though a risk for gas/liquid emulsions (foam). A cyclone with a solid dispersed phase cannot suffer from break-up effects, although there can be attrition.

There are some design choices that make a significant difference for the type of cyclone:

- **Inlet geometry:**
 - tangential: the input stream is typically distributed over multiple tubes that are tangentially connected to the cyclone, equidistantly distributed over the circumference;
 - axial: a static swirl element with vanes accelerates the liquid in azimuthal direction;
- **Swirl tube geometry:**
 - traditional: a shape with a conical-shaped reduction of the tube diameter from inlet to outlet of the heavy phase; this is the typical shape of a hydrocyclone;
 - cylindrical: no diameter reduction of the tube diameter - this design is adopted to reduce the required space of a cyclone;
- **Flow direction:**
 - counter current: the heavy phase outlet (HPO) is at the downstream side, the light phase outlet (LPO) at the upstream side (as seen from the inflow);
 - co-current: both outlets are positioned at the downstream side.

1.3 Previous work

The first cyclone aimed at phase separation was patented in 1891 by Bretney [2]. Extensive use, however, did not start before the 1950s [3]. The use of cyclones for removal of solid particles from a gas stream was the first major application. The large density difference and the particles being solid makes the separation of these streams relatively easy. The next development step were gas-liquid cyclones, for which the density difference is large, but additional difficulties are introduced through the possible breakup of droplets. The first application for liquid-liquid flow dates back to around 1980 (see Colman et al. [4]). The earlier systems had a traditional cyclone design, with tangential inlets, a conical body and counter-current flow. Dirkzwager [3] introduced an axial cyclone with a static in-line swirl element to decrease the turbulence production and pressure drop. However, his research was limited to single phase flow only.

In recent years, the research focused on different aspects. Numerical work concentrated on single phase cyclones in order to understand the flow phenomena occurring in the strong vortex flows. These results are compared with experimentally obtained data, e.g. Lu et al. [5], who applied a Reynolds stress model and compared predicted results with laser Doppler measurements. Also multiphase numerical work is conducted, e.g. Paladino et al. [6], Noroozi and Hashemabadi [7], Schütz et al. [8], Amini et al. [9], usually the comparison with experimental data was limited to the separation efficiency, but discrepancies were not understood.

Experimental studies focused primarily on the optimization of the separator design. For example Young et al. [10] carried out an optimization study of the separator dimensions, Oropeza-Vazquez et al. [11] proposes a cylindrical geometry with azimuthally positioned inlets and Husveg et al. [12] examines the cyclonic separator efficiency as function of the liquid intake.

1.4 Project organization

The work described in this thesis is part of Institute for Sustainable Process Technology (ISPT) project OG-00-004 “Development of an $\Omega^2 R$ separator focusing on oil/water separation” in which four industrial partners (FMC Separation Systems, Frames Separation Technologies, Shell and Wintershall) cooperate with three universities (Delft University of Technology, University of Twente and Wageningen University). The project aims at increasing the understanding of the physics involved in liquid-liquid axial cylindrical cyclones and using this knowledge to test design improvements.

Previous work did not fully resolve the fundamental of liquid-liquid cyclones lagging behind compared to gas-solid and gas-liquid cyclones. Two phenomena make an accurate prediction of the flow in a liquid-liquid cyclone difficult: (i) effects of turbulence in the strong (non-isotropic) swirling flow is difficult to model and

(ii) the breakup and coalescence of droplets is not fully understood, let alone that predictions can be made for millions of droplets in a cyclone. A direct numerical simulation is well beyond the capability of current computing power, with smallest scales to be resolved in the μm range and the integral scale in the meter range.

This project therefore exploits different means to gain understanding of cyclones and to improve design. At Twente University, PhD student Slot [13] performed numerical single and multiphase work on the design of the axial cylindrical cyclones used in the present thesis, the resulting fluid flow and on predicting separation with the Euler-Euler approach. The lack of a decent model of droplet break-up and of coalescence and turbulent dispersion hamper the accuracy of the results of these simulations. A postdoc in Wageningen (see Krebs et al. [14]) performed detailed experimental studies on droplet-droplet collisions and droplet breakup. This served as input for the numerical work in Twente. The present thesis presents the bulk separation; these results were compared to the separation process data discussed in the Twente thesis. The final conclusions aim at improved understanding of droplet break-up and coalescence effects in a physical bulk separation system system, as well as improved understanding of the effects of turbulent dispersion on phase separation.

1.5 Present work

Chapters 2 and 3 of this thesis introduce the flow rig and the experimental methods used to examine the flow. Results are ordered in the next four chapters.

Swirl The coupling between the static swirl element and resulting fluid flow is an important factor for the understanding and prediction of the performance of cyclones. In chapter 4 both the design and the resulting fluid flow are investigated. Furthermore, various sources in literature [3, 15, 16, 17] indicate the unsteady and non-axi-symmetric nature of swirling flows. Based on the velocity data of chapter 4 the time-dependencies involved in the system used during this research are discussed.

Turbulence Balancing only centrifugal buoyancy and drag results in a finite terminal velocity in the radial direction for all droplets, which would enable perfect separation. Turbulent dispersion, however, disturbs separation. Chapter 5 quantifies the effect of turbulence based on the single-phase, experimental LDA data from chapter 4. We relate the smallest captured droplet size to the swirl strength.

Droplet size Acceleration of droplets and shear in liquids affect the maximum stable droplet size and therewith the droplet size distribution. Since both acceleration and shear are present in cyclones, droplets will be broken. In chapter 6 the droplet break up is quantified, based on liquid velocity and swirl strength, at different locations upstream, downstream and inside the cyclone.

Design Chapter 7 evaluates a selected set of design parameters, such as diameter and vane angle. The effects of these variations are compared based on separation efficiency, from which for each parameter the importance in the design process is deduced. The work in this chapter has a somewhat empirical nature, since not all mechanisms are completely understood. Only the effect on separation is evaluated.

Results of the four preceding chapters are combined in chapter 8 to provide rules for the design of axial cyclones. The most important conclusion links the droplet breakup by acceleration to the required azimuthal velocity to achieve adequate separation, based on a non-dimensionalized dataset.

CHAPTER 2

Experimental facility for oil/water flow

This chapter describes the experimental facility built for the investigations presented in this thesis. It serves as a reference for the other chapters.

All parts of the experimental rig are introduced, we describe the typical measurement procedure, the resulting droplet size upstream of the swirl generation and the accuracy of the results. The design of the measurement section is not part of this chapter, but is extensively discussed in chapter 3.

2.1 Dimensions and scaling

A flow rig was constructed to investigate the swirl based separation process. The rig used in this project is located in the Kramers Laboratory, Prins Bernhardlaan 6 in Delft. The rig was designed to test the separation characteristics of an industrially relevant system. Since no standards exist for industrially relevant flows, the following choices were made:

Bulk velocity:	2.0 m/s
Tube diameter:	100 mm
Working fluids:	brine (9 wt% NaCl) mineral oil

Brine is used instead of water to provide more realistic field conditions and to allow comparison with Shell's Multiphase Test Facility in Rijswijk (The Netherlands). The broad range in viscosity of mineral oils requires a further narrowing down of the specifications. Tests with oils having a kinematic viscosity up to $150 \text{ mm}^2/\text{s}$ should be possible. The setup was designed such that the oil fraction fed to the system can range from 0 to 1.

The choices above provide the requirements for the material selection, pump capacity and downstream separation specifications. The main construction materials are Poly Vinyl Chloride (PVC) and stainless steel AISI 316L. Both materials are resistant to mineral oil as well as brine. The main tubing is made out of PVC, due to

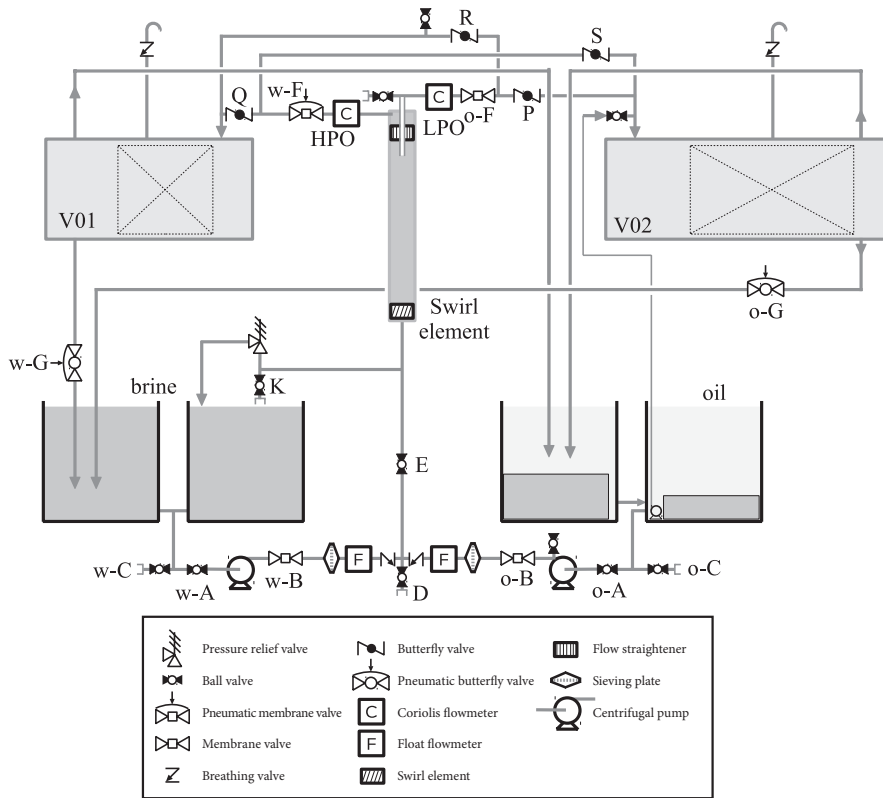


Figure 2.1: Scheme of the flow rig, status during the final experiments.

its relatively low price compared to stainless steel and good machining qualities. Pumps, valves and other appendages are made out of stainless steel AISI 316L. In the subsequent sections the various parts of the rig are discussed. One of the process liquids is brine, a solution of 9 wt% NaCl in tap water. Due to the electric conductivity and especially the presence of Cl^- ions, brine promotes corrosion of metals.

2.2 Description of the parts

Figure 2.1 presents a chart of the flow rig. This section describes the parts in the rig, starting with the storage vessels, continuing in the streamwise direction with the subsequent parts.

Storage vessels

The system contains 9.0 m^3 brine (100 kg NaCl per 1000 kg tap water) and 4.0 m^3 lubricant oil (density: 881 kg/m^3 at 15°C , kinematic viscosity: $19 \text{ mm}^2/\text{s}$ at 20°C). Both liquids are kept in separate storage vessels at the ground level (indicated with

“brine” and “oil” in figure 2.1, picture in figure 2.4). These vessels are made out of Poly Propylene (PP) which is strongly hydrophobic and inert for the applied liquids. In total there are 4 vessels of 2.5 m^3 each, two for brine and two for oil.

The centres of the outflow openings in the storage vessels are positioned about 15 cm above their bottom surface. It is therefore not possible to empty these vessels completely by gravity. For the oil storage vessel, a brine layer will form underneath the oil phase. During operation, this brine layer can slip into the feed line of the pump. High shear levels generated by the centrifugal pump result in small droplets that are hard to separate downstream. Brine flowing into the oil feed line also introduces an error in the measured oil flow rate. This problem is reduced by place holders at the bottom of the two oil storage vessels. These place holders reduce the available volume for water holdup. A small submerged pump removes continuously the liquids from 1 cm above the bottom of the vessel to reduce the remaining effect. Figure 2.1 presents the detailed positioning of the place holder and submerged pump in the right oil storage vessel.

Both the water vessel and the oil vessel are connected to the pumps with 10 cm diameter PVC tubes. Both connections can be closed with a ball valve with a PTFE fitting.

Centrifugal pumps with flow meters

Each liquid has its own centrifugal pump (Delta Pompen B.V., type “HPS 50-250”, see figure 2.4) with independent frequency drives. The maximum pressure difference that the pumps can generate is 8.8 bar for tap water at 3000 rpm (50 Hz) rotation. The maximum pressure difference for other liquids has not been measured. All parts that are exposed to the liquid are made out of stainless steel AISI 316L.

Float flow meters (Heinrichs BGN, see figure 2.4) measure the flow rate of each phase, after which they are mixed. The range of these flow meters is 8 to $80 \text{ m}^3/\text{h}$ with an error $\pm 1.6\%$ of the scale’s maximum. The time-averaged output of these flow meters was calibrated against the Coriolis flow meter present in the test rig (see figure 2.1), significantly improving the accuracy of the used flow meters.

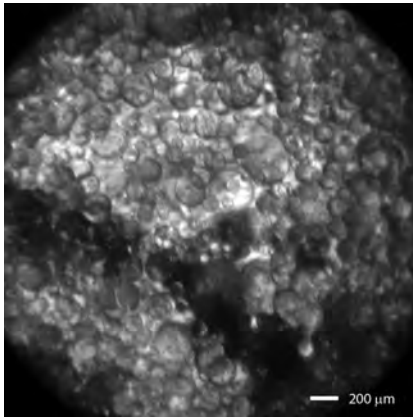
Mixing section

The oil and water phase are combined in a T-junction (see figure 2.4). During the research various parts were used to control the mixing of the two phases, i.e.:

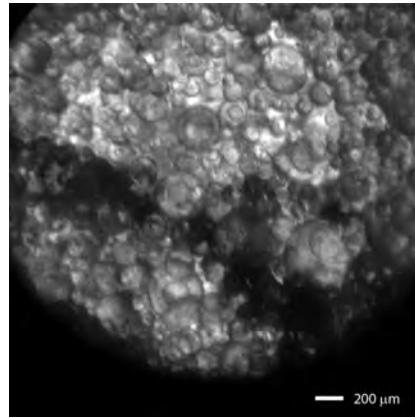
- **Separator plate in the T-junction:** To avoid a head-on collision between the water and oil stream, a separator plate was mounted in the T-junction. This plate changes the liquid momentum in the downstream direction before the phases mix, this reduces shear and therewith droplet breakup.
- **Static mixer:** Used during some experiments, a Primix stainless steel static mixer. This mixer consists of 3 helical elements with a L/D factor of 1.7. The resulting droplet size is specified by the supplier to be $102 \text{ }\mu\text{m}$, however, this was not experimentally verified.

- **Ball valve:** This ball valve can be partially closed to apply shear on the mixture. The shear will result into a broadband droplet size distribution.
- **Honeycomb flow straightener:** This aluminum device was originally mounted to straighten the flow in the single phase LDA experiments. The shear in this element, however, reduced the droplet size from a few hundred microns to the order of magnitude of $100\ \mu\text{m}$.

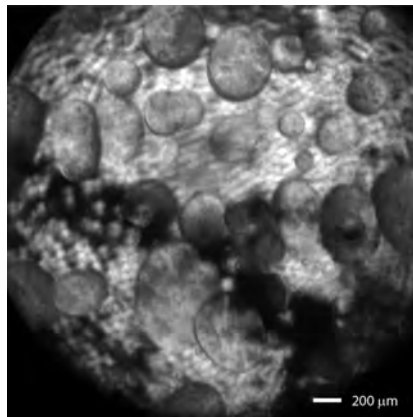
Figure 2.2 demonstrates the effect of these components on the dispersed phase.



(a) upstream: Head on T section and flow straightener



(b) upstream: T section with separation plate and flow straightener



(c) upstream: T section with separation plate and no flow straightener

Figure 2.2: Droplets photographed for different configurations of the rig and at different positions. Flow rate $\Phi = 56\ \text{m}^3/\text{h}$, volumetric oil concentration $c = 0.25$.

Measurement section

The measurement section is the region in which the in-line axial cyclone is placed. Tubes have been used with different lengths. Polymethylmethacrylate (PMMA) was

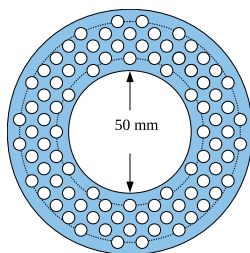


Figure 2.3: Cross section of the flow straightener mounted in the HPO. Diameter of each hole is 5.0 mm.

used for Laser Doppler Velocimetry tests due to its high transparency (see figure 2.5 and 2.15). For the tests in which the length was a parameter of study, the measurement section was made out of transparent PVC.

The swirl element is clamped between two flanges at the upstream side of the measurement section (see figure 2.6), with a flange to center the swirl element mechanically to the tube.

At the downstream side the end of the measurement section is formed by the pickup tube and a flow straightener for the annular region surrounding the pickup tube. The geometry in this region could be changed to promote separation, however, the only variation applied during this work in the outflow region was the diameter of the pickup tube. If not otherwise indicated, the pickup tube is a stainless steel tube with an outer diameter of 50.1 mm and an inner diameter of 46.6 mm. The length of the pickup tube is 234 mm. The flow through the inside of the pickup tube is referred to as Light Phase Outlet (LPO) and the flow through the annular region surrounding the pickup tube is called the Heavy Phase Outlet (HPO). At the downstream side of the pickup tube a flow straightener is placed in the HPO. This flow straightener consists of a 3cm thick block of PVC with 5 mm diameter holes in it, see figure 2.3.

Phase separation in settling tanks

The liquid streams from the HPO and LPO are mixtures that need to be separated into reasonably clean water and oil phases that can be fed back into the corresponding storage vessels. To this end, two stainless steel settling tanks are installed that separate the liquid streams using gravity. Butterfly valves allow the choice which stream (HPO or LPO) runs into which settling vessel (large or small).

The settling tank indicated at the left side of figure 2.1 has a volume of 2.5 m^3 (see also figure 2.7), the tank depicted at the right side has a volume of 4.5 m^3 , in combination with a flat plate to avoid short-circuiting of the flow in the tank. The plate packs and baffle are designed and supplied by Frames as partner of the ISPT project.

The plate packs are parallel stainless steel plates that form small channels. These channels reduce the Reynolds number enough to provide laminar flow. For laminar flow, only buoyancy forces and drag determine the droplet motion in the vertical

direction. The settling velocity using Stokes' drag law equals:

$$v_{\text{term}} = \frac{D_d^2 \Delta \rho g}{18 \mu_c} \quad (2.1)$$

The plate packs installed in the test rig are designed such that maximum separation for the applied liquids is obtained.

The settling tanks are open to the environment at the top via a breathing valve. This valve allows air to freely enter and escape during normal operation, while it blocks the opening with a float when liquid runs in. These valves ensure that the pressure in the system remains larger than zero barg at all times.

Control of the settling tanks

A mixture of oil and brine flows into the settling tanks, while the outflow ought to consist out of pure brine and pure oil. At the side of the outflow of the settling tank there is an oil/brine interface in the tank. The height of this interface is measured in both tanks with a guided wave radar (Rosemount type 3300). Based on this output a pneumatic butterfly valve in the lowest (water) outlet is controlled.

The difference between the actual level and a set point is multiplied with a constant to obtain the valve opening. A delay of 2 seconds is applied to compensate for errors in the measured location of the interface.

The interface set points are changed according to the measurement requirements: large oil flows through a settling tank require a lower interface level to ensure enough residence time of oil in the tank in order to allow time for phase separation.

Digital control

All parts of the rig that can be remotely controlled are such via an in-house developed software package, written in "LabVIEW". The following parts are controlled in this way, see figure 2.1 for the position of all parts:

- **Pump frequency**, individually for the oil and water pump
- **HPO valve**, the relative opening of the membrane valve in the HPO, w-F
- **Water discharge valves**, w-G en o-G

The other actuators are controlled manually.

The following sensors are monitored online via the "LabVIEW" programme:

- **Float flow meters**, for the water and oil inflow, respectively
- **Pressure sensors**, upstream and downstream of the swirl element, as well as in the LPO and the HPO
- **Coriolis flow meter**, in the HPO, measures both mass flow rate and density
- **Level sensor**, in each settling tank

All settings and measurements are stored for all operations with the rig.

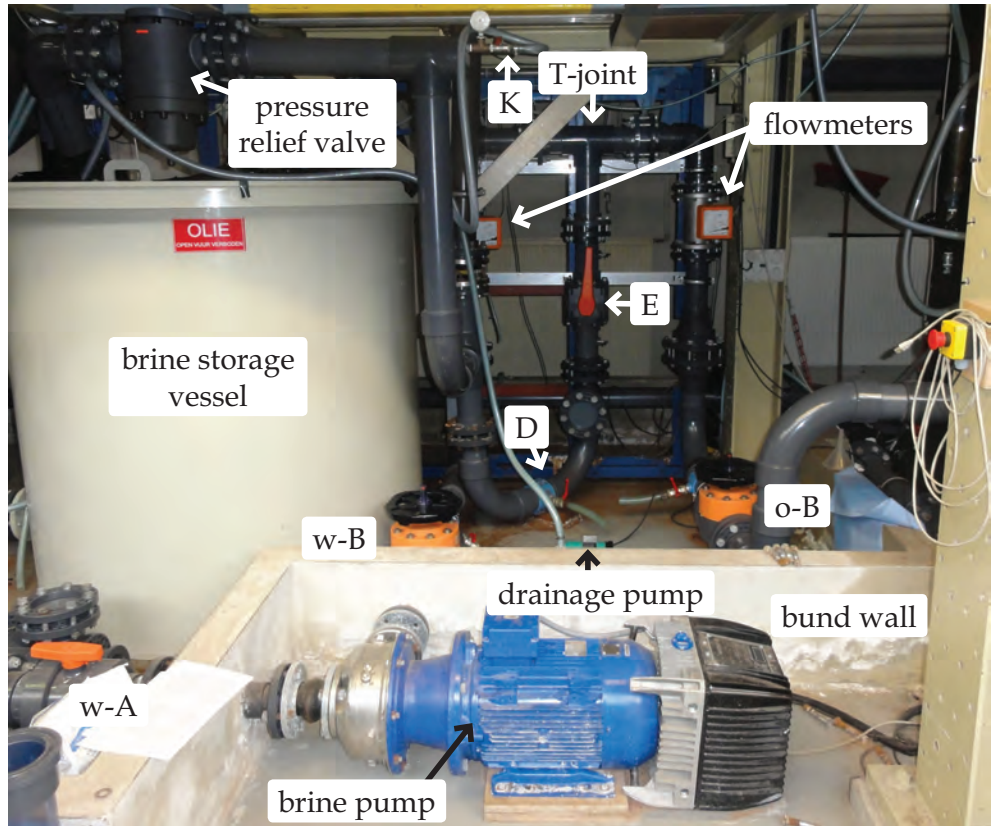


Figure 2.4: Photograph of the lower side of the experimental rig, where most pumps, valves and other controls are. Labels refer to the scheme in figure 2.1. Brine is pumped from the storage vessel, where the flow is measured and controlled with valve w-B into the T-joint, where it is mixed with the oil flow (not on picture). Via an U-bend, the mixed liquid flow in the upward direction to the swirl element.

Pressure rating

The maximum pressure difference generated by the pumps is 8.8 bar. To withstand this pressure, all tubing material used has rating “PN 10” or “PN 16”. The setup was tested at a static pressure of 10 barg. At this pressure only minor leaks from seals occurred.

Various parts of the rig cannot withstand the full pump pressure:

- **the PMMA measurement section** has been tested up to 5.0 barg with no mechanical failure. Therefore, it was decided to allow a maximum pressure for this element of 3.5 barg during normal use.
- **the settling tanks** are designed for a pressure of 0.5 barg. This is ensured via a 100 mm breathing valve at the top of each tank

To avoid exceeding the maximum pressure of the PMMA measurement section (which was mounted only if required for measurements), two safety systems were applied:

1. an electronic pressure sensor that interlocks the pumps when exceeding the pressure set point of 3.5 barg
2. a pressure relieve valve, connected to the system upstream of the swirl element, with a set point of 3.5 barg.

The operating procedures are such that a blockage of the flow is avoided. This procedure avoids exceeding the maximum pressure.

Spill prevention

Both personal and environmental safety was an important aspect during designing and building the flow loop. Emissions of the process liquids to the environment are highly undesirable: brine can cause short-circuiting of electric equipment, lubricant oil easily induces personal injury by slipped-caused falling and both liquids should not run into the sewer system.

To avoid a release of liquids from the rig, a two-fold safety system is applied:

1. all storage vessels are equipped with floats. Before a spill over, this float switches off the pumps and closes valves w-G and o-G (see figure 2.1)
2. a bund wall is built around the setup with enough volume to contain all liquid present in the rig. The pumps are positioned outside the bund, see figure 2.4.

2.3 Operating procedures

This section discusses the typical conditions during which the experimental rig was used and the procedures applied for start up, working and shutdown.

2.3.1 Startup

In case there is no liquid is present in the system, it is filled at a very slow pace. First, valve w-F is closed and o-F opened. The brine pump is regulated to just overcompensate gravity, such that the system is flooded with a few cm/s. When the complete measurement tube is filled, the pump pressure is increased to generate a flow up to 0.5 m/s. At this point, valve w-F is opened and the flow is increased to almost 1 m/s.

Prior to testing, both settling vessels should be completely filled with liquids and the brine/oil interface should be at an appropriate level. First, the brine level is adjusted by a flow of brine running into both vessels, with their respective control valves (valves o-G en w-G in figure 2.1) kept closed until the desired brine level is reached. The next step is flow of pure oil into both vessels to fill them completely, leading to an overflow of oil back into the oil storage vessels via the discharge lining. The oil running through the Coriolis flow meter provides a reference measurement for the water content of the oil.

In all cases a change in pump frequency is performed gradually to avoid excessive pressure changes on the rig.

2.3.2 Operating window

During the tests, the flow rates chosen should be within certain limits. The minimal flow rate that can be measured by both float flow meters is 8.0 m³/h. Lower flows are possible with respect to the pump, but they will not be detected by the flow meters downstream of the pumps. The maximum total flow rate depends on the separating characteristics of the settling tanks, the maximum flow rate for brine (being more than 60 m³/h) and the maximum flow rate for oil (being 35 m³/h, for higher flow rates, this is the maximum flow rate before air is sucked into the pump; the gravity driven flow from the first oil storage vessel to the second one limits this process). Measurement times are infinite as long as the flow in the measurement tube operates in a water continuous regime. The settling tanks can then deal with the process streams according to their design specifications (see section 2.2). In oil-continuous flow not all droplets smaller than 100 μm are separated. Partial separation in the settling vessels leads to a mixture running through the pumps, in which the high shear levels further reduce the droplet size. Experience learned that oil-continuous tests cannot last longer than approximately 10 minutes.

2.3.3 Shutdown

Before shutting down the system, the oil flow is stopped. Only brine flushes the system at an arbitrary flow rate. As soon as all visible traces of oil are removed from the system, the flow rate of brine is lowered by decreasing the pump frequency to 25 Hz or less. At this lower flow rate, valve w-F is closed, after which the brine pump can be switched off.

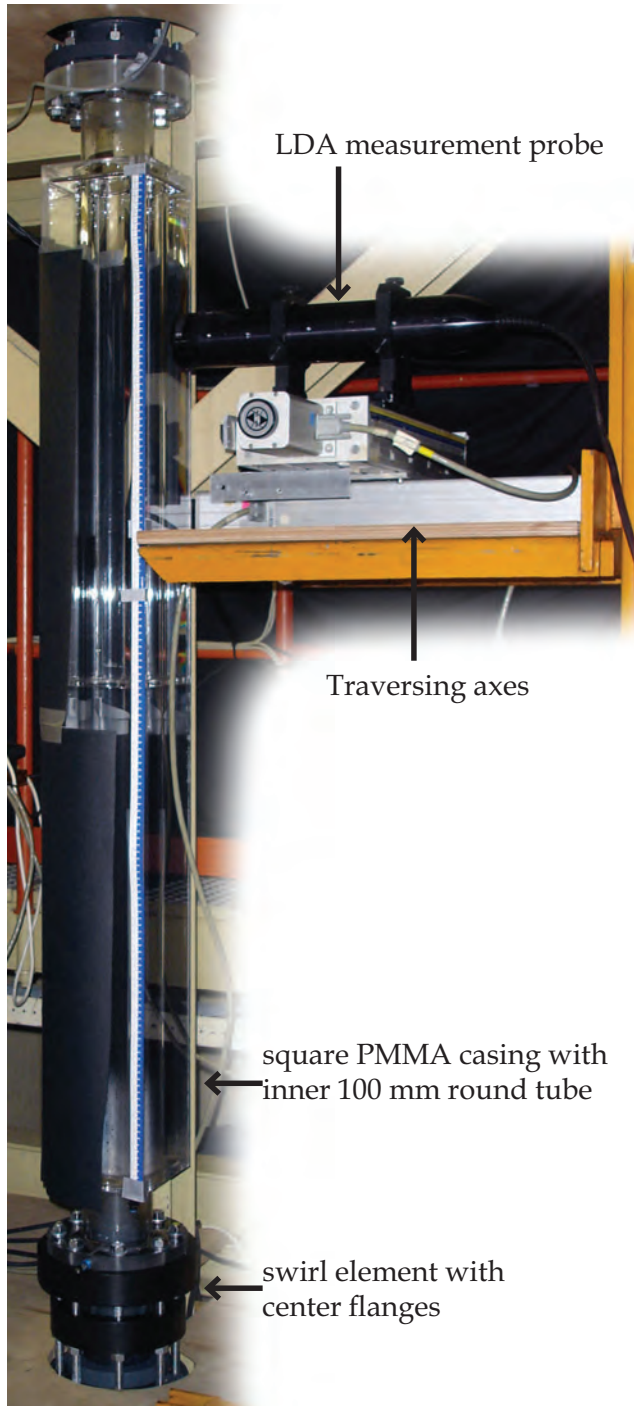


Figure 2.5: Photograph of the LDA measurements line-up: PMMA tube with square casing, traversing table and LDA probe.

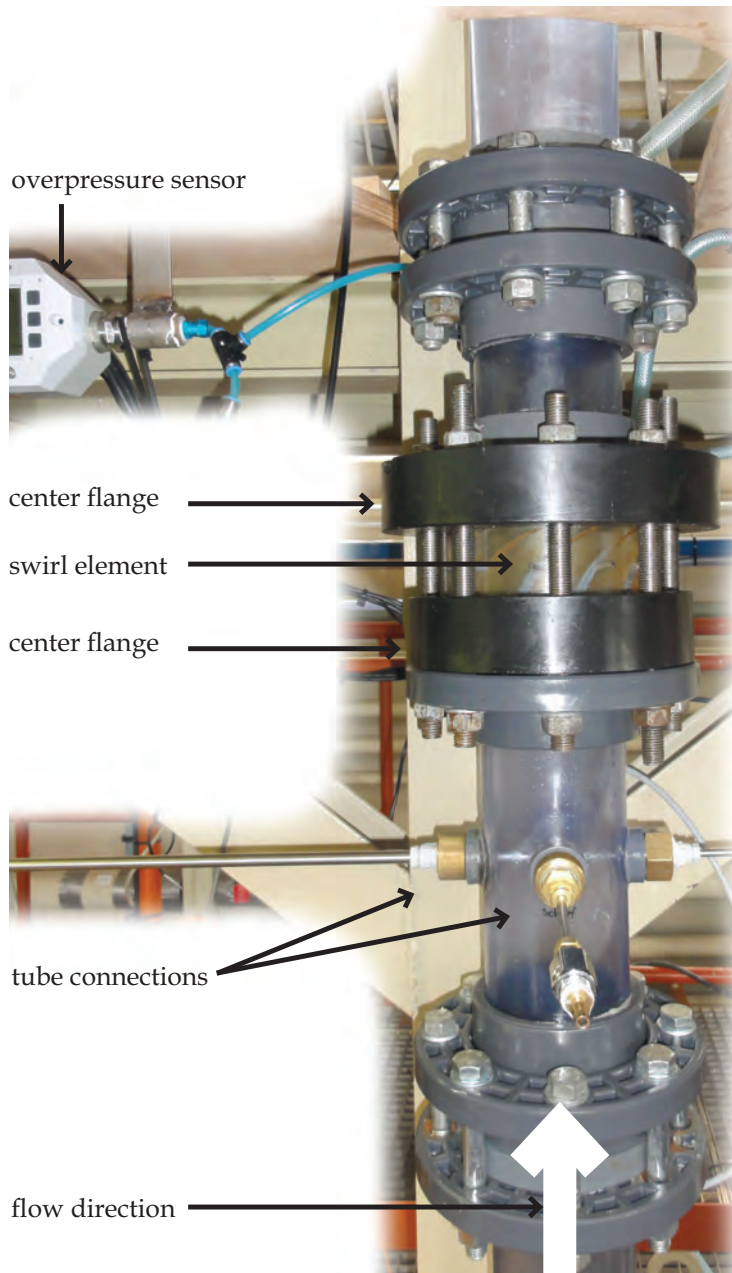


Figure 2.6: Photograph of the swirl element clamped between two tubes, with the two center flanges in black.

2.3.4 Maintenance operations

The settling tanks will never provide a perfect phase separation. Even if much less than 1% of the phase runs into the wrong storage vessel, over time a significant amount of that phase will build up.

Oil in the water storage vessel The oil layer floats on top of the water. When the water flow rate is not excessive, this oil remains in this position; the higher viscosity of oil avoids the leak of oil into the water pump.

A high hold up of oil in the brine storage vessel is undesirable, it reduces the oil volume available for tests, and in some occasions, oil can run into the brine pump, for example when the brine level in the storage vessel is low because the brine flow rate being high.

This layer is removed by lowering the liquid level below the openings of the water discharge lines from the settling tanks. The brine falling into the liquid breaks the oil layer, by which oil chunks are sucked into the brine pump and moved to the settling tanks. High shear levels in the centrifugal pump should be avoided to minimize droplet size reduction. For that reason, this procedure should be conducted at a low rotational speed of the pump.

Brine in the oil storage vessel Brine has a larger density than oil and will therefore settle at the bottom of the vessel. The lower viscosity of brine compared to that of oil results in an easy suction of brine into the oil pump. For this reason the brine layer should be kept to a minimum. A submerged pump is located at the bottom of one oil storage vessel - this continuously removes the lowest liquid layer from the vessel and transfers it directly into the largest settling tank, see figure 2.1.

2.4 Consistency of results

This section discusses the quality of the results - when are the results significant and how do the results reproduce over time.

2.4.1 Reproducibility

Comparability of the oils

Within the research described in this thesis, we used two different oils, indicated by oil A and oil B, see table 2.1. Furthermore, it is known that oil properties change in time due to aging effects. We measured the efficiency of separation for almost the same conditions at three different moments in time. The distance from swirl element to pickup tube was 170 cm and the flow rate $56 \text{ m}^3/\text{h}$.

1. March 8th, 2011, with oil A. The feed droplet sizes were not measured during the measurements, but likely to be below $100 \text{ }\mu\text{m}$.
2. March 13th 2012, with oil B. The average feed droplet sizes were measured to be approximately $80 \text{ }\mu\text{m}$.

Table 2.1: Physical properties of model oils used in this thesis.

Quantity	Unit	Oil A	Oil B
Density at 15° C	[kg/m ³]	869	881
Kinematic viscosity at 40° C	[mm ² /s]	10	10
Interfacial tension with brine at 20° C	[mN/m]	15	26
Constitution		solvent refined, non-additivated, naftenic mineral oil	solvent refined mineral oil blended with zinc free additives

3. September 13th 2012, with oil B. The average feed droplet sizes were measured to be 135 μm .

Figure 2.8 shows a difference in separation efficiency for the three cases. The differences are significant for the HPO. For the LPO, the measured difference in oil concentration appears to be smaller than the measurement error. The overall trend is, however, that the efficiency is equal for March 2011 and March 2012, where it is larger for September 2012. The most likely cause for this is the difference in droplet size in the feed.

Effect of previous tests

The consistency of the measurements has been checked by repeating the same experiment in different ways. In figure 2.9 the oil concentrations are shown in the LPO and HPO. The same experiment was performed running from a low oil concentration in the feed to a high concentration, followed immediately by the reverse order, i.e. from a high to a low concentration.

From these results, no significant difference is noted. In general for the case “high to low”, we observe a higher oil concentration in the LPO. A possible explanation for that is:

1. longer testing increases the volume of dispersed water in the oil;
2. leading to a higher density of the oil phase;
3. for the same reading of the oil intake, less oil is fed to the system;
4. a lower measured oil concentration in the HPO is interpreted as a higher oil concentration in the LPO. This effect should be considered when a series of tests is executed. A solution would be to measure the mass flow and density in the LPO with a Coriolis flow meter, or by measuring the density in the oil feed line online.

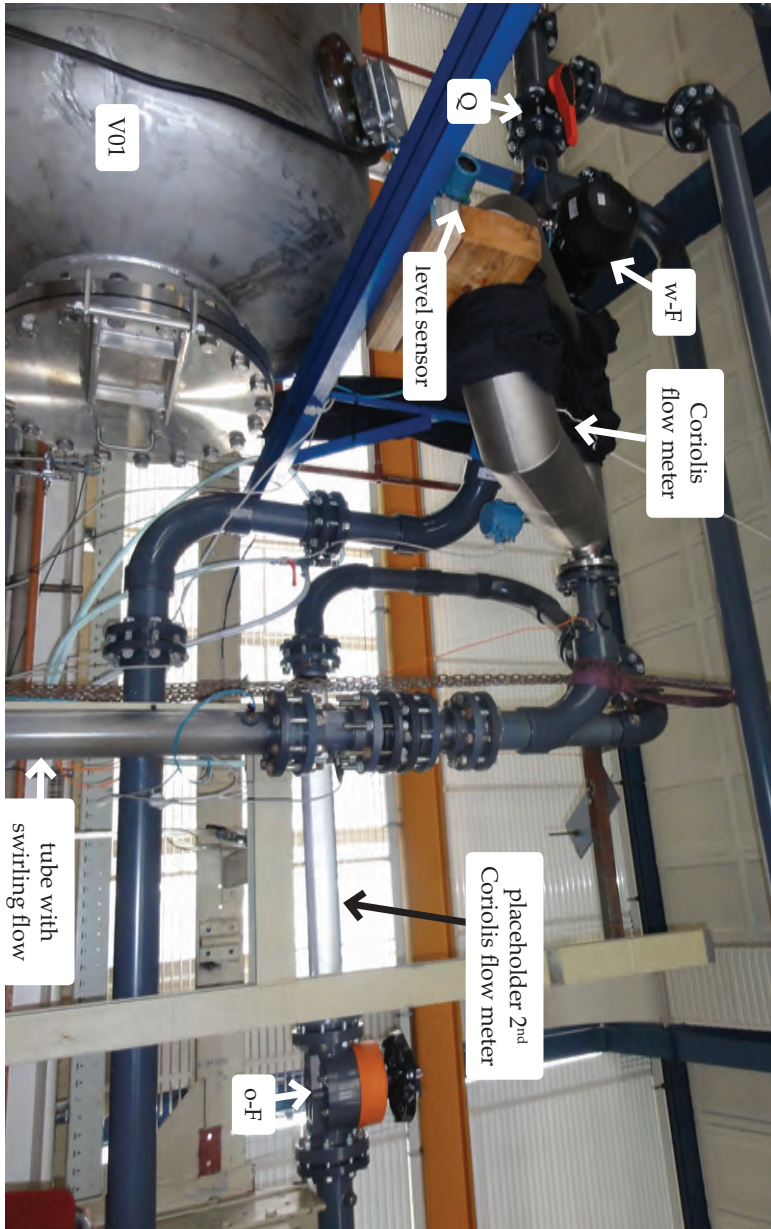


Figure 2.7: Photograph of the higher end of the measurement tube, with the actual separation section, measuring devices and the small settling tank. Labels refer to the scheme in figure 2.1

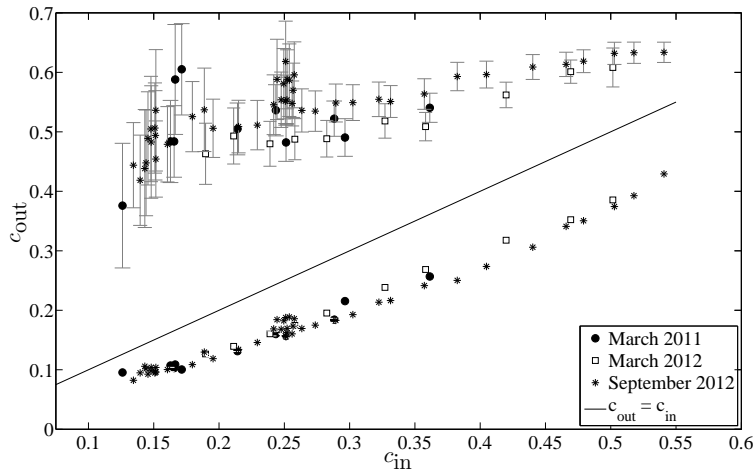


Figure 2.8: Oil concentration in the LPO (upper left) and HPO (bottom right). (c_{out}) as function of the oil concentration in the input (c_{in}) for three different days for a measurement system of 170 cm at a flow rate of $56 \text{ m}^3/\text{h}$. Error bars indicate uncertainty in the concentration, see appendix C. Feed oil and average droplet size differ. Results obtained with the strong swirl element.

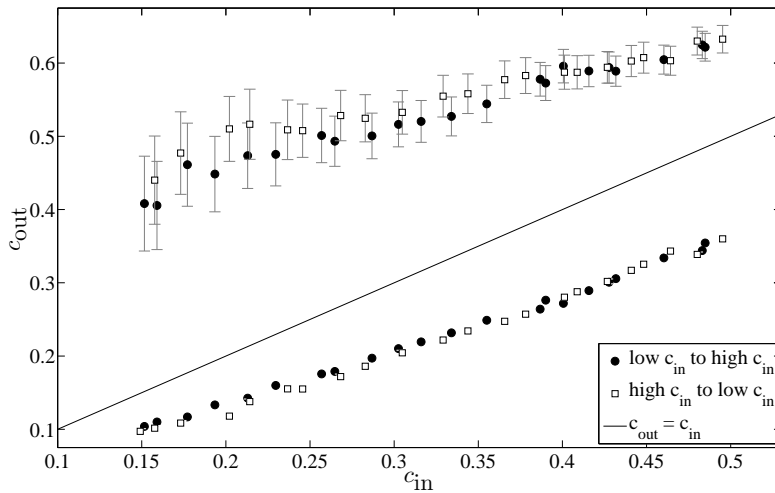


Figure 2.9: Oil concentration in the in- and output for measurement length of 190 cm. Measured in one run from low c_{in} to high c_{in} and vice versa. LPO results are in upper left part, HPO results in lower right part.

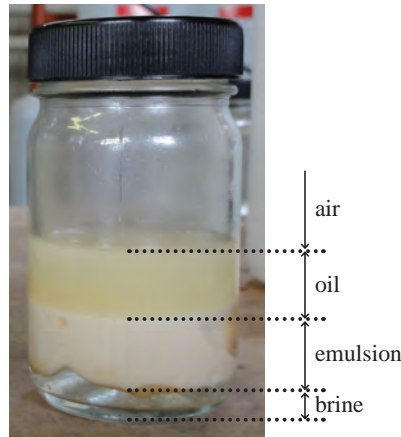


Figure 2.10: Sample of the “problem” liquids: brine, oil A and emulsion

2.5 Durability of the process liquids

During the tests performed for this research, it was noted that the separability of the process liquids changed over time. The interfacial tension decreased significantly, resulting in the formation of a white, viscous layer at the interface of brine and oil (see figure 2.10). When looking at this layer through a microscope, it was found that it consisted of oil and water droplets - this layer will be called the micro-emulsion layer. A micro emulsion can only be formed if the interfacial tension between two liquids is low (a high interfacial tension will prevent the droplet to break up into to the small sizes required for a micro emulsion) or when the applied shear stress is very high.

The original liquids were acquired in June 2010, the first problems arose in September 2011. At that time, the liquid properties were investigated, results are in table 2.2. The interfacial tension was measured and found to be less than 1.5 mN/m, a factor 10 smaller than the initial value. The interfacial tension for fresh oil A and fresh brine is 15 mN/m or more. The reduction in interfacial tension must have a chemical cause, either a surfactant was added to the system or the liquids changed over time.

The viscosity of the degraded oil A was about 20 % higher than that of the original oil A. This can be caused by the presence of water droplets in the oil. It is at least a strong suggestion that the oil molecules did not become shorter.

To understand whether a surfactant is present in the oil or water phase, the interfacial tension was measured for four different combinations: clean or used brine versus clean or used oil A. All samples were obtained from the bulk liquids, so far away from the interface layer. From table 2.3 it is clear that a surface active agent must be present in both phases. Typically, non-ionic surfactants are found in oil which can stabilize water-in-oil emulsions, while ionic surfactants are found in the watery phase which can stabilize oil-in-water emulsions.

2.5.1 Possible causes

To identify the surfactant, all possible entry routes for surface active agent(s) to the rig were considered. This section describes the different possibilities.

Loading of liquids

If the surface active agent(s) were introduced via the filling process, the effect must have been noticed from the first tests onwards. This was not the case, making this entrance route unlikely.

Brine Brine was prepared from tap water and commercially available food grade salt (NaCl). The tap water lines were used extensively before filling, which should have removed any possible pollution. The salt was doped with anti-caking agent: $K_4Fe(CN)_6$, i.e. Potassium Iron cyanide. Since this lacks a non-ionic tail, it is not considered as a possible surfactant.

Oil The oil was not analyzed upon delivery, it was assumed that this lubricant oil was delivered according to specification. A sample was taken and stored. The oil was transported from the vessels to the rig via hoses provided by Vidol, a transporting company. It is not known whether these hoses were clean from surfactants.

Structures in the flow rig

Polymer materials The system is constructed out of polymer materials that might interact with the oil. The different materials used are:

- **Polypropylene:** is not expected to interact with mineral oil
- **PVC (Poly Vinyl Chloride):** is according to the oil A safety sheet unsuitable for storage of oil A. Consultation of the oil manufacturer learned that mineral oil molecules could exchange for plasticizer molecules, making the PVC brownish and releasing plasticizer into the system. Analysis of oil A from the setup using the gas chromatogram technique did not show a traceable amount of plasticizer (phthalate). The Infra Red spectrum did not show clear peaks due to what could be phtalate. Furthermore, mixing clean oil A, clean brine and phtalate together did not result in a micro emulsion.
- **PMMA (Poly Methyl MethAcrylate):** no interaction with mineral oil in known.

Table 2.2: Physical properties of original and degraded oil A.

	Original oil A	Degraded oil A
Density (kg/m^3)	869 ± 1	870 ± 5
Interfacial tension with brine(mN/m)	15 ± 1	< 1.5
Viscosity (mPas)	16.6 ± 0.02	20.5 ± 0.03

Table 2.3: Interfacial tension of the process liquids (mN/m)

	Clean Brine	Degraded brine
Clean oil A	15 ± 1	9 ± 1
Degraded oil A	4 ± 2	< 1.5

- **EPDM (Ethylene Propylene Diene Monomer):** this is a rubber used in the applied appendages. It is known to be not resistant to mineral oil. The effect of mineral oil is that it diffuses into the rubber, making it grow in volume and loose strength. It is not expected that EPDM molecules get into solution and act as an emulsifier. However, this introduces an uncertainty.
- **NBR (Nitrile Butadiene Rubber):** a mineral oil resistant rubber, no negative effects are expected.

Metal parts The system was manufactured from different parts, containing both metal parts (stainless steel AISI 316L) and polymer parts. These parts can contain fatty substances on their surface when they are new. The system was only rinsed with tap water before the oil was added. This means that these fatty substances might be dissolved in the oil now. Their effect is unknown.

The pump shafts are lubricated using dry PTFE. This means that no lubrication oil can have leaked from the pumps.

The coating of the largest settling tank was replaced because it did not provide enough resistance against corrosion, this has caused different elements to get in touch with the liquids in the setup:

- **Coating chunks:** Novaguard 840 is a two-component solvent-free phenol/epoxy polyamine coating. It is oil resistant, but can get damaged by brine. Chunks getting loose and dispersing in the flow are not expected to have an emulsifying effect.
- **Rust particles:** the carbon steel vessel (Fe) corroded to iron oxides (Fe_2O_3) mainly, which is non-solvable in water or oil. The solid salt is completely polar, making it not a surfactant.
- **Solvents of re-coating:** the solvents used for the first recoating step are not present in the system. They are very volatile, and would have been noticed in the Gas Chromatograph analysis (see Appendix A).

In the end, the complete vessel was replaced by a new stainless steel vessel, made out of 316L steel. Stainless steel is treated after mechanical modifications using a mordant and a passivating agent. This passivating agent is nitric acid (HNO_3) which is ought to remove all mordant and to form a layer of chromium oxide on the steel. The passivating agent was not actively removed, other then with cold tap water. However, it was not found in the system, since the pH was almost neutral: 6.5.

Measurement equipment The only electric field present is that of the wire mesh. This has sufficient potential difference to create electrolysis, though that would lead to a high pH by the formation of OH⁻. The pH of the liquids in the system is 6.5, making this effect negligible.

Contamination from surroundings

Olive oil In the first tests, performed in 2009, some olive oil was added to the setup to study the behavior of oil droplets in water. The total amount of olive oil injected in the setup was 0.5 L. The water containing olive oil was removed, and the parts of the setup that were accessible were mechanically cleaned (being the measurement tube itself, the storage vessels and the settling tanks) and the rest of the setup was extensively rinsed with tap water. There will, however, have remained some olive oil residues at the walls.

Olive oil is a triglyceride that will decompose into glycerin and oleates. The latter can act as a surfactant due to their polar head and non-polar tail. To test this, a batch of olive oil was completely decomposed by adding NaOH, which was added in a higher concentration than present in the setup to a clean oil A/Brine system. From this test it was concluded that this soap could not account for the dense emulsion observed in the test rig.

Bacteria Mineral oil contains energy bacteria might use to live. The excreta produced by the bacteria can act as an emulsifier. Two tests were carried out to find bacteria:

- Saybolt performed a standard test, in which they grew the bacteria on standard soils. No bacteria were found for these soils.
- Since the conditions in the Delft test rig are extreme for bacteria (being very salty), also non-standard bacteria could be present. Some samples were therefore also investigated optically using phase contrast microscopes. This was done with the very kind help of dr. L. Robertson of TU Delft. There were some bacteria present, but there was definitely no flourishing bacteria colony. Figure 2.11 shows a single bacteria which we found after extensive searching.

Human error In case somebody deliberately wanted to frustrate our research, he or she could have added detergent to the system. Many detergents foam, where no foaming was observed. Some ionic surfactants (like SDS) have a low solubility in water with a high salt content. No solids have been observed in the water phase.

Suction of other substances The system sometimes contains regions with a lower pressure than the surroundings. The set-up is, however, constructed in such a way that the only surrounding substance is air. It is therefore highly unlikely that a surfactant was sucked into the system. From the surroundings, aerosols, dust and maybe insects might fall into the setup.

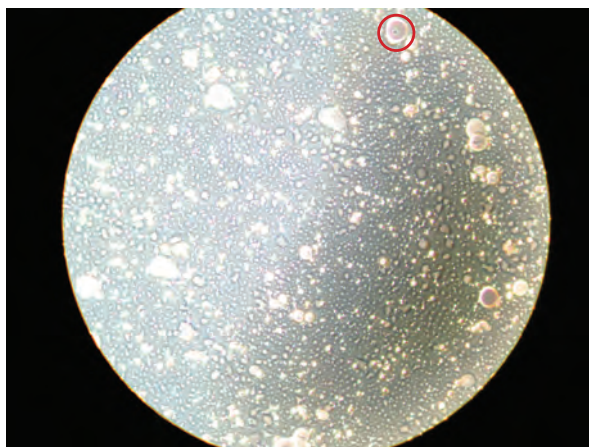


Figure 2.11: Microscope image of the oil layer. In the upper right corner, inside the red circle, there is a small black spot that might be a bacteria, bacteria show dark in the photograph. Scale is unknown.

Oxidation due to air The system is in contact with air: all the vessels are made breathing and during operation, the overflowing outlets of the settling tanks also introduce intense mixing of the oil and air. It is known from the Material Safety Data Sheet (MSDS) of oil A that the contact with strong oxidizing agents should be avoided - being a hint that oil A can oxidize.

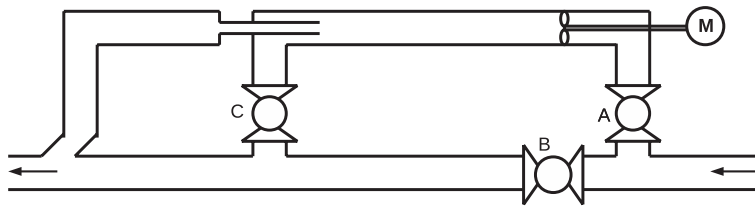
The oxidation process will create $=O$ groups on the long chains, which will create the possibility of forming polar bonds with other molecules. These polar bindings will increase the mixing with water and may be accounting for the lower interfacial tension.

An infrared transmittance spectrum was made of the oil. Infra red light with a wavelength of $174 \cdot 10^3 \text{ m}^{-1}$ is strongly absorbed by the " $=O$ " group, which is present in oxidized oil. The results are presented in figure 2.13. Based on these results, no significant amount of oxidized oil is found.

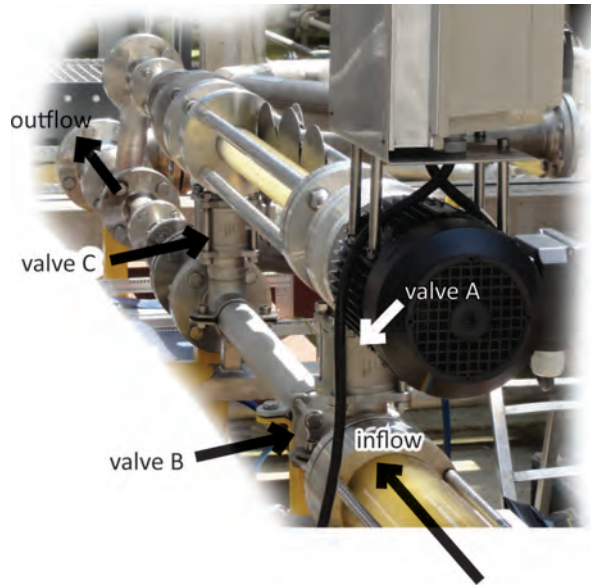
Conclusion

No clear reason for the decrease in interfacial tension was uncovered. To continue measurements all process liquids were replaced after having cleaned the rig thoroughly. Since the original oil (oil A) was not available anymore, the oil which closest resembles oil A was chosen: oil B. The physical properties of the different oils are provided in table 2.1 - all results presented in this thesis concern oil B, unless otherwise indicated.

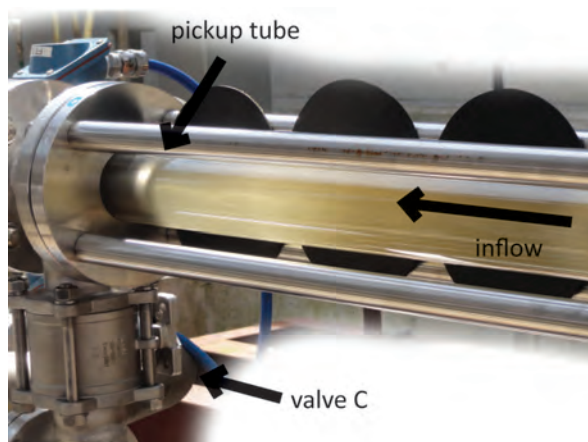
The quality of oil B was tested over time for its interfacial tension. A decrease in interfacial tension would result in a lower separation efficiency. The interfacial tension was determined with a Krüss Easydrop, a contact angle microscope. Water dispersed in the oil was removed in a centrifuge before measurements, since a transparent oil phase is required. Figure 2.14 shows the results over time. No decreasing trend for the interfacial tension is observed.



(a) Scheme



(b) Overview picture



(c) Detail picture

Figure 2.12: Test facility for the tests with the cyclone with rotating swirl generator.

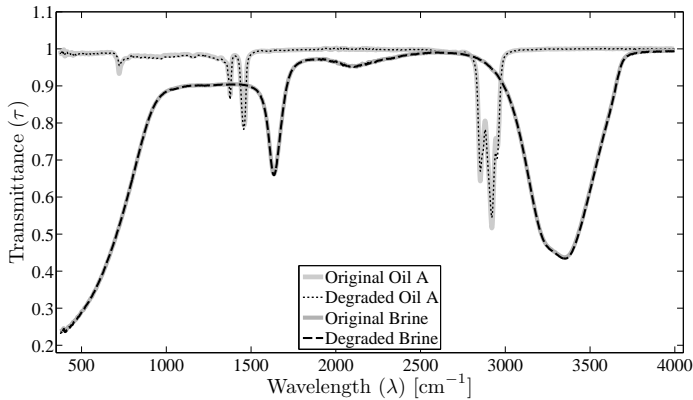


Figure 2.13: Infrared transmittance spectra for brine and original oil A, as well as degraded oil A and degraded brine. This measurement shows no degradation of the liquids.

2.6 Facility for rotating swirl element

Introduction Within the framework of the ISPT project of which this thesis is part, tests were executed with a cyclone based on a rotating impeller. This cyclone is the Easysep separator in the 2" edition, as produced by Peter de Voogt's company Aquatech International B.V., with its seat in Stellendam.

Experimental setup The tests with the rotating impeller were carried out in Shell's Multiphase Test Facility (Donau-loop), located in Rijswijk. To this end, the Easysep separator is attached to the existing infrastructure using stainless steel (AISI 316L) tubes. The easysep itself consists out of a glass tube (see figure 2.12(b)), with at the inlet side an impeller and at the outlet side a pickup tube (see figure 2.12(c)). Figure 2.12(a) shows a schematic of the rig with in the upper half the glass tube. In normal operation, the mixture enters the setup from the right side, flows through the glass tube (valve A is open and valve B is closed). The impeller can be rotated at any rotational frequency between 600 and 3000 rpm. Valve C is used to regulate the pressure in the heavy phase outlet (HPO) and therewith the flow split (distribution of flow between the HPO and the light phase outlet (LPO)).

Both outlets are equipped with Emerson MicroMotion 1" coriolis flowmeters that provide the flow rate and oil concentration. Results of this work are in section 7.3.

2.7 Conclusion

We constructed a flow rig in which mineral oil and brine can be mixed and used to test in-line axial cyclonic separators. The operating window of the rig is a fluid

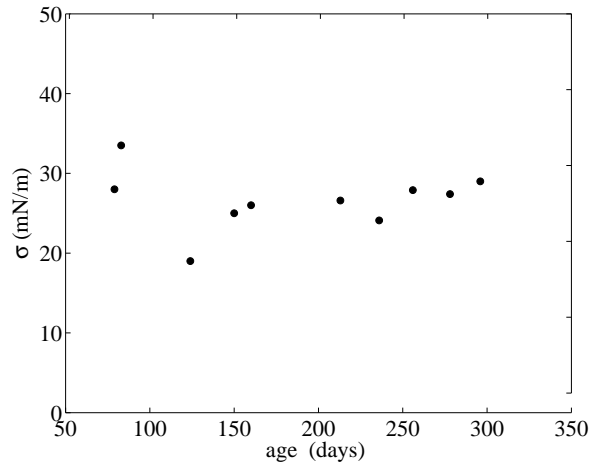


Figure 2.14: Interfacial tension of oil B and demineralized water. Age is relative to the filling of the rig with this oil

flow between 10 and 60 m³/h. The oil concentration in the mixture can be chosen as any value between 0.10 and 0.90.

Some bottlenecks in the rig hold back the optimal performance, for future work, one could consider taking the following measures:

- **Inlet flow meters:** the current float flow meters have a large measurement error, provide slow readings and are sensitive to density changes in the liquid, which are likely to occur for the oil phase during a measurement day; a better alternative is:
- **LPO flow meter:** a direct measurement of the density in the LPO, combined with the mass flow rate, reduces the accuracy of separation efficiency measurements to a great extent. Considering the mass balance, this extra Coriolis flow meter makes the inflow flow meters over complete, since the inflow can be computed from the outflow.
- **Rig alignment:** the measurement section is constructed out of PVC tubes and appendages. The limited stiffness of this material prevents a perfect axial alignment;
- **Storage vessel positioning:** the current position of the outflow openings of the storage vessels (15 cm above their bottom) is not convenient during maintenance operations: the tanks can not be fully drained by gravity, the last bit should be removed manually. The remaining liquid volume also introduces an operational problem since a floating oil layer in the brine storage vessels slips easily into the pumps, and the oil storage vessels suffer from water hold-up at the bottom. It is suggested to move the outflow to the ground plane of the tanks to minimize the pollution of the brine feed with oil and vice versa.

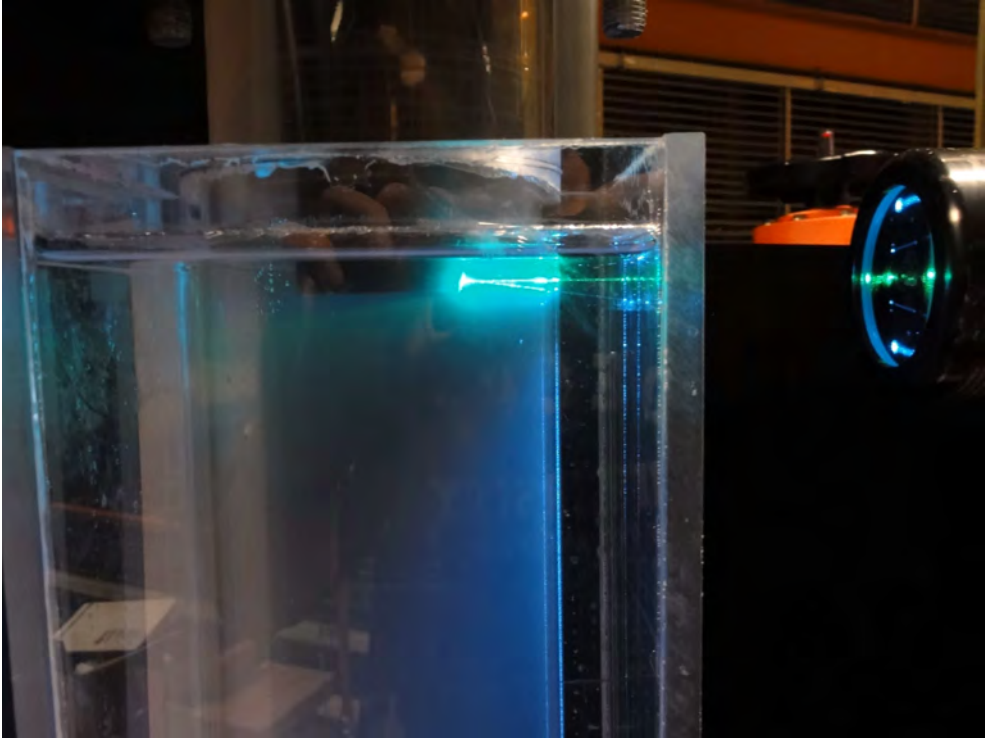


Figure 2.15: Picture of the LDA measurements close to the black pick-up tube. The measurement tube with 100 mm inner diameter can be seen, with a square transparent casing, which is filled with water. The LDA probe is at the right hand side of the picture.

Experimental methods

Where the previous chapter focussed on the flow rig in which the tests took place, explains this chapter all measurement methods used for the work in this thesis. Section 3.1 introduces Laser Doppler Anemometry, section 3.2 briefly explains the numerical methods used for fluid flow calculations. Separation efficiency is an important qualification of a separation device and the followed measurement strategy is introduced in section 3.3. Droplet sizes are measured using the direct photography method in section 3.4. A new capacity based wire-mesh technique in section 3.5 is applied for phase distribution measurements.

3.1 Laser Doppler Anemometry

There are various ways to measure velocities inside transparent fluid flows. In case of LDA, the Doppler-shift in the frequency of the light reflected from a particle is used to measure the particle velocity. This velocity -under appropriate conditions- is a measure for the fluid velocity. LDA is since its introduction in the 1980's a common technique in fluid dynamics research.

It is not within the scope of this thesis to explain the mechanism of LDA extensively. For an introduction in LDA and more background information, please see Durst et al. [18] or Tummers [19].

3.1.1 LDA apparatus

The fluid flow is examined using a 2D-Laser Doppler Anemometry (LDA) operated in back-scatter mode. The laser beams enter the experimental setup via a PMMA square water-filled box surrounding the tube (see figure 2.5). This box reduces the refraction of laser light at the tube wall. To reduce remaining refractive effects measurements are only done along the line perpendicular to the box surrounding the tube and through the center of the tube. Durst et al. [18] describe the measurement principle of LDA.

The light from a 4W Argon laser is split into two 488.0 nm beams for the axial

velocity and two 514.5 nm beams for the azimuthal velocity. For both colors one beam is shifted with 80 MHz to obtain a direction ambiguity. The beams are focused with a 132.0 mm lens, resulting in a measurement volume of 0.2 mm in the radial direction and 0.03 mm in the azimuthal and axial direction. The burst correlation is conducted in a Dantec F60 BSA signal processor.

The average velocity is calculated using an in-house developed software package, see Belt [20]. The following filter actions are performed: (i) removal of data points with a value more than 5 times the standard deviation from the average value; (ii) samples obtained from the same tracer particle by introduction of a dead time; (iii) velocity bias by overestimation of fast tracer particles is corrected using a 2D+weighing scheme as introduced by Tummers [19].

3.1.2 Measurement volume

The measurement volume is created at the point of intersection of two laser beams. Due to a Gaussian distribution of the intensity inside a laser beam, the measurement volume itself is ellipsoidal shaped, with a geometry as given in Figure 3.1. According to Adrian [21], the dimensions of the measurement volume in x -, y - and z -direction can be expressed as:

$$d_m = \frac{d_{e-2}}{\cos(\kappa)} \quad (3.1)$$

$$l_m = \frac{d_{e-2}}{\sin(\kappa)} \quad (3.2)$$

$$h_m = d_{e-2} \quad (3.3)$$

respectively, with κ being half of the angle between the incident laser beams and d_{e-2} the diameter of the focused laser beam, which can be expressed as

$$d_{e-2} \simeq \frac{4f\lambda_m}{\pi D_{e-2}} \quad (3.4)$$

where λ_m is the wavelength inside the medium and f the focal length of the lens. From equation 3.4 it can be seen that for small measurement volumes, either large incoming beam diameters are required or short focal lengths.

The TSI 9832 probe, with a diameter of 83 mm, has all optical components integrated to perform backscatter LDA. Each beam pair is emitted with an inter-beam distance of 50 mm and the different pairs are placed orthogonally. The beams are focused using a 132.0 mm lens. The blue light is used for the axial velocity, the green light for the azimuthal velocity, this due to the higher sampling frequency of the green beam pair.

The diameter of the laser beams has been determined to be 3.0 mm. The dimensions of the measurement volume are given in Table 3.1.

3.1.3 Tracer particles

With LDA, the velocity of the tracer particles is determined, not of the fluid itself. Therefore, the choice of the particles is very important for an accurate determination

Table 3.1: Measurement volumes in water for the used setup, according to Equation 3.1.

λ	d_m (μm)	l_m (mm)	h_m (μm)
488.0	27.6	0.205	27.3
514.5	29.1	0.216	28.8

of the fluid flow.

Various requirements for the particles need to be full filled:

- The particles must be small enough and its density close enough to make the particle naturally buoyant in order to follow the smallest vortices in the flow. This smallest scale is in the order of the Kolmogorov micro scale.
- Presence of the particles should not influence the fluid, nor dynamically, nor chemically.
- Particles should have a high reflectivity for the incident light.
- The particles must be naturally buoyant to avoid a bias in the vertical direction.

As a practical implementation of the requirements above, hollow glass spheres are a very suitable choice, which are cheap as well.

The ability of the particles to follow the flow, is mostly dependent on their density difference with the liquid and their size. Particle motion is determined by drag, buoyancy, gravity, lift and virtual mass forces. The Lagrangian motion of a rigid, spherical particle of diameter d and density ρ_p in a viscous flow can be described by the Basset-Boussinesq-Oseen (BBO) equation [19]. A simplified version of this equation can be used for seeding particles

$$\frac{\pi}{6}d^3\rho_p\frac{dv_p}{dt} = -3\pi\mu d(v_p - v_f) \quad (3.5)$$

where lift, gravity, virtual mass and buoyancy forces are neglected. The left-hand side of 3.5 is the acceleration force, the right-hand side represents Stokes' drag.

Another way to describe the ability of the particles to follow the flow, is by expressing their motion in Fourier components. As long as their maximum frequency is higher than the fluids highest frequency, the particles can track the smallest flow structures. The flow frequency is given by $\omega = 2\pi f_{turb}$. By using the substitution proposed by Tummers [19], $v_f = e^{i\omega t}$ and $v_p = \eta(\omega)e^{i\omega t}$ the amplitude ratio, $|\eta|$, can be expressed as

$$|\eta(\omega)| = \frac{\Omega}{\sqrt{\Omega^2 + \omega^2}} \quad \text{where} \quad \Omega = \frac{18\nu}{\sigma_r d_p^2}, \quad (3.6)$$

with σ_r the density ratio ρ_p/ρ_f . The amplitude ratio is a measure of the particles sensitivity to follow changes in fluid flow. It can be seen from equation 3.6 that for very high frequencies the amplitude ratio η becomes negligible and therefore the particles are not very sensitive to the fluids motion.

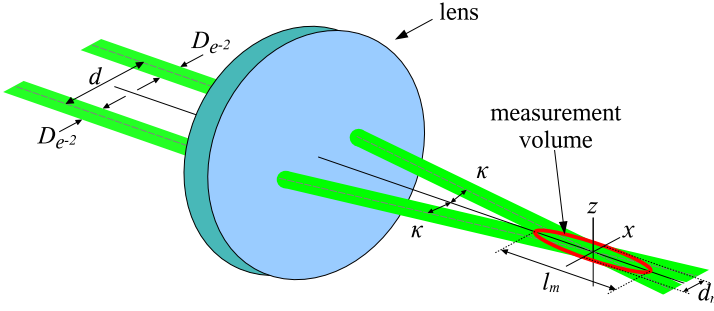


Figure 3.1: Geometry of the measurement volume for LDA. Two incident laser beams from the left are converged by a lens into the measurement volume.

To obtain a sufficient temporal resolution to capture the smallest flow structures, at the Kolmogorov microscale, enough particles should cross the measurement volume. As a criterion for the minimum sampling rate, Durst et al. [18] mention a minimal sampling frequency of $2f_{\text{turb}}$. Because particles are distributed randomly in the fluid, particle arrivals at the control volume are not equally distributed in time. To ensure enough samples during moments of high velocity fluctuations as well, the *average* particle arrival frequency should be larger than $2f_{\text{turb}}$ to meet the minimum condition.

In this work, we used two kinds of seeding particles:

1. neutrally buoyant glass spheres with a diameter with an average of $8 \mu\text{m}$ - these were used until multiphase experiments started. During the experiments with both oil and water, no seeding particles were present;
2. remaining small oil droplets and solids in the flow - these were used when the liquids in the system were used for oil/water experiments as well. Oil droplets with a diameter in the order of μm are very stable and have a high reflection efficiency.

3.1.4 Traversing system

The probe is mounted on a digital driven traversing system, such that the measurement volume covers the complete cross-section of the test section. The probe traverses along the vertical axis, i.e. in axial direction. The measurement tube is surrounded with a square PMMA box filled with water. The entrance of light through a flat surface reduces refraction.

Due to refraction, displacement of the probe will not correspond to the displacement of the measurement volume. The refractive index of water, n_w is higher than that of air n_a , changing the angle of the incident beam in the measurement volume.

The correction factor between the movement of the probe and the movement of the measurement volume, is given by:

$$C_L = \frac{\tan(\alpha)}{\tan\left(\arcsin\left(\frac{n_a}{n_w} \sin(\alpha)\right)\right)} \quad (3.7)$$

where α is given by $\arctan\left(\frac{D/2}{L}\right)$, with D the distance between the incoming laser beams and L the focal length of the lens.

Other refractive changes might be occurring, but since these are much smaller and more difficult to correct for, for the time being, they will be neglected.

3.1.5 Void kernel

During measurements, the center of the tube contained a region that was non-transparent, resembling an air or void kernel. This prevented the laser beams to reach the center of the pipe. The high pressure difference in radial direction caused by the centrifugal acceleration can make the water cavitate or result in dissolved gases coming out of solution. The pressure difference Δp between the center and the wall is estimated by

$$\Delta p = \int_0^R \frac{\rho v_\theta(r)^2}{r} dr, \quad (3.8)$$

with ρ the liquid density and $v_\theta(r)$ the azimuthal velocity at position r . For a typical case that will be discussed in section 4.4 (figure 4.8(a)) $\Delta p = 1.9$ bar. The pressure as measured at the wall was about 1.6 bar. A quick and dirty estimation suggests the pressure in the center of the tube to be negative. Most likely, enough gas escapes the liquid phase to build up a vapour kernel. A quantitative description of the pressure in this kernel is not produced in this work. Since the size of the void kernel was not constant over subsequent measurement series, not all measurement sets run to the same radial position.

Numerical results do not show a vapor kernel, for which various reasons can be given. First, the pressure difference between the wall and center is 1.05 bar. This lower value results from lower azimuthal velocities for $r < 35$ mm (see figure 4.8(a)). Furthermore, the numerical method does not incorporate two-phase-flow effects; even with negative pressure, the numerical approach assumes that the phase remains liquid. The continuous presence of liquid water with accompanying shear forces changes the flow pattern significantly compared to the experimental case with a void at the center of the tube.

3.2 Numerical method

The work described in this thesis is part of an ISPT project, which covers both experimental and numerical work on an in-line axial cyclone for liquid-liquid separation. The presented results further on are compared with numerical work of Slot [13]. This section gives a brief overview of the applied method.

3.2.1 Single Phase

The flow field is resolved by solving the Reynolds averaged Navier-Stokes equations for transient incompressible turbulent flow using the commercial package Ansys CFX 14.0. Reynolds stresses are modelled using the Reynolds Stress Model (RSM) implementation SSG. The typical computational domain consists out of 2.3 million hexahedral elements.

The boundary conditions applied are:

- Inlet: axial velocity $u_{z,b}$, density ρ and viscosity μ .
- HPO: pressure p_{HPO}
- LPO: mass flow rate dm_{LPO}/dt .

All simulations were performed for a time-dependent flow. The presented results are time-averaged flow solutions.

3.2.2 Two Phase Flow

For multi-phase flow, the problem is treated according to both the Euler-Lagrangian and Euler-Euler model. In the Euler-Lagrangian approach, the single phase solution for water is taken as the continuous phase velocity profile. In this work, the path of many droplets is computed based on the continuous phase time-averaged solution with a CFX implementation of turbulent dispersion. There is no coupling from the droplets motion towards the continuous phase velocity.

In the Euler-Euler model both phases (oil: o and water: w) are defined as continuous, interpenetrating fluids. In the formulation of the drag, however, the water is defined as continuous and the oil as dispersed with droplets of a certain diameter. For each computational cell in the setup, the following parameters are monitored: volumetric oil fraction, average velocity for both phases separately and the droplet size distribution (in discrete bins). Individual droplets are not considered in this approach. During the computation, based on drag laws for ensembles of dispersed droplets and the velocity difference between the phases, the drag, breakup and coalescence are calculated per cell.

The Euler-Euler method requires extensive models to accurately describe the drag between the phases and the consequences for the droplet size distribution.

The boundary conditions applied are:

- Inlet: axial velocity $u_{z,b}$, volumetric oil fraction α , droplet diameter D , densities ρ_o and ρ_w and viscosities μ_o and μ_w .
- HPO: pressure p_{HPO}
- LPO: axial bulk velocity $u_{z,\text{LPO}}$.

3.3 Efficiency measurements

There are various methods to express the separation efficiency of a cyclone. We will use three methods in this thesis. The first method is by calculating the fraction of the oil which runs into the LPO, the so-called dilute efficiency:

$$\eta_{\text{dilute}} = \frac{\Phi_{\text{oil, LPO}}}{\Phi_{\text{oil, in}}}, \quad (3.9)$$

this measure is a good qualification if the objective is to remove oil from the water stream.

The second efficiency considers the total amount of dispersed phase running into the 'wrong' outlet: it is the volumetric oil flow in the HPO plus the volumetric water flow in the LPO. This results in:

$$\eta_{\text{dispersed}} = 1 - \frac{\Phi_{\text{water in LPO}} + \Phi_{\text{oil in HPO}}}{\Phi_{\text{tot}}} \quad (3.10)$$

The final efficiency measure, we call the bulk efficiency. The advantage over the dispersed and dilute efficiency is that its range is from 0 to 1: if the oil concentration in the outputs is equal to that of the input, the bulk efficiency is 0, if there is only oil in the LPO and water in the HPO, it is 1:

$$\eta_{\text{bulk}} = \frac{1}{2} \left(\frac{c_{\text{in}} - c_{\text{HPO}}}{c_{\text{in}}} + \frac{c_{\text{LPO}} - c_{\text{in}}}{1 - c_{\text{in}}} \right). \quad (3.11)$$

An evaluation of the uncertainty in the calculated oil concentration can be found in Appendix C.

3.4 Droplet sizing

The size of the droplets is a very important parameter for the use and design of liquid-liquid cyclones. Measuring the droplet size distribution has been topic of extensive research. Bae and Tavlarides [22] give an extensive overview of possible measurement principles. Not all of these techniques are capable of dealing with high (> 1%) dispersed volume fractions. The following methods are feasible: direct photography, light scattering, chemical reaction, drop stabilization and scintillation. Direct photography is the standard method for calibration of other methods [23] and should be conducted in-situ, e.g. with an intrusive endoscope. Alternative techniques, like a laser scattering method discussed by Desnoyer et al. [24], traditionally required tapping of liquids to a by-pass for dilution. Nowadays, intrusive laser-scattering based methods are available. According to a review by Maaß et al. [23], none of them prove to deliver results with a quality comparable to the results of direct photography.

In this work, we use two different ways of droplet sizing: (i) direct photography with an endoscope system (section 3.4.1) and (ii) laser-scattering in an off-line manner (section 3.4.2). A third method using glass fibre probes (section 3.4.3) has been assessed, but not used. Direct photography proved to be the most precise, though elaborate [23]. The second method should be more efficient in execution.

3.4.1 Direct photography with an endoscope

The droplets inside the test rig are photographed via an endoscope configuration (see figures 3.2(a) and 3.2(b)). This consists of a 10 mm thick stainless steel tube with a lens at both sides. The distance between the lenses is adjustable to enable focussing.

The endoscope is mounted in the measurement tube orthogonal to the wall as in figure 3.2(b). From the opposite side, a light guide is inserted, such that light is emitted towards the endoscope. The position of the light-guide, and therewith the distance between the tip of the endoscope and the light-guide, is adjustable. The light-guide is illuminated with an adjustable halogen lamp, Schott 2500 LCD, which emits up to 1300 lumen in a spot with 5 mm diameter.

Images are captured using a high speed camera. Two different cameras were used:

- An IDT Motion Pro Y4
- An Olympus i-SPEED 2

Both cameras were used in combination with a 75 mm adjustable lens. The procedure for adjustment of the lighting and lens setting was such that optimal lighting conditions were obtained. First, the light guide was set to touch the endoscope lens. The focus of the lens on the camera was adjusted to provide sharp images of the fibers in the light guide. The light guide was then gradually pulled out, until there was just enough light to discriminate droplets at the selected shutter speed. This procedure resulted in a focal plane just ahead of the endoscope lens. The distance between the endoscope and light guide was not constant for all measurements.

The magnification of the camera system is determined by measuring the diameter in pixels of the light guide - this is done when the measurement section is filled with transparent brine. This scale is used to size the pictured droplets.

Influence of the endoscope

The endoscope is an intrusive measurement technique. The diameter of the endoscope is very significant compared to the tube diameter (10 mm vs 100 mm). To address the influence of the endoscope and light guide on the flow, two tests were performed. First, the single phase fluid velocity was measured using Laser Doppler Anemometry and secondly, the separation performance was measured with and without the endoscope.

Velocity profile Figure 3.3 demonstrates the influence of the presence of the endoscope on the fluid velocity. The most significant difference is the reversal of the axial velocity around the center of the tube, for a complete insertion, the velocity

is pointed upward on the axis - for the other two cases and the situation without endoscope, it points downward.

Efficiency The efficiency of separation was measured with and without the endoscope, according to the method introduced in section 3.3. Figure 3.4 points out that with the endoscope inserted into the measurement tube, the phase separation is reduced by roughly a factor of 2. This is most likely caused by a distortion of the flow in the center region, where an oil kernel should be formed. From the LDA results (figure 3.3(b)) we already understood the strong effect on the center region. When the presumed oil kernel is breaks up, mixing occurs, which reduces the phase separation.

The effect on the measured droplet distribution cannot be determined experimentally. It is expected that it is unlikely that droplet break-up occurs at the endoscope itself - the break-up event should then be captured by the camera. Changing flow patterns, however, will make it impossible to relate the measurement location and droplet size to the undisturbed situation.

Image processing

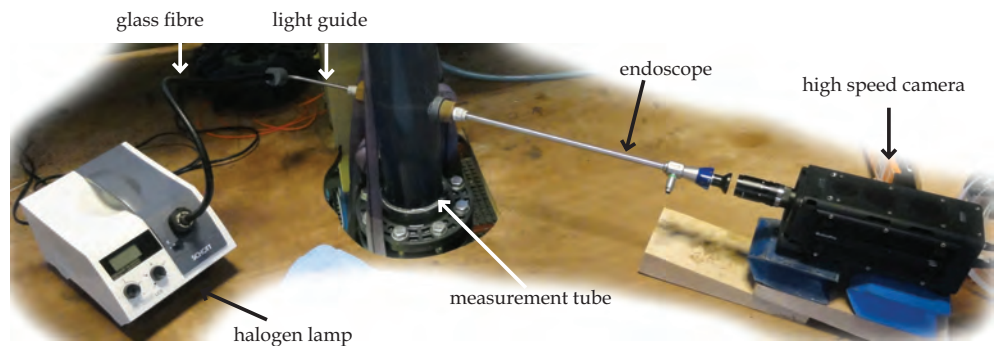
The obtained images contain the droplet size information. Although a human eye recognizes the droplet shapes, it is not straightforward to automate the recognition and therewith conversion of images to droplet size distributions. The following, manual, procedure was followed to obtain statistical information from the droplet images:

1. Recorded images (fig. 3.5(a)) are optimized using the “autotone” and “auto-contrast” features of Adobe’s Photoshop (fig. 3.5(b)).
2. Manually circles are drawn over droplets using ImageJ, about 300-400 for each case. Due to the manual fit, some circles will be too large, others too small. We assume that this effect averages out.
3. The area of the droplets in pixels is converted to the diameter, according to
4. The droplet diameters are distributed in bins with given droplet size intervals.
5. The number of droplets per bin is smoothed using a moving average over a 5 bin interval.
6. Using MATLAB, the following Gaussian function is fitted for the smoothed distribution:

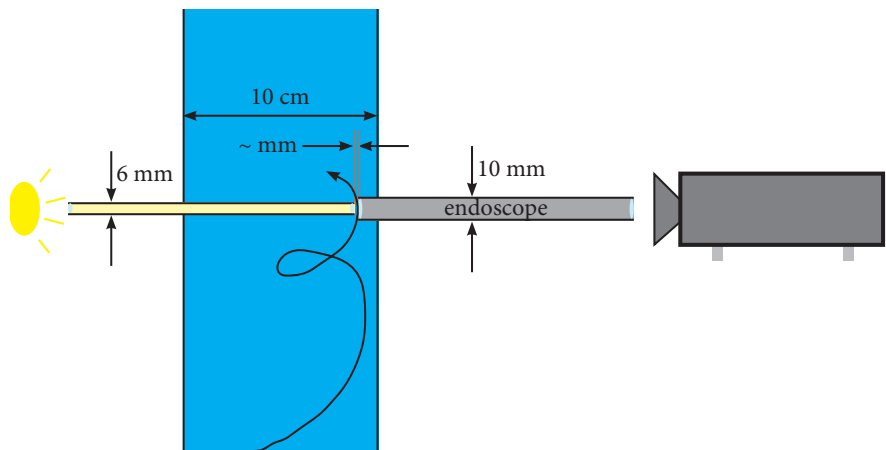
$$f(x) = a_1 e^{\left(\frac{x-b_1}{c_1}\right)^2} + a_2 e^{\left(\frac{x-b_2}{c_2}\right)^2} + a_3 e^{\left(\frac{x-b_3}{c_3}\right)^2} \quad (3.12)$$

(fig. 3.5(c)).

7. The resulting fitted curve represents the distribution of the number of droplets for given size. This is transformed to the volume occupied by the given size according to the relation $(f_v(D) = 1/6\pi D^3 f(D))$

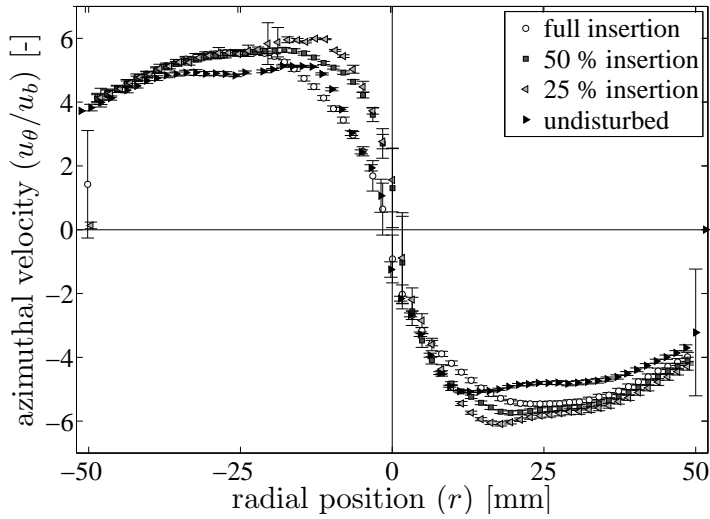


(a) Photograph of the equipment used for direct photography of droplets inside the measurement tube.

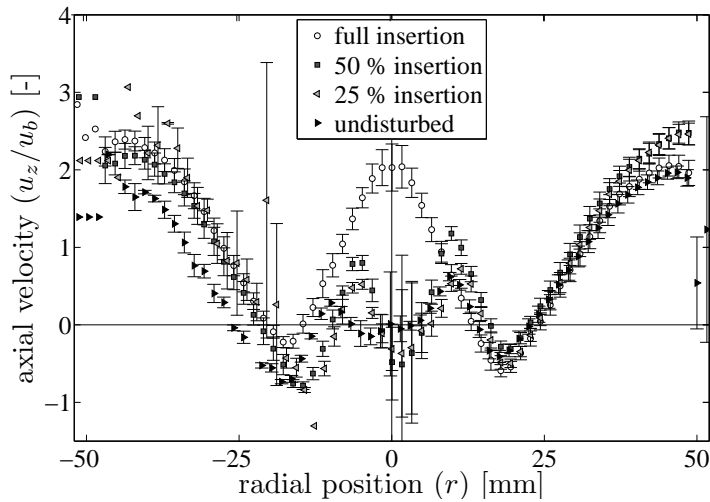


(b) Schematic drawing of the placement of the endoscope in the tube. Light-guide and Endoscope are aligned.

Figure 3.2: Schematic and photograph of the equipment used for the direct droplet photography measurements.



(a) Azimuthal velocity



(b) Axial velocity

Figure 3.3: Velocity profile for $42 \text{ m}^3/\text{h}$ downstream of the strong-swirl element for three different endoscope settings: (i) endoscope from $r = R$ to $r = 0$ and light guide from $r = 0$ to $r = -R$, (ii) endoscope from $r = R$ to $r = 0.5R$ and light guide from $r = -0.5R$ to $r = -R$ and (iii) endoscope from $r = R$ to $r = 0.12R$ and light guide from $r = -0.12R$ to $r = -R$. The endoscope and light-guide were mounted 55 mm downstream of the swirl element. The fluid velocity was measured 670 mm downstream of the swirl element.

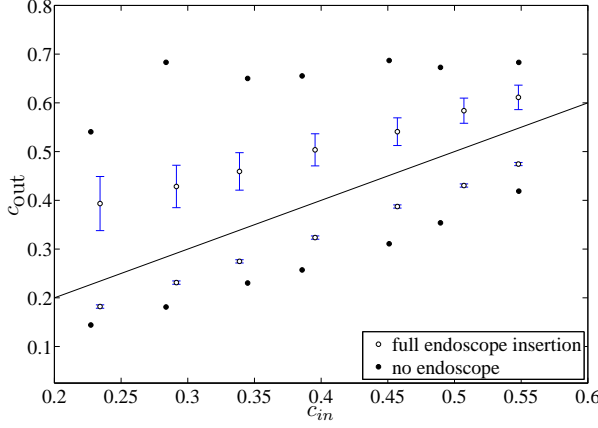


Figure 3.4: Comparison of the oil concentration in LPO (upper left) and HPO (lower right), with and without endoscope present. Strong-swirl element, 170 cm length and 50 mm pickup tube diameter.

3.4.2 Liquid sampling and off-line analysis

As an alternative to the in-situ investigation of the droplet size distribution, tests were also done with off-line analysis in a device based on laser diffraction: a Beckman Coulter LS 230. The procedure to obtain a droplet size distribution exists of three parts (i) liquid tapping (ii) liquid conservation and (iii) feeding into the laser diffraction apparatus.

Mechanism During the 1970s, several authors suggested the possibility to use the forward scattering of coherent light to deduce the particle size distribution [25]. Based on this work, different devices were brought to market like Malvern Instruments and Coulter. These devices first used only the Fraunhofer diffraction approximation, however, nowadays these methods also include the full Mie scattering theory, being the complete solution of Maxwell's equations for the scattering of electromagnetic radiation by a sphere.

According to Syvitsky [25], the scattering by spheres of radius a at small angle θ is reasonably equal to the diffraction by apertures of the same diameter:

$$I(\theta) = a^4 C \left[\frac{J_1^2(ka\theta)}{(ka\theta)^2} \right], \quad (3.13)$$

with λ the wavelength of light, $k = 2\pi/\lambda$, C a constant and J_1 the first order Bessel function of the first kind.

For a range of particle sizes $n(a)$, the intensity pattern changes to:

$$I(\theta) = \int n(a) a^4 \left[\frac{J_1^2(ka\theta)}{(ka\theta)^2} \right] da. \quad (3.14)$$

The aim of the laser-diffraction sizing method is to obtain a measure for $n(a)$, which

means to invert equation 3.14. The equation cannot be inverted in a straight-forward way. Syvitsky [25] provides an overview of the different solution techniques. The commercially available devices have these solution techniques implemented, such that they estimate the particle size distribution $n(a)$ based on the measured light pattern. The output of a laser-diffraction based device consists of an estimation of the droplet size distribution.

Sample requirement The oil/water mixture which is fed to the cyclone investigated in this thesis has a high droplet density which scatters the light uniformly (the mixture is opaque). This opaqueness prevents the determination of the droplet size distribution and can be resolved by tapping liquid, dilution and subsequent off-line analysis. The required liquid loading is device dependent. For the Beckman-Coulter LS 230 used in this research, at maximum of 10 % of incident light may be scattered to provide a successful measurement.

Liquid tapping Liquid is removed from the flow rig using a stainless steel tube. This tube has a diameter in the order of mm's, while the tube from which the liquid is sampled is 100 mm wide. See figure 3.6 for a scheme. The small tube is inserted perpendicularly to the flow rig, such that its depth of penetration in the tube can be adjusted. The inlet of the tube is bent, such that its opening points towards the upstream direction of the flow.

From tests with the endoscope (see figure 3.3) we know that the insertion of a rod in the swirling flow region severely effects the flow pattern in the tube. These tests were not repeated for the tube we used for liquid tapping, but the basic effect is likely to be very similar. We do therefore not know whether the tapped liquid originates exactly from the tapping location in absence of the tapping tube.

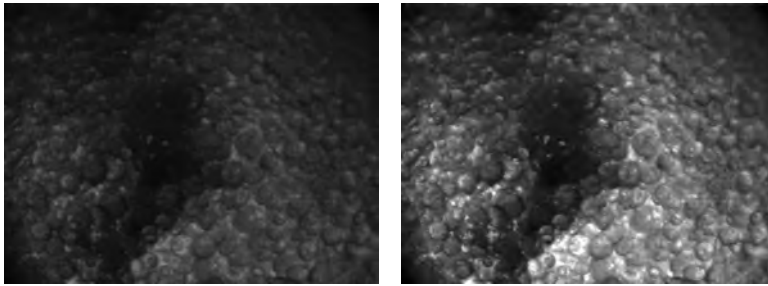
In an ideal situation, the velocity at the positions far upstream (1), just upstream (2) and in the sampling tube (3) as indicated in figure 3.6 is equal. We do, however, not impose an under pressure at the outlet of the tube and therefore the fluid velocity in the tube at location (3) is significantly lower than at (1).

Two effects can be distinguished that affect the droplets entering the sampling tube:

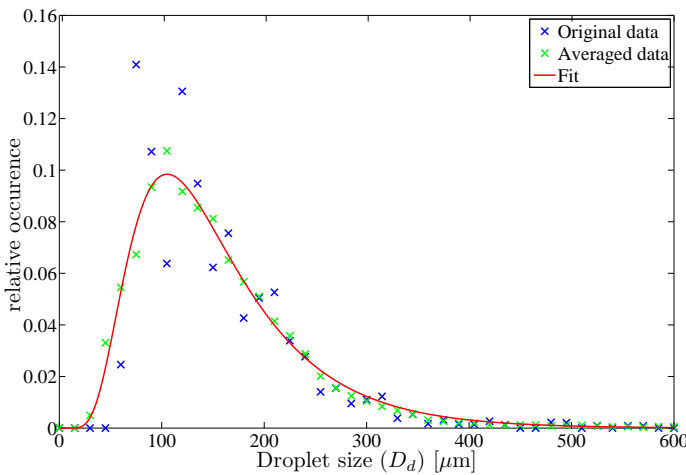
1. the obstacle imposed by the sampling tube diverts some of the liquid from its otherwise undisturbed trajectory. Due to inertia, smaller droplets will follow the stream lines more easily, leading towards a bias to sample large droplets;
2. the diameter of the sampling tube is smaller than that of the swirl tube, which leads to a lower Reynolds number ($\sim 10^6$ outside and $\sim 10^4$ inside). Viscous effects apply a larger shear force on the droplets, tearing them apart. This leads to an under prediction of the droplet size;
3. the Reynolds number is lower inside the pickup tube. The lower turbulence leads to an increase in the size of the smallest eddies, which will lead to reduced droplet breakup. This follows from Hinze's theory that will be introduced in section 6.1.1. From this reasoning, the flow in the small tube promotes coalescence and will bias the end result towards larger droplets

The order of magnitude of these three effects has not been determined during the present research. Effect 1 can be avoided by actively controlling the velocity in the

sampling tube with the aid of a vacuum system. Since effects 2 and 3 cannot be mitigated, we did not put effort in an expensive, controllable vacuum system.



(a) Original photograph, due to the low contrast no droplets can be seen (b) Same photograph with enhanced contrast



(c) Counted, averaged and fitted fractions of droplet size bins. Averaging procedure was a moving average over 5 bins, fitting to a lognormal distribution.

Figure 3.5: Illustration of the process used for the estimation of droplet size distributions based on direct droplet photography.

Emulsion conservation The tapped liquid is collected in a beaker. The stationary liquid settles due to gravity, destroying the droplets. To conserve the droplets, the beaker contains a solution of 50 g/l BRIJ-35, which is proven to prevent droplet coalescence (see Gunning et al. [26] and Hibberd et al. [27]) and be unaffected by salt (see Mapstone [28]). BRIJ-35 is a non-ionic surfactant with normal solubility for brine compared to water. During tests conducted in the present research, we confirmed the stabilizing effect of BRIJ-35 on the liquids used. This was done by measuring the droplet size in the same sample at different times after obtaining the sample. Up to 2 hours of rest, no changes in the measured droplet size distributions were observed.

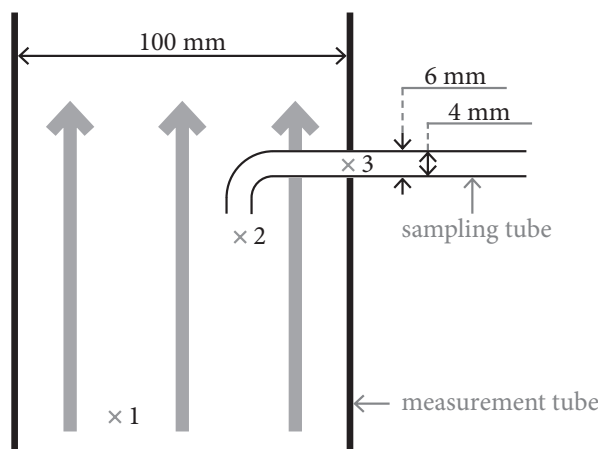


Figure 3.6: Schematic of liquid tapping in the test tube. Three points are indicated: 1. upstream, far from the tube, 2. just upstream the sampling tube and 3. inside the sampling tube.

Dilution and insertion The actual measurement is performed in a Beckman Coulter LS 230. According to the manual, the system is prepared with tap water for background measurements. The sample is added using a pipette until the required light attenuation is obtained.

The liquid is circulated through the measurement chamber with a pump. This pump is likely to break up droplets due to shear. This effect was determined experimentally, see figure 3.7: the measured droplet size gets smaller when the sample resides longer in the Coulter.

3.4.3 Glass fiber sensor

Glass fibres form a common technique for both size and velocity measurement of dispersed droplets. Hartevelde [29] extensively investigated glass fiber probes in gas/liquid systems. In principle, the same method can be applied to other multiphase flow systems. This section investigates the possibility of the use of glass fiber probes inside the oil/water system of an axial cyclone.

Device A typical glass fiber probe sensor consists of four glass fibres: three in a triangular configuration, the fourth somewhat larger fibre in the middle of the others. The glass fibres face upstream and their extremities are sharpened. Figure 3.8 provides a top and side view of the sensor.

Measurement principle Light is fed to each glass fiber, which is emitted into the liquid at the tip. Reflected light is collected through the same glass fiber. A Y-splitter is used to separate the incident and reflected light, after which the intensity of the reflected light is recorded. The transmission of light depends on the refractive index of the liquid surrounding the tip. Typically, glass has a refractive index in the order of 1.5, oil also about 1.5 and water 1.3. When present water will therefore

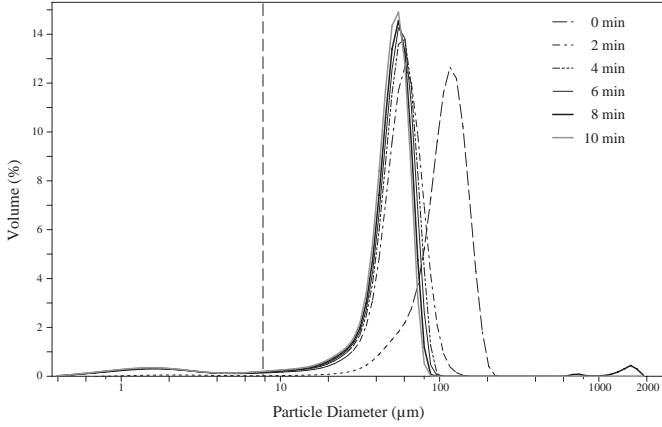


Figure 3.7: Droplet size distribution as measured with the Beckman Coulter LS230. The same sample was analyzed at the indicated times.

reflect more light than oil. When a liquid-liquid interface is present close to the tip, more light will be reflected into the glass fiber. In conclusion, the obtained signal contains information on the phase in which the tip is submerged and the presence and type of interface close to the tip.

Measurements of droplet size and velocity To measure both the droplet size and the droplet velocity, two requirements need to be met:

1. the droplet interface must be pierced by the tip end. The pressure by thrust is given by $\Delta p_t = \rho_d v^2$ which can be interpreted as the droplet inertia exerting a force on the contact surface. The Laplace pressure $\Delta p_L = \sigma/D$ is required to break the interface. The Weber number compares these pressures: $We = \rho v^2 D / \sigma$.

However, this Weber number does not take into account the tip diameter. A very sharp tip will easily break the droplets interface and pierce the droplet itself, while a blunt tip will not. We therefore introduce the diameter of the tip extremity d and propose an alternative Weber number: $We = \rho v^2 D^2 / \sigma d$ for which we do not know the critical value. The sharpest tips obtained in this research were 20 μm in diameter. In combination with a fluid velocity of 10 m/s a density of 1000 kg/m^3 and $\sigma = 30 \text{ mN}/\text{m}$, we obtain a Weber number ≥ 100 . This makes it unlikely that these droplets get pierced, which is confirmed in experiments.

2. the droplet must cover more than one glass fiber. If pierced, the glass fiber measures a chord of the droplet. Even from many chords, it is not straightforward to obtain the average droplet size and velocity. Figure 3.9 shows a droplet approaching a glass fiber probe. If the diameter of the droplet D is much larger than the distance between the fibres w , the curvature of the droplet can be determined and therewith its size and velocity. Typically, the

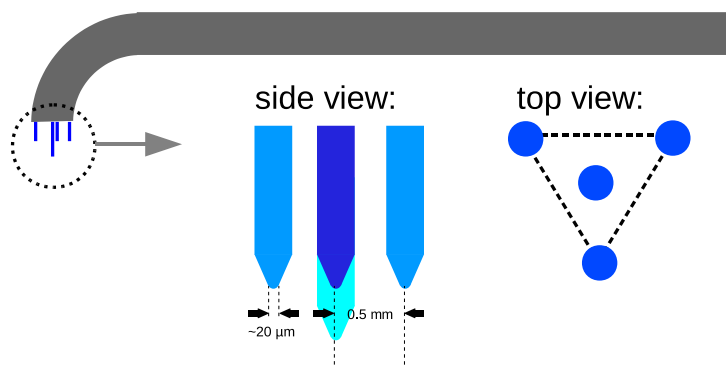


Figure 3.8: Schematic representation of an optical fiber probe. The four glass fibre tips are on the left side, where a stainless steel rod on the right side guides them to the measurement electronics.

minimum distance between the glass fibres $\mathcal{O}(10^{-4})$ m and the smallest detectable droplets are therefore $\mathcal{O}(10^{-6})$ m.

Conclusion Glass fiber sensors are not capable of measuring dispersed oil droplets in an axial cyclones of the dimensions as used in this thesis. The droplets will not be pierced by the glass fibres and if they were pierced, they would only be pierced by a single fiber instead of multiple fibres.

3.4.4 Comparison of methods

The endoscope and Coulter method are compared for equal conditions (namely a swirling flow of $56 \text{ m}^3/\text{h}$ downstream of the initial swirl element with 25 % volumetric oil input. Figure 3.10 shows the good agreement in results between both methods. Although there are some differences, the order of magnitude and the shape of the distribution are found to be in reasonable agreement.

The Coulter method looks to be the least reliable, since the longer tail on the right side of the graph might indicate coalescence somewhere in the sampling process. The peak in the graph at a smaller diameter might be caused by droplet breakup in the Coulter's pump. Therefore, the endoscope method is our preferred method for in-situ droplet sizing.

3.5 A novel capacitance based wiremesh technique

3.5.1 Introduction

Dispersed multiphase flows are opaque, therefore non-intrusive measurement techniques such as LDA can not be used to measure the velocity, whereas the phase distribution is also a parameter of interest.

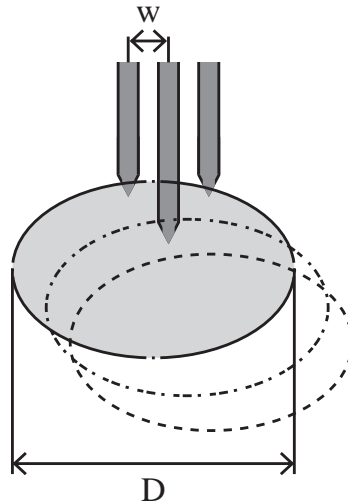


Figure 3.9: Droplet approaching a four-point glass fiber probe. One glass fibre is hidden by the centre one.

The electrode-mesh or wire-mesh sensor was first introduced in 1996 by Prasser et al. [30]. The system consists of two planes with wires. The wires within the same plane are positioned parallel to each other but orthogonal to the wires in the other plane. Emitting an electric pulse sequentially via the wires in one plane (the “sending” wires), depending on the medium between the wires, a current is measured in the wires in the other plane (the “receiving” wires). Since 1996 the system has been improved, both from the perspective of spatial and temporal resolution, but also for different applications. The three-layer wire-mesh, introduced by Ito et al. [31] allows velocity measurements of a dispersed phase. For media with a small difference in specific electrical resistance, the capacitance wire-mesh sensor, as introduced by Da Silva and Hampel [32], gives a much better contrast. For media with a very low impedance, like conductors, the current wire-mesh systems cannot measure the phase distribution, due to smearing of the electric pulses over the complete cross-section.

This thesis introduces a new wire-mesh-based method to measure the phase distribution in multiphase systems with one medium with a very low specific impedance. This work has been executed in cooperation with the Helmholtz Zentrum Dresden Rossendorf (HZDR), being the driving force for the wire-mesh measurement technique. From the perspective of the ISPT project as described in this thesis, the

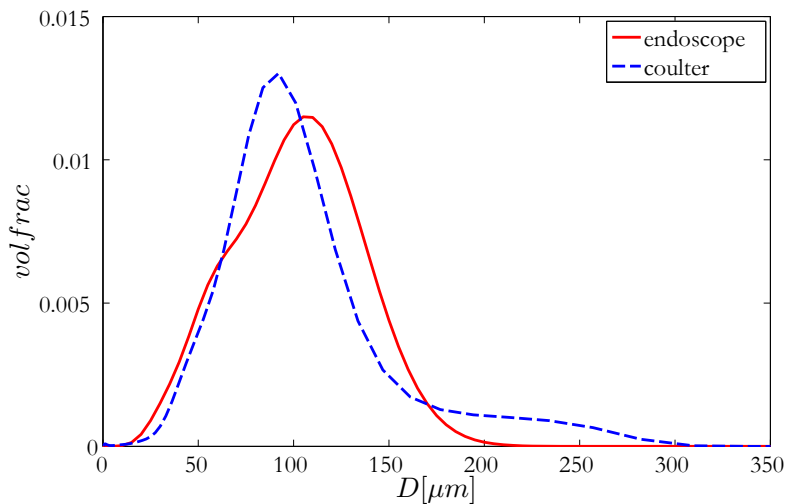


Figure 3.10: Comparison of the measured droplet size distribution with a laser diffraction based system (Coulter) and with the intrusive endoscope method

time-dependent phase distribution in the axial cyclone is of great interest: the aim is to coalesce the droplets into a continuous phase in the center of the tube: the oil core. Furthermore it is relevant to know the stability of this kernel, for example Yazdabadi et al. [15] showed that a cyclone has a precessing vortex core with a period of a very small time scale, in the order of ms.

3.5.2 Geometry

The wire-mesh sensor considered in the present study consists of three planes. The motivation for these planes is discussed below. The sensor itself is a stainless steel flange with three planes of wires. The wire planes are orthogonal to the tubes wall and separated a few mm in the stream wise direction. Within one plane, all wires are parallel. The orientation of the wires between subsequent layers differs 90° . Two layers are coated, such that the wires are electrically insulated from the liquids in the sensor. Figure 3.11 shows the geometrical configuration of the wires. The sending and receiving wires are insulated from the fluida with a coating, whereas the wires in the ground plane are blank stainless steel. The sending and receiving wires are insulated from each other, while the ground plane wires are all mutually connected and kept at ground potential.

3.5.3 Electric fields

We want to measure the complex-valued impedance of the liquid. The impedance is characterized with a real part, normally known as resistance and an imaginary part, normally known as capacitance. Both quantities are relevant to characterize the substance.

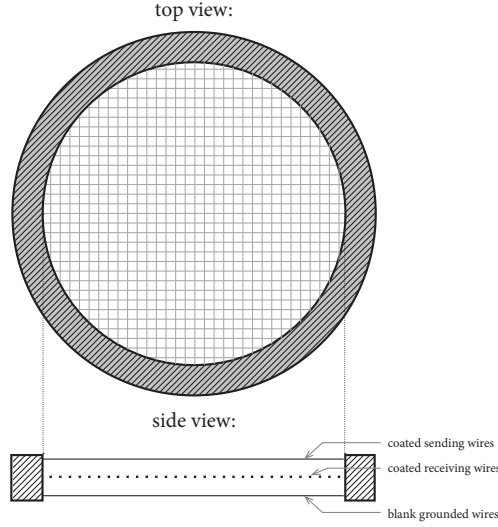


Figure 3.11: Top and side view of the different wire-planes in the three layer wire-mesh.

Resistance The resistance of a substance is given by the relation between the Direct Current (D.C.) voltage and the D.C. current, according to $R = V/I$. The ability of a liquid to conduct an electric current is, however, not constant in time, it is caused by the capacitance of the electrodes, the ion layers in the liquid and the cables [30].

Capacitance The concept of resistance holds for D.C.. When the applied voltage is time-dependent, there is the additional effect of the phase angle. The ability to store electric charges gives capacitors the ability to store charges and pass it on with a time delay - this delay is represented by the phase angle, i.e. an imaginary part that corresponds to the phase change of a sinusoidal function.

Impedance effect of insulated wires Fluids with a very low specific impedance, namely conductors, prevent the normal operating procedure of the wire-mesh system as described by Prasser et al. [30]. The pulses emitted by a single sending wire are guided throughout the complete system. The signal picked up by the receiving wires shows a uniform phase distribution, even if some wire crossings are covered with a less conducting phase. To avoid this phenomenon, we coat the wires. Of the local impedance, we then only measure the capacity, which can be calculated from:

$$C = \epsilon_r \epsilon_0 k_g. \quad (3.15)$$

The permittivity of vacuum ϵ_0 is 8.85 pF/m, ϵ_r is the material's relative permittivity and k_g is a geometry factor. The geometry factor accounts for the region of influence of the local substance, the simplest model consists of square regions, more sophisticated models use diamond shapes (see for example Smeets [33]). In this work, we use the simple mode with square regions. For a wire distance w and a inter-plane distance d it follows that:

$$k_g = \frac{w^2}{d}, \quad (3.16)$$

which is valid for a flat plate geometry. The system of a single excited sending wire and an array of receiving wires does not fit this geometrical model very well. However, for an understanding of the physics it is adequate.

Current induction

Inside the conducting wires, a potential difference does not exist. The electric field is therefore by definition equal to 0. The sending and receiving wires are insulated, and between them, assuming a flat plate geometry, an electric field \vec{E} will form, with its magnitude equal to:

$$|\vec{E}| = \frac{V}{d}. \quad (3.17)$$

This electric field follows the block pulse of the sending wire potential, so

$$\frac{\partial \vec{E}}{\partial t} \neq 0. \quad (3.18)$$

and we can determine the change in magnetic field from Ampère's law:

$$\vec{\nabla} \times \vec{B} = \mu_0 \vec{J} + \mu_0 \epsilon_0 \frac{\partial \vec{E}}{\partial t} \quad (3.19)$$

The current \vec{J} through the wires is negligible and therefore the magnetic field \vec{B} is proportional to the change in potential in the wire. The change in the magnetic field \vec{B} implies a change in the electric field \vec{E} via Faraday's law:

$$\vec{\nabla} \times \vec{E} = -\frac{\partial \vec{B}}{\partial t}. \quad (3.20)$$

The electric displacement \vec{D} is coupled to the electric field \vec{E} via

$$\vec{D} = \epsilon_0 \epsilon_r \vec{E}. \quad (3.21)$$

The displacement \vec{D} drives a displacement current:

$$\vec{J}_d = \frac{\partial \vec{D}}{\partial t}. \quad (3.22)$$

This displacement current \vec{J} is proportional to the potential in the receiving wire. It is proportional to $\epsilon_r \frac{\partial^2 V}{\partial t^2}$. This derivation holds as long the problem can be treated quasi-static [34]. The measured potential is therefore a measure for the electric permittivity ϵ_r of the material between the wires.

Table 3.2: Relative permittivities of materials used in this work

<i>material</i>	ϵ_r
air	1.0
mineral oil	2.1
tap water	≈ 80

Material properties

The relative permittivities of dielectric materials is a specified parameter, the relevant values for this research are listed in table 3.2.

The relative permittivity increases for increasing salt concentration in the water due to the increasing number of ions that act as free charges. At a given concentration, the brine (salt water) can be considered to be a conductor: there are enough free charges to extend the potential throughout the complete material, reducing the electric field to 0. The induction of current in the receiving wires is highly efficient, for all receiving wires covered with the conducting phase simultaneously. This disables the distinction of substances with a lower relative permittivity in the complete region covered by the affected sending and receiving wires.

Ground plane

To overcome the problem with the high electric permittivity of brine, short circuiting all wires submerged in brine, a ground plane is added to the sensor. This plane consists of blank stainless steel wires, such that the continuous region of brine is kept at ground potential. The induced current in the receiving wires is 0 for the wire crossings covered with brine. With this method it is therefore not possible to distinguish different phases being conductors.

3.5.4 Measurement circuit

The sensor as applied in this research consists of three planes with wires, each positioned orthogonal to the tube wall, with a small intermediate distance in the order of mm's. The wires in each plane are equidistant and parallel, sharing their function: either sending, receiving or grounding (see figure 3.11). Figure 3.12 shows a simplified sensor with 4×4 wires. The principle can easily be extended to more wires. The sending (S#) and receiving (R#) wires are coated with an insulating paint, and have an orthogonal orientation. The grounding wires consist of blank stainless steel, are oriented parallel to the sending wires and they connect to ground potential at all times.

The sending wires are switched sequentially to a block pulse generator. To each wire, a single block (consisting of a first half of $+U_s$ and a second half of $-U_s$) is supplied at a time. Not-activated sending wires are grounded. The receiving wire sample the potential of the receiving wires at the end of the sending block pulse. From experimental findings, we know that this sampling overlaps with the region in which $dV_{\text{send}}/dt \neq 0$.

Figure 3.13 shows the sending signal of an arbitrary sending wire and the potential

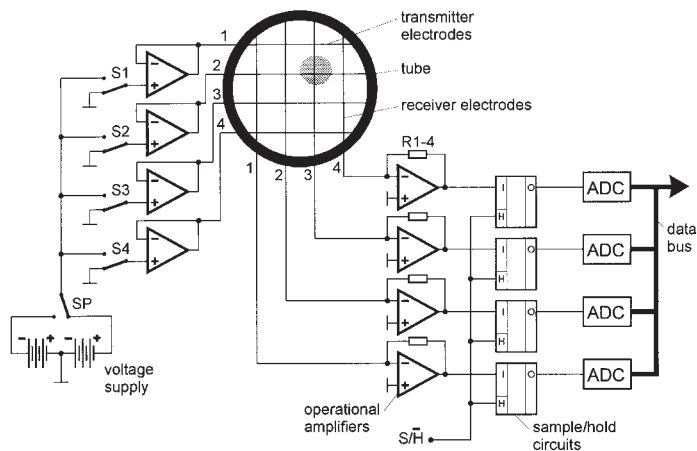


Figure 3.12: Simplified scheme of the electrode mesh and electronics [30].

of an arbitrary receiving wire for four different fluids: brine, tap water, oil and air. The signals were sampled at 9.97 MHz, providing a gradual shift in sample points of the signal, allowing to reconstruct the signals with a temporal resolution beyond 10 MHz.

In section 3.5.3 we deduced the relation $V_{\text{receive}} \propto \epsilon_r \frac{\partial^2 V}{\partial t^2}$. Figure 3.13 proves the validity of this relation: the potential on the receiving wires is proportional to dV_{send}/dt . Furthermore, we can distinguish between different stagnant liquids that are present in the wire-mesh: brine has the largest ϵ_r and the largest signal, then tap water, while oil and air provide the smallest signal.

The measured pulses have some unexpected features: (i) the average value for the receiving potential is smaller than 0, (ii) oil and air yield the same measurement value and (iii) brine does not provide a zero measurement value as was designed.

In contrast to the expectation that $V_r \propto \epsilon_r \frac{\partial^2 V_s}{\partial t^2}$, there is also an excited potential on the receiving wires when the send potential is constant in time for oil, air and demineralized water. A possible cause is the electric field that exists between the sending wire and the ground plane. A field that is stable for non-conducting liquids, and one that is compensated by a conducting liquid.

The bias can be caused by an offset in the measurement procedure, or by an offset in the potential caused by the wire-mesh electronic system. This does not appear to affect the results.

The small difference in signal between oil and air could be caused by remaining oil on the wire-mesh wires. Due to the stagnant nature of the liquids during these tests, the wires are not flushed that well.

If the brine potential was zero, no signal would be picked up. There are two reasons why the brine potential is not homogeneous zero: the conducting nature of brine relies on the movement of ions. They have the tendency to spread based on the surrounding electric fields, the Cl^- ions will gather to the wire with a positive charge, the Na^+ ions to a negative charged wire. This leads to effects that differ from metal conductors, for which the charge carriers have less freedom. Furthermore

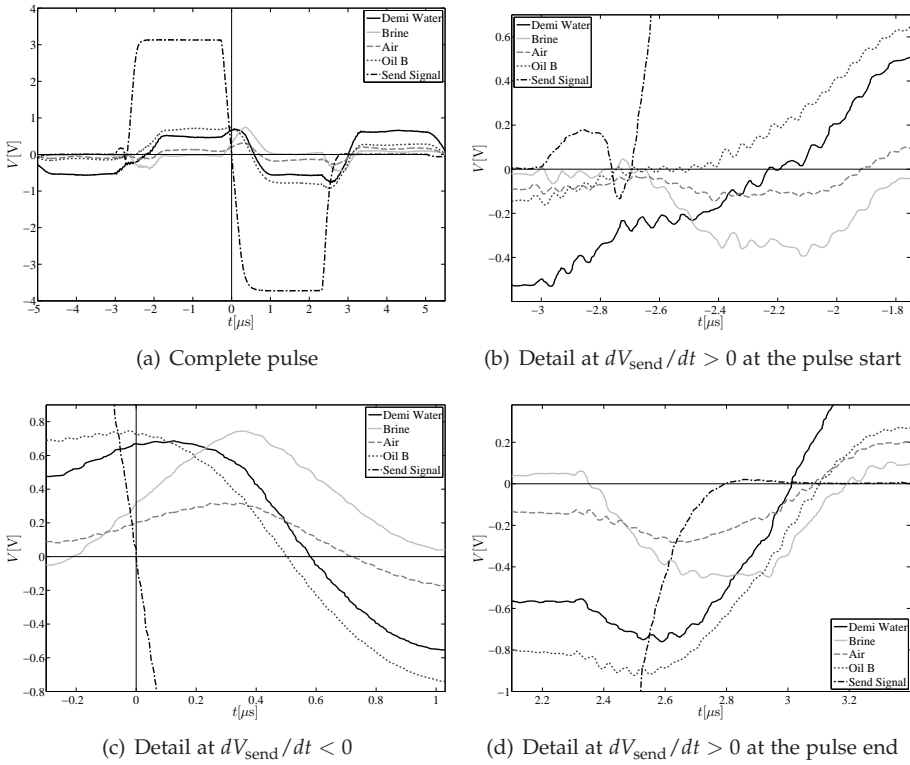


Figure 3.13: Potential on a receiving wire for given send pulse in four different liquids. The wiremesh sensor was fully submerged in the indicated liquid.

there is a finite current through the grounding system.

3.5.5 Fluid-sensor interaction

The wire-mesh sensor has been tested in the axial cyclone as described in this thesis. During this experimental work, wires broke at their connection to the wall. Different solutions with thicker wires or other mechanical connection methods could not withstand the forces introduced by the flow on the wires.

From acoustic observations, we know that the wires in the wire-mesh vibrate. This vibration is caused by the vortex streets in the wakes of the wires and can be expressed by the Strouhal number:

$$St = \frac{fD}{v}, \quad (3.23)$$

expressing the relation between vibration frequency f , wire diameter D and velocity v . The Strouhal number depends on the wires Reynolds number ($Re_{\text{wire}} = \frac{u_c D}{\nu}$, with u_c the velocity of the continuous phase) and can be described by a relation given by Williamson and Brown [35]:

$$St \approx 0.2234 - \frac{0.3490}{\sqrt{Re}} \quad (3.24)$$

For typical conditions ($u_c \approx 10$ m/s and $D = 0.2$ mm) the Reynolds number is 1000, leading to a Strouhal number of 0.21 and a frequency of 11 kHz. At the connection point of the wires, each oscillation means a sharp bend in the metal. With these high frequencies, the material fails in a short period of time due to fatigue.

A solution to this mechanical problem is possible, for example by damping the wire oscillation with a spring. Due to constraints of time and budget, we did not pursue such a solution.

3.5.6 Visualization of an oil kernel

Since it was not possible to apply the method in swirling flow at design conditions, due to mechanical constraints as described above, we created an alternative system to test the phase distribution measurement method. The expected phase distribution in an axial cyclone is to have the lightest phase (possibly air, or otherwise oil) in the center and a gradient towards denser phases at larger radial positions. By injecting oil directly into the center of a tube, such a phase distribution can be created without the high physical load on the wires as is the case for swirling flow.

The tube element has a 50 mm wide tube inside a 100 mm tube, see figure 3.14. The wire-mesh sensor is mounted a few mm above the tube outlet. The brine flow rate was set to 26 m³/h, while the oil flow rate was 5 m³/h.

The wire-mesh used in figure 3.15 has one broken wire, which can be seen from the white line in all results. The objective of these tests was to detect an oil kernel which is surrounded by brine. We succeeded in doing so, however, the contrast is moderate: the signal of the “oil” cell with the lowest value is only 2 times the value of the strongest “water” cell. The time- and space-averaged contrast is 17:1.

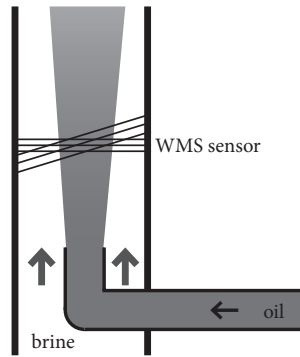


Figure 3.14: Schematic of the setup to create a low-velocity oil kernel at the wire-mesh, figure is not to scale

3.5.7 Discussion and Conclusion

In this study, we combined existing wire-mesh components to form a system capable of measuring in liquids with a high conductivity. The measured variable is the relative permittivity ϵ_r which proves to be a discriminating parameter for many gases and liquids. For the conducting phase ϵ_r is not measured - due to a grounded plane the measured value is 0 in these regions.

Tests with a two phase oil/water system show the capability of distinguishing the two phases with a minimum contrast of at least 2:1 and an average contrast of 17:1. These values are obtained with an unmodified electronics box and software. By optimizing the timing of sampling of the receiving wires, this contrast should be significantly improved.

For measurements in liquid-liquid cyclones, wire fatigue is problematic. The flow introduces high-frequency vibrations in the wires, which fail in a rather short time at the connection point to the wall.

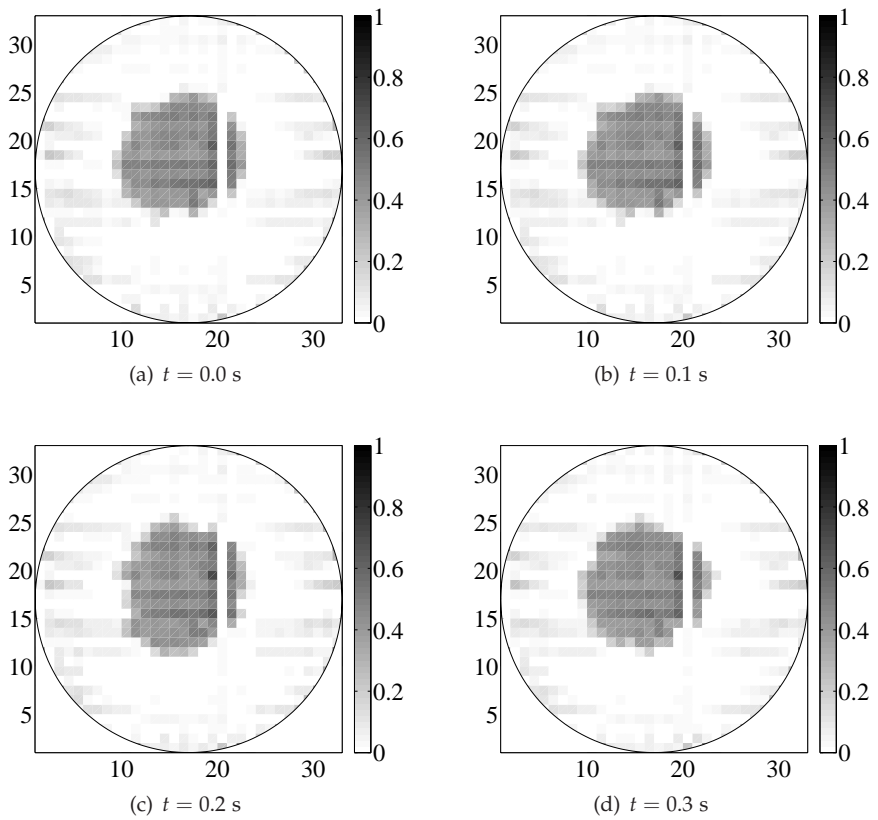


Figure 3.15: Four snapshots of the phase distribution measurement with the capacitance based wire-mesh system.

CHAPTER 4

Strength of generated swirl

This chapter describes the liquid velocity profile for different swirl elements used in this thesis. It aims at understanding the flow pattern generated by a specific swirl element and deducing the acceleration in the radial direction experienced by the droplets.

4.1 Theory

The acceleration of a dispersed liquid-liquid system can lead to the break-up of droplets. Since larger droplets can be separated with a weaker centrifugal pressure field, it is preferable to design a cyclone such that droplets will not break below a critical size or will not break at all. This section discusses models to predict the droplet break-up behavior.

4.1.1 Force balances

Droplets can exist due to the interfacial tension force. Forces acting on the interface, such as shear and viscous forces, deform the droplets. If these forces exceed the interfacial tension force by a critical extent, the droplet will break into two or more smaller droplets.

The critical value for droplet break-up is given by the Weber number and the Capillary number:

$$\text{Weber:} \quad \text{We} = \frac{\text{shear force}}{\text{interfacial tension force}} = \frac{|\vec{t}| D_d}{\sigma}, \quad (4.1)$$

$$\text{Capillary:} \quad \text{Ca} = \frac{\text{viscous force}}{\text{interfacial tension force}} = \frac{\mu u}{\sigma}, \quad (4.2)$$

with \vec{t} the shear on the droplet, D_d the droplet diameter, σ the interfacial tension between dispersed and continuous phase, μ the dynamic viscosity and u the characteristic velocity.

For flows at high Reynolds numbers ($Re > 1000$) such as in industrial cyclones, the shear forces dominate over viscous forces.

The actual force balance of the Weber number can be written in many different ways. Below, I will introduce some well known and convenient formats.

Acceleration induced breakup

Droplets experiencing a large enough shear force are prone to be torn in multiple pieces. This effect is known as shear induced droplet break-up, for which the interfacial tension force ($F_\sigma = \sigma_d \pi D_d$) tries to keep the droplet together, while the shear forces ($t \pi D_d^2$, with t the tangential force per unit area) try to tear the droplet apart. The balance of these forces is given by the Weber number (We) which is introduced above.

According to experimental results discussed by Kolev [36] the critical Weber number depends on the Reynolds number, but for $Re > 2000$ it is reasonable to approximate the critical Weber number as $We_{\text{critical}} = 5$.

The tangential force per unit surface t is estimated as the drag force divided by the surface area of the droplet (assumed to be a sphere):

$$\vec{t} = \frac{\vec{F}_{\text{drag}}}{\pi D_d^2} = \frac{1}{8} C_D \rho_c \left| \Delta \vec{u}_{\text{slip}} \right| \Delta \vec{u}_{\text{slip}}, \quad (4.3)$$

with $\Delta \vec{u}_{\text{slip}}$ the difference between the droplet velocity and the continuous phase velocity surrounding. From the two equations above, the critical velocity is derived:

$$\Delta u_{\text{slip}} > \sqrt{\frac{8 We_{\text{crit}} \sigma_d}{C_D \rho_c D_d}}. \quad (4.4)$$

The following example is based on typical conditions of the research in this thesis (with $\sigma_d \approx 30 \cdot 10^{-3}$ N/m and $\rho_c \approx 1000$ kg/m³). For the maximum local velocity occurring in numerical simulations [13] ($|u_{\text{max}}| = 18$ m/s), the maximum droplet Reynolds number for a $10 \mu\text{m}$ droplet is approximately 200, which leads to a $C_D \approx 0.7$ (see Appendix D). The critical size is then given by:

$$\left| \Delta \vec{u}_{\text{slip}} \right|^2 D_{d,\text{crit}} = 1.7 \cdot 10^{-3} \left[\frac{\text{m}^3}{\text{s}^2} \right], \quad (4.5)$$

which this provides a maximum stable droplet size of $5 \mu\text{m}$ with the assumption that the droplet is accelerated instantaneously to the terminal velocity. The estimated maximum droplet size is therefore judged to have a too small value, since larger droplets are found, as we will see in chapter 6.

Break-up by turbulent eddies

Hinze [37] proposed a model for the maximum droplet size in turbulent flow:

$$D_{\text{max}} \left(\frac{\rho_c}{\sigma} \right)^{3/5} \epsilon^{2/5} = 0.725, \quad (4.6)$$

where ρ_c is the density of the continuous phase and ϵ the turbulent dissipation rate.

The appropriate estimation of ϵ is essential for a correct prediction of the maximum droplet size. The turbulent length scale can be estimated by:

$$\ell = \left(\frac{\nu^3}{\epsilon} \right)^{1/4} = \ell_0 \text{Re}^{-3/4}, \quad (4.7)$$

where ν is the kinematic viscosity and ℓ_0 the scale of the largest eddy (the tube diameter). Taking this into account, the turbulent kinetic energy can be expressed as:

$$\epsilon = \frac{\nu^3 \text{Re}^3}{\ell_0^4}. \quad (4.8)$$

Figure 4.1 relates the maximum droplet size according to Hinze's model (equation 4.6) to the flow rate. At nominal conditions for the flow rig used in this investigation the flow rate equals $56.5 \text{ m}^3/\text{h}$, so that the maximum droplet size is predicted to be 0.23 mm . As could be expected, a lower flow rate results in a larger maximum droplet size.

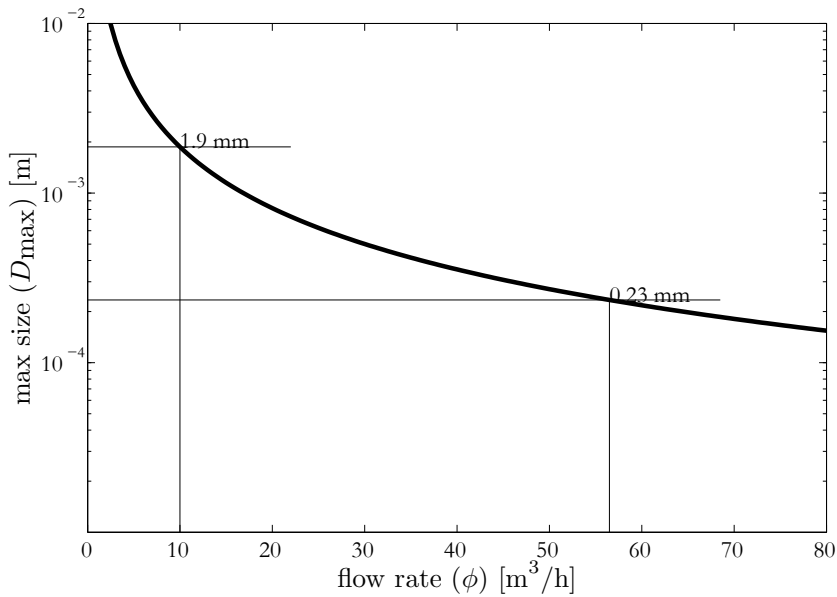


Figure 4.1: Maximum droplet size as function of the flow rate, according to equation 4.6, for a 10cm tube with a flow rate of $56 \text{ m}^3/\text{h}$ with a continuous liquid density of $1064 \text{ kg}/\text{m}^3$.

Break-up by strain

The strain rate $\dot{\gamma}$ is the magnitude of the velocity gradient tensor. The velocity difference across the droplet is proportional to the strain rate. Within the actual static swirl element and downstream tubing, the largest strain occurs close to the walls. Especially swirling flow is pushed towards the wall, leading to high velocity gradients. Actual velocity measurements, as in figure 4.6 indicate a distance between the

maximum velocity ($\sqrt{v_\theta^2 + v_z^2}$) and the wall in the order of a few mm. This results in a typical strain with an order $\mathcal{O}(10^4) \text{ s}^{-1}$.

Galinat et al. [38] define a droplet Weber number based on the strain rate $\dot{\gamma}$:

$$\text{We} = \frac{\rho_c (\dot{\gamma} D_d / 2)^2 D_d}{\sigma}. \quad (4.9)$$

For typical conditions in our cyclone ($\rho_c = 1064 \text{ kg/m}^3$ $D_d = 100 \mu \text{ m}$ and $\sigma = 30.10^{-3} \text{ N/m}$), this leads to a Weber number of 0.9, which is smaller than the critical Weber number of 5. For droplets of about 0.2 mm, the critical Weber number of 5 is exceeded and these are therefore expected to break-up in the near wall zone.

4.1.2 Droplet elongation

The acceleration of droplets stretches them along their trajectories, i.e. in case of Stokes flow along the streamlines, forming streaks of dispersed fluid. Based on the Plateau-Rayleigh instability, these elongated droplets will break if their length exceeds the perimeter (πD_d) of the elongated droplet.

Consider a droplet with diameter D_1 flowing through an area with a flow area A_1 . When the same flow rate is squeezed into a region with a flow area of $A_2 < A_1$, the liquid is accelerated and the droplet gets elongated to a wire-shape with diameter

$$D_{d,2} = \frac{A_2}{A_1} D_{d,1} = \frac{D_{f,2}^2}{D_{f,1}^2} D_{d,1}, \quad (4.10)$$

with D_f the diameter corresponding to the flow area A_1 and A_2 , see figure 4.2.

Approximating this elongated droplet as a cylindrical shape with diameter $D_{d,2}$ and a length L leads to a length of

$$L = \frac{2}{3} \frac{D_{d,1}^3}{D_{d,2}^2} = \frac{2}{3} \left(\frac{D_{f,1}}{D_{f,2}} \right)^4 D_{d,1} \quad (4.11)$$

From the Plateau-Rayleigh instability, we know that the maximum stable length for a stretched droplet is in the order of πD_d . Based on this criterion, we derive that all droplets break-up if

$$D_{f,2} < \sqrt[6]{\frac{2}{3\pi}} D_{f,1} \approx 0.77 D_{f,1} \quad (4.12)$$

This relations holds when the residence time in the contraction is much smaller than the time required for the droplet to restore its spherical shape. We use the estimate in equation 4.12 at the end of the next section 4.1.3.

4.1.3 Time scales

Instead of the length scales of the droplets, we can also consider the time scales: what time does a droplet need to adapt to its surroundings and how quickly does the surrounding liquid change its velocity. In this section, we these characteristic quantities.

Particle relaxation time

The droplets need to adapt to the velocity of the surrounding fluid - the fluid accelerates due to conservation of angular momentum and its incompressibility. The dispersed phase therefore experiences a drag force which accelerates the droplets. For the design of the tapered section it is important that the acceleration of the liquid is such that the maximum slip velocity, i.e. the velocity difference between continuous phase and dispersed phase is limited.

The equation of motion of a dispersed droplet driven by the drag force of the surrounding continuous phase is given by [39]:

$$\frac{\pi}{6} \left(\rho_d + \frac{1}{2} \rho_c \right) D_d^3 \frac{d\vec{v}}{dt} = \frac{C_D}{2} \frac{\pi D_d^2}{4} \rho_c (\vec{u} - \vec{v}) |\vec{u} - \vec{v}|, \quad (4.13)$$

with \vec{u} the continuous phase velocity and \vec{v} the dispersed phase velocity. In equation 4.13, we include the virtual mass effect, but we neglect other contributions to the force on the droplets. In this equation the droplet Reynolds number $\text{Re}_d = \frac{\rho_c D_d |\vec{u} - \vec{v}|}{\mu_c}$ can be substituted to get:

$$\frac{d\vec{v}}{dt} = \frac{18\mu_c}{\left(\rho_d + \frac{1}{2} \rho_c \right) D_d^2} \frac{C_D \text{Re}_d}{24} (\vec{u} - \vec{v}) \quad (4.14)$$

For low droplet Reynolds numbers, which are likely to occur for the small droplets having a moderate velocity difference with the surrounding liquid, we may assume Stokes flow: $\frac{C_D \text{Re}_d}{24} \approx 1$. We introduce the characteristic time scale

$$\tau_d = \frac{\left(\rho_d + \frac{1}{2} \rho_c \right) D_d^2}{18\mu_c} \quad (4.15)$$

such that the original equation of motion can be approximated by

$$\frac{d\vec{v}}{dt} = \frac{1}{\tau_p} (\vec{u} - \vec{v}). \quad (4.16)$$

A droplet will adjust to $\frac{1-e}{e}$ of the terminal velocity within the particle relaxation time τ_p .

For conditions typical in this research ($\rho_d = 872 \text{ kg/m}^3$, $\mu_c \approx 1.10^{-3} \text{ Pas}$), the characteristic time scale of the droplet ranges from $\mathcal{O}(10^{-5}) \text{ s}$ for a $10 \text{ }\mu\text{m}$ droplet to $\mathcal{O}(10^{-3}) \text{ s}$ for a $250 \text{ }\mu\text{m}$ droplet.

Timescale of the acceleration

Consider the fluid moving through a sudden contraction, where the diameter of the tube with circular cross section is reduced from D_{f1} to D_{f2} for a fluid path length of L . Due to the incompressibility of the fluid and conservation of mass, the velocity in the latter surface is

$$v_2 = \frac{D_{f1}^2}{D_{f2}^2} v_1 \quad (4.17)$$

The time scale for the contraction is estimated by dividing the path length L for the fluid by the mean velocity:

$$\tau_f = \frac{L}{\frac{1}{2}(v_1 + v_2)} \quad (4.18)$$

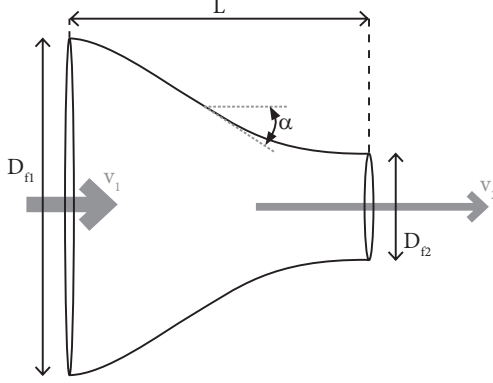


Figure 4.2: Sketch for the estimation of the time scale in a gradual contraction.

For characteristic conditions in this research ($v_1 \approx 2$ m/s, $D_{f1}/D_{f2} \approx 2$ and $L \approx 0.1$ m), the time scale τ_f is in $\mathcal{O}(10^{-2})$ s. This is larger than the particle relaxation time scale τ_p .

Droplet restoration time

Droplets are deformed by forces acting on their surface. The interfacial tension tends to keep the droplet in a spherical shape to reach a minimum energy. The restoration from a deformed state to a spherical shape can be treated as a damped harmonic oscillator, for which we will employ the following parameters:

- D_d : diameter of the undisturbed droplet
- $m = \frac{\pi}{6}\rho_d D_d^3$: droplet mass
- x displacement parameter, given by the difference between the actual droplet perimeter and the undisturbed one (πD_d).

The forces included in the equation of motion are:

- **Spring force:** caused by interfacial tension, $F_s \sim -\sigma x$;
- **Viscous damping force:** caused by viscous friction $F_\mu \sim -\mu_d \dot{x} \frac{D_d}{2}$.

Leading to the equation of motion:

$$m\ddot{x} = -\sigma x - \mu_d D_d \dot{x}. \quad (4.19)$$

To derive an estimate for the maximum velocity of the droplet contraction, we consider the position at which $\ddot{x} = 0$ and the deformation velocity \dot{x} is at its maximum. Then:

$$\begin{aligned}\mu_d D_d \dot{x}_{\max} &= -\sigma x \\ \Downarrow \\ |\dot{x}| &= \frac{\sigma}{\mu_d}\end{aligned}$$

For typical conditions in this research ($\mu_d \approx 10 \cdot 10^{-3}$ Pa s and $\sigma \approx 30 \cdot 10^{-3}$ N/m) this leads to a contraction velocity $v_{\text{contraction}}$ of 3 m/s during the rebound of the deformed droplet to a spherical shape.

Time scale estimate Equation 4.11 relates the gradual reduction in tube diameter to the stretching of a droplet. The order of time required for the droplet to contract from this elongated shape to a spherical shape is:

$$\tau_{\text{contraction}} = \frac{L}{v_{\text{contraction}}} = \frac{2}{3} \frac{\mu_d}{\sigma} \left(\frac{D_{f,1}}{D_{f,2}} \right)^4 D_{d,1}. \quad (4.20)$$

For typical conditions in the cyclone as used in this thesis ($D_{f,1} = 0.3$ m, $D_{f,2} = 0.1$ m and $D_d = 100 \mu\text{m}$), the time required to contract the droplet is in the order of $\mathcal{O}(10^{-3})$ s, which is smaller than the residence time in the contraction. The droplets can therefore contract before they break-up by the Rayleigh-Plateau instability.

Conclusion

The chance of droplet breakup can be assessed by looking at the time scales. If the time a droplet needs to restore to its original, spherical shape is much shorter than the time in which a droplet is deformed, it is likely that a droplet stays in tact. If its is deformed faster than it can restore itself, the droplet will break.

4.2 Swirl element design

Three different swirl elements were used in this research. This section provides the background of the design of these swirl elements.

The swirl elements have been designed based on the centrifugal pressure field that is required for the separation of 100 μm oil droplets with a density difference $\rho_{\text{brine}} - \rho_{\text{oil}} = 200$ kg/m³ at a flow rate of 56.5 m³/h in a 10 cm diameter tube (bulk velocity of 2 m/s) with a length of 2 m.

4.2.1 Strong swirl element

The most essential part of an in-line axial cyclone is the swirl element, which generates a swirling motion. This section provides the considerations for the design of the first swirl element, being the one generating a strong vortex. The work in this section was executed in the framework of ISPT project OG-00-004 by Slot [13].

Azimuthal acceleration

The first design for an in-line swirl element was based on various assumptions. This section introduces the assumptions and concludes with the summary of the basic design parameters.

1. Separating force The rotating motion of the continuous phase exerts a pressure on a dispersed droplet which would maintain a droplet with no density difference in a circular motion with constant radius. A droplet with a larger density than that of the continuous phase lacks enough inward force to maintain the same radial distance and spirals outward, a droplet with a smaller density than that of the continuous phase is pushed more inward than required for a circular motion with constant radius and spirals therefore inward. The net force, pointing inward, is:

$$F_{\text{inward}}(r) = \frac{\pi D_d^3 \Delta \rho u_\theta^2}{6 r_d}, \quad (4.21)$$

with D_d the droplet diameter, $\Delta \rho$ the density difference ($\rho_c - \rho_d$), u_θ the azimuthal velocity of the continuous phase and r_d the radial position of the droplet.

This force accelerates the droplet in the radial direction, with a velocity different from that of the surrounding liquid. This slip velocity induces a drag force which is counteracting the accelerating force. For small droplet Reynolds numbers ($\frac{v_s D_d}{\nu} \ll 1$), Stokes' drag law can be applied:

$$F_{\text{stokes}} = 3\pi\mu D_d v_s, \quad (4.22)$$

with μ the dynamic viscosity of the continuous phase and v_s the settling velocity of the droplet. For a droplet moving at its settling velocity, we obtain the relation:

$$v_r = \frac{\Delta \rho D_d^2 u_\theta^2}{18 \mu r_p}, \quad (4.23)$$

with v_r the velocity of the droplet in the radial direction towards the center of the tube.

2. Velocity profile Dirkzwager [3] found that the velocity profile in an axial cyclone can be described reasonably accurate by the velocity distribution of the Burgers vortex:

$$u_\theta(r, z) = U_\theta(z) \quad \text{for } r > R_c, \quad (4.24)$$

$$u_\theta(r, z) = \frac{U_\theta(z)r}{R_c} \quad \text{for } r < R_c. \quad (4.25)$$

Typical values for R_c of $0.25R$ have been reported [3].

3. Oil core The cyclone moves the lighter phase, oil, inward. The existence of an oil-continuous core in the center is therefore likely. When 10 % of the volume is occupied by this core, this corresponds to a radius of $0.3R_i$, which is larger than the critical radius R_c in equations 4.24 and 4.25. The inward moving oil droplets are therefore mostly in the outer region of the Burgers vortex for which $v_\theta = \text{constant}$.

4. Velocity coupling From the coupling between the axial and azimuthal velocity components, the following relation for the droplet position as function of the axial distance is derived:

$$v_r = \frac{\partial r_d}{\partial t} = \frac{dz}{dt} \frac{\partial r_d}{\partial z} = v_z \frac{\partial r_d}{\partial z} \quad (4.26)$$

As a simple assumption, we apply the axial velocity to be equal to the bulk velocity: $v_z = u_b$. Over the length of the cyclone, the azimuthal velocity decays according to:

$$v_\theta(z) = v_\theta(0)e^{-zC_d/D}, \quad (4.27)$$

with C_d an experimentally determined dimensionless parameter, determined to be 0.04 [3] and D the tube diameter. Substitution of equations 4.26 and 4.27 in equation 4.23 and subsequent integration, yields:

$$v_z \frac{\partial r_d}{\partial z} = - \frac{\Delta \rho D_d^2 (v_\theta(0)e^{-zC_d/D})^2}{18\mu r_d}, \quad (4.28)$$

$$r_d^2(z) = \frac{\Delta \rho D D_d^2 v_\theta^2(0)}{18\mu C_d u_b} \left(e^{-2zC_d/D} - 1 \right) + r_d^2(0). \quad (4.29)$$

This equation can be interpreted as the equation of motion for any droplet with given properties in the specified swirling velocity field.

5. Droplet path For effective separation, the droplet has to move from its initial position $r_d(0)$ to the oil core ($\frac{D_{\text{core}}}{D} = \sqrt{\alpha}$, α being the oil concentration) within the separator length L :

$$r_d(L) = \frac{1}{2}D\sqrt{\alpha} \quad (4.30)$$

The wall is the position from which the droplet has to travel the longest distance to the core:

$$r_d(0) = \frac{D}{2}. \quad (4.31)$$

For the conditions in equations 4.30 and 4.31 and under the above mentioned assumptions, all droplets are separated. This results in a minimum requirement for the azimuthal velocity of:

$$\frac{v_\theta(0)}{u_b} = 3 \frac{D}{D_d} \sqrt{\frac{(1-\alpha)C_d}{2(1-e^{-2zC_d/D})}} \frac{1}{\widetilde{\text{Re}}_d} \quad \text{with} \quad \widetilde{\text{Re}}_d = \frac{\Delta \rho u_b D}{\mu}, \quad (4.32)$$

or as a prediction for the cut-off size of:

$$D_{d,\text{crit}} = \frac{3}{v_\theta(0)} \sqrt{\frac{\mu C_d u_b D (\alpha - 1)}{2\Delta \rho (e^{-2zC_d/D} - 1)}}. \quad (4.33)$$

Table 4.1: System properties used for the calculation of the required azimuthal acceleration

Quantity	Unit	Value
$\Delta\rho$	[kg/m ³]	190
D_d	[μ m]	90
L	[m]	1.70
u_b	[m/s]	2
R	[m]	0.05
α	[-]	0.1
μ	[Pa.s]	$1e^{-3}$
C_d	[-]	0.04

6. Neglected effects In the above mentioned analysis, we neglected many hydrodynamic effects on the droplet. These effects include: (i) the dispersive effect of **turbulent eddies**, (ii) the **lift force** experienced due to a velocity gradient, (iii) **droplet-droplet interactions**, (iv) **inner-droplet effects**, such as flow in the droplet induced by the drag force, (v) **droplet-fluid coupling**, the change of the continuous flow due to the presence of the droplets. The latter includes hindered settling, as described by the Richardson & Zaki correlation [40], which is particularly relevant for accounting repression of droplets towards the core. All these effects are expected to have a counteractive effect on separation performance.

7. Conclusion From equation 4.32 and the values provided in table 4.1 the required azimuthal velocity is calculated: 5.4 m/s. This corresponds to a certain amount of angular momentum of the continuous phase:

$$|\vec{L}| = \int_0^R (p_\theta \times r) 2\pi r dr \approx 2\pi\rho_d \int_{R_c}^R v_\theta(0)r^2 dr = \frac{2}{3}\pi\rho_d(R^3 - R_c^3)v_\theta(0), \quad (4.34)$$

with ρ_d the droplet density and assuming that all angular momentum is in the region $r > R_c$.

According to equation 4.23, the maximum velocity for 100 μ m droplets in the radial direction is 0.15 m/s. The droplet Reynolds number for this velocity equals 15 - we violate the condition for the Stokes' drag law.

Inner body and vane angle

Static swirl elements consist of vanes mounted to the tube wall. At the tube center, these vanes need to be connected to a central body. Furthermore, the resulting azimuthal velocity is linked to the axial velocity at the swirl element and the vane angle. For fixed vanes, there is a proportional relation between the axial velocity upstream and the azimuthal velocity downstream of the swirl element.

In this section, we derive the required vane angle based on the required azimuthal velocity calculated above, using the upstream axial velocity as boundary condition.

1. Axial velocity The static swirl element will transfer kinetic energy from the axial direction towards the azimuthal direction to induce the swirling motion. The element consists of an internal body, centered at $r = 0$ and vanes connecting the internal body to the wall of the tube. The diameter of the internal body is a design parameter: a thin body results in a low axial velocity and therewith steep vanes to create sufficient azimuthal acceleration; a thick internal body results in a high axial velocity. The relation between the inner body radius R_i and the axial velocity is governed by conservation of mass:

$$u_{z,\text{swirl}} = u_b \frac{R^2}{R^2 - R_i^2}. \quad (4.35)$$

2. Angular momentum The swirl element should generate enough angular momentum to generate the swirl velocity as prescribed by equation 4.32. The angular momentum per unit of height h at a plane in the swirl element (SE) is:

$$\frac{L_{\text{SE}}}{h} = \frac{2}{3} \pi \rho_c u_{\theta,\text{swirl}} (R^3 - R_i^3), \quad (4.36)$$

combined with equation 4.34 this yields the requirement for the azimuthal velocity:

$$u_{\theta,\text{swirl}} = \frac{R^3 - R_c^3}{R^3 - R_i^3} u_{\theta}(0) \frac{\rho_d}{\rho_c}. \quad (4.37)$$

3. Vane angle The vanes deflect the flow from the axial direction to the azimuthal direction. The relation between these is given by the vane angle, $\alpha_{\text{deflection}}$:

$$\alpha_{\text{deflection}} = \arctan \left(\frac{u_{\theta,\text{swirl}}}{u_{z,\text{swirl}}} \right) = \arctan \left(\frac{u_{\theta}(0)}{u_b} \frac{(R^3 - R_c^3)}{R^2 (R^3 - R_i^3)} \frac{(R^2 - R_i^2)}{\rho_d} \frac{\rho_d}{\rho_c} \right) \quad (4.38)$$

A larger diameter R_i of the internal body has two effects: (i) the required vane angle is decreased and (ii) the velocity magnitude at the swirl element increases. The liquid acceleration at the swirl element results in the break-up of droplets. Vanes at a large angle and an acceleration to a high velocity result in droplet break-up. The total velocity increases substantially for $D_i > 0.8D$, therefore, we chose the diameter of the internal body to be 80 mm. For this value, the relevant quantities are shown in the left column of table 4.2.

Table 4.2: Parameters for the vane design for $56.5 \text{ m}^3/\text{h}$ in a 10 cm diameter tube.

parameter	no friction	with friction compensation
$\alpha_{\text{deflection}} [^\circ]$	62.6	74.3
$u_{\text{tot}} [\text{m/s}]$	12.0	20.6
$u_{\theta,\text{swirl}} [\text{m/s}]$	10.4	19.9
$u_{z,\text{swirl}} [\text{m/s}]$	5.6	5.6

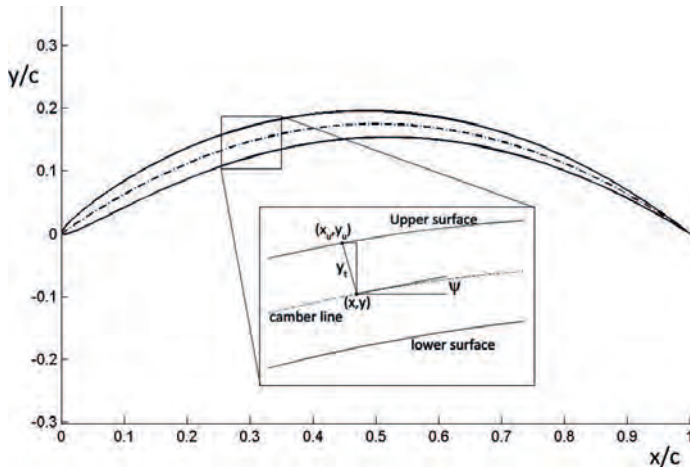


Figure 4.3: Geometry of the vane in its local coordinate system. Inset: detail of the camber line and vane thickness. c is the chord length which is set to 100 mm. [13]

4. Frictional losses From previous work by Dirkzwager [3] it is known that 46 % of angular momentum was lost between the swirl element and the first measurement position at $L/D = 10$. To ensure enough separation according to the relation derived in section 4.2.1, the angular momentum at the downstream side of the swirl element needs to be compensated, resulting in the column at the right of table 4.2.

Vane design

The fluid parameters at the downstream side of the swirl element were derived in the preceding section. The vanes, which are mounted on the internal body, have to convert potential energy (pressure) into angular momentum of the liquid. Too sudden changes in the fluid path can cause flow separation and therewith regions with high shear. This shear exerts forces on droplets, causing break-up. Smaller droplets have a lower chance of separation, this is the main reason why a gradual liquid acceleration along the vanes is important.

The software package CASCADE [13] was used to find a vane shape which meets the criteria derived in this chapter. The vane shape is based on the NACA four-digit airfoil series [41]. With these tools, a vane was designed as shown in figure 4.3.

The final design has vanes with $\alpha_{\text{vane}} = 73^\circ$.

Nose and afterbody design

The liquid should flow smoothly and without distortions from the upstream direction towards the section with vanes. There are three criteria for this nose section: (i) $r(z)$ is continuous, (ii) $\partial r/\partial z$ is continuous and (iii) both $r(z)$ and $\partial r/\partial z$ should both match at the vane section.

The nose section is designed based on Hermite polynomials. Slot [13] provides an extensive derivation of the procedure.

The design of the tail section follows the same procedure, with two differences: (i) 5th order Hermite polynomials are used and (ii) the downstream end of the tail is rounded.

Tube and Outflow design

Besides the swirl element, an axial cyclone consists of a tube and a separation part. The tube used in this project has a 10 cm internal diameter. The separation itself is accomplished using a so-called pick-up tube which is placed in the center of the main tube. The lighter phase should flow into this tube, while the heavy phase should flow around the pick-up tube. Downstream of the pick-up tube, a device needs to be placed to remove the swirling motion from the flow, in order to avoid high mechanical loads on downstream equipment.

Summary

The design of the swirl element has been based on the centrifugal pressure field that would be required for the separation of 100 μm oil droplets with a density difference of $\rho_{\text{brine}} - \rho_{\text{oil}} = 200\text{kg/m}^3$ at a flow rate of 56.5 m^3/h in a 10 cm diameter tube, resulting in a required flow deflection of 64°. Blades have been designed with this flow deflection. The design was evaluated with a computational method for inertial flow as well as using CFX, a computational method for viscous flow. The final blade angle was 73°.

4.2.2 Weak swirl element

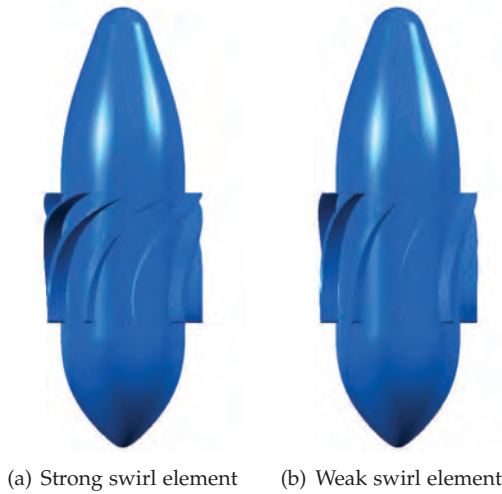
The swirl number is coupled to the vane angle in the swirl element. Therefore, to study the effect of the swirl number (eq. A.14) on separation, a different element was required. To reduce the differences between the swirl elements and to promote easy comparison with the previous (strong) swirl element, only the vane angle is modified.

For the existing element, the blade angle, flow deflection and resulting azimuthal velocity are measured, see table 4.3. From the measured values, the centrifugal acceleration of the liquid is determined for the center of the gap between the internal body and the wall of the swirl element ($r = 45\text{ mm}$). Two flow deflection angles were calculated to double and half the liquid centrifugal acceleration: 70° and 53°. For the strong swirl element, the liquid does not fully adapt to the angle of the vanes. The swirl efficiency is defined as the relation between the vane angle and the flow angle. This ratio is applied to both swirl elements, resulting in vane angles of 82° and 63°.

For the new swirl elements, the existing vanes were redesigned. The profile was stretched in the azimuthal direction without thickening the vanes. The strong element was designed such that no flow detachment should occur. Reducing the vane angle should therefore not introduce flow detachment. The design was not optimized using a software package such as CASCADE. The original and the resulting, constructed swirl element are drawn in figure 4.4; the number of vanes is equal for both swirl elements.

Table 4.3: Parameters of the strong swirl element and design parameters of two additional swirl elements

	$\alpha_{\text{blade}} [^\circ]$	$\alpha_{\text{fluid}} [^\circ]$	$u_\theta [\text{m/s}]$	$u_\theta^2/r [\text{m/s}^2]$
strong (constructed)	73	62	11.3	$2.9 \cdot 10^3$
stronger (not constructed)	82	70	16.3	$6.0 \cdot 10^3$
weak (constructed)	63	53	8.1	$1.5 \cdot 10^3$

**Figure 4.4:** Swirl element designs, fluid flows from bottom to top

Considering the importance of droplet break-up for separation performance and the knowledge that the acceleration in the strongest swirl element leads to more shear and therewith droplet breakup, only the element with a reduced vane angle was constructed. This element is referred to as the weak swirl element.

4.2.3 Large swirl element

The acceleration of a dispersed flow leads to breakup of droplets and small droplets are harder to separate. Separation performance should therefore be promoted by a reduction in shear. This section introduces the design of a swirl element with less acceleration of the liquid aimed at reducing the droplet break-up.

The design described in this section is based on the theory discussed in section 4.1.

Velocity reduction

The velocity can be reduced by increasing the surface available to the flow in the swirl element. The axial velocity in the swirl element is a function of the diameter of the internal body and the gap between the internal body and the tube wall. The azimuthal velocity is coupled to the axial velocity through the vane angle.

Axial velocity The axial velocity in the swirl element depends on the size of the internal body, i.e. the gap between the internal body and the surrounding wall. The axial velocity in the swirl element is given by the flow rate divided by the area of the gap at the swirl element:

$$v_{z,\text{swirl}} = \frac{\Phi}{A_{\text{flow}}}, \quad (4.39)$$

$$= \frac{\Phi}{\pi \left(\left(R_{\text{body}} + d_{\text{gap}} \right)^2 - R_{\text{body}}^2 \right)}, \quad (4.40)$$

$$= \frac{\Phi}{\pi \left(2d_{\text{gap}}R_{\text{body}} + d_{\text{gap}}^2 \right)}, \quad (4.41)$$

where ϕ is the flow rate in m^3/s .

Azimuthal velocity The combination of a large diameter swirl element and the 10 cm inner diameter tube as used for other tests in this work, requires a connecting tube element, a tapered section. Details of this section will be introduced in the next section, 4.2.4. For design purposes, we neglect friction and assume conservation of angular momentum of the continuous phase over the length of the tapered section:

$$\vec{L} = \vec{r} \times \vec{p}. \quad (4.42)$$

Since the position vector \vec{r} is orthogonal to the azimuthal velocity u_θ , we obtain the following relation for the velocity increase due to the tapering:

$$\frac{u_{\theta,1}}{u_{\theta,2}} = \frac{|\vec{r}_2|}{|\vec{r}_1|}, \quad (4.43)$$

where index 1 is upstream of the tapered tube section and 2 downstream of that section.

Vane angle The vane angle depends on the relation between the axial and azimuthal velocity according to:

$$\tan(\alpha) = \frac{u_\theta}{u_z} \quad (4.44)$$

The vane angle should not exceed 70° in order to avoid possible flow detachment. The strong and weak swirl element showed a difference in the resulting liquid velocity angle and the vane angle. The same ratio is assumed to hold for the new swirl element. The vane angle is therefore increased with this slip factor (divide by 0.85).

Number of vanes The number of vanes should be such that all liquid is accelerated in the azimuthal direction. The number of vanes should, however, not be that large that the wall friction breaks more droplets. The number of vanes follows from

the required minimum overlap of neighboring vanes. To maintain an equal overlap as the strong swirl element, the maximum intervane distance in the azimuthal direction is defined as 64 % of the vane width in the azimuthal direction.

Swirl element characteristics

Combining the above discussed constraints, the design parameters for the swirl element were determined, see table 4.4.

Table 4.4: Parameters for the large diameter swirl element

parameter	Symbol	Value
Axial velocity	$u_{z,swirl}$ [m/s]	3.0
Azimuthal velocity	$u_{\theta,swirl}$ [m/s]	3.9
Internal body diameter	D_{body} [mm]	251.7
Gap width	d_{gap} [mm]	6.5
Vane angle	α_{vane} [°]	63
Intervane distance	(w_{vane}) [vane width]	0.64

4.2.4 Tapered tube section

The large diameter swirl element has a diameter of 264.7 mm. To connect it to the existing 10 cm inner diameter swirl tube requires a tube section with tapering. The reduction of diameter D_{tube} in the axial distance z should be such that the acceleration of the liquids does not lead to break-up of the dispersed droplets.

Acceleration time scale Consider a gradual contraction of a tube with a wall shape described by $dD/dz = f(z)$. Assuming conservation of angular momentum, the azimuthal velocity u_{θ} as function of the tube diameter D is given by:

$$u_{\theta}(D) = \frac{D_0 u_{\theta}(D_0)}{D(z)}. \quad (4.45)$$

By taking the derivative of $u_{\theta}(D)$ with respect to z , the change of u_{θ} over the axial distance becomes:

$$\frac{\partial u_{\theta}(D(z))}{\partial z} = -\frac{D_0 u_{\theta}(D_0)}{D^2(z)} \frac{dD(z)}{dz}. \quad (4.46)$$

Table 4.5: Requirements for the tapered tube section

		Upstream side	Downstream side
Diameter	D [mm]	264.7	100
Azimuthal velocity	u_{θ} [m/s]	3.9	10.3
Axial velocity	u_z [m/s]	3.0	2.0
Maximum stable droplet size	$D_{d,max}$ [μ m]	100	100

A measure for the time scale of the inward motion is the time the azimuthal velocity requires to increase with $(1 + e)$ times the original value. We estimate this time scale with a conservative estimate: a minimum tube diameter D of 10 cm, an axial velocity u_z of 2 m/s and the rest of the data provided in section 4.2.3 and table 4.2.4. This leads to:

$$\begin{aligned} \frac{\partial u_\theta}{\partial t} &= \frac{\partial u}{\partial z} \cdot \frac{dz}{dt} \\ &= -\frac{D_0 u_\theta(D_0) u_z}{D^2(z)} \frac{dD(z)}{dz}, \\ &\approx -a \frac{dD}{dz} \quad \text{with } a \approx 200 \left[\frac{\text{m}}{\text{s}^2} \right]. \end{aligned}$$

Considering the azimuthal velocity at the upstream side of the taper, $u_\theta = 4$ m/s, the characteristic time-scale is the time required to increase u_θ to 5.4 m/s. For these conditions, the dependence on time-scale and dD/dz equals

$$\tau_{\text{taper}} = -\frac{7 \cdot 10^{-3} [\text{s}]}{dD/dz}. \quad (4.47)$$

The characteristic time scale for droplets to adapt to its surroundings (τ_d) is $\mathcal{O}(10^{-3})$ s, the time needed for the droplet to contract is $\tau_{\text{contraction}}$ is also in $\mathcal{O}(10^{-3})$ s. The time scale of the displacement in the radial direction must be larger in order to avoid shear an elongation of the droplet and therewith break up. This implies $dD/dz < 1$. Based on the time estimate and the other design parameters, the constraints for the design of the tapering section are:

α_{upstream}	0°
α_{max}	40°
$\alpha_{\text{downstream}}$	0°
$\frac{\partial \alpha}{\partial z}$	minimal and constant
r_{upstream}	135 mm
$r_{\text{downstream}}$	50 mm

Based on these parameters, Matlab has been used to numerically solve the shape of the tapering section. Figure 4.5 shows the inner wall positions for the tapering section.

4.3 Profile of the swirling flow

This section shows the effect of the swirl generating element on the resulting velocity profile.

The velocity profiles for the three different swirl elements are depicted in figure 4.6. There profiles are normalized with the axial bulk velocity as measured upstream of the swirl element.

The azimuthal velocity in the region $|r| < 10$ mm is not affected that much by the different swirl elements, the value $\partial v_\theta / \partial r$ is almost equal for all cases. The

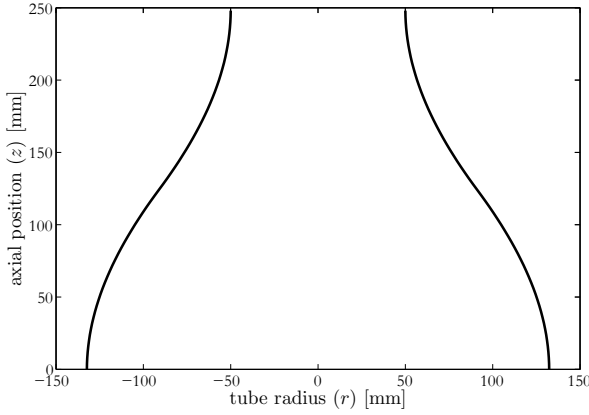


Figure 4.5: Numerical result for the calculation of the taper shape.

strength and size of the solid body rotating core are therefore almost swirl-element independent.

The outside layer ($|r| > 10$ mm) is significantly influenced by the swirl element. The strong and weak element provide a relative flat profile with their respective maxima at the edge of the solid-body rotating core that is proportional to the azimuthal velocity at the swirl element. The large swirl element is different and generates significantly more swirl in the outside layers. The assumed slip between the vanes and the liquid flow (see section 4.2.3) is much smaller than for the other two elements, the slip factor $\alpha_{\text{flow}}/\alpha_{\text{vane}}$ is 0.94 instead of 0.85. The lower total velocity in the swirl element (5 m/s instead of 12 m/s) is a likely cause for the more efficient fluid deflection - the residence time in the swirl element is namely inverse proportional to the average axial velocity due to the equal vane size in the axial direction.

The swirl elements are characterized by a swirl number, which we calculate according to equation A.14. Table 4.6 indicates the significant differences in swirl strength between the strong and weak element. The swirl number for the large element is slightly larger than for the strong element, in contrast with the expectation based on the azimuthal velocity in figure 4.6(a), where the azimuthal velocity for $|r| > 20$ mm is larger than for the strong swirl element. However, the upstream velocity in the center region is larger for the large swirl element - this decreases the swirl number. As a correction, we introduce the following swirl number:

$$\Omega' = \frac{2\pi \int_0^R |u_z u_\theta| r'^2 dr'}{\pi R^3 u_b^2} \quad (4.48)$$

From the values of this swirl number Ω' in table 4.6, the difference in swirl strength between the different elements becomes clear.

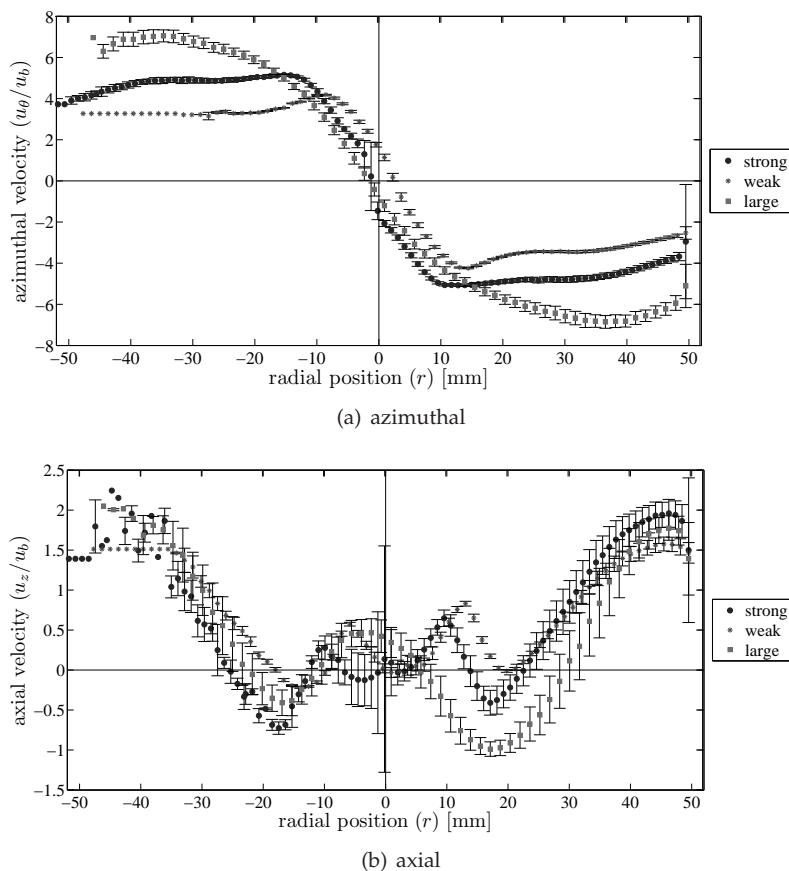


Figure 4.6: Velocity profile for three different swirl elements, divided by the bulk velocity u_b upstream of the swirl element. Measurements obtained approximately 500 mm downstream of the swirl element. Flow rate was $56 \text{ m}^3/\text{h}$ for the strong and weak swirl element and $30 \text{ m}^3/\text{h}$ for the large swirl element.

4.3.1 Experimental conditions

The velocity profile was measured using Laser Doppler Anemometry (see section 3.1). The laser was operated at an output power of approximately 3 W, measurement time interval per point was in the range of 5 to 10 s.

LDA produces point measurements for the velocity. All measurement points are on a line parallel to the LDA probe through the center of the tube, resulting in measurements for the axial and azimuthal components of the velocity. Measurement points are typically 0.5 mm to 1.0 mm apart.

4.3.2 Strong swirl element

The velocity profile has been studied for single phase brine flow for all three swirl elements. Investigations of the strong swirl element are most elaborate. This section discusses the insights obtained with the strong swirl element.

Table 4.6: Swirl number for the three different swirl elements, calculated for the profiles in figure 4.6 based on a 2 m/s bulk velocity.

	Swirl number Ω	Swirl number Ω'
strong element	3.7	3.8
weak element	2.3	2.3
large element	3.9	4.8

For the strong swirl element described in section 4.2.1, figure 4.7 shows a typical velocity profile, measured at the designed flow rate of 56.5 m³/h, together with the numerical result for equal conditions.

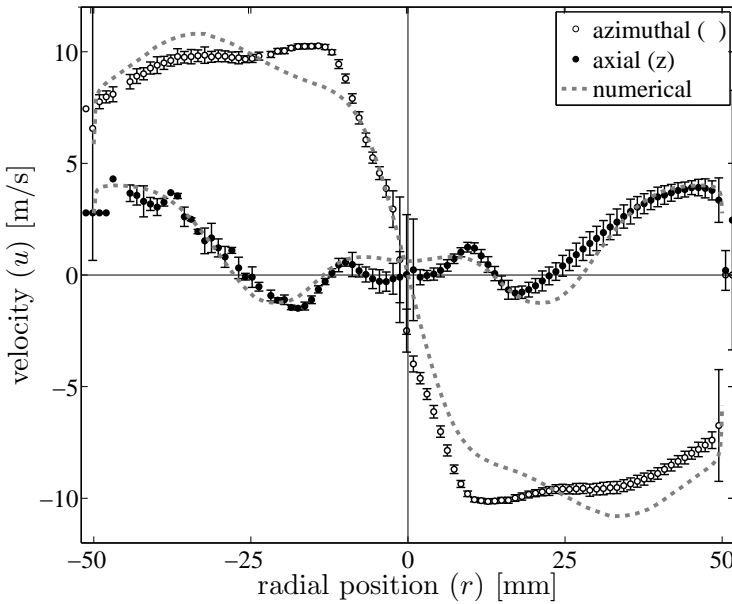


Figure 4.7: Velocity measurement for the strong swirl element, 0.532 m downstream of the swirl element, swirl section length was 1.7 m, pick-up tube diameter: 50 mm and the flow split was 0.3. Numerical data of Slot [13].

Vortex breakdown The most interesting phenomenon in the axial velocity profile (figure 4.7) is the appearance of regions in which the liquid flows upstream, the so-called vortex breakdown (see section A.4). This is caused by the pressure distribution in the system: the lowest pressure is present at the downstream side of the swirl element. The pressure in the center region closer to the outlet is higher, which introduces a flow from the high pressure area towards the low pressure area. Both numerical and experimental data feature this reverse flow, though there are some differences.

Swirl number The swirl number for this swirl element at this position has been calculated according to equation A.14. The experimental data results in a swirl number of $\Omega = 3.7$, which is about 10 % lower than the value predicted with the numerical simulation [13]: $\Omega = 4.0$. Apart from the significance of these numbers, the most likely cause is the presence of more friction in the real cyclone compared to the perfect symmetric numerical case.

Solid body rotation zone The outer liquid layers ($r > 35$ mm) show a reasonable resemblance between the experimental and numerical data. The center region severely differs: the size of the solid-body rotation core is much larger for the numerical case than for the LDA measurements. The inertia in the real case apparently is dominant over viscosity in the radial direction. The physical cyclone has some dispersed oil in the center of rotation. This dispersed kernel can explain a step at the kernel, but not the large difference in behavior for $0.1 < \frac{r}{R} < 0.6$.

4.4 Properties of swirling flow

4.4.1 Vortex decay

Figure 4.8 illustrates the change in the velocity profile of the swirling brine for increasing axial distance from the swirl element. This effect is driven by a decrease in angular momentum due to friction in the system. Apparently, the friction occurs both at the wall and in the center of the tube, since both regions loose angular momentum in favor of the region around $r \approx 20$ mm: The velocity increases for that position from 10 m/s at $z = 0.5$ m to 12 m/s at $z = 1.3$ m.

The LDA results are time-averaged velocity measurements. From these results it is clear that the time-averaged velocity at $r = 0$ is not always 0, as would be expected for an axial symmetric cyclone. Despite effort to optimize the alignment of the system and to avoid other sources that could trigger an asymmetry, we did not succeed. Swirling axi-symmetric flow is not a stable situation.

The discrepancies between the numerical data and the experimental results are numerous. Except for the profile at $z = 532$ mm, the outer layer ($r > 32$ mm) is accurately predicted. The transition to a solid-body rotating kernel is for all measurements with $z < 1300$ mm calculated to be at a larger radial position than actually observed in the experimental data. Consequently, the $\partial u_\theta / \partial r$ is smaller in the numerical simulation than for the velocity distribution determined using LDA measurements. The applied treatment of the RANS approach with first order closure may not be capable of an accurate description of the swirling flow.

The swirl number as introduced in equation A.14 is a measure for the strength of the swirling flow. Based on both the LDA and the numerical data, the swirl number was calculated for all axial locations presented in figure 4.8. Figure 4.9 presents the rapid decrease in the swirl number for the cyclone in the experimental set-up. The decrease of swirl predicted by the numerical method is more gradual. An increase in friction due to the non-axi-symmetry could contribute to this difference.

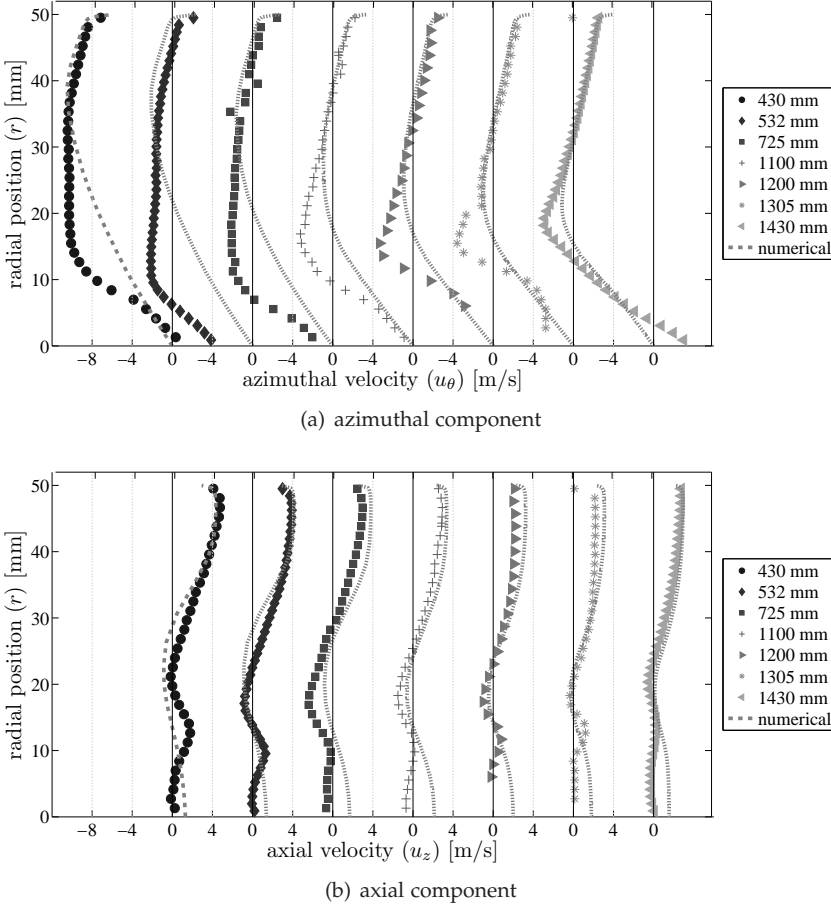


Figure 4.8: Measured and predicted velocities at different axial distances from the swirl element. The graphs are shifted in axial direction for clarity. Numerical data of Slot [13].

4.4.2 Precessing Vortex Core

It is beyond the scope of this thesis to derive an analytical description for the precessing vortex core. Alekseenko et al. [42] provide an extensive description, while Yazdabadi et al. [15] discuss the resulting measured velocities. From this experimental work, it is concluded that the center of the vortex is not always in the geometrical center of the tube.

To evaluate the possible existence of a precessing vortex core in the swirling flow used in the present study, we calculated the spectrum of the velocity data for various conditions using ARMAseL [43]. Figure 4.10 shows six different spectra. Except for the azimuthal velocity in the center with a short (5 s) time series, all profiles show a peak around 43 Hz, indicating an autocorrelation in both the axial and the azimuthal velocity.

If the core is precessing, this would show up as a cyclic sequence in the velocity distribution, leading to a peak in the autocorrelation function. An alternative source

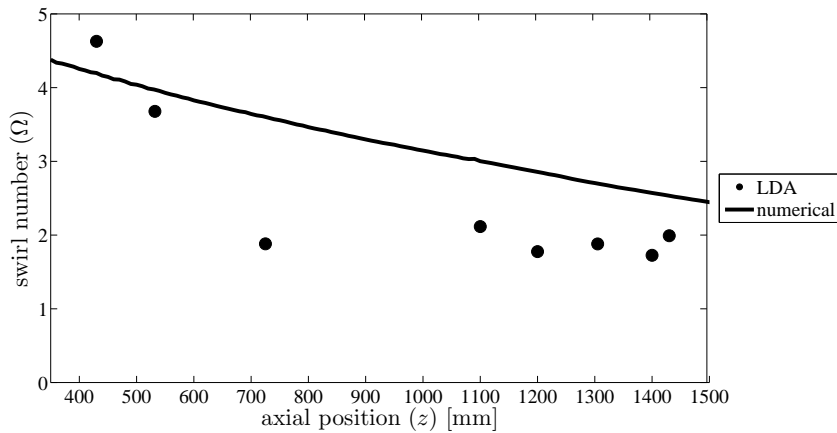


Figure 4.9: Swirl number for different downstream distances of the swirl element obtained from LDA and numerical velocity profiles

of this peak could be a vibration of the flow rig. The pump frequency for these measurements was 43 Hz. Since that frequency is exactly the same as the frequency in the autocorrelation spectra, it is not possible to attribute the peaks to a precessing vortex core. The 83 Hz peak is not present in all spectra. Other peaks are not observed. From the single phase LDA data we can therefore not conclude on that there is a precessing vortex core.

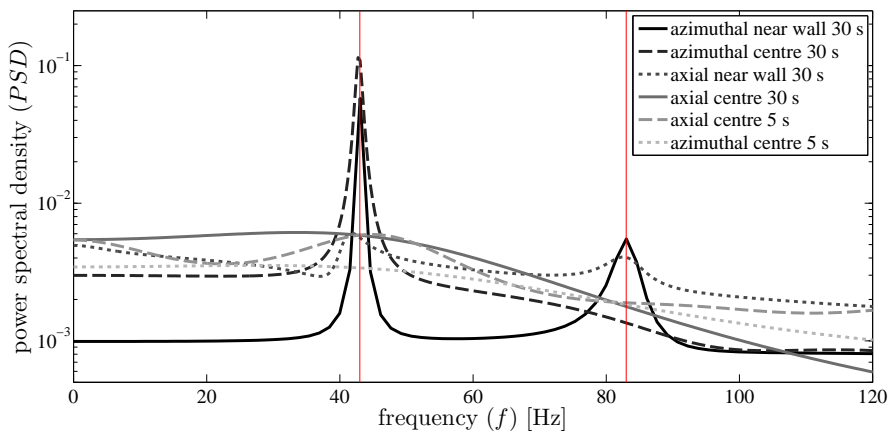


Figure 4.10: Power spectral density of the LDA time series at different locations for the strong swirl element. Solid vertical lines are drawn for 43 Hz and 83 Hz.

4.4.3 Detail at the pick-up tube

At the downstream end of the tube with swirling flow, a pick-up tube is located. During multiphase flow conditions, the lighter phase ought to leave the separator tube through the pick-up tube, the heavy phase should leave through the annular

region surrounding the pick-up tube. The flow near the pick-up tube is therefore of relevance for the performance of the phase separator: additional shear can lead to break-up of droplets and disturb the possible formation of an oil-continuous kernel. The flow near the pick-up tube has been investigated in two ways: the velocity profile in the annular ring has been measured with LDA and the velocity profile just upstream of the pick-up tube has been measured with LDA, see figure 2.15.

Annular region

The size of the measurement volume is 0.2 mm in the radial direction, meaning that the measured velocity is an average over that distance. The position of the wall in figure 4.11 has been set to the point where both the axial and the azimuthal velocity are 0.

Figure 4.11 presents velocity measurements for the axial and the azimuthal components of the velocity as function of the wall distance for the annular region surrounding the pick-up tube at 3 mm downstream of the leading edge of the pick-up tube. The azimuthal velocity does not slip at the wall, and a thin boundary layer is formed as is common for turbulent flows. An interesting phenomenon is observed for the axial velocity component, which is pointing in the upstream direction in the layer of the first 2 mm from the wall. This points at a pressure at the pick-up tube wall which is low at the upstream side of the pick-up tube and high at the downstream side of the pick-up tube. This can be understood from the swirl strength as function of axial distance: the pressure gradient towards the wall is proportional to the swirl strength. Since the swirl decays over length, the pressure at the outer wall of the pick-up tube is lowest at the pick-up tube tip and higher for positions further downstream. This pressure difference can drive the observed upward flow. The numerical results as in figure 4.11 also features this near-wall reverse flow.

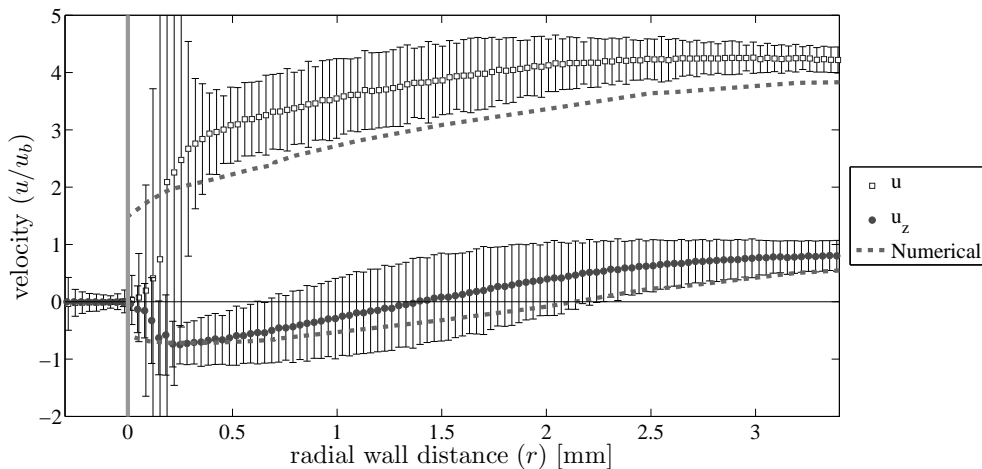
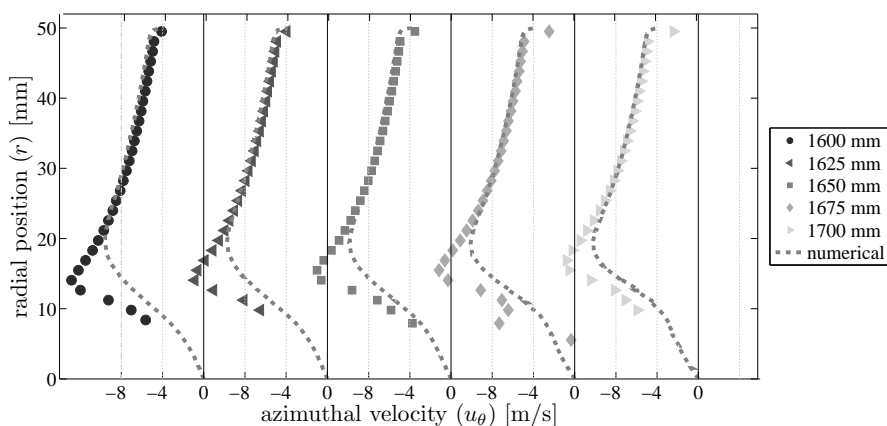


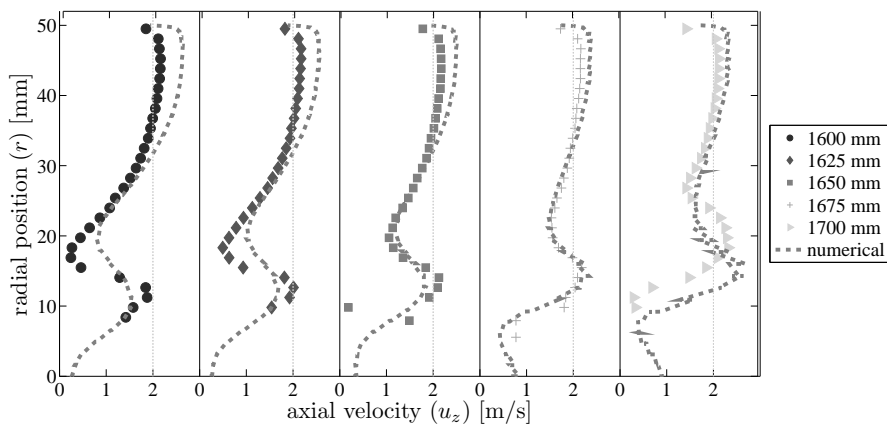
Figure 4.11: Velocities near the pick-up tube, 3 mm downstream of the pick-up tube leading edge. Wall position is derived from velocity measurements.

Just upstream of the pick-up tube

Just upstream of the pick-up tube, the fluid velocity must adjust in order to accommodate the flow split - by changing the setting of the valves downstream of the outflow section, the flow rate through both the LPO and HPO can be set. The central region with upstream flow (see figure 4.8(b)) that exists for the axial locations up to 1430 mm has disappeared near the pick-up tube. The radial position of the pick-up tube is clear in the velocity profile as a dip in the axial velocity.



(a) azimuthal



(b) axial

Figure 4.12: Velocity profiles just upstream of the pick-up tube (at $z = 1.7$ m). Numerical results are indicated.

4.5 Influence of operational parameters

4.5.1 Flow split effect

During operation of an axial cyclone, the distribution of the liquid streams over the Heavy Phase Outlet (HPO) and Light Phase Outlet (LPO) can be changed using valves downstream of the cyclone. The distribution of the streams over the two outlets is called the Flow Split (FS) and is defined as:

$$FS = \frac{\phi_{LPO}}{\phi_{HPO} + \phi_{LPO}}, \quad (4.49)$$

with ϕ the volumetric flow rate.

The velocity profiles have been measured for different flow splits for all three swirl elements, see figures 4.13, 4.14 and 4.15.

For the strong swirl element and weak swirl element, a higher flow split (more liquid through the pick-up tube) leads to an increase of the azimuthal velocity in the region $|r| < 20$ mm. This increase in angular momentum relates to an increase in the pressure drop, as can be seen in table 4.7.

The total angular momentum was computed for the different flow splits according to an area-weighted method:

$$|\vec{L}| \approx 2 \sum_{i=1}^{N(r=R)} \frac{v_{\theta}(i) \rho_c \Delta z r(i) \Delta A(i)}{\sum_{i=1}^N \Delta A(i)} \quad (4.50)$$

with

$$\Delta A(i) = \pi \left(\left(\frac{r(i+1) + r(i)}{2} \right)^2 - \left(\frac{r(i) + r(i-1)}{2} \right)^2 \right) \quad (4.51)$$

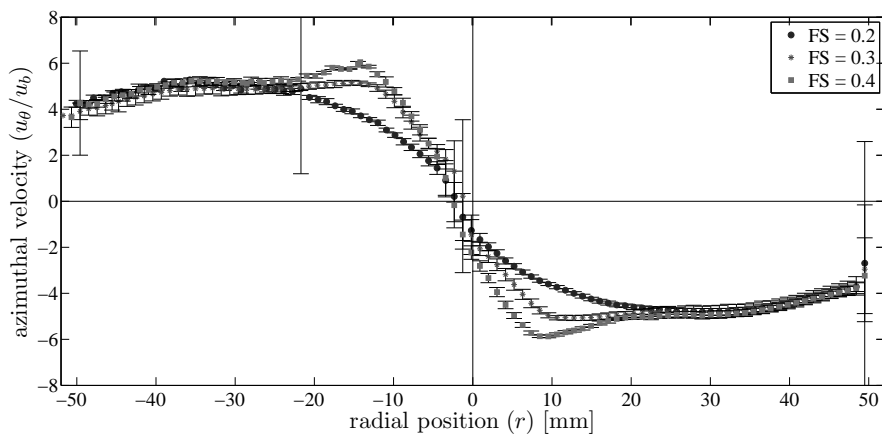
and Δz an infinitesimal height. Since both density ρ_c as Δz are constant, we simplify equation 4.50 to a relative version:

$$|\vec{L}| / (\rho_c dh) \approx 2 \sum_{i=1}^{N(r=R)} \frac{v_{\theta}(i) r(i) \Delta A(i)}{\sum_{i=1}^N \Delta A(i)}. \quad (4.52)$$

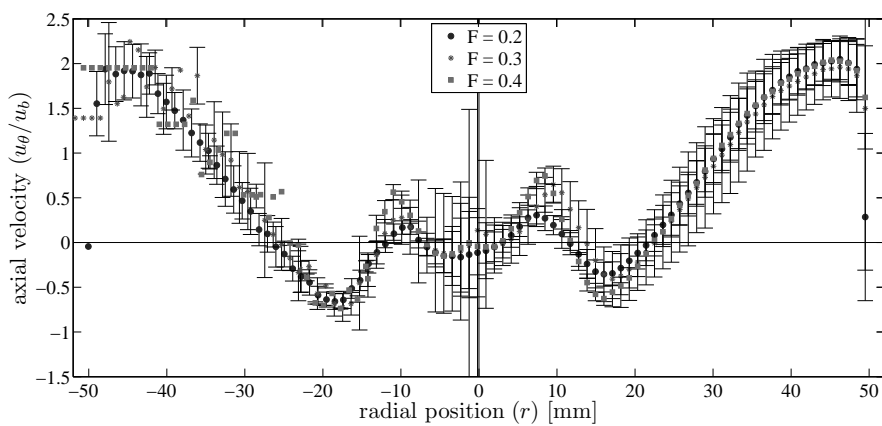
Table 4.7 shows the results of this numerical operation and it demonstrates the significant reduction of the angular momentum with length and the relation between the flow split and angular momentum.

For the strong swirl element, a high pressure gradient following from the steep $\frac{\partial v_{\theta}}{\partial r}$ leads to a kernel consisting of dispersed material present in the cyclone. It introduces additional noise for the measurements at $r > 0$ mm.

The large swirl element (figure 4.15) is less sensitive to changes in the flow split compared to the strong and weak swirl element. Around $|r| = 20$ mm, the azimuthal velocity increases for a larger flow split, while the overall profile shape changes hardly.

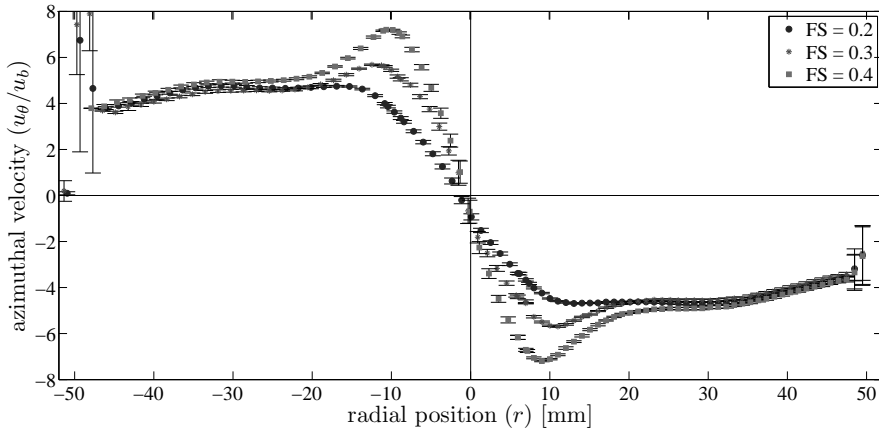


(a) azimuthal

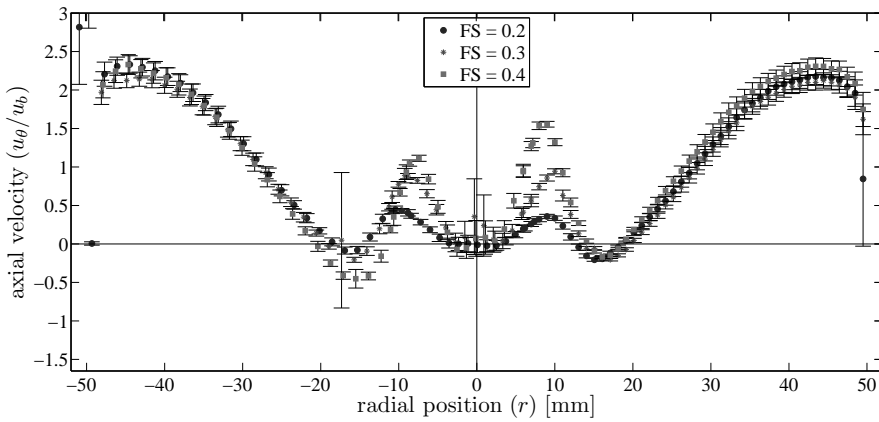


(b) axial

Figure 4.13: Velocity profiles for three different flow splits, normalized with the liquid bulk velocity. All profiles were obtained 532 mm downstream of the strong swirl element.



(a) azimuthal



(b) axial

Figure 4.14: Velocity profile for three different flow splits for the weak swirl element, divided by the axial bulk velocity. All profiles were obtained at an axial distance of 532 mm downstream of the swirl element for a flow rate of $42 \text{ m}^3/\text{h}$.

Table 4.7: Angular momentum divided by density for the strong swirl element according to equation 4.52 for different downstream positions and different flow splits. The pressure difference is measured between a point upstream of the swirl element and the LPO.

Relative angular momentum $|\vec{L}| / (\rho_c dh)$ [m^2/s]

z (mm)	$FS = 0.2$	$FS = 0.3$	$FS = 0.4$
532	0.43	0.42	0.43
782	0.36	n.a.	n.a.
1180	0.36	0.33	0.38
1430	0.25	0.34	0.34
Δp (bar)	1.79	1.83	1.90

Table 4.8: Swirl numbers for different flow rates and flow splits, calculated from velocity data obtained with LDA.

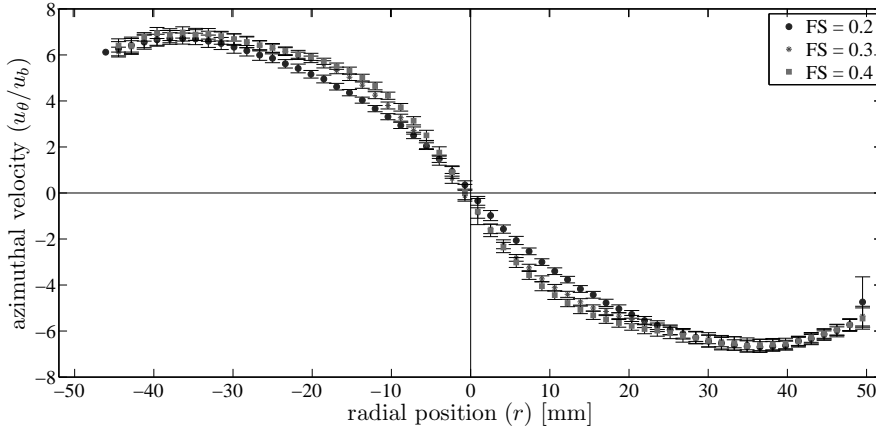
	[m^3/h]	FS = 0.2	FS = 0.3	FS = 0.4
strong element	56	-	3.24	-
	42	3.12	3.32	3.39
weak element	56	-	2.30	-
	42	2.46	2.22	2.05
	30	-	2.05	-
	20	-	1.30	-

4.5.2 Effect of flow rate

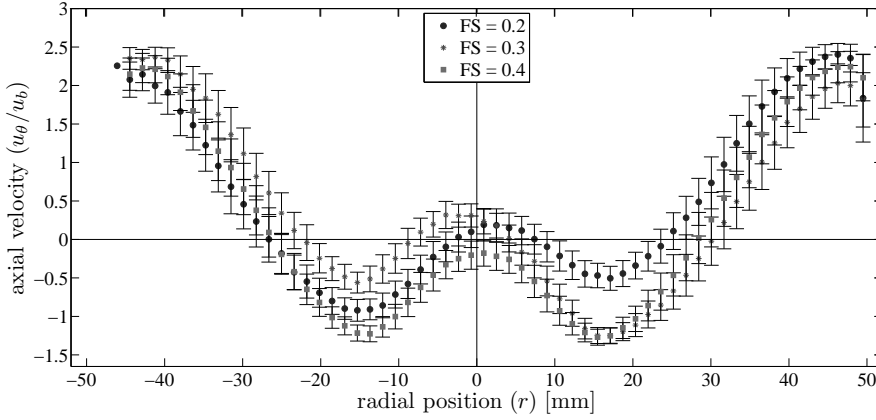
The effect of flow rate on the velocity profile was compared for both the strong and the large swirl element. Figure 4.16 presents the profiles for the strong element at 30, 42 and 56.5 m^3/h , figure 4.18 contains the velocity distribution for the large element at 10, 20, 30 and 40 m^3/h . All profiles are normalized with the bulk velocity for appropriate comparability.

The azimuthal velocity distribution shows limited dependence on the flow rate. The azimuthal velocity increases more than proportional with flow rate, see the region around $|r| = 10$ mm in figure 4.16(a) and around $|r| = 35$ mm in figure 4.18(a). The variation of the velocity distribution increases more than proportional for increasing flow rate.

The axial velocity for the strong swirl element (figure 4.16(b)) does not show notable changes, except for an increase in variation of the velocity. The axial velocity of the large swirl element (figure 4.18(b)) appears to differ for changing flow rate. The observed changes can be explained by assuming a steady-state helical structure between the swirl element and the pick-up tube. By changing the flow rate, the wavelength of this structure changes, resulting in a different intersection of the LDA traverse with the vortex core. The 10 and 40 m^3/h case appear to be flipped at $r = 0$ mm.



(a) azimuthal



(b) axial

Figure 4.15: Velocity profile for three different flow splits for the large swirl element, divided by the axial bulk velocity. All profiles were obtained at an axial distance of 395 mm downstream of the swirl element for a flow rate of $30 \text{ m}^3/\text{h}$.

4.6 Conclusion

In this chapter, we introduced three different swirl elements to generate in-line swirling flow and we investigated these elements using laser Doppler anemometry. The aim of these tests was to understand the fluid flow that results from a certain swirl element and to predict the phase separation performance resulting from the swirling flow.

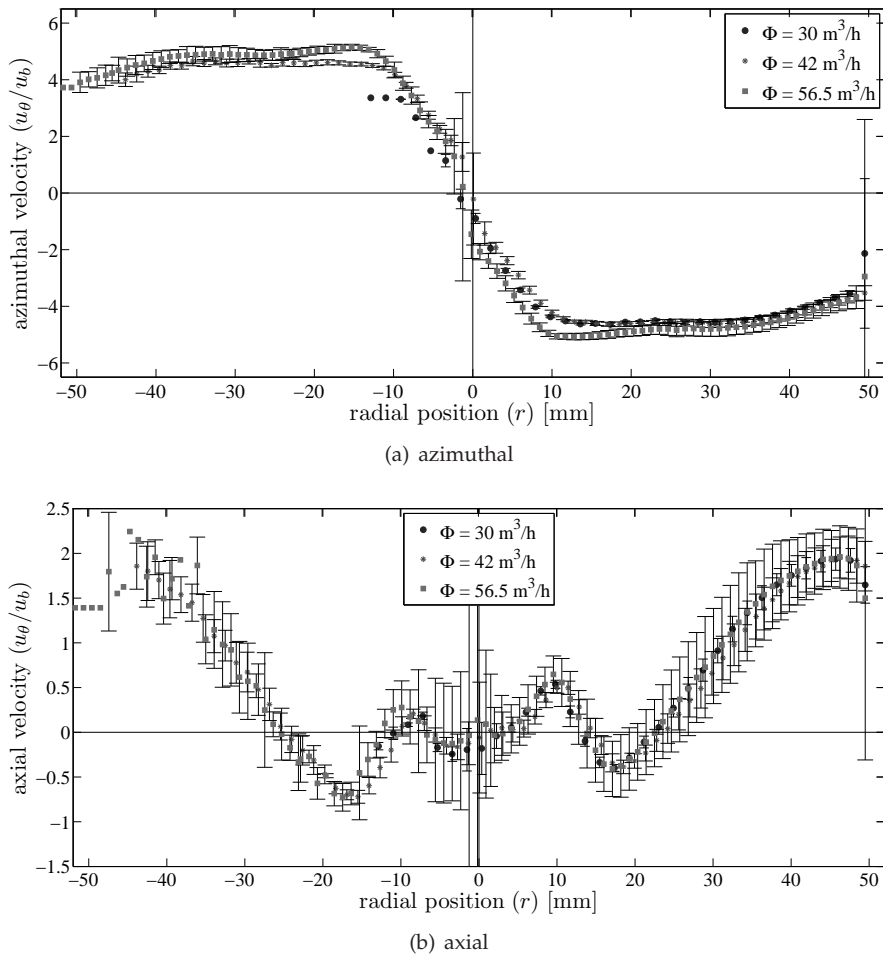


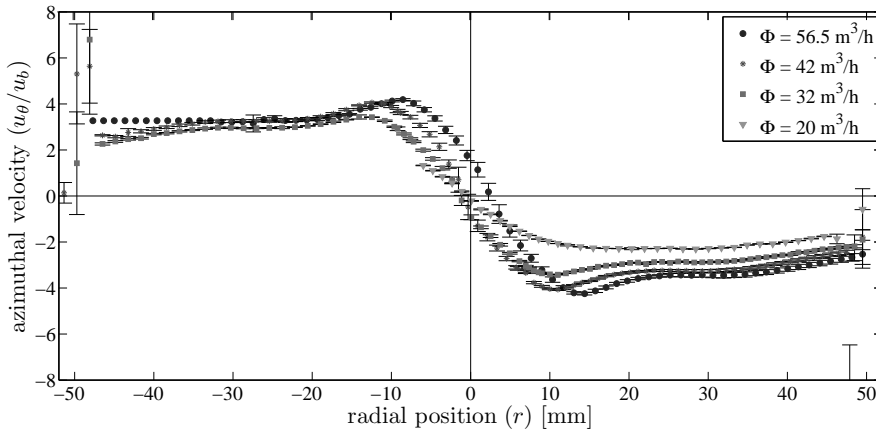
Figure 4.16: Velocity profile for three different flow rates, divided by the axial bulk velocity. All profiles were obtained at an axial distance of 532 mm downstream of the strong swirl element.

4.6.1 Prediction of the velocity profile

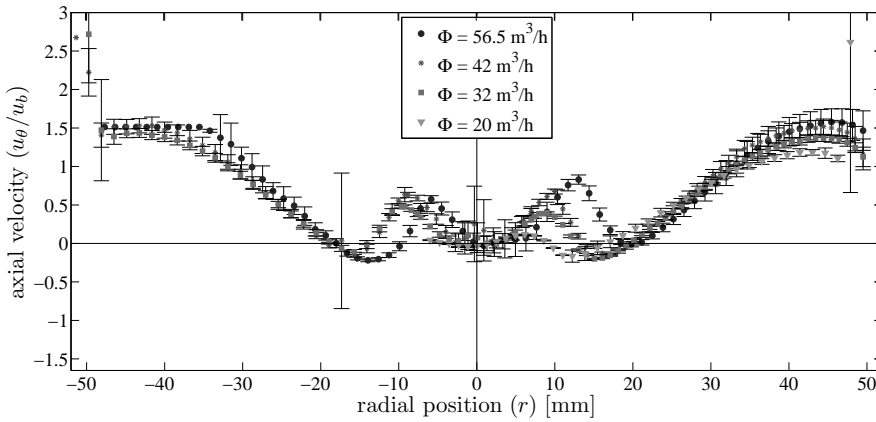
This section provides the conclusions on the investigations of the single phase flow. The fluid velocities are likely to be different for two phase (water and oil) flow. However, the velocity distributions of two-phase flow are not measured within the scope of this project.

The swirl element does not affect the solid-body-rotation core for the three swirl elements investigated in this research. This concerns the region where $|r/R| < 0.2$. The value of $\partial(u_\theta/u_b)/\partial r$ is equal, but the size of the region differs.

The velocity in the outer layer depends on the angular momentum generated in the swirl element where the maximum azimuthal velocity is adequately described



(a) azimuthal



(b) axial

Figure 4.17: Velocity profile for four different flow rates, divided by the axial bulk velocity. All profiles were obtained at an axial distance of 532 mm downstream of the weak swirl element.

by the relation:

$$u_{\theta} = u_{\theta, \text{swirl}} \frac{r_{\text{body}}}{r_{\text{tube}}} \quad (4.53)$$

The slip between the fluid angle and the vane angle is swirl element dependent

Results are not conclusive on the relation between the vane angle and the resulting fluid angle: the swirl efficiency. The strong and weak swirl elements show a slightly larger fluid deflection at higher flow rates and therefore a higher axial velocity in the swirl element. The larger swirl element produces a significantly smaller axial velocity at the vanes, and the relative difference between the angle at which the fluid flows and the vane angle is smaller. The different construction of both elements and the tapered section for the large swirl element might contribute to this effect.

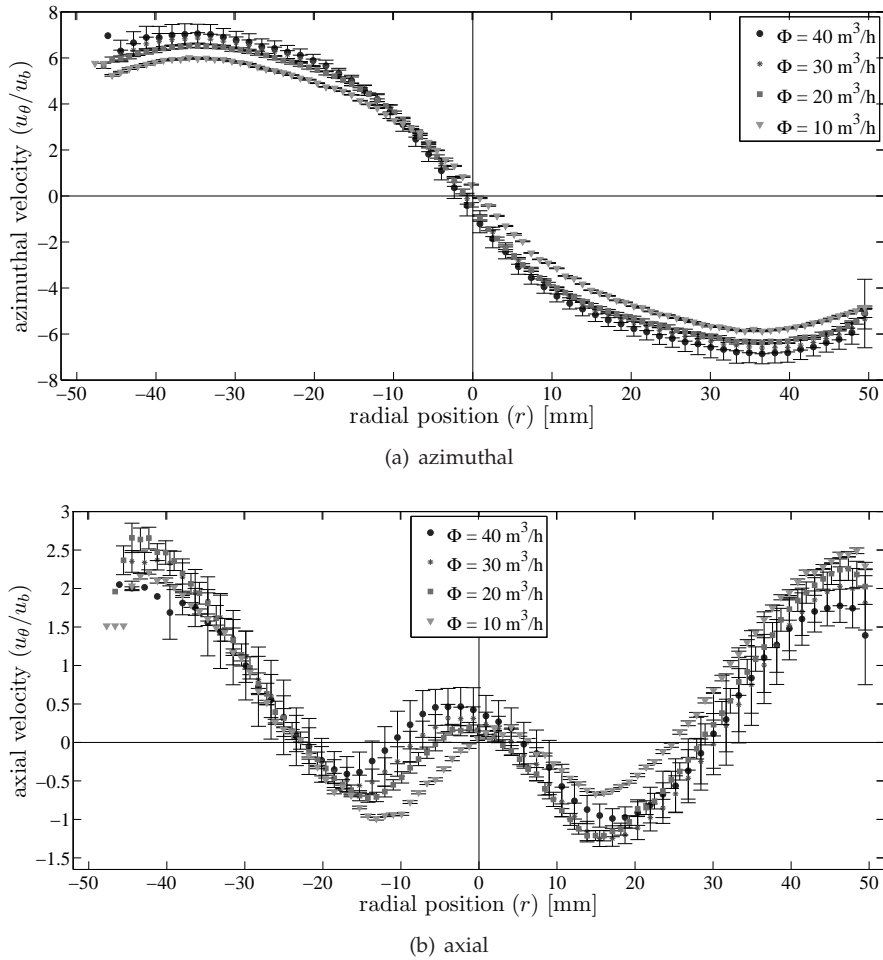


Figure 4.18: Velocity profile for three different flow rates for the large swirl element, divided by the axial bulk velocity. All profiles were obtained at an axial distance of 395 mm downstream of the swirl element.

4.6.2 Operational effects on phase separation

A higher flow rate leads to more centrifugal acceleration A higher flow rate leads to a higher centrifugal acceleration according to:

$$F_c \propto v_\theta^2 \propto \Phi^2 \quad (4.54)$$

However, it also introduces more turbulence, which can be seen from the larger variation in the velocity as is observed in this chapter. The effect of droplet break-up and turbulent dispersion is extensively discussed in chapter 5.

A higher flow split has a small favorable effect A higher flow split leads to regions in the cyclone with a larger azimuthal velocity. It can therefore lead to a

larger centrifugal acceleration of dispersed droplets, which on its turn might be beneficial for the separation performance.

CHAPTER 5

Dispersed droplets in dilute swirling flow

The preceding chapter discussed the velocity profiles and derived quantities for single phase swirling flow. The aim of the swirling flow is to separate two phase liquid-liquid streams. In this chapter, we use the experimental data obtained in the preceding chapter to predict the droplet trajectories for dispersed oil droplets in swirling brine.

The Reynolds number of the flow based on the bulk velocity and tube diameter in our cyclone is larger than 10^5 and it is therefore turbulent. The nature of turbulence implies fluctuations of the continuous phase fluid velocity in time, which affects the velocity of the dispersed droplets. In this chapter, we derive a model for the droplet motion based on experimental single phase flow data obtained for the three swirl elements.

The ability to produce simple predictions of the effect of turbulence in swirling flow on dispersed droplets is of value for understanding the separation characteristics and to aid design. The method suggested in this method is a hybrid approach, which should provide quicker results than Computational Fluid Dynamics alone.

5.1 Theory

The motion of the dense dispersed swirling flow can not be solved analytically, nor is it possible with current technology to provide a numerical solution accurately describing the behavior of each individual droplet. Therefore, we focus on a single droplet moving in a single phase flow, which serves as a first reference for such a droplet in a dense multiphase flow.

Centrifugal acceleration

The liquid in the cyclone performs a swirling motion. The velocity of each fluid parcel can be decomposed in an axial (u_z) and an azimuthal (u_θ) component. To maintain the rotating motion in the radial plane, a centripetal force needs to be exerted on the liquid parcel at radial position r in the radial direction equal to:

$$F_c = \frac{mu_\theta^2}{r}, \quad (5.1)$$

with m the mass of the liquid element. This force points towards the axis of rotation of the swirling motion.

Consequently, swirling flow has a pressure gradient in the radial direction. Fluid parcels with volume V_d experience the following centripetal force:

$$F_{\text{centripetal}} = \frac{V_d \rho_c u_\theta^2}{r} \quad (5.2)$$

with ρ_c the density of the continuous phase.

The force required to keep the droplet at a certain radial position r is given by the centrifugal force:

$$F_{\text{centrifugal}} = \frac{V_d \rho_d u_\theta^2}{r}, \quad (5.3)$$

with ρ_d the density of the dispersed phase.

The net force driving the droplet within the rotating frame of reference is:

$$F_{\text{net}} = \frac{V_d (\rho_d - \rho_c) u_\theta^2}{r}, \quad (5.4)$$

this force points towards the center of the swirling motion if $\rho_d < \rho_c$ and is the driving force for centrifugal phase separation.

Drag force

An object which is moving through a viscous medium experiences a drag force. A general expression for this force is [44]:

$$F_d = \frac{1}{2} \rho_c u_{\text{rel}}^2 C_D A, \quad (5.5)$$

with u_{rel} the velocity of the object relative to the surrounding liquid, C_D the drag coefficient and A the projected area of the object perpendicular to the direction of motion. For the remainder of this chapter, we will assume the droplets in the liquid-liquid axial cyclone to be spherical.

The drag coefficient depends on the droplet Reynolds number and therewith the viscosity of the surrounding fluid and the droplet velocity relative to the continuous fluid. For the remainder of this section we apply the empirical correlation for C_D as proposed by Almedeij [45], which holds in the range $\text{Re} < 10^6$ and can be found in Appendix D.

For low Reynolds numbers ($\text{Re} < 1$) the C_D can be approximated by Stokes' relation $C_D = \frac{24}{\text{Re}}$ [39].

Turbulent dispersion

When the inertial forces in a fluid flow exceed the viscous forces, a flow becomes turbulent. A turbulent flow is characterized by momentum exchange between the

various directions, which drives the formation of eddies, ranging from the large scale (typically the bounding geometry) down to the smallest eddies in which their kinetic energy is dissipated into heat. For our cyclone, this means that there are vortical structures from 10 cm (the tube diameter) down to a few micrometer (the Kolmogorov scale).

A droplet moving through the cyclone will experience the presence of the eddies by a change in the local velocity as function of time. Large droplets will not be affected that much, due to their large inertia. Very small droplets, however, will act like passive flow tracers.

Turbulent dispersion is an important parameter when modeling droplet transport in an axial cyclone. When only the acceleration due to the centrifugal pressure field is taken into consideration with as only counteracting force the drag due to the velocity in the radial direction, the inward droplet velocity and therewith the phase separation efficiency are substantially over predicted. The remainder of this chapter elaborates on this topic.

Turbulent dispersion is not a true force, but an effect of the changing velocity of the continuous phase that acts on a droplets surface. The way in which this force can be addressed depends on the method of modelling. For our Euler-Lagrangian approach, we deal with this by introducing the local continuous phase velocity and couple this to the drag force as introduced in the preceding section.

Time-averaged effect Applying a Reynolds decomposition to the velocity field separates the time-averaged velocity from the time-dependent fluctuations:

$$u_i(t) = \overline{U}_i + u'_i, \quad (5.6)$$

The time-averaged velocity of the continuous phase in the radial direction is very small, so $\overline{U}_r \approx 0$. The time-dependent velocity changes appear to be random and have instants with both positive and negative values in the radial direction. The drag force is proportional to the difference between the droplet velocity v_d and the continuous phase velocity u_c squared: $(v_d - u_c)^2$ pointing in the direction opposite to the direction of motion relative to the surrounding liquid velocity. Consider a droplet with a velocity in the radial direction of $v_r = -a |u_{r,\text{peak}}|$ towards the center of the tube; $v_r < 0$. and $0 < a < 1$. The continuous phase velocity alternates as a block signal between $+u_{r,\text{peak}}$ and $-u_{r,\text{peak}}$, with zero-average. The impulse by the drag force when the droplet feels a 'tail wind' is

$$J_{\text{tail wind}} = F_{\text{drag}} \Delta t \propto (u_c - v_d)^2 = (1 - a)^2 u_{r,\text{peak}}^2. \quad (5.7)$$

In the case of 'head wind', this works out to:

$$J_{\text{head wind}} = F_{\text{drag}} \Delta t \propto (v_d - u_c)^2 = (1 + a)^2 u_{r,\text{peak}}^2. \quad (5.8)$$

Based on this comparison, we see that a droplet with a finite velocity in a continuous phase is slowed down by an alternating velocity of the continuous phase.

Virtual mass

An accelerating droplet accelerates the surrounding liquid. Crowe et al. [39] provide an extensive derivation for the amount of liquid that is accelerated. The mass that needs to be added to the mass of a spherical droplet to account for the acceleration of the continuous phase is

$$\Delta m = \frac{\rho_c V_d}{2}. \quad (5.9)$$

Basset force

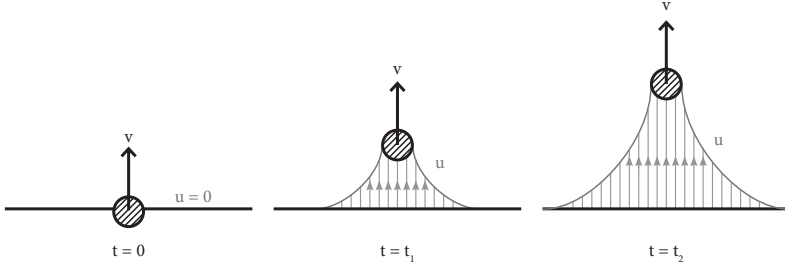


Figure 5.1: Three time steps for a droplet moving through a liquid to illustrate the Basset force. The amount of momentum of the droplet ‘leaking’ into the continuous phase depends on the history along the droplet path.

While the virtual mass accounts for the fact that the droplet pushes liquid forward, the Basset force considers the momentum of the droplet that leaks into the continuous phase due to viscosity, see figure 5.1. Considering the velocity of the continuous phase (velocity u , kinematic viscosity ν_c) at a distance y perpendicular to the droplet velocity (v):

$$\frac{\partial u}{\partial t} = \nu_c \frac{\partial^2 v}{\partial y^2}. \quad (5.10)$$

This equation can be solved imposing the initial and boundary conditions $u(y, t) = 0$ for $t = 0$, $u(0, t) = u_0$ for $t = 0$ and $u(\infty, t) = 0$ for $t = t$:

$$u(y, t) = u_0 \operatorname{erf}(\eta) = \frac{2u_0}{\sqrt{\pi}} \int_0^\eta e^{-\lambda^2} d\lambda, \quad (5.11)$$

with erf the error function and $\eta = \frac{y}{2\sqrt{\nu_c t}}$.

Crowe et al. [39] cast the above result into an expression for the force on a particle

$$F_{\text{Basset}} = \frac{3}{2} D^2 \sqrt{\pi \rho_c \mu_c} \left[\int_0^t \frac{d}{dt'} (u - v) \frac{dt'}{\sqrt{t - t'}} + \frac{(u_i - v_i)_0}{\sqrt{t}} \right]. \quad (5.12)$$

Here $(u - v)$ is the velocity difference between the droplet and the continuous phase. $(u - v)_0$ is this at $t = 0$.

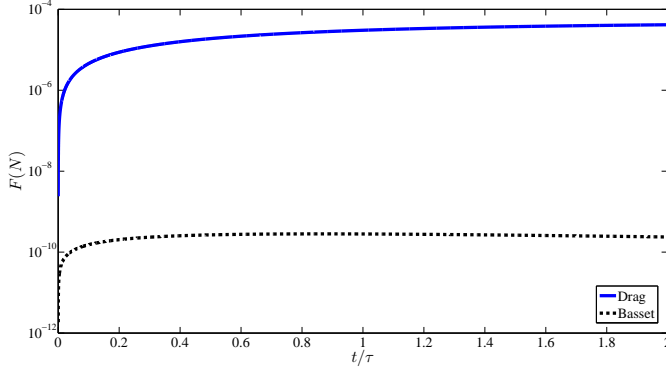


Figure 5.2: Comparison of the magnitude of the Basset force (eq. 5.12) and the magnitude of the drag force for an oil droplet of $10 \mu\text{m}$ accelerated in a centrifugal flow field with an azimuthal velocity of 10 m/s at a radial position of 40 mm

Order of magnitude Due to the complex nature of equation 5.12, we investigate the influence of neglecting the Basset force for the accuracy of the droplet trajectory. To this end, we compare the drag force acting on a droplet which is accelerated in the cyclone with the Basset force for the same droplet.

The droplets acceleration is calculated using equation 5.17, for $D = 10 \mu\text{m}$, $u_d(t = 0) = 0$, $u_r = 0$, $\rho_d = 872 \text{ kg/m}^3$, $\rho_c = 1064 \text{ kg/m}^3$, $\mu_c = 1.0 \cdot 10^{-3} \text{ Pas}$ and $u_\theta = 10 \text{ m/s}$. The time step Δt of the numerical integration was chosen such that a further decrease in Δt did not yield a noticeable improvement. Δt was $0.5 \cdot 10^{-3} \text{ s}$.

Figure 5.2 clearly shows the significant difference between the drag force and the Basset force - the latter being about five orders of magnitude smaller. Therefore, it is reasonable to neglect the Basset force in further computations of the droplet trajectory.

Saffman lift force

The velocity in the cyclone is not uniform, therefore the droplets experience a velocity gradient. This gradient develops a shear difference over the droplet, that creates a rotating motion. Based on the theory of Saffman [46] many authors elaborated on the direction and magnitude of this so-called Saffman lift force.

Crowe et al. [39] provide a convenient relationship for the magnitude of the force, being:

$$F_{\text{saff}} = 1.61 \mu_c D |u_i - v_i| \sqrt{\text{Re}_G}, \quad (5.13)$$

where the shear Reynolds number Re_G is defined as:

$$\text{Re}_G = \frac{D^2}{\nu_c} \frac{du}{dy}. \quad (5.14)$$

We compare the magnitude of the Saffman lift force with the magnitude of the drag force for an oil droplet of $10 \mu\text{m}$ accelerated in a centrifugal flow field with an

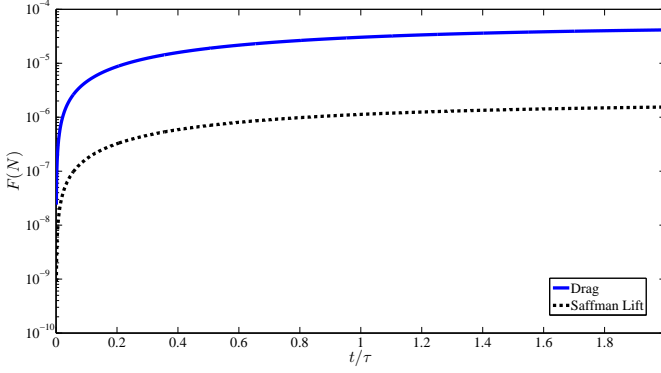


Figure 5.3: Comparison of the magnitude of the Saffman lift force and the magnitude of the drag force for an oil droplet of $10 \mu\text{m}$ accelerated in a centrifugal flow field with an azimuthal velocity of 10 m/s at a radial position of 40 mm

azimuthal velocity of 10 m/s at a radial position of 40 mm in figure 5.3. To this end, we use the same parameters as we used for the comparison in the preceding section for the Basset force. For the velocity gradient $\frac{\partial u}{\partial y}$, the maximum gradient present in the cyclone was selected: $\frac{du_\theta}{dr}$ at $r = 0$: $\frac{du_\theta}{dr} = 3.25 \cdot 10^3 \text{ s}^{-1}$. For this case, the magnitude of the Saffman lift is about two orders of magnitude smaller than the drag force - therefore this effect will be neglected too.

5.2 Droplet model

In this section, we cast the physics into an equation of motion that can be solved numerically. This is done using the theory derived in section 5.1.

5.2.1 Equation of motion

From section 5.1 we know that the following forces are relevant for the droplets in our cyclone: the net centrifugal pressure, drag, turbulent dispersion and virtual mass.

This leads to the equation of motion for an oil droplet accelerated in the water continuous cyclone:

$$\underbrace{\frac{\pi}{6} D_d^3 \left(\frac{1}{2} \rho_c + \rho_d \right) \frac{dv_r}{dt}}_{\text{Droplet acceleration, including virtual mass}} = \underbrace{\frac{\pi}{6} D^3 \frac{(\rho_d - \rho_c) u_\theta^2}{r}}_{\text{Centrifugal buoyancy force}} + \underbrace{\frac{\pi}{8} D_d^2 C_D (\text{Re}_d) \rho_c (v_r - u_r)^2}_{\text{Drag force}}. \quad (5.15)$$

Recall that the liquid velocity is indicated with u , the droplet velocity with v . The index d denotes the droplet and c the continuous phase. In equation 5.15 the droplet

Reynolds number (acting in the radial direction, relative to the surrounding fluid) is:

$$\text{Re}_d = \frac{\rho_c D |u - v|}{\mu_c}. \quad (5.16)$$

Turbulent dispersion is included in the drag through the continuous phase velocity u_c . We only take the turbulent dispersion in the radial direction into account; it is assumed that there is no slip between the droplet and the continuous phase in the axial and azimuthal direction.

For convenience, we rewrite the equation of motion in the radial direction to:

$$\frac{dv}{dt} = \frac{1}{\tau_d} \frac{C_D(\text{Re}_d)\text{Re}_d}{24} (u - v) + \frac{\rho_d - \rho_c}{\frac{1}{2}\rho_c + \rho_d} \frac{u_\theta^2}{r} \quad (5.17)$$

with the droplet relaxation time:

$$\tau_p = \frac{\left(\frac{1}{2}\rho_c + \rho_d\right) D_d^2}{18\mu_c}. \quad (5.18)$$

5.2.2 Experimental input to the model

The Laser Doppler Anemometry (LDA) measurements provide the velocity as function of time for the axial and azimuthal velocity. The radial velocity is not measured. The velocity in the radial direction, and especially the time-dependent velocity fluctuations, determine to a great extent the drag experienced by the droplet moving in the radial direction. The time-averaged velocity in the azimuthal direction determines the centrifugal acceleration of the droplet towards the center and the axial velocity is necessary to predict the residence time in the cyclone.

Since we lack the measured velocity data for the radial direction, an assumption is made for the radial velocity. Although the turbulence inside a swirling flow at high Reynolds number cannot be assumed to be isotropic we nevertheless assume that the magnitude and time scale of the radial velocity fluctuations is of the same order of magnitude as for the measured axial velocity component. The velocity of the azimuthal velocity is larger, where that component is confined by the tube wall. Therefore, the frequency and magnitude of the axial velocity will be more comparable with the radial velocity statistics.

This leads to the following relation for the velocity used in the model for the droplet trajectory, all experimentally obtained datasets, with the Reynolds decomposition applied ($u(t) = \bar{U} + u'(t)$):

$$\begin{aligned} \text{Axial:} \quad u_z(r, \phi, z, t) &= \overline{U_z(r)} \\ \text{Azimuthal:} \quad u_\theta(r, \phi, z, t) &= \overline{U_\theta(r)} \\ \text{Radial:} \quad u_r(r, \phi, z, t) &= 0 + u'_z(r, t) \end{aligned}$$

The time-averages of the velocities $\overline{U_z(r)}$ and $\overline{U_\theta(r)}$ are huge compared to the time-dependent velocity fluctuations (results described in section 4.3.2, example dataset in figure 5.6). The particle relaxation time τ_d is small compared to the residence time of the droplet in the cyclone, therefore we can assume the droplet to have the

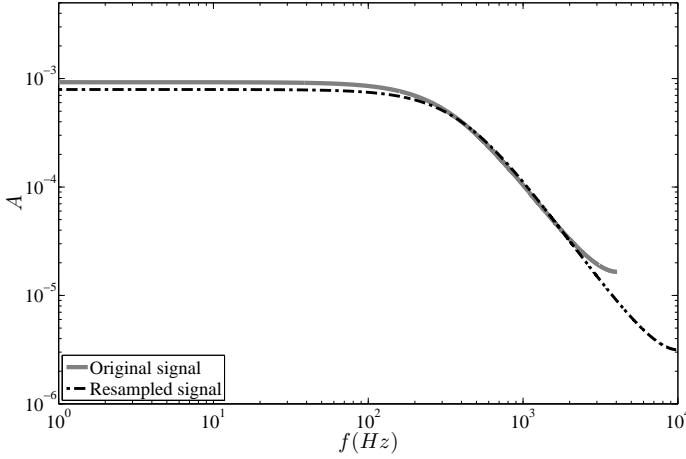


Figure 5.4: Amplitude of the power spectrum of an original dataset and that of the reconstructed data

same velocity as the continuous phase in the z - and θ -direction. We calculate the movement of the droplet in the r -direction.

Frequency in LDA signal

Velocity measurements performed with Laser Doppler Anemometry (LDA) measure the velocity of tracers dispersed in the flow. The frequency of the particles arriving in the measurement volume is irregular, and therewith the LDA velocity time series. Due to this irregularity, the signal contains frequency information exceeding the sampling frequency (see Durst et al. [18]). According to Broersen [43], the frequency spectrum cannot be calculated using common methods like fast Fourier transforms. Instead, we use the software package ARMAsel [43].

ARMAsel computes the power spectrum of the original signal, which is used to construct a new velocity profile as function of time, according to:

$$v(t_i) = \sum_{f_i=0}^{f_{\max}} \sum_{t_i=0}^T \text{PSD}^2 \cos(f_i \cdot (t_i - t_0)) \quad (5.19)$$

The data is resampled at a frequency higher than the highest frequency obtained in the original signal with ARMAsel. The time series is multiplied with a constant to render the variance of the signal equal to the variance of the original signal, while the mean value is kept at 0. The spectrum of the resulting time series is compared with the original spectrum. Figure 5.4 shows good agreement of the two spectra.

The mean difference of the velocities of the droplets with the mean fluid velocity $(\bar{v} - u)$ has been calculated for a range of droplet sizes for a constant centrifugal acceleration according to equation 5.17. Figure 5.5 shows the difference in the velocity for droplets between 15 and 70 μm .

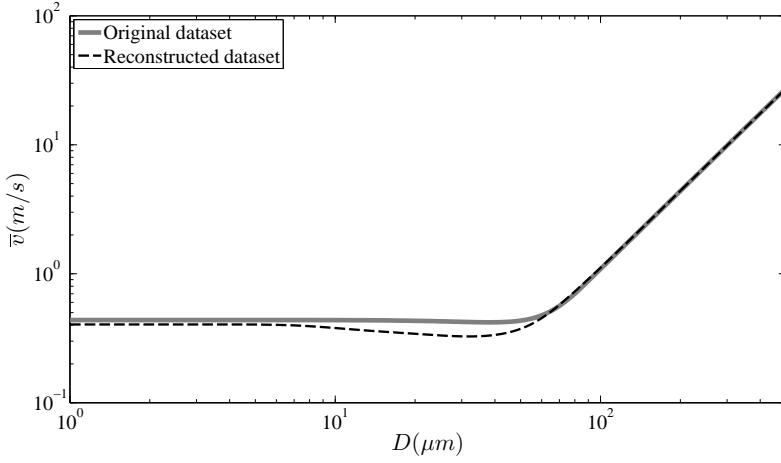


Figure 5.5: Comparison of the averaged droplet velocity and the mean continuous phase velocity for a constant centrifugal acceleration as function of droplet size for the original LDA dataset and for the reconstructed data.

5.2.3 Numerical implementation

This section describes the strategy and the equations used for numerically solving equation 5.17. Figure 5.6 depicts the scheme of the method to calculate the droplet position and velocity.

Loop structure The particle trajectory is calculated for a range of droplet sizes D_d . Each time step, $\Delta t'$, is chosen based on the interval between the chosen samples for the radial velocity. The resulting time series is therefore irregular.

Input parameters The continuous phase is represented using the time-average velocity data for the azimuthal and axial direction and by a time series for the radial velocity. This time series is estimated by using the velocity fluctuations in the axial direction with zero average, as discussed in section 5.2.2, with 5 mm spacing between measurement points.

For each time step, the following data is stored for the droplet:

$$\begin{cases} t'_i \\ v(t'_i) \\ r(t'_i) \end{cases}$$

The properties of the continuous phase are obtained from the available datasets for the same time instance:

$$\begin{cases} u_\theta = \overline{U_\theta}(r) \\ u_z = \overline{U_z}(r) \\ u_r = u_r(r, t'_i) \\ r(t'_i) \end{cases}$$

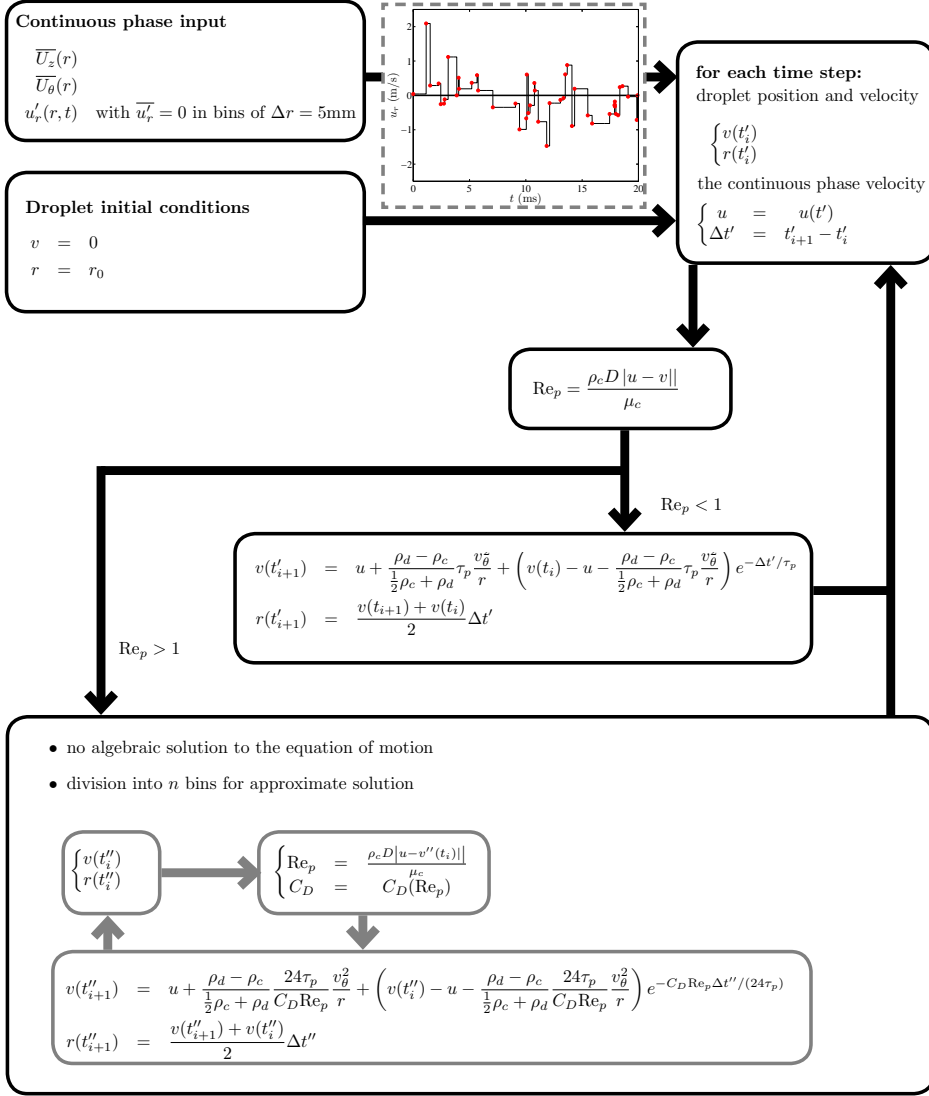


Figure 5.6: Scheme of the numerical implementation to solve the droplet equation of motion in the axial cyclone

Equation of motion Based on the data available for each point, the net force on the droplet is estimated for each time step. Using Newton's second law, the droplet's trajectory is determined. The strategy for this estimation depends on the droplet Reynolds number Re_d (equation 5.16). If $Re_d < 1$ an analytical solution (Stokes flow) exists for the equation of motion (equation 5.17), since then $C_D Re_p / 24 \approx 1$. The equation of motion then simplifies to:

$$\frac{\partial v_r}{\partial t} = \frac{1}{\tau_d} (u_r - v_r) + \frac{\rho_d - \rho_c}{\frac{1}{2}\rho_c + \rho_d} \frac{u_\theta^2}{r} \quad (5.20)$$

which is analytically solved for $v_r(0) = v_{r,0}$ to yield:

$$v_r(t'_{i+1}) = u_r + \frac{\rho_d - \rho_c}{\frac{1}{2}\rho_c + \rho_d} \tau_d \frac{u_\theta^2}{r} + \left(v_r(t'_i) - u_r - \frac{\rho_d - \rho_c}{\frac{1}{2}\rho_c + \rho_d} \tau_d \frac{v_\theta^2}{r} \right) e^{-(t'_{i+1} - t'_i) / \tau_d}. \quad (5.21)$$

When $Re_d > 1$ the equation of motion cannot be solved analytically due to the dependence of C_D on the Reynolds number. It is not possible to assume C_D to be constant during an interval $\Delta t'$, since we would then overestimate the drag exerted by the continuous phase on the droplet. To resolve this, the bin is split into an integer number of n subbins that just fits the criterion $\Delta t'' < \tau_p$. Within these intervals, C_D is kept constant. For each subbin, the approximate velocity is given by:

$$v_r(t''_{i+1}) = \left(v_r(t''_i) - u_r - \frac{\rho_d - \rho_c}{\frac{1}{2}\rho_c + \rho_d} \frac{24\tau_d}{C_D Re_d} \tau_d \frac{v_\theta^2}{r} \right) e^{-C_D Re_d (t''_{i+1} - t''_i) / (24\tau_d)} + u_r + \frac{\rho_d - \rho_c}{\frac{1}{2}\rho_c + \rho_d} \frac{24\tau_p}{C_D Re_d} \tau_p \frac{u_\theta^2}{r}, \quad (5.22)$$

where we estimate for each time step:

$$C_D(Re_p) = C_D(Re_p(v(t''_i))).$$

Axial displacement The solution for the position in the axial direction is straightforwardly calculated by $\Delta z = \overline{U}_z \Delta t'$.

5.2.4 Droplet break-up

For each droplet being released in the system as described in this chapter, the path and velocity can be calculated. We know from the theory discussed in section 4.1 that droplets break-up when the shear forces on the interface exceed the force that the interfacial tension can withstand. This is expressed by the Weber number:

$$We = \frac{\rho_c D (v - u)^2}{\sigma}, \quad (5.23)$$

The critical Weber number at which the droplet breaks, depends on the droplet Reynolds number $Re_d = \frac{|v-u|D}{\nu}$, according to a model proposed by Brauer [47]:

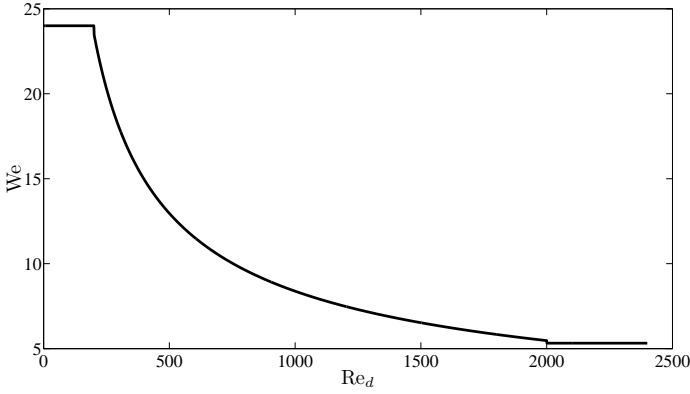


Figure 5.7: Weber number as function of the droplet Reynolds number based on the relation in equation 5.24.

$$We_{crit} = \begin{cases} 24 & \text{for } Re_d < 200 \\ 55 \left(\frac{24}{Re_d} + \frac{20.1807}{Re_d^{0.615}} - \frac{16}{Re_d^{2/3}} \right) & \text{for } 200 < Re_d < 2000 \\ 5.32 & \text{for } Re_d > 2000 \end{cases} \quad (5.24)$$

The critical Weber number is kept constant for Reynolds numbers smaller than 200 at the value at $Re = 200$, being 24. For $Re > 2000$, the critical Weber number is kept constant at 5.32. A graphical representation of this relation is in figure 5.7.

For each time step t' in figure 5.6, the velocity relative to the fluid ($|u - v|$) is compared with the critical velocity:

$$v_{crit} = \sqrt{\frac{We_{crit}\sigma}{D\rho_c}} \quad (5.25)$$

In case the slip velocity exceeds the critical velocity at any time step, the droplet is assumed to be broken apart. In this model, we count the number of broken droplets, no tracking of the secondary droplets is done, since we cannot predict the size of the droplet fragments.

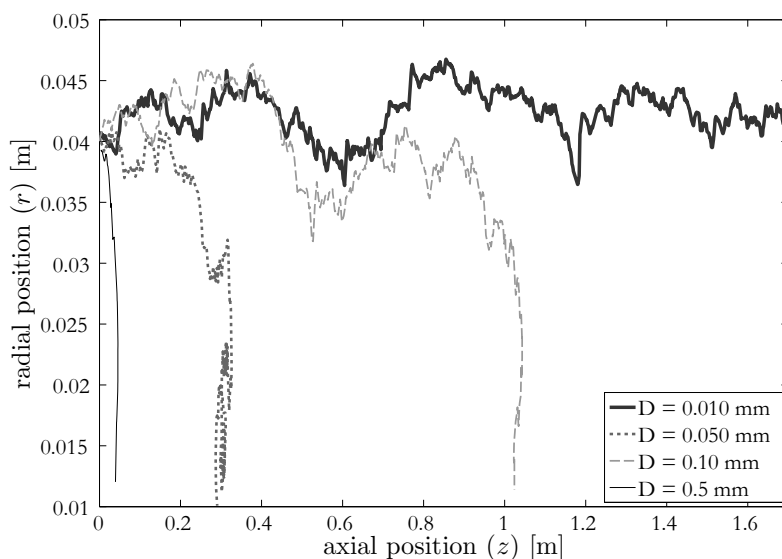
The LDA data used in the model has a random nature, both with respect to the sampling rate and turbulent velocity statistics. We therefore run the model repeatedly with a different initial condition for the time-dependent fluid velocity. This provides us with the probability that a droplet of given size breaks up in the cyclone.

5.3 Dilute droplets simulation results

The basis of the model derived in this chapter cannot be used to describe the dense multiphase flow as is encountered in a liquid-liquid axial cyclone, simply because

Table 5.1: Available LDA datasets for the numerical method introduced in this chapter.

<i>Swirl Element</i>	<i>Flowrate [m³/h]</i>				
	10	20	30	42	56
Strong swirl			x	x	x
Weak swirl		x	x	x	x
Large swirl	x	x	x	x	

**Figure 5.8:** Examples of simulated droplet paths for four different droplet sizes for the strong swirl element at 56 m³/h flow.

we approach the device as a dilute system in which the turbulence levels are as measured for the water-only case are true and we neglect any droplet-droplet interactions. However, the model is used to obtain insights why some droplets can and others cannot be separated with our cyclone. The available LDA datasets are listed in table 5.1.

From these available datasets, we make two comparisons: (i) an equal swirl element at different flow rates and (ii) three different swirl elements at an equal flow rate. For (i) we use the weak swirl element and for (ii) we use the flow rate of approximately 42 m³/h.

An example of the raw output generated by the model introduced in this chapter is presented in figure 5.8. The trajectory for four different droplet sizes is plotted in its axial and radial coordinates based on the measured velocity data for the strong swirl element at 56 m³/h. Due to the random selection of the starting point in the model, the result is different for each simulation batch.

5.3.1 Smallest separated droplets

Droplets with a small size (much smaller than the critical size d_{crit}) have a very small τ_p and will follow each fluctuation in the continuous phase velocity. A very large droplet (much larger than the critical size d_{crit}) will only follow the time average velocity. It is likely that droplets larger than d_{crit} will be separated in our cyclone, and droplets smaller than d_{crit} will not.

The model as introduced in this chapter was used to evaluate the time required for a range of droplet sizes to reach the center of the tube (where $r/R < 0.2$), normalized by the average residence of the liquid in the cyclone T (streamwise length divided by the bulk velocity). If the time needed by a certain droplet to reach the center of the tube exceeds the residence time, we can be sure that it will not coalesce into a possible oil-continuous core.

Figure 5.9(a) compares for four different flow rates in the weak swirl element the time required to reach the center as function of the droplet size. For the three highest flow rates, the separation time exceeds the residence time for droplets smaller than $50 \mu\text{m}$. For the $20 \text{ m}^3/\text{h}$ case, the residence time is not exceeded. For all simulations, it holds that the swirl decay with axial distance has not been considered - the LDA datasets were too limited to do so. The data used for these simulations were obtained about 30 cm downstream of the swirl element and will therefore over predict the separation performance. Droplets that need the order of the residence time to get separated will therefore most likely not separate in reality. When we use a non-dimensional time t/T (time to center over residence time) of 0.5 as criterion for separation, the smallest separated size is listed in table 5.2.

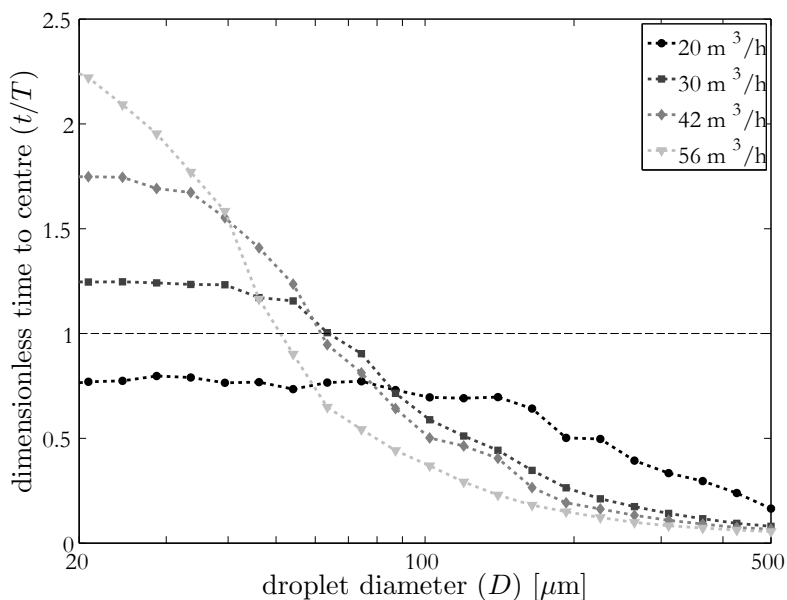
Table 5.2: Smallest droplet size that can be separated, based on the criterion that the $t/T < 0.5$.

Flow rate Φ (m^3/h)	Droplet size D (μm)
56	90
42	100
30	110
20	220

Figure 5.9(b) compares for the strong, weak and large swirl element the time required for droplets to reach the center, where the droplets are assumed to stay intact. We see significant differences for the three swirl elements: the stronger swirl generated by the large element is capable to separate smaller droplets - already for $60 \mu\text{m}$, the time to get to the center is less than half of the residence time. The strong and weak swirl element perform nearly equal, the threshold of half the residence time is passed for droplets smaller than $130 \mu\text{m}$.

5.3.2 Droplet break-up

As we have seen in section 5.3.1, it is favorable to increase the flow rate as well as the swirl strength to promote separation of droplets with a small diameter. The downside of this increase in flow rate or swirl strength is, however, that for a constant droplet diameter the velocity difference between the droplet and that of the



(a) Weak swirl element: four flow rates.

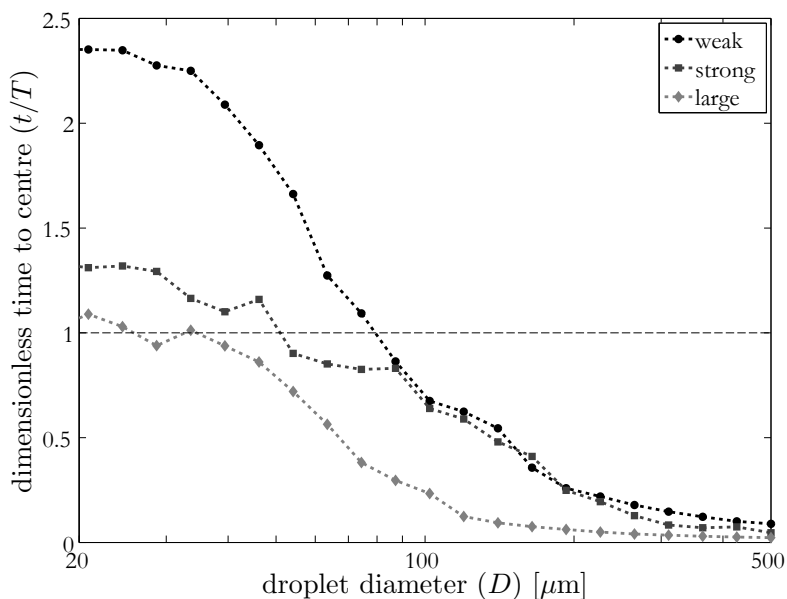
(b) Three swirl elements at $\sim 40 \text{ m}^3/\text{h}$.

Figure 5.9: Time required for the droplets to reach the center of the tube ($r/R < 0.2$) divided by the average residence time of the fluid in the cyclone LA/ϕ . Each point is the average of 100 simulations for the same droplet size: $t = \frac{1}{N} \sum_{i=1}^N t_i$.

continuous phase increases. The drag force experienced by a droplet is proportional to this velocity difference. The shear on the droplets interface therefore increases for increasing swirl strength or flow rate. In this section, we compare the probability of droplet break-up for different conditions, according to the break-up model introduced in section 5.2.4.

The model was executed at least 100 times per droplet size, with two possible outcomes: the droplet breaks-up or does not break-up. The fraction of break-up events leads to the expected chance of break-up.

Figure 5.10 compares the chance of breakup for the three swirl elements at a flow rate of $42 \text{ m}^3/\text{h}$ and for the weak swirl element for four different flow rates. These break-up probabilities are predicted values based on the velocity profile measured at a single axial position in the tube. Break-up events due to the acceleration in the axial direction are therefore not taken into account. Since the velocity profile used was obtained close to the swirl element and swirl decay was not taken into account, the number of break-up events is most likely over predicted.

The comparison of the performance of the swirl elements in figure 5.10(b) shows that the flow downstream of the weak swirl element does not lead to break-up for droplets smaller than $200 \text{ }\mu\text{m}$. The flow downstream of the strong swirl element leads to break-up of all droplets larger than $120 \text{ }\mu\text{m}$, but even droplets as small as $50 \text{ }\mu\text{m}$ have a chance to be break-up. The stronger swirl element shows a clear step in the plot at $60 \text{ }\mu\text{m}$.

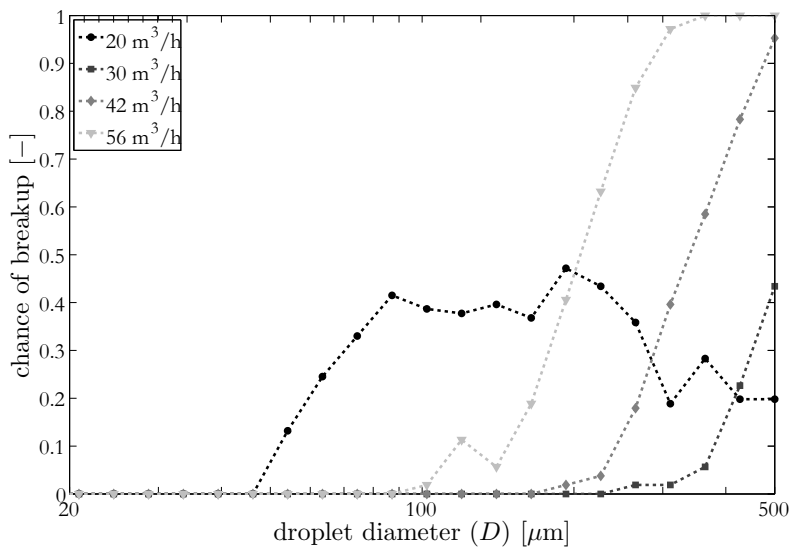
Figure 5.10(a) illustrates the effect of flow rate on droplet break-up. For 30, 42 and $56 \text{ m}^3/\text{h}$, we see the trend that a higher flow rate leads to break-up of smaller droplets. The estimation of the critical droplet size is presented in table 5.3.

Table 5.3: Smallest droplet size that is expected to be broken by the weak swirl element for different flow rates.

Flow rate $\Phi \text{ [m}^3/\text{h}]$	Droplet size $D \text{ [}\mu\text{m}]$
20	> 400
30	400
42	300
56	200

For the $20 \text{ m}^3/\text{h}$ case, an increase in break-up events is found for droplets of $70 \text{ }\mu\text{m}$ and larger, however, for no flow rate 100% of the droplets breaks-up. This breaks with the observed trend that a lower flow rate leads to an increase in the critical size at which droplets break-up. This observation can have different causes:

1. the sampling rate of the LDA signal for $20 \text{ m}^3/\text{h}$ is lower than for the other flow rates. This leads to an overestimation of the fluctuations in the velocity, e.g. the jumps in velocity are measured larger than they actually are;
2. the lower azimuthal velocity leads to a weaker confinement in the swirling motion. This allows more turbulent structures in the axial direction, which we chose to be equal to the turbulent structures in the radial direction;
3. the residence time is proportional to the axial velocity - an extended exposure



(a) Weak swirl element: four flow rates

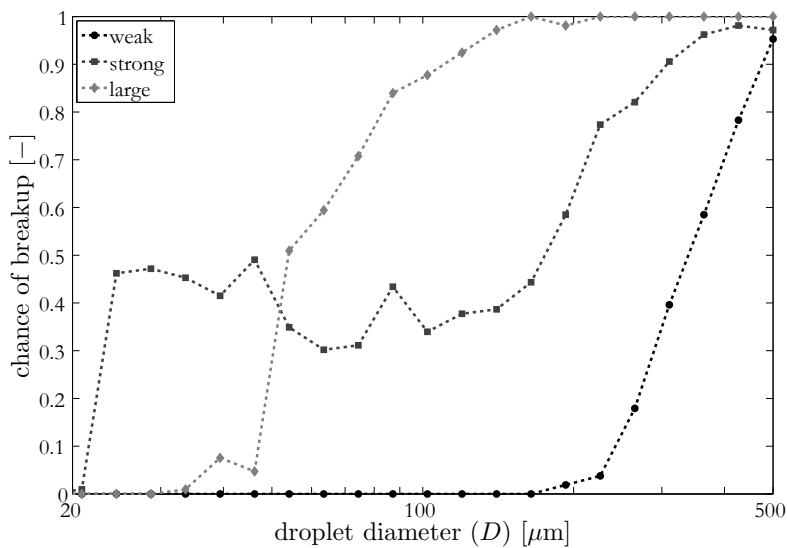
(b) Three swirl elements at $\sim 40 \text{ m}^3/\text{h}$.

Figure 5.10: Probability for a droplet to break-up during its residence in the cyclone. Each datapoint represents at least 100 runs of the model in section 5.2.4. Each model run is different due to the chaotic nature of turbulent velocity measurements.

to swirling flow promotes break-up.

Interpretation of predicted break-up

The model introduced in this chapter assumes droplets to break when they exceed a critical Weber number, see section 5.2.4. This does not provide information on the resulting droplet sizes, the so called daughter droplet size distribution. Many measurements and models have been developed to provide an accurate description of this distribution. However, the available models show a very wide spread in predictions of the daughter droplet size distribution [48]. According to the model introduced by Martínez-Bazán et al. [49] and validated by Eastwood et al. [50], the daughter droplet size distribution depends on the turbulent dissipation rate ϵ . For the runs of the model in this chapter, we cannot produce an accurate description of the turbulent dissipation. From theory [48, 49], we therefore should assume the daughter droplets to range in size from almost 0 times the mother droplet to 0.95 the diameter of the mother droplet.

5.3.3 Separation window

In the preceding subsections, we obtained both a minimum size of the droplets that can be separated and a maximum size before droplets are broken. When droplets in this range are fed to the cyclone, the optimal separation performance can be expected.

Figure 5.11 compares the time required for a droplet to get to the center of the tube ($r/R < 0.2$) with the number of break-up events during its path to the center. There is a chance of droplet separation when:

- $t/T < 1$, with t the time to center and T the average residence time of liquid in the cyclone;
- $NT/t < 1$, with N the total number of break-up events. By dividing this number by the dimensionless time to the center (t/T), we know whether it is certain that a droplet will break-up (if $NT/t > 1$) or that a certain number of droplets will not be broken. If a droplet is broken, some daughter droplets can still be within the separation window, but certainly a certain fraction will be smaller than the lower limit, which reduces the separation efficiency.

The comparison of the three swirl elements (figure 5.11(b)) shows that the above mentioned criterion is not met for the large swirl element. The strong swirl element has a small range in which separation is likely: $60 < D < 90 \mu\text{m}$ and the weak element has the largest separation window: $70 < D < 200 \mu\text{m}$.

For the series of calculation in which we varied the flow rate (figure 5.11(a)), table 5.4 shows a shift in the separation window.

Table 5.4: Separation window for the weak swirl element for four different flow rates.

Flow rate Φ [m ³ /h]	Smallest separated size D_{\min} [μm]	Max stable size D_{\max} [μm]
20	250	-
30	100	350
42	70	220
56	50	140

5.4 Conclusions

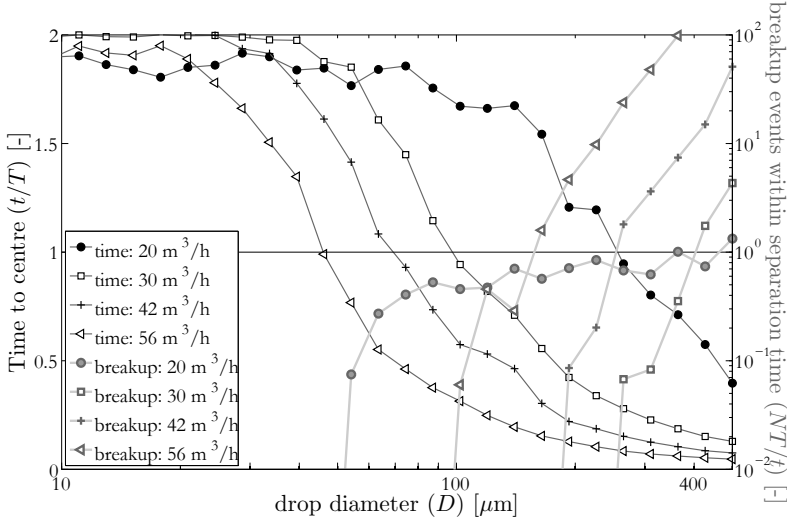
Based on experimental data obtained with Laser Doppler Anemometry, a model has been constructed to predict the movement of oil droplets in brine for a very dilute case. The model evaluates the droplet acceleration based on three forces: (i) buoyancy in the centrifugal pressure field, (ii) drag force relative to the surrounding continuous phase and (iii) the additional inertia due to the acceleration of the surrounding liquid (added mass). The available velocity information consisted out of time series for the axial and azimuthal velocity. The velocity fluctuations in the axial directions were used to mimic the velocity fluctuations in the radial direction. Results obtained with the model indicate a range of droplet sizes in which droplets are likely to be separated with the cyclone:

- droplets smaller than the size at which the droplets will certainly break-up;
- larger than the size at which the turbulent dispersion effect is stronger than the acceleration due to the centrifugal motion.

Within this range, there is a window of separation. The daughter droplet size distribution following the break-up event has not been considered within this work. Of course, droplets that are too large can break into multiple smaller droplets of which some are still larger than the lower critical size for separation. Based on statistics from literature, there will certainly be daughter droplets that are too small to be separated. Therefore, exceeding the maximum droplet size of the separation window leads to a reduction in separation quality.

For simulations with different flow rates for the same swirl element, the width of the window remains of equal order of magnitude. The critical droplet sizes shifts - a lower flow rate leads to an increase in the size of the smallest droplet captured, but also allows larger droplets not being broken up.

For tests for three different cyclones at equal flow rate, the width of the separation window changed. The weakest swirl element provides the largest window of separation. Stronger swirl elements are likely to separate smaller droplets for a given flow rate.



(a) Weak swirl element: four flow rates

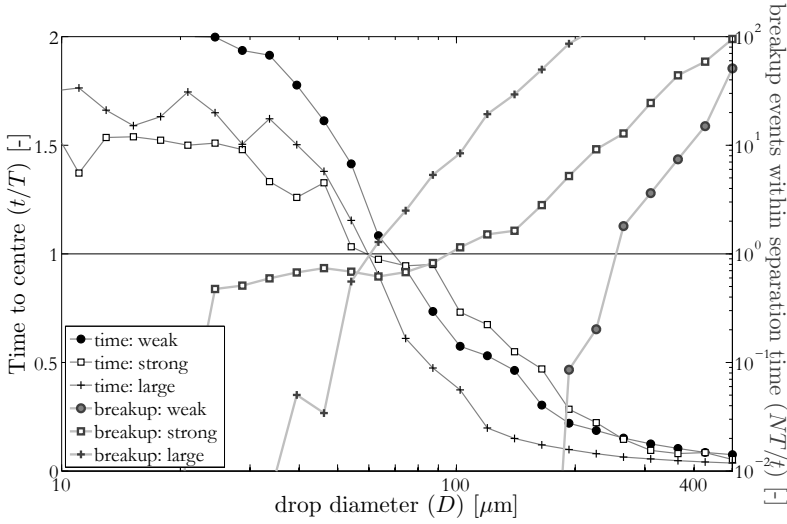
(b) Three swirl elements at $\sim 40 \text{ m}^3/\text{h}$.

Figure 5.11: Comparison of the time for a droplet to reach the center and the chance that a droplet breaks up within this period. Each datapoint represents at least 100 runs of the model in section 5.2.4.

5.5 Outlook

The model in this section is a valuable tool to compare the droplet trajectories of Lagrangian simulations with experimental data, since it includes an accurate description of turbulent dispersion. As a design tool, it lacks a very important parameter, namely the droplet break-up due to the acceleration of the liquid. Although droplet break-up is extensively discussed in this thesis (chapter 6, it does not provide an accurate prediction of the droplet break-up phenomenon, meaning that we cannot use single phase flow statistics to calculate the droplet size distribution downstream of the swirl element. Further insight in the droplet break-up mechanism can be used to improve the model to gain practical separation predictions.

CHAPTER 6

Droplet break-up and coalescence

Two phase liquid-liquid flows can occur in many different flow regimes. The transportation at relative high velocities and therewith high Reynolds numbers leads to dispersed flow. Shear forces applied on the liquid leads to break-up of droplets, where the overall aim of a separator is to coalesce all dispersed droplets into a continuous phase.

In this chapter, we investigate the droplet break-up and coalescence in the axial cyclones used within this research. The droplet size distribution has been measured at multiple spots with an intrusive endoscope technique and leads to conclusions on break-up and average coalescence versus break-up behavior. Understanding of droplet break-up can be used during the design of cyclones to minimize the droplet size reduction.

6.1 Droplet size upstream of the swirl element

6.1.1 Turbulent liquid-liquid pipe flow

Turbulent flow is characterized by eddies, ranging in size from the integral scale, down to the Kolmogorov microscale. These eddies exert a force on the droplet that can break droplets. According to Kolev [36] the droplet size distribution will approach the size distribution of the smaller turbulent eddies present in the flow.

Hinze model As discusses in chapter 4 Hinze [37] proposed a model for the maximum droplet size in turbulent flow:

$$D_{\max} \left(\frac{\rho_c}{\sigma} \right)^{3/5} \epsilon^{2/5} = 0.725, \quad (6.1)$$

where ρ_c is the density of the continuous phase and ϵ the turbulent dissipation rate. The estimation of ϵ is essential for a correct prediction of the maximum droplet size. The turbulent dissipation rate is connected to the size of the smallest eddies ℓ , which on its turn depends on the microscale to:

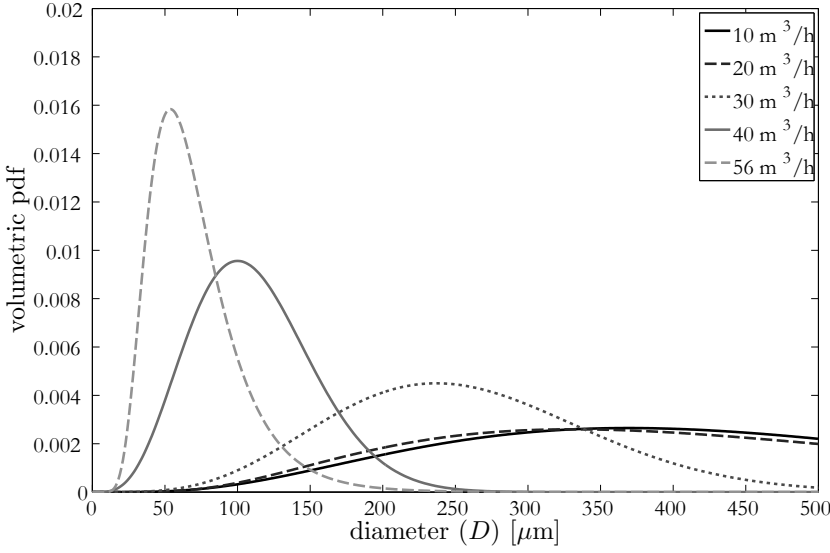


Figure 6.1: Estimation of the volumetric occupation of the dispersed phase based on droplet photographs for five different flow rates. Measurements taken at 10 cm upstream of the swirl element, according to the method in section 3.4.1.

$$\ell = \left(\frac{\nu^3}{\epsilon} \right)^{1/4} = \ell_0 \text{Re}^{-3/4}, \quad (6.2)$$

where ν is the kinematic viscosity and ℓ_0 the scale of the biggest eddy (the tube diameter). Taking this into account, the turbulent dissipation rate can be expressed as:

$$\epsilon = \frac{\nu^3 \text{Re}^3}{\ell_0^4}. \quad (6.3)$$

The relation between flow rate and droplet size was already introduced in chapter 4, see figure 4.1. This figure relates the maximum droplet size according to Hinze's model (equation 6.1) to the flow rate. At nominal conditions for the flow rig used in this investigation ($56.5 \text{ m}^3/\text{h}$), the maximum droplet size is predicted to be $234 \mu\text{m}$. As could be expected, a lower flow rate results in a larger maximum droplet size.

Experimental data

The theory for the droplet size distribution described above was tested for the turbulent multiphase non-swirling pipe flow upstream of the swirl element. The droplet sizes were measured upstream of the swirl element with the intrusive endoscope method introduced in section 3.4.1. Figure 6.1 shows the probability of the droplet sizes. The trend for the maximum droplet size in figures 4.1 and 6.1 shows good agreement.

6.1.2 Droplet size reduction with valves

Since the droplet size is an important parameter affecting the performance of an axial cyclone, the need exists to control the droplet size that is fed to the cyclone. The nature of turbulent pipe flow creates a certain droplet size distribution as is discussed in the previous section. To reduce the droplet size further, two types of valves are used to break droplets with shear: a ball valve and a membrane valve.

Ball valve The ball valve used has a 100 mm inner diameter and a PTFE fitting. The region with high shear is the sharp edge of the port, that can gradually be turned into the flow.

Figure 6.2(a) demonstrates the dispersing effect of the ball valve. As an indication of the additional shear applied to the droplets the pressure drop over the valve is used. The median droplet size at 10 m³/h can be reduced to a median value of 300 μ m, which is still significantly larger than the droplet size measured at 56.5 m³/h.

Diaphragm valve To reduce the droplet size further than with the ball valve, a membrane valve was used instead. Figure 6.2(b) demonstrates the ability to reduce the droplet size further with a lower pressure drop as compared to the ball valve. Comparing the case at 10 m³/h with 0.56 bar pressure drop over the membrane valve and the 56 m³/h case with no pressure drop, the average droplet size is equal (110 μ m). The median differs, since more large droplets are present at the higher flow rate of 56 m³/h.

6.2 Droplet size reduction with a swirl element

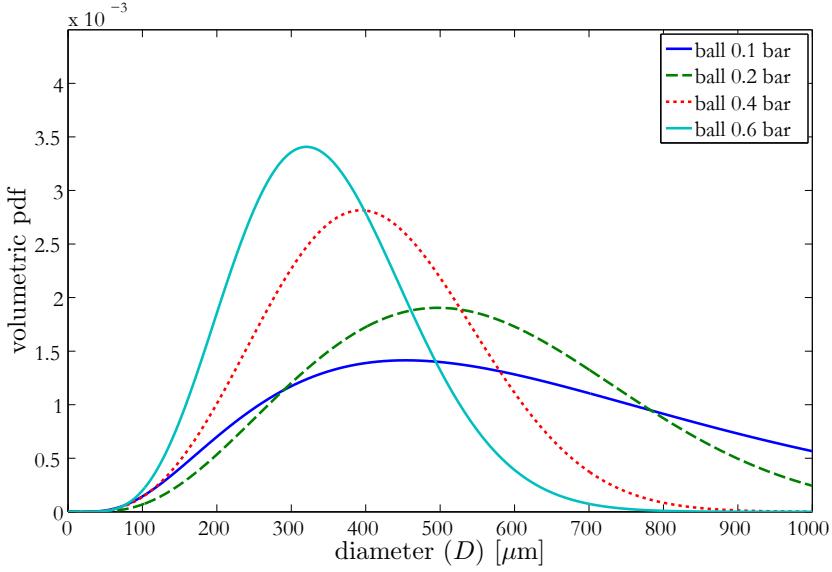
6.2.1 Model of the break-up in a swirl element

For most applications, the fluid flow that is accelerated by the swirl element will consist of dispersed oil droplets in a continuous watery phase. The spherical droplets are stretched by the acceleration. Let us assume that the area occupied by the droplet in a cross-sectional plane remains constant:

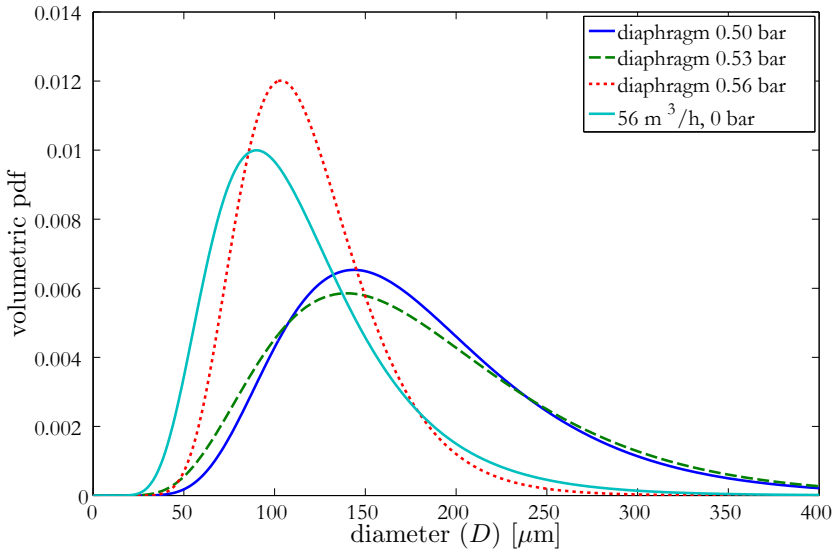
$$\frac{D_1^2}{A_1} = \frac{D_3^2}{A_3}, \quad (6.4)$$

here, D_1 is the droplet diameter upstream of the swirl element, A_1 is the cross-sectional area of the tube upstream, A_3 is the cross-sectional area at the vane tips, where the liquid leaves the swirl element measured in the direction perpendicular to the fluids velocity, and D_3 is the droplet diameter in that plane. The indices are illustrated in figure 6.3: 1 is upstream of the swirl element, 2 is at the upstream side of the vanes and 3 is at the vane tip on the downstream side.

The area through which the volume is ejected, A_3 , is determined by the velocity at the vane tip, governed by the relation $A_3 = \frac{\Phi}{v_3}$ with Φ the flow rate and v_3 the magnitude of the velocity at the vane tip. The first depends on operational settings, the latter on the swirl element of choice. The velocity is discussed in section 4.2.



(a) Ball valve



(b) Membrane valve

Figure 6.2: Volumetric probability density functions (PDFs) of the droplet size distributions for two different valves at different valve settings for $10 \text{ m}^3/\text{h}$ at an oil cut of 25 %, compared with the droplet size distribution at $56 \text{ m}^3/\text{h}$ without additional shear. Measurement location was downstream of the valve and upstream of the swirl element

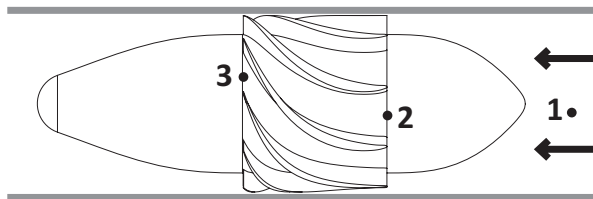


Figure 6.3: Positions at the swirl element used for the estimation of the shear induced break-up.

Since the velocity profile cannot be flat due to wall friction, the effective opening is smaller, like the liquid contraction downstream of an orifice as described by van den Akker and Mudde [44]. We therefore divide this area by 2.

The mass and therewith the volume of the droplet, that is stretched by the accelerating flow, is conserved. Due to the smaller diameter, the length \tilde{L} of the droplet will increase. We assume a cylindrical shape with spherical caps:

$$\tilde{L} = \frac{2D_1^3 - 2D_3^3}{3D_3^2} + D_3, \quad (6.5)$$

The outer surface of this long droplet is:

$$A_{\text{drop},3} = \pi \tilde{L} D_3 + \pi D_3^2 \quad (6.6)$$

The shear force on the droplet is assumed to be equal to the force required to accelerate the droplet to have the same velocity as the liquid, where the force results from Newton's second law, $F = m \cdot \Delta v / \Delta t$ with $\Delta v = v_3 - v_2$ in the streamwise direction and $\Delta t = 2\Delta s / (v_3 + v_2)$. Dividing by the outer surface of the elongated droplet leads to the shear on the drop:

$$\tau = \frac{D_1^3 \rho_d}{12\Delta s} \frac{v_3^2 - v_2^2}{LD_3 + D_3^2}, \quad (6.7)$$

with Δs the length of the vanes along the streamlines. For this shear τ , the Weber number can easily be calculated according to equation 4.1. The critical Weber number leads to the maximum size of droplets upstream (position 1) that can pass the swirl element intact. Figure 6.4 provides the maximum stable droplet size as function of the flow rate for two different swirl elements: the initial and the weaker element (see section 4.2). For the nominal conditions of design, 56 m³/h, the maximum stable droplet size passing the initial swirl element is 0.16 mm and for the weaker swirl element 0.25 mm. Based on this model, we predict that droplets larger than the respective sizes will break. The resulting size distribution is not predicted

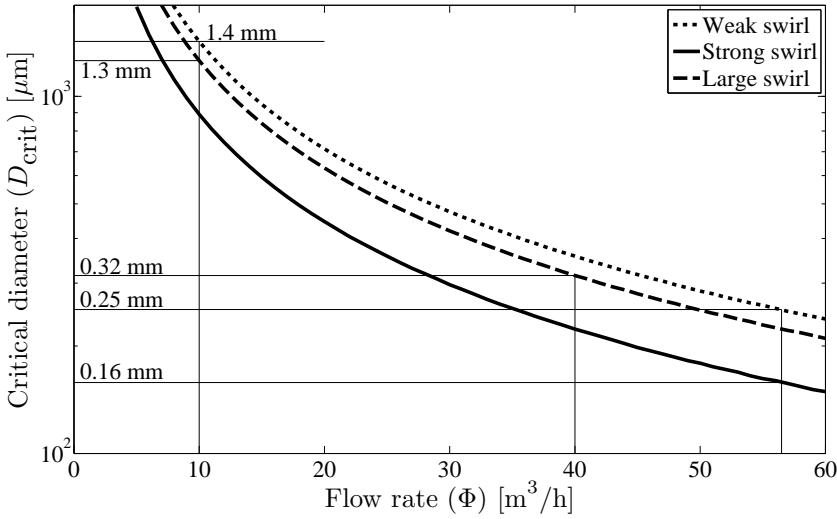


Figure 6.4: Size of the droplets at the critical Weber number in the swirl element for given flow rate.

using a model. The size will range from a sphere with the diameter D_3 (equation 6.4) up to a droplet with half of the droplet volume before the break-up event.

6.2.2 Experimental results

Figure 6.5 compares the droplet size downstream of the swirl element for various input droplet sizes - the indicated droplet sizes (300, 400 and 500 μm) refer to the median droplet size obtained with a specific ball valve setting as can be found in figure 6.2(a). The expected critical droplet size is larger than 1 mm for this specific setting and therefore, we originally did not expect that droplets would be broken by the swirl element. These results, however, indicate that the mechanism that we introduced is not complete, effects like shear stress at the wall are neglected in our model.

The effect of break-up at 56 m^3/h flow was studied for two different swirl elements. Figure 6.6(a) shows that the droplet size is reduced by passing the swirl element. The estimated critical droplet size for the initial swirl element was 0.16 mm and for the weaker swirl element 0.25 mm. For both elements, the droplet size is reduced to sizes far below this critical size. However, some of the observed droplets are larger than the predicted maximum size. It could be caused by coalescence just downstream of the swirl element, since the minimum distance between the swirl element and the droplet size measurement location was 20 cm.

The minimum droplet size observed for the initial swirl element is 4 μm and for the weaker swirl element 10 μm . These diameters are smaller than the diameter of the elongated droplets in the swirl element at the critical Weber number.

Figure 6.6(b) compares the droplet size downstream of the swirl element at 10 m^3/h for the weaker and larger swirl element. The size of the droplets in the feed is most likely not correct, since the expected droplet size (> 1 mm) does not fit in the field

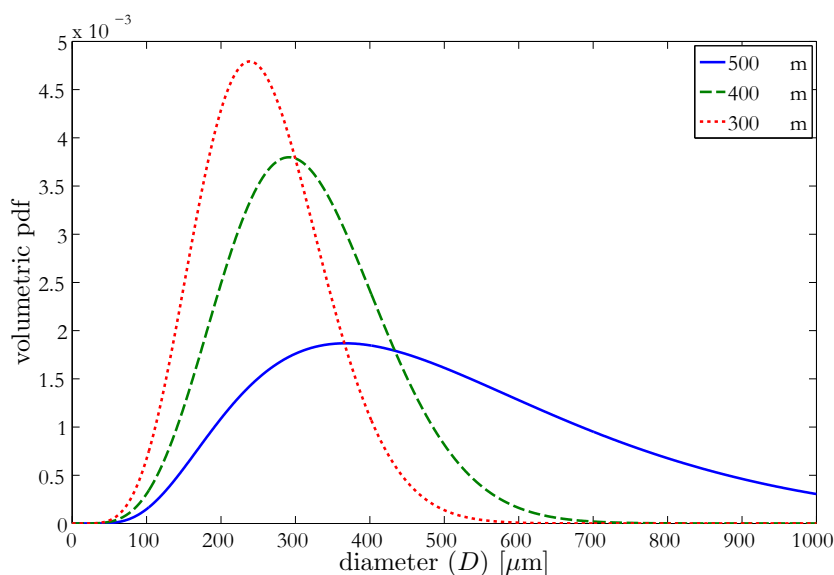


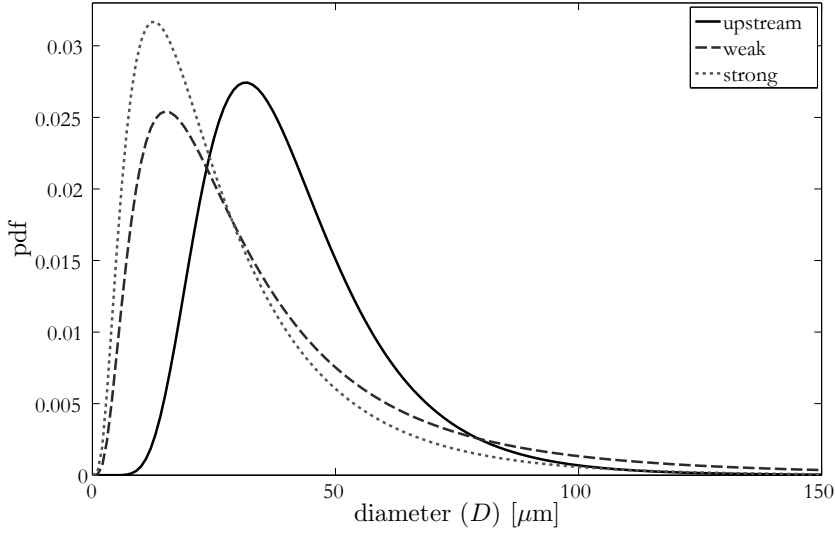
Figure 6.5: Fits of experimentally measured droplet sizes downstream of the weak swirl element. Three different median droplet sizes in the feed were tested for $10 \text{ m}^3/\text{h}$ at an oil cut of 25 %.

of view of the endoscope and those droplets can therefore not be measured. We see that the size downstream of the swirl element is very large for the weaker element, some break-up occurs, but the critical size limit of 1.4 mm seems to correspond with these results. For the larger swirl element, the largest observed droplets are significantly smaller than the largest expected droplet size (1.3 mm). This can be caused by the additional shear stress at the wall, since the larger swirl element contains much more wall surface than the smaller swirl element.

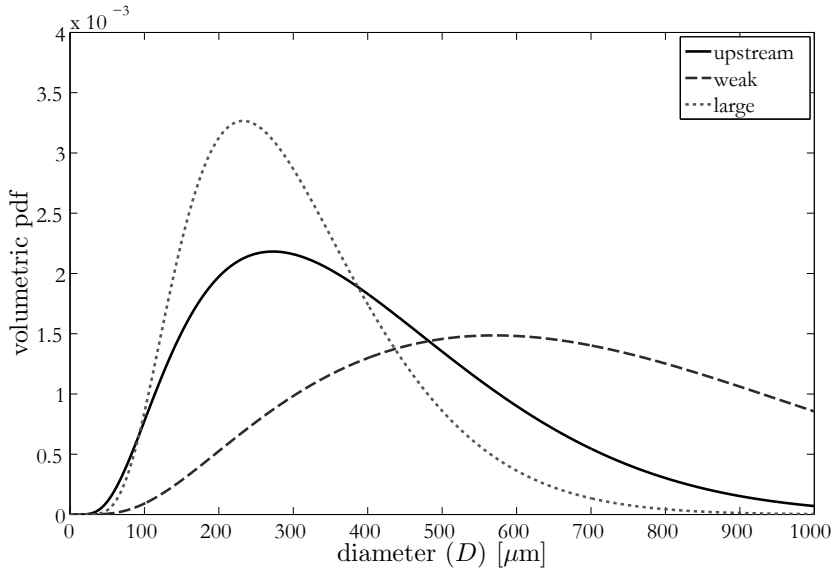
Trend for droplet size

The theoretical background provided at the beginning of this section deals with the maximum stable droplet size and provides an upper limit for the droplet size. For practical purposes, the droplet size of the largest volume fraction is most important, since they represent the largest volume stream that needs to be separated. The models discussed in this work do not provide a conclusion on the mean of the volumetric droplet PDF. Experimental work, however, does provide the median value.

Figure 6.7 compares the median of the droplet size as function of the maximum azimuthal velocity. The graph is composed out of measurements performed for three different swirl elements: the initial swirl element (73°), the weaker swirl element (62°) and the large diameter swirl element with tapering (equivalent to 73°). Based on the results, it seems that the results of the three swirl elements follow the same trend. The graph shows a bend at a velocity of about 4 m/s. Below that velocity, the median of the droplet size is very sensitive for changes in the maximum azimuthal



(a) PDF of the *number* of droplets upstream and downstream of the initial and weaker swirl element. Flow rate: $56 \text{ m}^3/\text{h}$, oil concentration in the feed: 0.25. The number is chosen to express the small difference in median size more clearly.



(b) PDF of the volume fraction per droplet size, for two different swirl elements. Flow rate: $10 \text{ m}^3/\text{h}$, oil concentration in the feed: 0.25. The weak swirl element shows significant coalescence just downstream of the swirl element.

Figure 6.6: Break-up by different swirl elements.

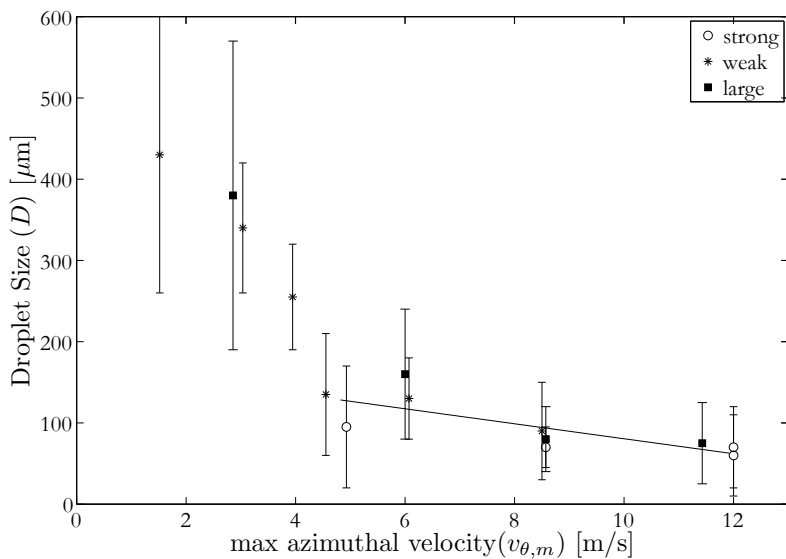


Figure 6.7: Droplet size in the swirling flow as function of the maximum azimuthal velocity in the swirl element for the available droplet sizing datasets. Error bars indicate the standard deviation in the droplet size distribution function. Solid line indicates fit of equation 6.8.

velocity. For velocities larger than 4 m/s, the sensitivity is smaller and there seems to be a linear dependence of the median droplet size on the maximum azimuthal velocity present in the system. The drawn linear fit is:

$$D_{\text{median}} = -8v_{\theta, \text{max}} + 160 \quad (6.8)$$

with D_{median} the median droplet size in μm and v the maximum azimuthal velocity in m/s.

6.3 Droplet coalescence inside the cyclone

During their stay in the axial cyclone, droplets will break and coalesce due to the forces caused by the fluid flow. To quantify the net effects, the droplets size distribution was measured at four distinct positions in the cyclones, see figure 6.8:

1. upstream of the swirl element;
2. downstream of the swirl element, but upstream of the outlets - the results are spatially averaged. The disturbances of the flow pattern do not allow an accurate measurement of the gradient in droplet size distribution within the swirling flow.
3. in the Heavy Phase Outlet stream, 60 cm downstream of the actual outlet.
4. in the Light Phase Outlet stream, 30 cm downstream of the actual outlet.

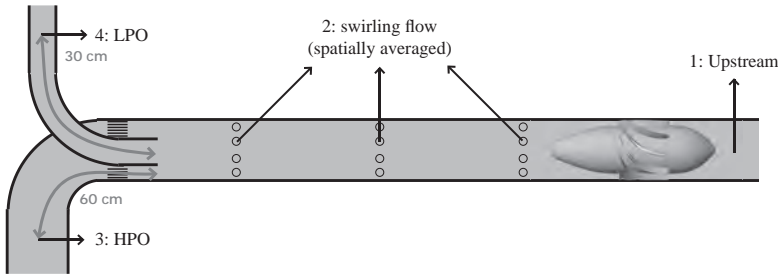


Figure 6.8: Measurement locations for the endoscope-based droplet sizing method.

Figure 6.9(a) compares the four different positions and leads to the following factual observations:

- the smallest droplet size downstream of the swirl element is smaller than upstream of the swirl element.
- downstream of the swirl element there is an increase in the volume fraction of larger droplets
- comparing both outlets, the smaller droplets are more represented in the lighter phase outlet and the larger droplets more in the heavy phase outlet.

The shear in the swirl element will break the droplets, as discussed in section 6.2, this explains why the smallest droplet size downstream of the swirl element is smaller than the smallest droplet size upstream of the swirl element. However, there must also be coalescence events, since the volume of large droplets increases. From the available experimental dataset, we can not conclude where these events occur.

Downstream of the swirl element, the fraction of larger droplets increases slightly. This indicates coalescence takes place. Despite the high velocity of the system, different droplets merge to larger ones.

Based on the results of chapter 5, we would expect the larger droplets to be present in the center region at the outlet and the smaller droplets to be spread around over the complete cross section, leading to a higher fraction large droplets in the LPO. This is different from our experimental results. The difference can be caused by droplet break-up at the pickup tube wall, or by zones with high shear in the tube before measuring the droplets in the LPO. During these measurements, no phase inversion was observed; phase inversion leads to very bright droplets instead of dark droplets due to the refractive indices of oil and water.

Figure 6.9(b) compares the droplet size distribution in the swirling flow region with the flow rate-averaged droplet size distribution in both outlets. This averaging procedure is based on the flow split: 25 % of the LPO distribution plus 75 % of the HPO droplet size distribution. The average droplet size in both outlets is smaller than the average droplet size in the swirling flow region. Therefore, break-up events dominate over coalescence events in the downstream section of the swirltube or at the beginning of the pickup tube.

6.4 Conclusion

Inlet conditions The droplet size for two-phase turbulent pipe flow is well predictable. We tested the model by Hinze [37] and saw good comparability. The droplet sizes upstream of the cyclone can be controlled via two types of valves. A membrane valve reduces the droplet size stronger than a ball valve, where the ball valve produces a larger spread than the membrane valve.

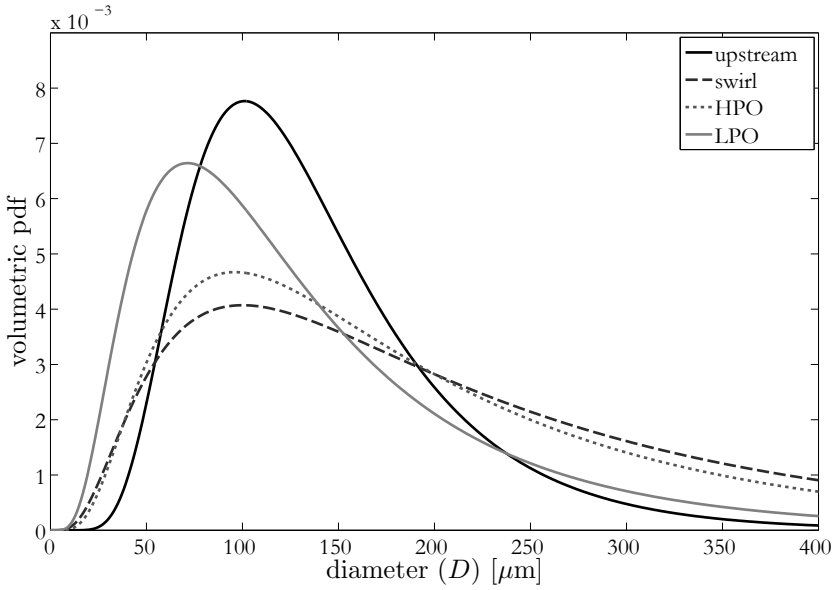
Break-up due to swirling flow Droplet break-up in swirling flow can be accounted for by two major effects: (i) acceleration of the liquid at the swirl element and (ii) acceleration of the droplet in the radial direction due to centrifugal buoyancy forces. Theory applied to both effects delivers a maximum droplet size that can withstand the flow. This maximum size agrees with experimental data reasonably. From experimental data, we derived a relation for the median droplet size D_{median} in μm as function of the maximum azimuthal velocity $v_{\theta, \text{max}}$:

$$D_{\text{median}} = -8v_{\theta, \text{max}} + 160 \quad (6.9)$$

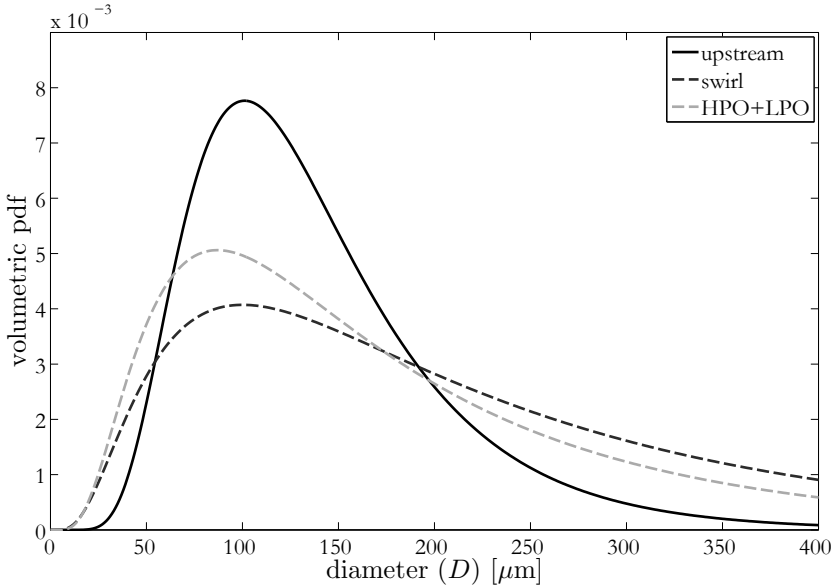
This relation holds for $v_{\theta, \text{max}} > 4 \text{ m/s}$ and can be used to predict the resulting droplet size distribution when designing a new swirl element. Results are not conclusive what effect causes this break-up, whether the swirl element itself or the swirling flow are the cause.

Outlets In contrast to the concept that larger droplets are more easily accelerated to the center than smaller droplets, we find that the droplets in the light phase outlet are on average smaller than in the heavy phase outlet. For this phenomenon, no satisfactory explanation has been found.

Considering the weighed-averaged droplet size distribution in both outlets, the droplets are on average smaller in the outlet than just downstream of the swirl element. This indicates droplet break-up in the swirling flow.



(a) HPO and LPO separate



(b) flow rate-averaged sum of the outlets

Figure 6.9: Fits of experimentally measured droplet size distributions for four positions in the cyclone equipped with the weak swirl element: upstream of the swirl element, downstream of the swirl element in the swirling flow, downstream of the HPO and downstream of the LPO.

CHAPTER 7

Analysis of swirl separation performance

The preceding chapters 4, 5 and 6 looked at specific parts of the in-line axial cyclone to increase understanding. This chapter focuses on the optimization of the geometry by comparing the separation result for changes in: swirl element, length, pick-up tube diameter. Operational effects are discussed in section 7.2.

The method to assess separation efficiency which is used in this chapter is introduced in section 3.3.

7.1 Geometric optimization

7.1.1 Swirl element type

The three different swirl elements as used in this research (see section 4.2) were compared with respect to separation efficiency at their nominal conditions: for the strong and weak swirl element this is 56 m³/h flow in a 170 cm swirltube with a 50 mm pick-up tube. These results are compared with the large swirl element at 30 m³/h flow for a 170 cm swirl tube and a 50 mm pick-up tube.

Figure 7.1(a) displays the oil concentration in the outlets for the condition that the flow split was kept equal to the oil concentration in the feed. The most significant difference is found for the region where c_{in} varies between 0.1 and 0.3. The weak swirl element performs best, then the strong swirl element and the large swirl element shows a relative poor performance. Considering the dispersed efficiency (see equation 3.10) in figure 7.1(b), the weak swirl element performs better on bulk separation for all conditions. The large swirl element performs for all conditions worse than the others.

Figure 7.1(a) and 7.1(b) also depict numerical separation predictions based on numerical simulations by Slot [13]. The Euler-Euler model (see section 3.2) results show a comparable trend for the oil concentration in the outlets: a higher oil cut in the feed leads to more oil in the HPO and less water in the LPO. The predicted separation is, however, much higher. This can be seen from the dispersed efficiency graph, where all three numerical data points over predict the lab results. Parameters

that can cause this wrong predictions are: (i) underestimation of turbulent dispersion, (ii) the lack of droplet breakup models or (iii) insufficient ensemble-averaged drag relations.

The before mentioned performance difference could have been expected based on results in figure 5.10(b). In this figure, the window of separation is largest for the weak swirl element (55 - 120 μm), then for the strong swirl element and negligible for the large swirl element (around 60 μm). The droplet size distribution fed to the system is equal for both the strong and weak swirl element. The droplet size distribution that enters the large swirl element has a larger average diameter.

Dependence on oil cut

Figure 7.1(a) relates the oil concentration in the feed to the oil concentration in both outlets: HPO and LPO. For all swirl elements, the concentration of oil in the HPO relates severely to the oil concentration in the feed, where up to 10 vol % of oil is removed. This stream could be further treated in the water treatment system.

The Light Phase Outlet (LPO) does not show a proportionality to the oil concentration in the feed. Especially for the weak swirl element, the volumetric oil concentration c_{out} is steady between 0.55 and 0.65 for a range in the feed oil concentration of 0.15 to 0.55. No phase inversion in the LPO was observed in this range. This LPO stream is suitable for the oil treatment system.

The large swirl element has a more gradual increase in the LPO c_{out} as function of the feed oil cut compared to the weak swirl element. This indicates the necessity for more processing of its output stream.

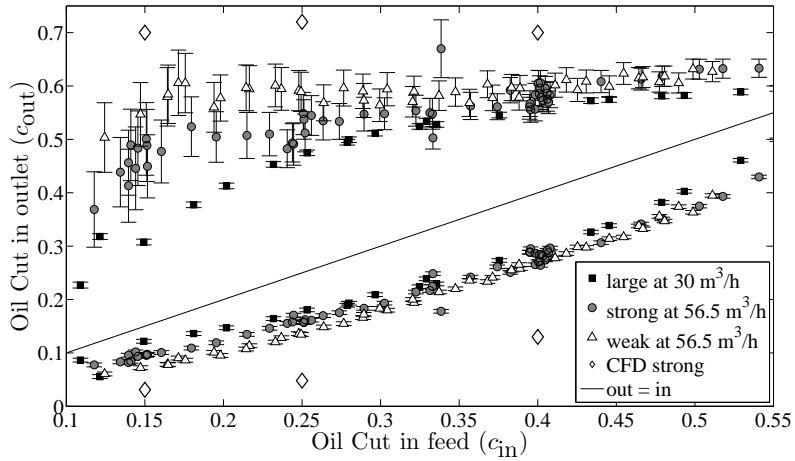
Tapering

From LDA measurements in single phase brine, we know that the swirl intensity decreases over length and therewith the separating force on the droplets decreases over length. As introduced in section 4.2.4 a reduction in tube diameter in the downstream direction can be used to increase the azimuthal velocity and therewith to compensate for the reduction of swirl strength due to drag. However, within this research, we use only tapering for the short tube section immediately downstream of the large swirl element.

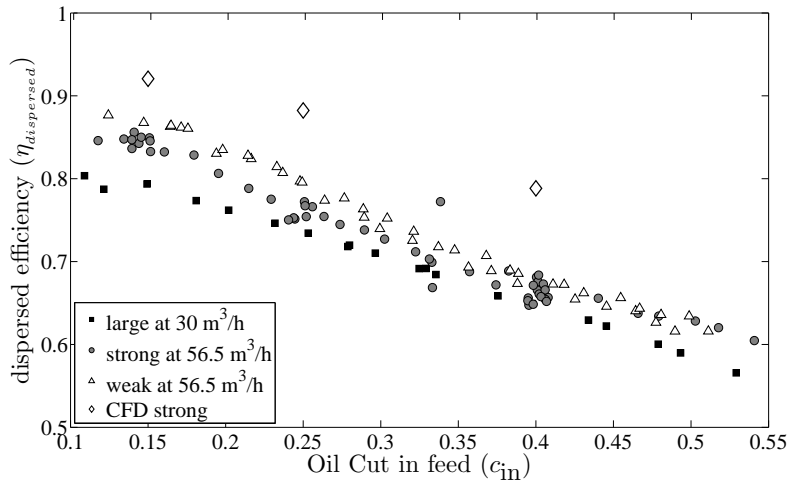
From this work, we cannot discriminate between the effect of the large swirl element with less azimuthal acceleration and the relatively rapid tapering. Although the liquid acceleration itself in the taper should not be that large that it can break droplets, high shear can occur due to recirculation patterns that might break droplets. Due to the opaque nature of the tube, this phenomenon could not be investigated. The high pressure drop over the combination of large swirl element and taper indicates regions with high shear.

7.1.2 Swirl tube length

Separation by an axial cyclone depends in various ways on the length of the swirl tube. (i) The residence time in the swirl tube is proportional to its length (ii) The



(a) Oil concentration in both outlets.



(b) Dispersed efficiency.

Figure 7.1: Separation results for the three different swirl elements for a pick-up tube of 50 mm and a swirltube length of 170 cm. The flow split is equal to the oil concentration in the feed. The weak swirl element shows best performance of the three tested swirl elements. CFD results of Slot [13] for the strong swirl element at 56.5 m³/h.

swirl intensity decays over length, where turbulence intensity does not. The combination of both effects means that there should be an optimum for the length.

A change in length of the swirltube is also very likely to change the upstream pointing flow in the center of the tube. This flow is namely driven by the pressure difference in the center region between the point just downstream of the swirl element and at the upstream side of the pick-up tube. For longer swirltubes, the pressure gradient per unit of length is smaller and therewith the back flow should be smaller. This has not been tested experimentally within this research.

Based on coarse tests in steps of more than 50 cm, it was found that the optimal length should be between 1.5 and 2.0 m. Figure 7.2(a) compares four different lengths of the swirltube in combination with the weak swirl element and a 50 mm pick-up tube. The lengths of 150 and 170 cm seem to perform best, where the difference is very small. This is confirmed by the dispersed efficiency in figure 7.2(b). For other tests, the length of 160 or 170 cm is therefore used.

7.1.3 Pick-up tube diameter

At the downstream side of the swirltube, the liquid streams are physically separated with a pick-up tube. The lighter phase ought to flow through the pick-up tube, the heavy phase ought to flow through the surrounding annular region.

The size of the pick-up tube affects separation in multiple ways. An increase in the pick-up tube diameter reduces stability of the flow pattern. This has not been quantified with LDA measurements, but is observed as a reduction in the stability of the flow split during tests. For a larger pick-up tube, more active steering in valve w-F (see figure 2.1) is required to maintain a constant flow split.

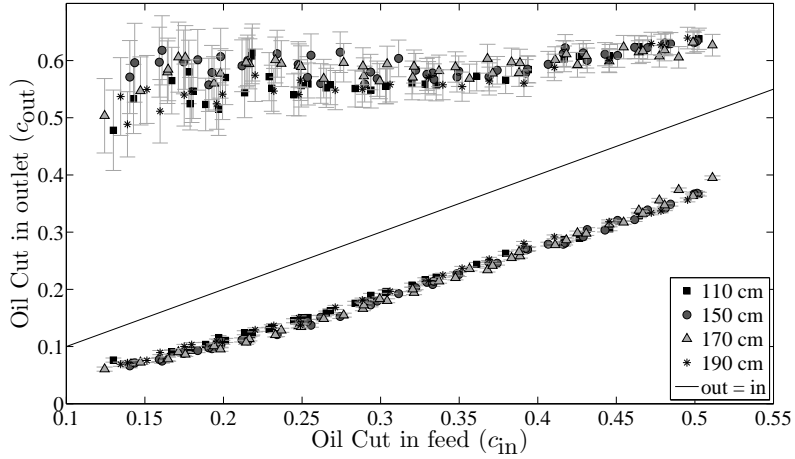
First order model A simple model for a liquid-liquid cyclone is that centrifugal forces sweep all oil droplets to the center of the tube. The cross-sectional area in the center of the tube should then scale with the volumetric oil fraction in the inlet of the system. If the pick-up tube has the same diameter as the diameter of this oil kernel, the dispersed separation efficiency should be 100 %. If the pick-up tube is smaller, some oil leaks to the HPO where the LPO still should have 100 % of oil. If the pick-up tube diameter is too large, some water will enter the LPO, where the HPO should be 100 % water.

Efficiency results Figures 7.3 and 7.4 relate pick-up tube diameter to the separation efficiency. In figure 7.3(b), the 70 mm performs worst, than the 60 mm and 50 mm provides best separation. Figure 7.4(b) shows that 50 mm separates better than 60 mm, however, 40 mm does not show much difference with 50 mm.

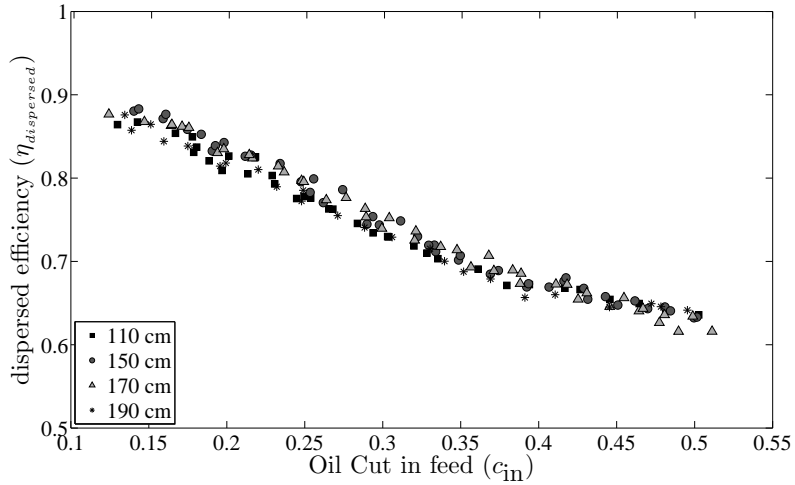
The results do not show an increase in selectivity for a changing pick-up tube diameter. The oil cut in the HPO does not decrease for increasing pick-up tube.

In figure 7.4, at about $c_{in} = 0.33$, two samples deviate from the general trend. These samples were most likely obtained during transient conditions in the flow rig, where the total inflow and outflow of oil were not yet steady state.

Model falsification The first order model introduced above suggested that an increase in the pick-up tube diameter would capture a volumetric amount of oil. The



(a) Oil concentration in both outlets.



(b) Dispersed efficiency.

Figure 7.2: Separation results for the weak swirl element at $56.5 \text{ m}^3/\text{h}$ for four different swirl tube lengths, measured from the swirl element tail to the upstream side of the pick-up tube, pick-up tube diameter was 50 mm.

results do falsify this hypothesis. In contrast, a pick-up tube with a smaller diameter leads to a larger oil capture efficiency. An increase in stability of the vortex and therewith of the oil kernel explains this behavior. The optimal situation is therefore such that there is an axial velocity difference between the two outlets.

7.2 Operational optimization

7.2.1 Flow split

For the results presented in section 7.1 a constant flow split was chosen according to $FS = c_{in}$. This choice was made for the simple reason that only for this flow split perfect separation can occur: all oil through the LPO and all water through the HPO. In this section, we investigate the influence of the flow split on separation performance.

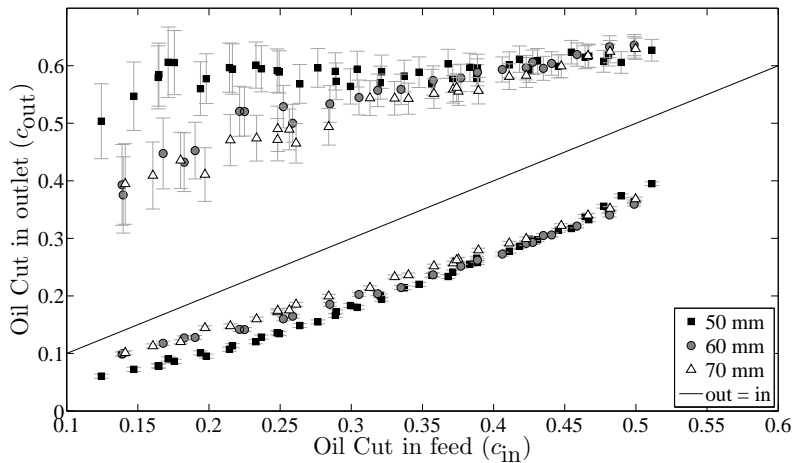
For three different oil concentrations, 0.15, 0.25 and 0.40, the separation efficiency was determined for a range of flow splits. Figure 7.6(a) shows the dilute efficiency (equation 3.9). This efficiency expresses the amount of oil captured in the LPO. As can be easily understood, a higher flow split means more flow through the LPO and therewith a larger part of the total oil flow in the system.

The dispersed efficiency (equation 3.10) considers the volumetric liquid flows through the “correct” outlets: if all oil runs through the LPO and all water through the HPO, the dispersed efficiency is 100 %. Figure 7.6(b) shows the general trend that a smaller flow split leads to a higher dispersed efficiency. Considering figure 7.5 we see mainly an increase in the oil concentration for the LPO for smaller flow split. The maximum dispersed efficiency is obtained for all cases where the flow split is smaller than or equal to the oil concentration in the feed. In figure 7.6(b) this region is indicated with a dashed line. Reduction of the flow split below c_{in} is not profitable, therefore $FS = c_{in}$ seems optimal for most applications.

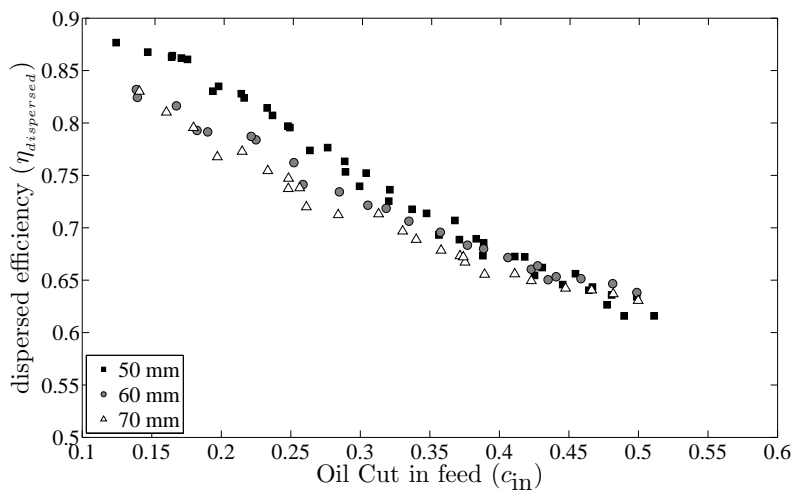
Numerical results by Slot [13] with the Euler-Euler model (see section 3.2) show the same trend for both the dilute and dispersed efficiency. The efficiency is, however, over predicted for all cases. Parameters that can cause this wrong predictions are: (i) underestimation of turbulent dispersion, (ii) the lack of droplet breakup models or (iii) insufficient ensemble-averaged drag relations.

Different swirl elements The hypothesis that the optimum for the dispersed efficiency is reached for the condition $FS = c_{in}$ was tested for the strong and weak swirl element. Figure 7.7 compares the strong and weak swirl element for an oil cut of 25 % in the feed. We see that the trend is comparable, where the weak swirl element obtains a slightly higher efficiency.

Different droplet sizes Figure 7.8 compares the efficiency as function of the flow split for two different input cases: (i) $10 \text{ m}^3/\text{h}$ with 10 % oil dispersed in droplets with a mean diameter of over $500 \text{ }\mu\text{m}$ and (ii) $10 \text{ m}^3/\text{h}$ with 25 % oil dispersed in droplets with a mean diameter of $100 \text{ }\mu\text{m}$.

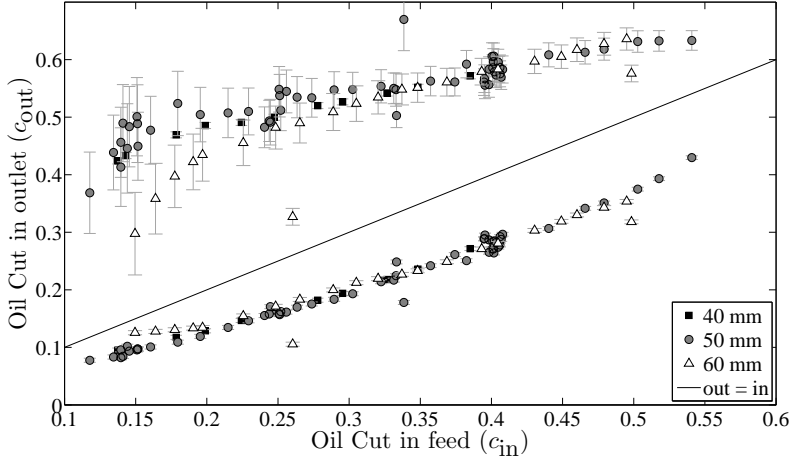


(a) Oil concentration in both outlets.

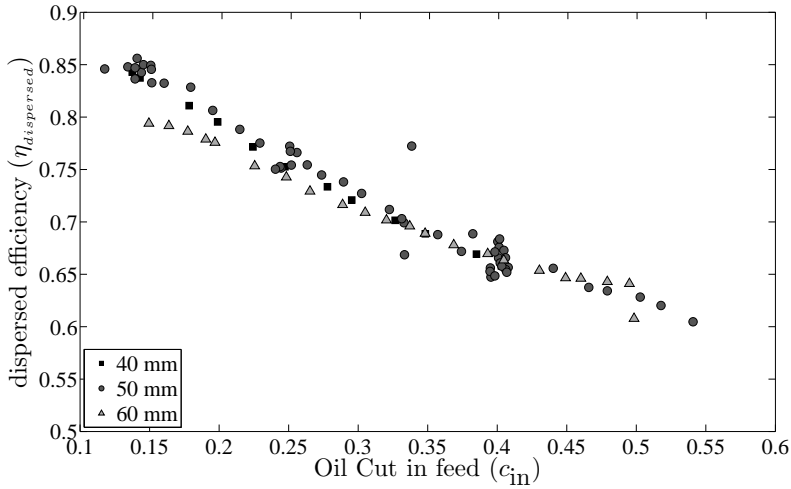


(b) Dispersed efficiency

Figure 7.3: Separation results for the weak swirl element at $56.5 \text{ m}^3/\text{h}$ for three different pick-up tube diameters, for a swirltube length of 170cm.



(a) Oil concentration in both outlets.



(b) Dispersed efficiency

Figure 7.4: Separation results for the strong swirl element at $56.5 \text{ m}^3/\text{h}$ for three different pick-up tube diameters, for a swirltube length of 170cm.

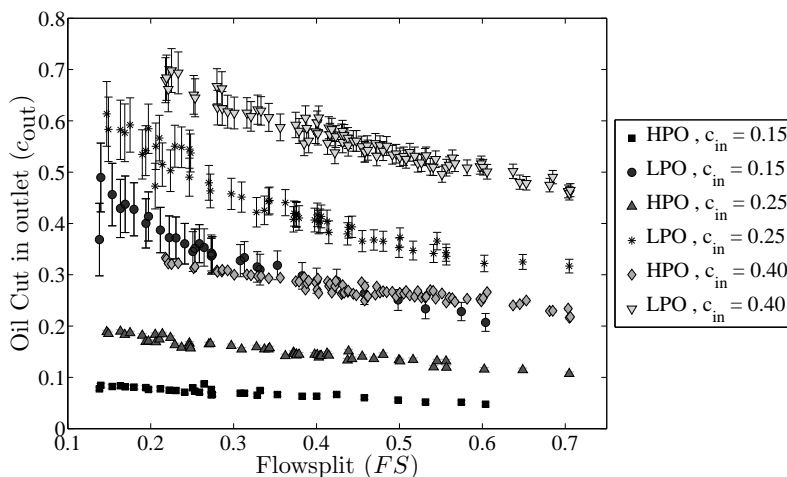


Figure 7.5: Oil concentration in both outlets for three different oil cuts in the feed as function of the flow split. Strong swirl element, $\Phi = 56.5 \text{ m}^3/\text{h}$, tube length: 170 cm, pick-up tube diameter: 50 mm

As expected, the efficiency is lower for the smaller droplets. We can see, however, from figure 7.8 that the bend for the dispersed efficiency at $FS = c_{in}$ also exists for these cases.

Conclusion Based on the different cases tested in this chapter, the hypothesis is supported that for bulk separation, the best setting is to make the flow split between the HPO and LPO equal to the oil cut in the feed. For specific needs, a shift in flow split can promote different behavior. We do, however, not see complete oil removal from the water stream at nominal design conditions ($100 \text{ } \mu\text{m}$ droplets at $56 \text{ m}^3/\text{h}$).

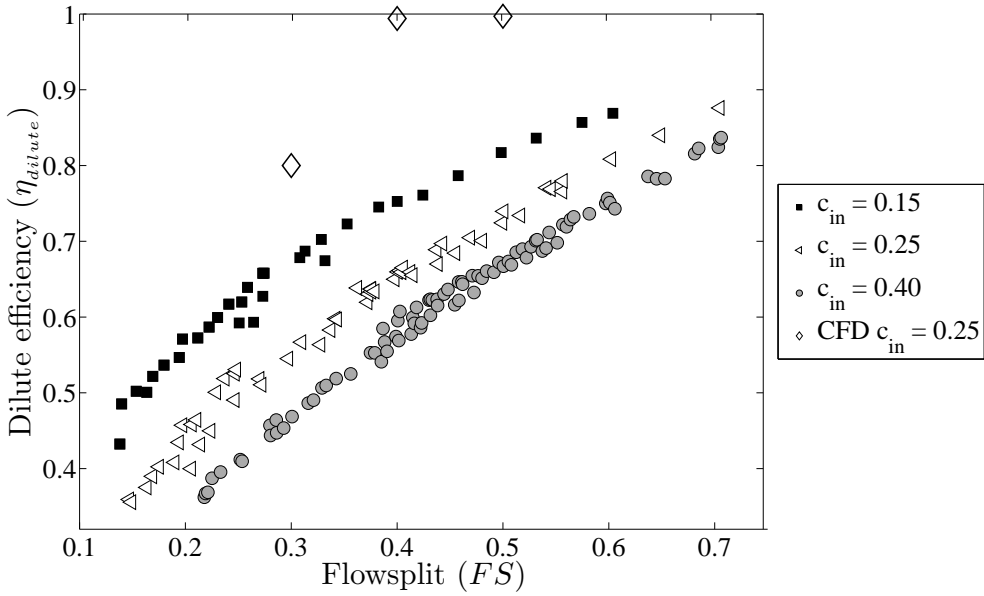
7.2.2 Flow rate

In this section, we look at the effect of flow rate and therewith velocity on the separation performance of the different axial cyclones as used in this thesis. Since the flow rate affects the droplet size distribution in a turbulent pipe flow, a variation in the flow rate will also lead to a change in the droplet size distribution fed into the system. This effect was addressed by reduction of the droplet size using a diaphragm valve.

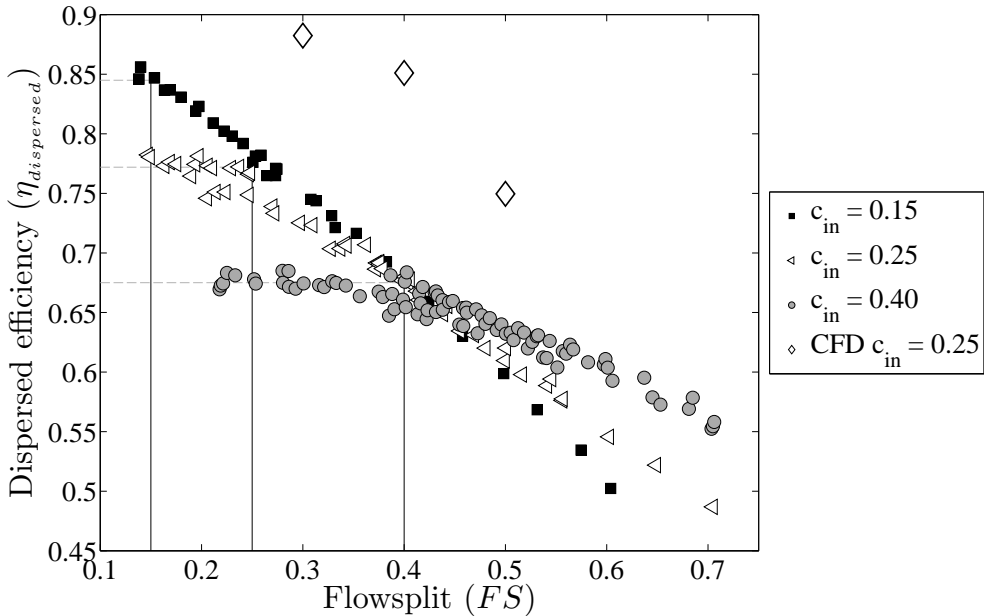
Droplet size depending on flow rate The flow rate has effect on the separation performance. Figure 7.9 shows three different flow rates in the large swirl element. It is clear from these results that a lower flow rate and therewith a lower velocity is beneficial for separation performance.

Different effects account for the increase in separation performance:

1. due to the lower flow rate, the droplets upstream of the swirl element are larger;



(a) Dilute efficiency.



(b) Dispersed efficiency.

Figure 7.6: Separation results as function of the flow split for the strong swirl element. $\Phi = 56.5 \text{ m}^3/\text{h}$, three different oil cuts in the feed, tube length: 170 cm, pick-up tube diameter: 50 mm. Numerical results by Slot [13].

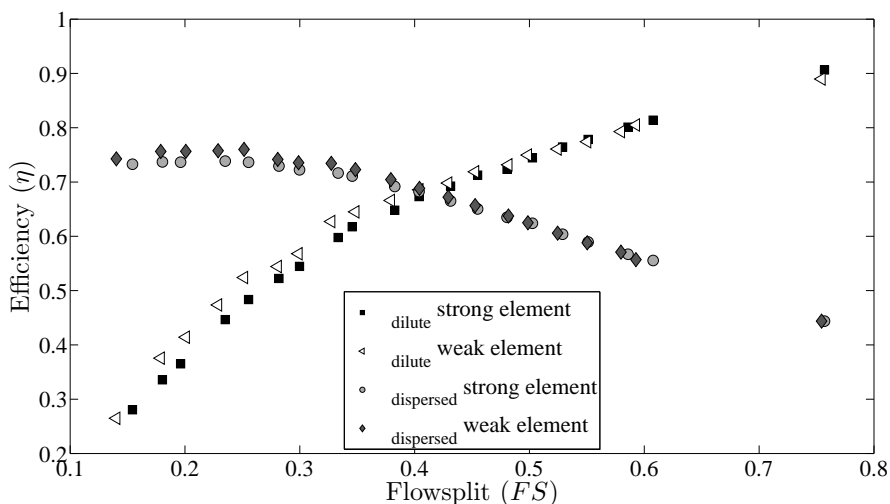


Figure 7.7: Separation results as function of the flow split for the strong and weak swirl element. $\Phi = 56.5 \text{ m}^3/\text{h}$, $c_{\text{in}} = 0.25$ tube length: 170 cm, pick-up tube diameter: 50 mm.

2. the lower axial velocity leads to a lower velocity along the vanes of the swirl element and a lower azimuthal velocity in the swirltube. Therewith, the droplet breakup during the swirl generation is reduced;
3. the centrifugal acceleration of dispersed droplets is reduced due to the lower azimuthal velocity.

Considering figure 5.11(a), we see that a lower flow rate shifts the window of separation towards larger droplets. This graph does not consider the larger droplet sizes upstream caused by the lower flow rate. From the observations presented in this section, we learn that for a decreasing flow rate, the average droplet size upstream increases more than the shift of the separation window, being beneficial for separation performance. For a low flow rate, the droplets downstream of the swirl element are larger compared to a high flow rate. Due to the proportionality of the drag force with surface (D_d^2) and of the centrifugal buoyancy force with volume (D_d^3), we easily see the advantage of larger droplets, even at a lower azimuthal velocity.

Constant droplet size In the previous section 7.2.2, we saw that a lower flow rate leads to larger droplets upstream and that it is beneficial on separation behavior. For liquid-liquid flows, the separation equipment should not reduce the droplet size below the droplet size of the feed, since larger droplets tend to separate more easily than smaller droplets.

To study the effect of flow rate with constant droplet size, a membrane valve was used to reduce the droplets upstream of the swirl element at lower flow rates. Section 6.1.2 shows the resulting droplet size distributions fed to the swirl element.

Figure 7.10 shows the separation behavior at three different flow rates where the droplets sizes are on average equally sized at $100 \mu\text{m}$. Due to the differences in the

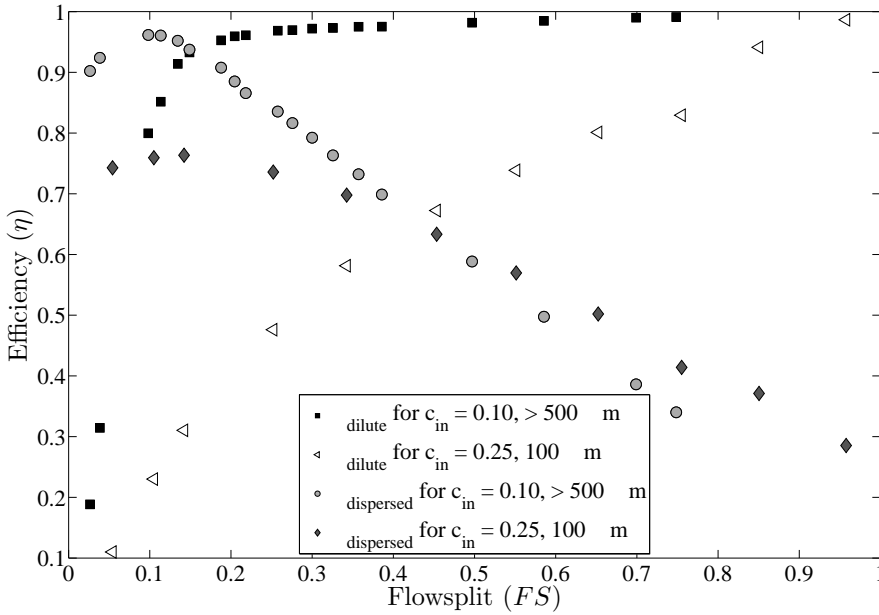


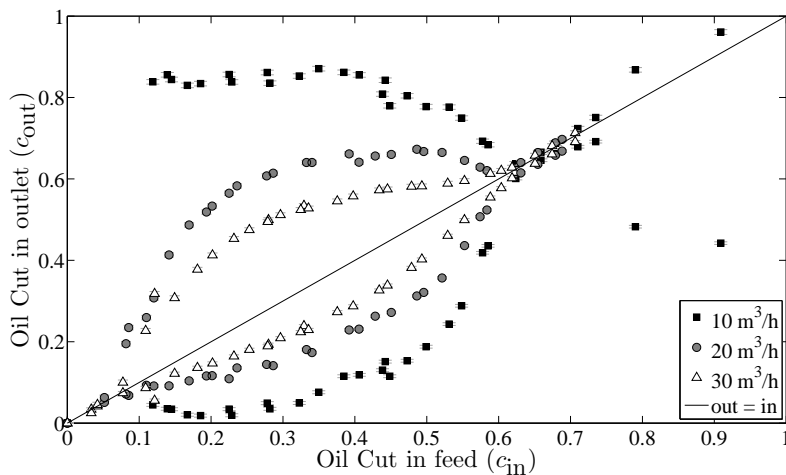
Figure 7.8: Separation results as function of the flow split for the large swirl element. $\Phi = 10 \text{ m}^3/\text{h}$, tube length: 160 cm, pick-up tube diameter: 50 mm. A case with 10 vol. % oil and large droplets is compared with 25 vol.% oil and $100 \mu\text{m}$ droplets.

breakup for the various flow rates, the droplet size distributions are different (see section 6.1.2).

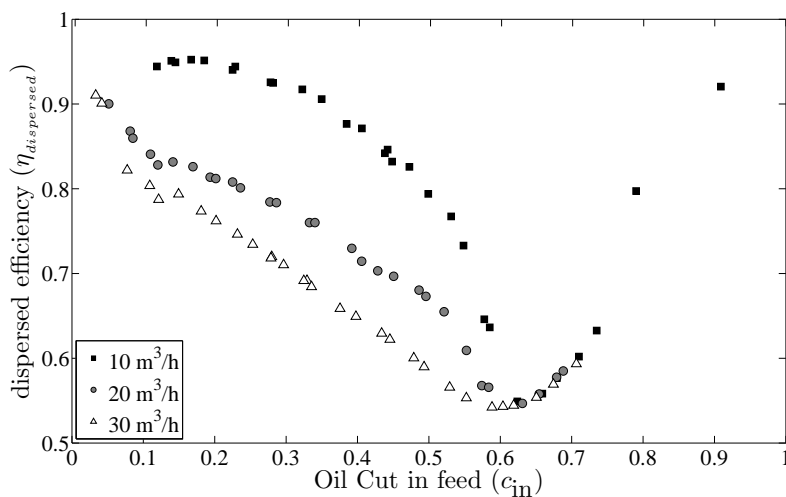
The droplets of $100 \mu\text{m}$ are broken at the swirl element at $56 \text{ m}^3/\text{h}$ to about $60 \mu\text{m}$ on average. For $10 \text{ m}^3/\text{h}$ and $40 \text{ m}^3/\text{h}$ they are hardly broken and remain at $100 \mu\text{m}$. In figure 7.10 we can therefore make two comparisons:

- Effect of azimuthal velocity on separation for constant droplet size downstream of the swirl element ($10 \text{ m}^3/\text{h}$ vs $40 \text{ m}^3/\text{h}$). For the $40 \text{ m}^3/\text{h}$, there is a small increase in separation over the $10 \text{ m}^3/\text{h}$ case.
- Effect of azimuthal velocity on separation for known difference in droplet size downstream of the swirl element ($100 \mu\text{m}$ for $40 \text{ m}^3/\text{h}$ vs $60 \mu\text{m}$ for $56.5 \text{ m}^3/\text{h}$). The centrifugal accelerating body force per unit of volume increases with a factor of $(56.5/40)^2 = 2$, where the average drag per unit of volume increases with $100/60 = 1.7$. Based on this order of magnitude comparison, the separation for $56.5 \text{ m}^3/\text{h}$ should not be significantly improved over $40 \text{ m}^3/\text{h}$, which is in contrast with observations.

Conclusion If the upstream velocity of the liquid-liquid flow is low and the flow regime contains large dispersed droplets or liquid chunks, a lower flow rate and therewith centrifugal acceleration is preferred, at least within the operational boundaries used within this research.

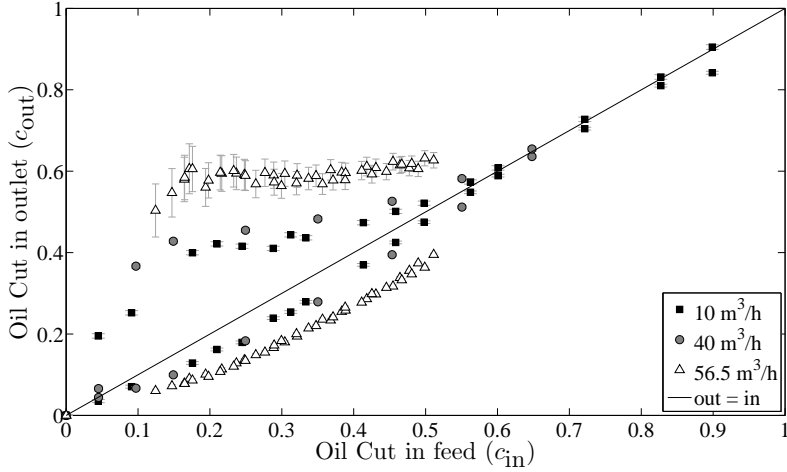


(a) Oil concentrations in the output

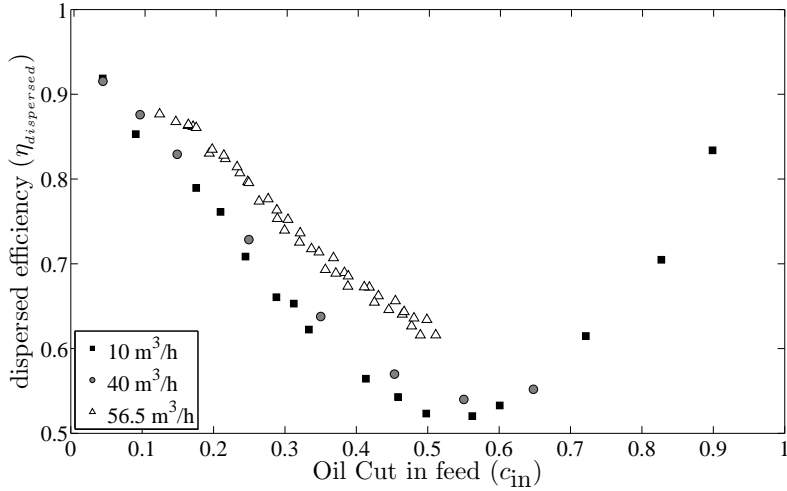


(b) Dispersed efficiency

Figure 7.9: Effect of flow rate on separation behavior for the large swirl element, a swirltube of 160 cm and a pick-up tube of 50 mm. The upstream droplet size depends on the flow rate, average droplet size for $10 \text{ m}^3/\text{h}$ was $500 \mu\text{m}$, for $20 \text{ m}^3/\text{h}$ $400 \mu\text{m}$ and for $30 \text{ m}^3/\text{h}$ $250 \mu\text{m}$. Viscosity measurements at $c_{in} > 0.6$ show a high viscosity in the LPO which is related to phase inversion. The inversion of water-continuous to oil-continuous flow explains the drop in phase separation around $c_{in} = 0.7$.



(a) Oil concentrations in the output



(b) Dispersed efficiency

Figure 7.10: Effect of flow rate on separation behavior for the weak swirl element, a swirltube of 160 cm and a pick-up tube of 50 mm. The upstream droplet size were kept approximately constant at $100 \mu\text{m}$.

For small droplets fed to the cyclone, best separation performance is obtained at a maximum azimuthal velocity, as long as the droplet size is not reduced significantly.

The optimal azimuthal velocity for separation seems to be that velocity where the droplet size to which the droplets are broken is equal to the droplet size upstream. This hypothesis was tested for a limited range of cases as was available within this research.

- For a constant droplet size with a mean of $100\ \mu\text{m}$, we see that an increase in swirling velocity is favorable.
- For $56.5\ \text{m}^3/\text{h}$ flow, we see an increase in performance for a reduction of swirl strength, see figure 7.1(a). The feed consists out of average $100\ \mu\text{m}$ droplets, the strong swirl element reduces droplets at the given flow rate to $40\ \mu\text{m}$, the weak swirl element to $60\ \mu\text{m}$. No swirl element was available with a droplet size reduction to $100\ \mu\text{m}$ at the given flow rate.

It is best to operate at a flow rate which corresponds to the droplet size produced by that specific flow rate.

7.2.3 Droplet size

In the previous section (7.2.2) we saw that the droplet size distribution has a significant effect on separation performance. Turbulent dispersion breaks droplets in pipe flow (see section 6.1.1), which puts a maximum at the droplet size for given flow rate. To study the effect of droplet size on separation, we measured the separation performance for the lowest flow rate used in this work ($10\ \text{m}^3/\text{h}$) for droplets with a median size of 100 , 300 and $500\ \mu\text{m}$.

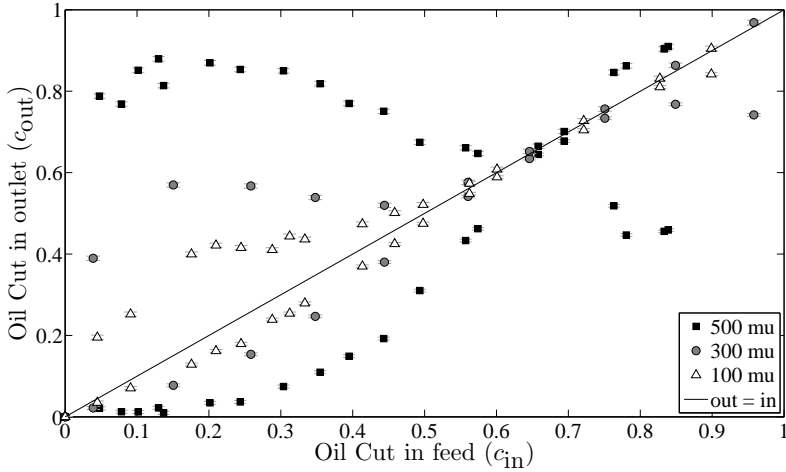
Figure 7.11 shows the huge effect on separation. For a flow rate of $10\ \text{m}^3/\text{h}$, the weak swirl element does not significantly breaks droplets of $500\ \mu\text{m}$ and smaller (chapter 6, figure 6.5). This graph illustrates the need to avoid droplet breakup as much as possible, since smaller droplets are harder to separate than larger droplets.

7.2.4 Phase inversion

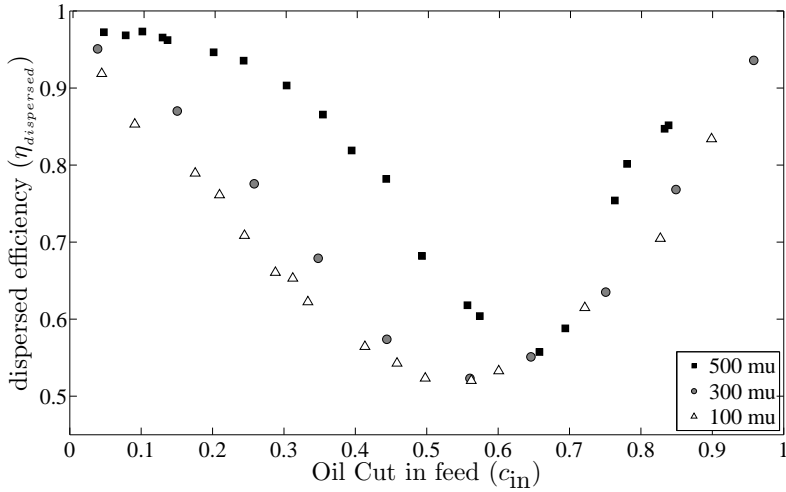
During the tests, such as in figure 7.9 the oil cut in the flow was varied between 0.05 and 0.9 . The dispersed efficiency curve has a dip around $c_{\text{in}} = 0.55$ and the oil concentration in HPO and LPO is almost equal for the region where c_{in} ranges between 0.55 and 0.8 .

The most likely explanation for this dip in performance in the indicated region is phase inversion, where (a part of) the dispersed system converts from an oil-in-water emulsion to a water-in-oil emulsion, the structure of the fluids changes. One of the observed effects is a peak in viscosity and a step in the electrical conductivity of the liquid.

In this research, we measured the viscosity with an Endress+Hauser Promass 83I Coriolis flow meter in the LPO, which measures the fluids response to a torsional moment. Since a dispersed two-phase system does not necessarily behave like a Newtonian fluid, the viscosity measurement will be off with an unknown factor. However, it is certain that there is a certain proportionality.



(a) Oil concentrations in the output



(b) Dispersed efficiency

Figure 7.11: Effect of droplet size on separation behavior for the weak swirl element, a swirltube of 160 cm, a pick-up tube of 50 mm and a flow rate of $10 \text{ m}^3/\text{h}$. The upstream droplet size were reduced with a membrane valve to a distribution with the median indicated in the figure. The flow split was equal to the oil concentration in the feed. Large droplets yield a higher separation performance.

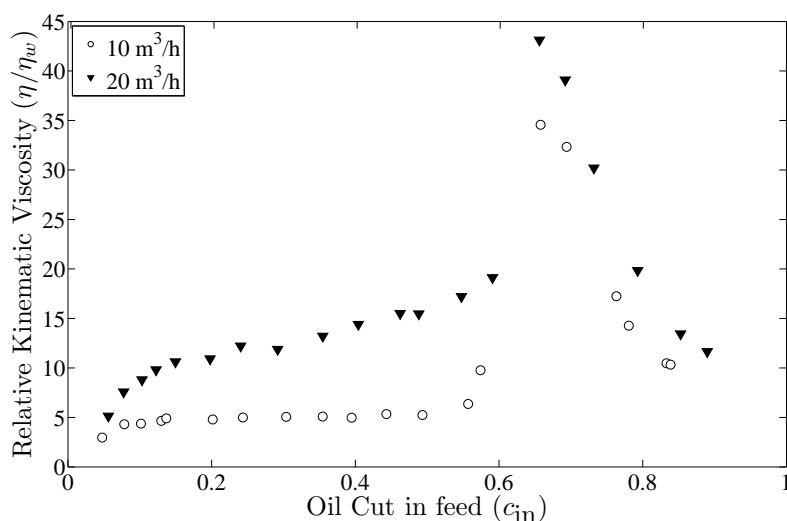


Figure 7.12: Measured viscosity of the mixture in the LPO as function of the oil cut at two different flow rates. Weak swirl element, 160 cm swirltube and 40 mm pick-up tube. The Flow split was chosen to be equal to the oil cut. Measurements are normalized using the measured viscosity of pure brine. No compensation has been applied for errors in the method of measurement in the Endress+Hauser Promass 83I.

Viscosity at the inversion point Figure 7.12 shows the normalized data for the kinematic viscosity in the LPO. The measured values were divided by the measured value for pure brine. Two different flow rates are compared. The graph shows a steeper increase as function of the oil cut for the higher (20 m³/h) flow rate compared to the lower (10 m³/h) flow rate. This can be caused by the smaller droplets created at higher velocities, where smaller droplets introduce more apparent viscosity.

For both cases, the viscosity peaks at an oil cut of 0.66 up to a measured value of 40 times the viscosity of brine. This should therefore be the point at which the phase inversion is occurring. During normal operation of a cyclone, one should avoid operation at these conditions, since they hamper separation, leaving the axial cyclone as mixing-only device.

The reason why the separation holds back at the phase inversion point is two fold:

1. The high viscosity dampens the swirling motion and therewith the centrifugal acceleration.
2. The drag of droplets moving in the radial direction is proportion to the liquid viscosity. A high viscosity leads to a lower separation quality.

As a consequence above a critical viscosity of the mixture, no separation is expected. This threshold at which separation stops seems to be a viscosity in the order of 20 times the viscosity of brine.

7.3 Static versus Rotating element

This section provides results obtained with a rotating swirl element - in a different flow rig than used for the rest of the work in this thesis. Details on this flow rig can be found in section 2.6. The following differences between the rotating swirl element rig and the rest of the work described in this thesis are found:

- **Tube diameter:** 50 mm for the rotating swirl element vs 100 mm for the static swirl element. The linear upstream velocities were matched.
- **Droplet size:** the droplet size distribution upstream was not measured for the rotating swirl element. From the colour of the mixture, the expectation is that the droplet size distribution had a larger average size for the rotating swirl element than for the static swirl element.
- **Swirl strength:** The swirl number generated by the rotating swirl element is not known. The velocity of the impeller tips is 7 m/s in the 50 mm tube. However, the slip between the impeller and the liquid is not predicted within the scope of the present research. Based on figure 6.7, we can be sure that this results into less droplet breakup than the static swirl element at 12 m/s. Further work could consider propulsion theory (of ships and aircrafts).

Figure 7.13 demonstrates better separation performance for the rotating swirl element. As mentioned above, conditions are not equal. Apparently, the moving nature of the rotating swirl element does not seem to introduce additional droplet breakup. Furthermore, we see that a lower azimuthal velocity in the swirl region is beneficial for separation performance. A smaller diameter reduces the distance required for a droplet to get separated. This effect is also advantageous for the tests with a rotating swirl element.

7.4 Conclusion

In this chapter, we compared the separation efficiency for different designs and different conditions of our in-line axial cyclone. If the flow rate and droplet size distribution are constant, then the design of the swirl element has most influence. The effect of the swirl element on separation performance is likely to be caused by the droplet breakup that occurs in the swirl element. The length of the swirl section has a relative mild effect on the separation quality, with an optimum in this research of a length $L/D = 16$. For the diameter of the pick-up tube, it seems that a smaller size is favorable within the range D_{pu}/D from 0.4 to 0.7.

During the operation of the cyclone, especially the fluid velocity has a large influence on separation performance. The origin of this strong correlation is droplet breakup, caused by the shear exerted on the droplets interface, as is explained in section 4.1. Figure 6.7 shows the correlation between the maximum velocity present

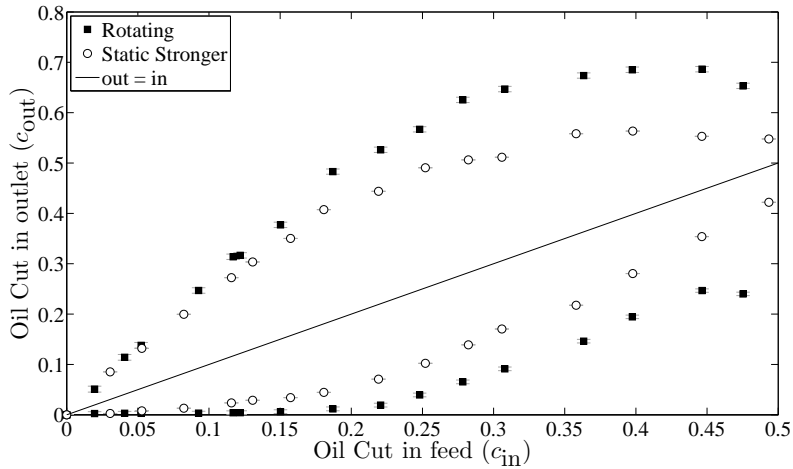


Figure 7.13: Oil concentration in both outlets for a rotating swirl element (impeller) and a static swirl element (strong swirl element of this work). The impeller was operated at 50 Hz (maximum frequency) in a 17 m³/h flow in a 50 mm tube with 21 mm diameter pick-up tube. The static swirl element was operated at 56.5 m³/h in a 100 mm tube with a length of 160 cm and a pick-up tube of 50 mm diameter.

in the system and the resulting droplet size distribution. From the work in section 7.2.2 we learn that for given droplet size distribution, the separation performance increases with decreasing azimuthal velocity, until the azimuthal velocity is such that the droplets are not broken anymore by the swirl element. The optimal axial cyclone therefore breaks droplets down to the size in the feed, or actually, is designed such that there is just no droplet breakup. We should keep in mind that the droplet size distribution is not necessarily known for producing oil wells.

Design considerations for Liquid-Liquid Cyclones

The aim of the research presented in this thesis is the development of understanding of in-line axial cyclones for bulk oil/water separation. Although a thorough understanding of the dispersed, multiphase, turbulent and swirling flow is required to know what to change in the design, current research progress does not allow an easy, full-scale numerical simulation nor an exact theoretical prediction. In the design process of liquid-liquid cyclones, a solution to the design challenge is relying on non-dimensional scaling of cyclone separation performance data. Therefore, this concluding chapter provides basic guidelines on the optimization of cyclone design based on non-dimensional numbers.

8.1 Scaling parameters

Within this research, we limited ourselves to three different cyclones with a limited range of flow rates, and only a single oil/water system. By proper non-dimensional scaling, the results can be extended to more generic cases.

Efficiency To compare efficiency, the bulk efficiency as introduced in equation 3.11 is used:

$$\eta_{\text{bulk}} = \frac{c_{\text{in}} - c_{\text{HPO}}}{2c_{\text{in}}} + \frac{c_{\text{LPO}} - c_{\text{in}}}{2 - 2c_{\text{in}}}. \quad (8.1)$$

The bulk efficiency is 0 when the oil concentrations in the output are equal to the oil concentration in the input and 1 when only oil flows through the LPO and only water through the HPO.

8.1.1 Reynolds number

The Reynolds number compares the inertial forces and viscous forces. The median droplet size downstream of the swirl element is related to the Reynolds number,

which we calculate based on the azimuthal velocity and downstream droplet diameter:

$$\text{Re}_\theta = \frac{v_\theta D_{\text{downstream}}}{\nu_c} \quad (8.2)$$

Figure 8.1 relates the swirling Reynolds number (eq. 8.2) to the bulk efficiency (eq. 8.1). The different measurement points represent different settings in the flow rig: three different swirl elements, a range of flow rates and a range of droplet sizes. All samples were obtained for a swirltube with a length of about 170 cm and a pickup tube diameter of 40 or 50 mm. Both the oil cut in the feed and the flow split were 0.25.

From the results, we observe the trend that the highest obtained efficiency is larger for higher Re_θ . The Reynolds number balances inertial forces against viscous forces. When viscous forces dominate, the droplet is easily dispersed by turbulent eddies. When inertial forces dominate, the droplet will move according to the centrifugal buoyancy force and get separated. Based on this theory and the measurement data in figure 8.1, a linear relation for the maximum obtainable efficiency η_{bulk} is suggested as function of Re_θ .

8.1.2 Weber number

The Weber number expresses the balance between the shear forces that tear a droplet apart and the interfacial tension force that holds the droplet together:

$$\text{We} = \frac{|\vec{t}| D^2}{\sigma D}. \quad (8.3)$$

For an axial cyclone, the location with the highest velocity is the annular gap of the swirl element: the droplets that have an upstream diameter D_{upstream} are exposed to the high azimuthal velocity generated in the swirl element. The acceleration of the droplets to this high velocity applies a force on their surface which leads to a Weber number of the form:

$$\text{We} = \frac{\rho_d v_\theta^2 D_{\text{upstream}}}{\sigma} \quad (8.4)$$

Figure 8.2 relates the Weber number (eq. 8.4) to the bulk efficiency (eq. 8.1). The measurement points are the same as used in figure 8.1, as described in the previous paragraph on the Reynolds number results.

From the results, we observe the trend that the highest obtained efficiency is larger for lower We . The Weber number relates the shear forces caused by the droplet acceleration in the swirl element to the interfacial tension force that holds the droplet together. A lower Weber number therefore means that the droplets are more stable when passing the swirling flow. Unstable droplets break, leading to smaller droplets that are harder to separate.

Similar to the figure with the Re -number results, we draw a suggested line that represents maximum separation as function of the Weber number. Although we cannot exclude the possibility of cases where this line is exceeded, the line seems to

be a feasible maximum. An interesting property of the fit is that it predicts $\eta_{\text{bulk}} = 1$ for $We = 0$.

8.2 Prediction of current swirl elements

Based on the experimental data for the three different swirl elements described in this thesis (see chapter 4), we can relate the Weber and Reynolds number for the behavior in the Delft flow rig used for this work, meaning that the interfacial tension and liquid densities of the experiments in this thesis are used ($\sigma = 30$ mN/m, $\rho_d = 872$ kg/m³ and $\rho_c = 1064$ kg/m³).

8.2.1 Method

For each flow rate, the droplet size upstream was calculated, according to an exponential relation fitted through the maxima of figure 6.1:

$$D = 836e^{-1.04u} \quad [\mu\text{m}], \quad (8.5)$$

with u the continuous phase velocity containing the droplets and with a maximum droplet size of $500 \mu\text{m}$.

The flow rate is directly coupled to the azimuthal velocity in each swirl element and the relations between flow rate and azimuthal velocity as derived from the LDA measurement data found in chapter 4:

$$u_\theta = \begin{cases} 5.0u_b & \text{strong swirlelement} \\ 3.5u_b & \text{weak swirlelement} \\ 7.0u_b & \text{large swirlelement} \end{cases} \quad (8.6)$$

The value of u_θ is used for both the We as Re_θ number. The droplet sizes downstream of the swirl element are calculated according to equation 8.5 for the azimuthal velocity downstream of the swirl element (eq. 8.6).

The set of equations is evaluated for a range of flow rates, from 0.5 to $80 \text{ m}^3/\text{h}$. Each flow rate combined with a swirl element results in a Weber number upstream and a Reynolds number downstream as in figure 8.3.

8.2.2 Reynolds depends on Weber

Figure 8.3 shows the relation for the three swirl elements between Re_θ and We . Due to the common rules used in the method of section 8.2.1 and the link between the flow rate and azimuthal velocities, the curves coincide almost. The kink in the curve at $We \approx 10$ is caused by the restriction that droplets are not larger than $500 \mu\text{m}$. Actual measurements are plotted as dots in figure 8.3. For some cases, the droplet size is reduced with a membrane valve (see section 7.2.3) leading to a decrease in both We as Re_θ number. All performed tests follow more or less the predicted curve for $Re_\theta(We)$.

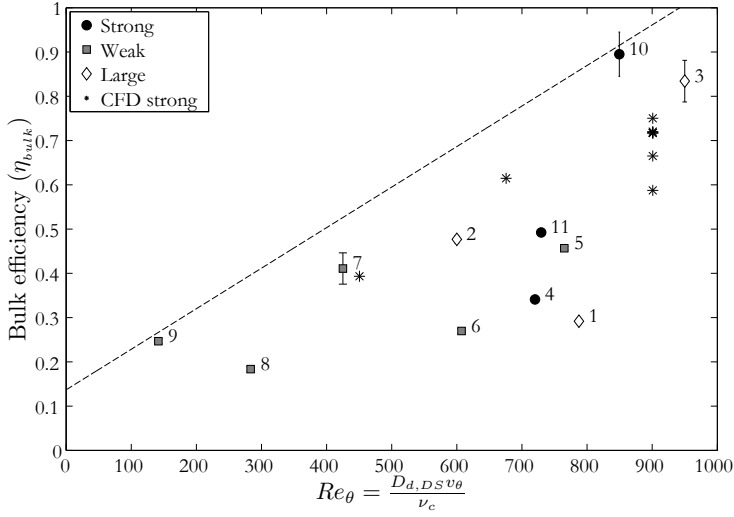


Figure 8.1: Separation efficiency as function of the droplets Reynolds number (eq. 8.2). Error bars indicate the non-dimensionalized median of the droplet size in swirling flow, data points are number as in figure 8.2. CFD results for the strong swirl element by Slot [13]. There seems to be a maximum separation for each Reynolds number; a linear function is plotted to represent this possible maximum. This seems feasible, since more droplet inertia makes it less vulnerable to turbulent dispersion.

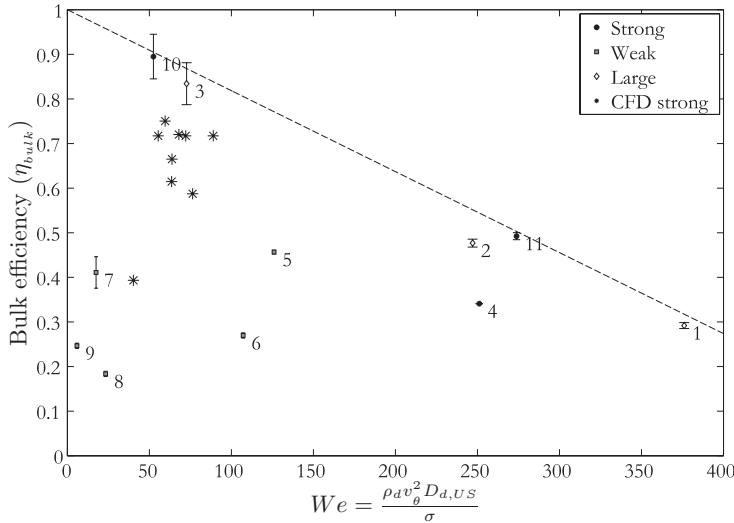


Figure 8.2: Separation efficiency as function of the Weber number of the median droplet size at the maximum azimuthal velocity in the swirl element. Error bars indicate the droplet size downstream of the swirl element, data points are number as in figure 8.1. CFD results for the strong swirl element by Slot [13]. There seems to be a maximum separation efficiency, a visual exponential decay. A lower Weber number enables a higher separation efficiency.

8.2.3 Optimal point of operation

Measured separation efficiency results show a dependency on the Re_θ and We number. A high Re_θ is favorable for separation, where a high We works counter effective on separation. We should therefore operate an in-line axial cyclone at a point where we have a high Re_θ and a low We . From figure 8.3 we see that the azimuthal velocity couples the Reynolds and Weber number and that the swirl element design itself cannot significantly change this.

From the suggested maximum bulk efficiency in figures 8.1 and 8.2, we obtain the following relations:

$$\eta_{\text{bulk, max}} = a_1 Re_\theta + b_1 \propto c_1 v_\theta + d_1 \quad (8.7)$$

$$\eta_{\text{bulk, max}} = -a_2 We + b_2 \propto c_2 v_\theta^2 + d_2, \quad (8.8)$$

with a , b , c and d constants. Due to the quadratic nature of equation 8.8 and the linear behavior of 8.7, a higher azimuthal velocity is not beneficial for separation. In figure 8.3, we see that the maximum value for Re_θ is obtained at a low We number. This is, again, caused by the upper limit for the droplet size of $500 \mu\text{m}$.

Numerical results In chapter 7, we saw an over prediction of separation performance in the numerical simulations done by Slot [13]. In figure 8.3, many measurement points for the CFD work are above the predicted lines based on the work in this thesis. Cause is the lack of droplet breakup in some of the numerical datasets; a consequence is an over prediction of separation.

8.2.4 Dependence on droplet size

The curve in figure 8.3 shows a kink. Where the droplet size upstream of the cyclone depends on the velocity according to Hinze's theory, we imposed a maximum of $500 \mu\text{m}$: beyond this level, the dispersed phase does not behave like droplets anymore. The same curve has been computed with smaller maximum upstream droplet sizes: 100 , 200 , 300 and $400 \mu\text{m}$. Figure 8.4 shows the Re_θ - We -plots for those conditions. For these smaller droplets, the peak in Re_θ shifts to a larger value of We . This translates to a cyclone with a higher azimuthal velocity that obtains the maximum possible efficiency for given Weber number. The graph does not predict the efficiency at that specific point.

A remarkable observation from figure 8.4 is the splendid resemblance of the model and measurement data for the $100 \mu\text{m}$ droplets.

8.3 Guide on cyclone design

From section 8.2 and previous chapters in this thesis, we know the importance for cyclones of droplet break up in relation to the azimuthal velocity. This section provides a guide on the design of cyclones considering the optimal balance between

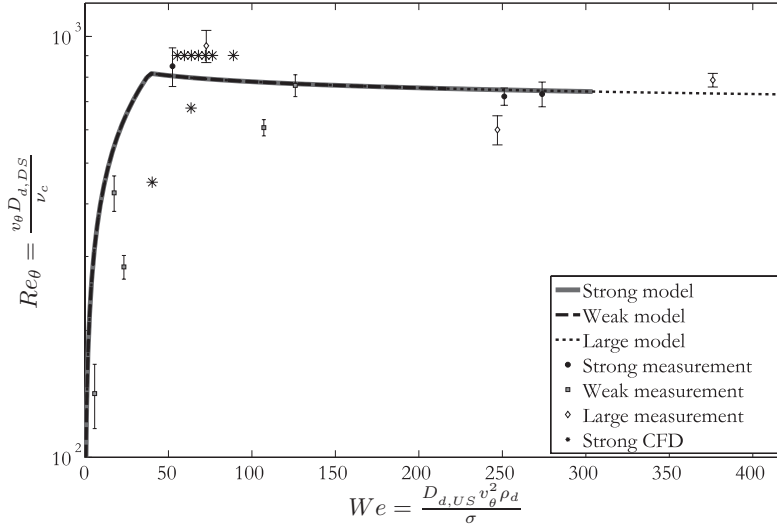


Figure 8.3: Weber and Reynolds number of figures 8.1 and 8.2. The theoretical relation for each swirl element is depicted, and actual measurement results. The coupling between Re_θ and We is strong. Future swirl element design should strive for a larger Re at minimal We . The bend in the curves originates from the maximum droplet size of $500\ \mu\text{m}$ that I've imposed.

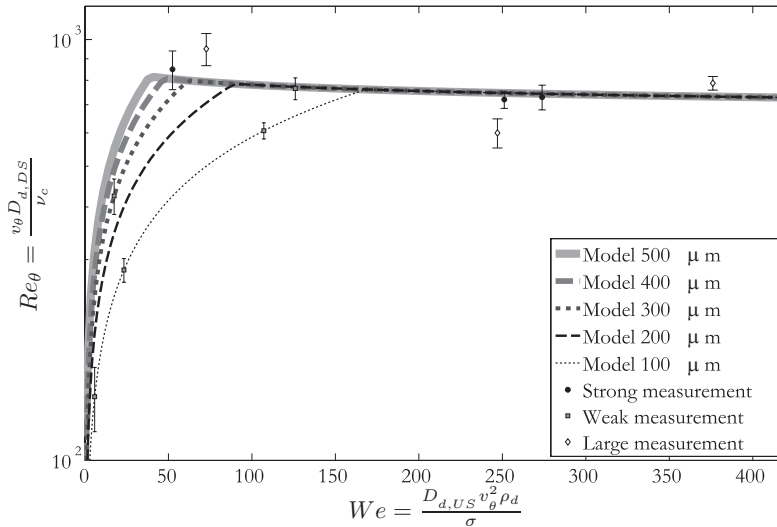


Figure 8.4: Weber (eq. 8.4) and Reynolds number (eq. 8.2) like figure 8.3. The relation is shown with different maximum values for the droplet size. Smaller droplets shift the maximum of Re_θ to a larger Weber number. Good resemblance is found for the $100\ \mu\text{m}$ droplets with experimental results.

droplet break up and centrifugal separation. Details on the design of the vanes in an axial cyclone can be found in chapter 4; they are not part of this design guide.

8.3.1 Input parameters

Before designing an axial cyclone, the following boundary conditions are required for the cyclone design:

- volumetric flow rate of the stream that needs to be separated;
- volumetric oil concentration in the feed;
- interfacial tension (σ) between the watery and oily phase;
- viscosity η_c of the continuous phase;
- density of both phases (ρ_c and ρ_d);
- upstream tube diameter;
- droplet size distribution upstream ($f(D_d)$) of the swirl element, or at least the median droplet size upstream.

If no information is available on the droplet size distribution upstream of the swirl element, Hinze's theory can be used to predict the droplet size, see section 6.1.1.

Single or multi stage The shear applied in an axial cyclone puts shear on droplets, which can reduce the average droplet size. If the droplet size distribution function is very broad, the balance between droplet break up and required azimuthal acceleration is such that the separation efficiency will be low. Large droplets require a low azimuthal velocity to move by centrifugal buoyancy forces. These low forces will not separate small droplets. The high azimuthal velocity required to separate small droplets, breaks larger droplets, possibly resulting in very small satellite droplets. Small droplets are harder to separate since the centrifugal buoyancy force scales with the diameter cubed and the drag force with the diameter squared. The choice for a cascade of cyclones with a subsequent increase in azimuthal acceleration can therefore be beneficial to obtain good separation and minimize the pressure drop required to do so.

8.3.2 Single cyclone design

The optimal configuration of the cyclone can be read from figure 8.4, considering the median droplet size upstream in the flow. Optimal separation occurs at the maximum of $Re_\theta(We)$, which follows from the droplet size upstream of the swirl element. The required azimuthal velocity in the swirl element then follows from the Weber number:

$$v_\theta = \sqrt{\frac{\sigma We}{\rho_d D_{\text{upstream}}}} \quad (8.9)$$

The expected bulk separation efficiency (η_{bulk}) can be estimated by multiplying the efficiency curves of figures 8.1 and 8.2:

$$\eta_{\text{bulk}}(\text{Re}_\theta, \text{We}) \approx \eta_{\text{bulk}}(\text{Re}_\theta) \cdot \eta_{\text{bulk}}(\text{We}) \quad (8.10)$$

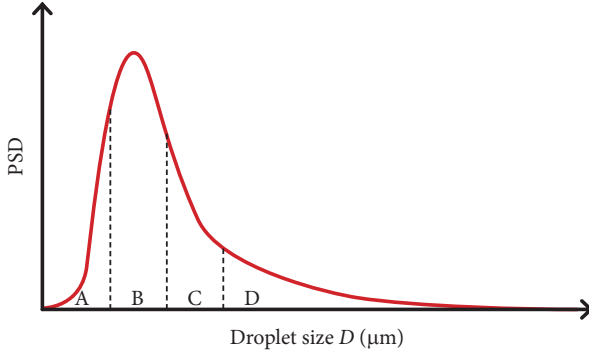
The axial bulk velocity is not used in this design optimization. From experience with the flow rig used in this research, we know that for axial bulk velocities that are an order smaller than the azimuthal velocity, it works. Lower axial bulk velocities should work as well, higher axial bulk velocities shall introduce additional turbulence that enhances turbulent dispersion.

8.3.3 Multi-stage cyclone design

To enhance separation performance over a single-step cyclone, an integrated cascade of multiple cyclones is proposed. Figure 8.5 introduces an example design. The feed enters the system via a wide swirl element that provides a low azimuthal velocity. Large droplets ought to move to the center, where they are captured in a pickup tube. The tapering of the tube preserves the azimuthal velocity downstream. At the end of the first section, the HPO is formed by a new stronger swirl element, which enhances the swirl. The second stage should remove smaller droplets than the first, and can end into the next stage, and so on.

Divisioning into bins

For an accurate design of a multi-stage cyclone, knowledge of the droplet size distribution $f(D_d)$ is essential. We divide this distributions into N bins:



For the last bin (D in the figure above), we apply the strategy as introduced in section 8.3.2, using the mean droplet diameter of the bin. The oil stream that can be separated follows from an integration of $f(D_d)$ over the width of the bin, multiplied with the volumetric oil concentration present in the total flow. As we have seen in chapter 7, section 7.2, the highest separation is achieved when the flow split is equal to the oil cut in the feed. In this case, the flow split should be matched to the oil cut of the fraction for which this bin is designed.

The efficiency of this bin can be estimated by equation 8.10.

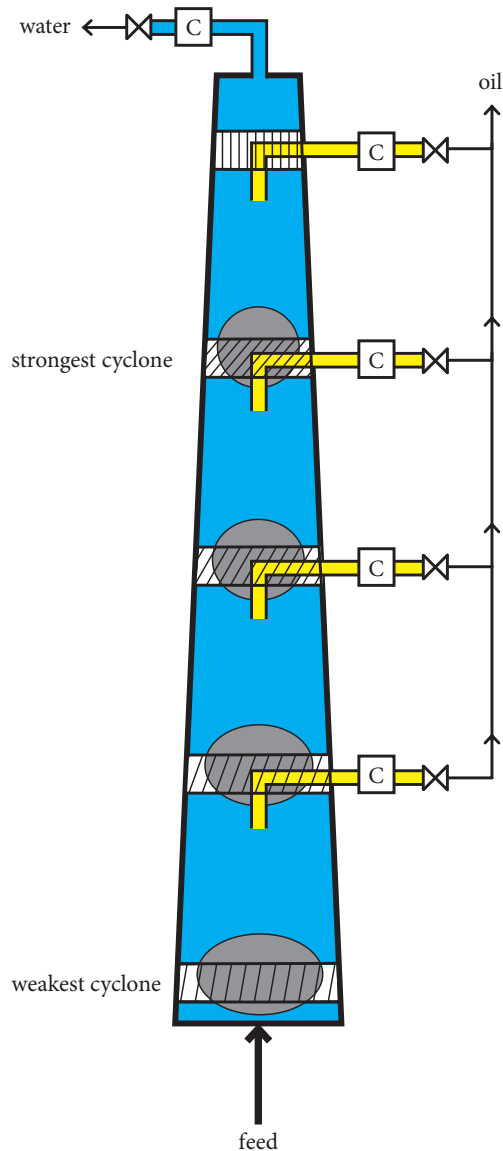
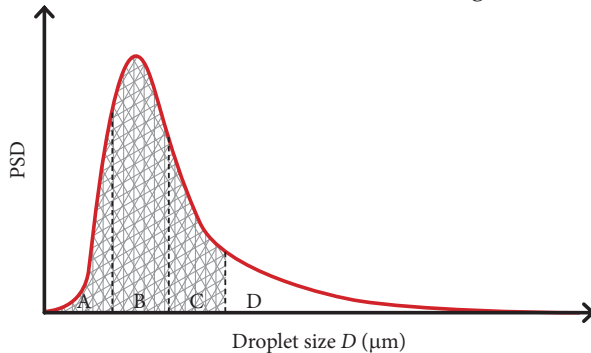


Figure 8.5: Rough idea for the sequential placement of multiple cyclones.

Subsequent bins

For design purposes, we assume that all oil of the previous bin has been removed, the marked area indicates the remaining oil fraction.



The volumetric flow rate follows from the inflow of the previous bin and its flow split. The swirl element should be designed with vanes that start at the angle at the end of the previous section. The rest of the design follows from the procedure described earlier in this section (8.3.3).

Practical implications

The original aim of in-line separators is weight and plot space reduction. Constructing a process with multiple cyclones as in figure 8.5 is therefore less attractive than a single stage separation step due to the addition steel, utilities (valves and pressure controls) and therefore space required for such a design. The pressure drop should, however, not be different then for a single stage cyclone aiming at the same droplet cut-off size, since the pressure is proportional to the azimuthal velocity achieved in the final stage. This statement is supported by conservation of momentum.

Since the total pressure drop is equal, a cascade system like in figure 8.5 will not break out more gas than a single stage cyclone. Gas break-out is the evaporation of a gaseous fraction from the crude. However, each stage suffers a fraction of gas break-out.

8.3.4 Sizing

Estimation of required length

The required length of the swirl tube depends on the velocity of the dispersed droplets in the radial direction. The velocity depends on the equation of motion, for which we take three effects into account: (i) the acceleration by the centrifugal buoyancy force, (ii) the drag force due to the droplets velocity relative to the surrounding fluid and (iii) the turbulent dispersive effects moving the droplet around. The first two forces are real and can be estimated using the droplet size and density difference with the surrounding fluid. For an estimation of the turbulent dispersion we cannot use such an estimation. To estimate the effect of turbulent dispersion, we include a rough estimation by using the root mean square (RMS) value of the time-dependent velocity signal as function of the Reynolds number.

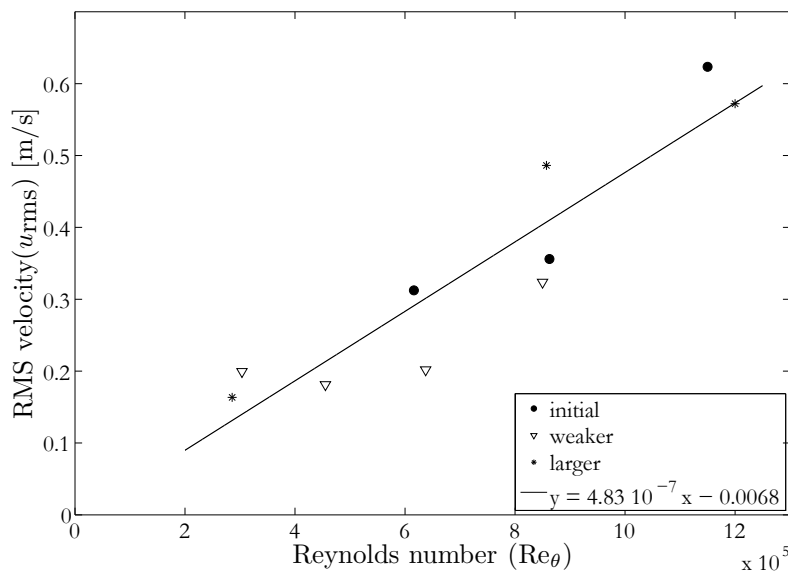


Figure 8.6: RMS velocity as function of the Reynolds number based on the azimuthal velocity.

The method to approximate the required length of the cyclone does not consider all relevant effects. Although we do not intend on providing a full explanation why the phase separation in a liquid-liquid cyclone lacks behind the expectancies based on an ‘easy’ theory like below, there is one neglected effect. Droplets moving inward to the oil kernel push away the water, where the importance of droplet-droplet interactions increases rapidly. This effect is known as hindered settling, as described by the Richardson & Zaki correlation [40]. Increasing the length of a cyclone beyond a critical value works counter effective on separation (see section 7.1.2). The problem of hindered settling can thus not be ‘resolved’ with adding more length to a cyclone.

Figure 8.6 contains the root mean square averages for all different conditions as discussed in chapter 4. Although the relation is not fully linear, there is a positive correlation between the Reynolds number and the RMS velocity. The linear fit of the results is:

$$u_{rms} = 4.4 \cdot 10^{-7} Re_\theta - 0.0068, \quad (8.11)$$

with the velocity in m/s.

During the derivation of the droplets equation of motion, we treat the turbulent dispersive effect as a headwind equal to the rms-velocity of the single phase flow. The equation of motion then reads:

$$\frac{\pi}{6} D_d^3 (\rho_c - \rho_d) \frac{u_\theta^2}{r_d} = \frac{\pi}{8} D_d^2 \rho_c C_D (v_r + u_{rms})^2, \quad (8.12)$$

where v_r is the droplet radial velocity, which is < 0 for an inward moving droplet and u the continuous phase velocity. This leads to an estimation for the droplet velocity in the radial direction:

$$v_r = -\sqrt{\frac{4}{3} \frac{D_d u_\theta^2 (\rho_c - \rho_d)}{r_d \rho_c C_D}} + u_{\text{rms}}. \quad (8.13)$$

The average displacement of all droplets can not become negative, if turbulent dispersion dominates, the droplets will be equally distributed over the complete cross section of the tube. Therefore, the interpretation of equation 8.13 is that for those cases no separation is to be expected.

The suggested length of the swirltube follows from the required displacement of oil droplets inward towards the oil kernel. The average distance that the droplets need to travel is estimated to be 1/4 of the tube diameter (not all droplets are at the wall, the oil kernel in the center has a finite size). The minimum required residence time in the cyclone is therefore:

$$\Delta t = \frac{D_t}{4v_r} \quad (8.14)$$

From chapter 4 we learned that the maximum axial velocity in the cyclone is in the order of 2 times the bulk velocity upstream of the swirl element. Therefore, the minimum required length is:

$$L = \frac{2\Phi}{\pi D_t v_r} \quad (8.15)$$

Swirl tube diameter

The effect of diameter of the swirltube has not been tested within this research. The available data in literature on cyclone design are limited to gas-solid cyclones with a different inlet geometry.

When deciding on the diameter of a cyclone, the following considerations should be taken into account:

1. To separate the phases, droplets should move in the radial direction, increasing the diameter, increases the maximum radial distance droplet should move and works therefore counteractive on separation.
2. Drag at the wall slows down the vortex and is characterized by a large $\partial v / \partial r$. This high shear is capable of tearing the droplets apart. From this perspective, a larger diameter is favorable.
3. The diameter is coupled to the axial velocity. The flow rate per cyclone and its diameter dictate the average axial velocity, where the axial velocity and length determine the residence time in the cyclone.
4. The volume flow requiring treatment and the composition of the stream are not equal over the entire lifetime of a production facility. The water cut increases over time, where the total volume typically decreases. "Turn down" is operating a facility below design specification. Turn down in a cyclone affects the azimuthal velocity and therewith the separation characteristic. For process design, it is therefore highly recommended to install multiple cyclones

in parallel to be able to run each cyclone at its optimal flow rate for given separation requirements.

The size of the swirl tube used in this research, being 10 cm, seems to be a reasonable compromise for points 1 to 3. Further research should be done to determine the optimal diameter. The application of a gradual reduction of the tube diameter in the streamwise direction (tapering) can be beneficial, since it compensates for the loss of vortex strength due to friction. It is suggested to design the tapering such that the azimuthal velocity in the tube is kept as constant over length as possible, to avoid droplet breakup due to sudden regions with high shear.

The total available cross section in the cyclones should be equal to, or larger than the cross section of the tube with the feed. A reduction in the cross section leads to an acceleration of the fluid and those shear forces will break droplets, working counteractive on separation.

8.3.5 Process control

During operation of a cyclone, the pressure difference between the HPO and LPO of each cyclone(stage) determines the flow split ($F = \phi_{\text{LPO}}/\phi_{\text{tot}}$). From an operational perspective, the flow split needs to be controlled, which can be done by the application of valves in one or both outlets. All valves used for pressure regulation exert a shear force on the liquids. This shear can break droplets and therefore hamper downstream separation. Therefore, it is suggested to mount only a regulation valve in one outlet, the one which requires least downstream treatment.

8.3.6 Swirl element design

Within the ISPT project OG-00-004, a swirl element has been designed. This work was performed at Twente University by Slot [13]. The considerations for the swirl element design are discussed in section 4.2. The optimal design of the vanes and internal body was not the scope of this thesis. the work of for example Slot [13] can be used as design guide for the internal swirl element.

8.4 Concluding remarks

The motivation of the work presented in this thesis is to increase understanding of in-line axial liquid-liquid cyclones, to strive for an optimal design, ready for application in industrial installations. In the preceding chapters, different aspects of the cyclone in our experimental facility were investigated.

Chapter 4: Single phase water study of the velocity and turbulence levels. From the LDA data, the correlation between the swirl element design and resulting velocity profile is better understood. The time series at different conditions form input for the modelling of turbulent dispersion.

Chapter 5: The time series of the velocity obtained in chapter 4 was used to solve

a simplified equation of motion for droplets in swirling flow, which provides a method to predict the chance of separation for a specific droplet size in axial cyclones at a low numerical cost.

Chapter 6: Measurements of droplet sizes upstream and downstream of the swirl element and cyclone itself provided relations for droplet breakup and coalescence. The breakup of droplets in a cyclone is the most important counteracting effect on separation. From results in this chapter, a relation for the droplet sizes in the cyclone is obtained.

Chapter 7: The design was modified in many different ways to study the sensitivity of the separation efficiency to these changes. All changes that affected the droplet size, such as flow rate and vane angle, proved to be of major influence on the separation quality, where the exact sizing such as the pickup tube diameter and length did not affect separation much.

This chapter: Experimental data from chapters 6 and 7 is non-dimensionalized to obtain general conclusions on the expected separation efficiency for a broad range of cases. This leads to an aid for future design of liquid-liquid axial cyclones.

The conclusions of this thesis are not “ready to use” for companies that want to construct a device immediately applicable for field use. Although both experiments and data evaluation were performed in a very careful manner, it is highly recommended to test the final conclusions. One can think of the construction of a multi-stage cyclone and the use of different liquids, to see whether the non-dimensional results work also for the other interfacial tension and density.

Bibliography

- [1] D. Yergin. *The Prize: The Epic Quest for Oil, Money & Power*. Free Press, 2008.
- [2] E. Bretney. Water-purifier. US Patent 453105, May 26 1891.
- [3] M. Dirkzwager. *A New Axial Cyclone Design for Fluid-Fluid Separation*. PhD thesis, TU Delft, December 1996.
- [4] D.A. Colman, M.T. Thew, and D.R. Corney. Hydrocyclones for oil/water separation. In *Proceedings of the 1st International Conference on Hydrocyclones*, Cambridge UK, pages 143–165, 1980.
- [5] Y.J. Lu, L.X. Zhou, and X. Shen. Numerical simulation of strongly swirling turbulent flows in a liquid-liquid hydrocyclone using the Reynolds stress transport equation model. *Science in China Series E-Technological Sciences*, 43(1):86–96, 2000.
- [6] E.E. Paladino, G.C. Nunes, and L. Schwenk. CFD analysis of the transient flow in a low-oil concentration hydrocyclone. In *Proceedings of the AIChE 2005 Annual Meeting*. AIChE, October 30 - November 4 2005.
- [7] Sooran Noroozi and Seyed Hassan Hashemabadi. CFD Simulation of Inlet Design Effect on Deoiling Hydrocyclone Separation Efficiency. *Chemical Engineering & Technology*, 32(12):1885–1893, 2009.
- [8] Steffen Schütz, Gabriele Gorbach, and Manfred Piesche. Modeling fluid behavior and droplet interactions during liquid-liquid separation in hydrocyclones. *Chemical Engineering Science*, 64(18):3935–3952, 2009.
- [9] Sina Amini, Dariush Mowla, and Mahdi Golkar. Developing a new approach for evaluating a de-oiling hydrocyclone efficiency. *Desalination*, 285:131–137, 2012.
- [10] G.A.B. Young, W.D. Wakley, D.L. Taggart, S.L. Andrews, and J.R. Worrell. Oil-water separation using hydrocyclones - an experimental search for optimum dimensions. *Journal of Petroleum Science and Engineering*, 11(1):37–50, 1994.
- [11] C. Oropeza-Vazquez, E. Afanador, L. Gomez, S. Wang, R. Mohan, O. Shoham, and G. Kouba. Oil-water separation in a novel liquid-liquid cylindrical cyclone (LLCC (c)) compact separator - Experiments and modeling. *Journal of Fluids*

- Engineering-Transactions of the ASME*, 126(4):553–564, 2004. 8th International Symposium on Gas-Liquid Two-Phase Flows, Honolulu, HI, JUL 06-10, 2003.
- [12] Trygve Husveg, Odile Rambeau, Tormod Drengstig, and Torleiv Bilstad. Performance of a deoiling hydrocyclone during variable flow rates. *Minerals Engineering*, 20(4):368–379, 2007. Hydrocyclones 2006 Conference, Falmouth, ENGLAND, 2006.
- [13] J.J. Slot. *Development of a Centrifugal In-Line Separator for Oil-Water Flows*. PhD thesis, Twente University, 2013.
- [14] T. Krebs, K. Schroën, and R. Boom. Coalescence dynamics of surfactant-stabilized emulsions studied with microfluidics. *Soft Matter*, (8):10650–10657, 2012.
- [15] P.A. Yazdabadi, A.J. Griffiths, and N. Syred. Characterization of the PVC Phenomena in the Exhaust of a Cyclone Dust Separator. *Experiments in Fluids*, 17(1-2):84–95, June 1994.
- [16] S. Leibovich. The Structure of Vortex Breakdown. *Annual Review of Fluid Mechanics*, 10:221–246, 1978.
- [17] O. Kito. Axi-Asymmetric Character of Turbulent Swirling Flow in a Straight Circular Tube. *Bulletin of the JSME-Japan Society of Mechanical Engineers*, 27(226):683–690, 1984.
- [18] F. Durst, A. Melling, and J. H. Whitelaw. *Principles and Practice of Laser-Doppler Anemometry*. Academic Press Inc., 1976.
- [19] M.J. Tummers. *Investigation of a turbulent wake in an adverse pressure gradient using Laser Doppler Anemometry*. PhD thesis, Delft University of Technology, 1999.
- [20] R.J. Belt. *On the liquid film in inclined annular flow*. PhD thesis, Delft University of Technology, 2007.
- [21] R.J. Adrian. *Fluid mechanics measurements edited by R.J. Goldstein*. Springer Berlin, 1983. Chapter V: Laser Velocimetry.
- [22] J.H. Bae and L.L. Tavlarides. Laser Capillary Spectrophotometry for Drop-Size Concentration Measurements. *AIChE Journal*, 35(7), 1989.
- [23] S. Maaß, S. Wollny, A. Voigt, and M. Kraume. Experimental comparison of measurement techniques for drop size distributions in liquid/liquid dispersions. *Experiments in Fluids*, 50(2), 2010.
- [24] C. Desnoyer, O. Masbernat, and C. Gourdon. Experimental study of drop size distributions at high phase ratio in liquid-liquid systems. *Chemical Engineering Science*, 58:1353–1363, 2002.
- [25] James P.M. Syvitsky, editor. *Principles, methods and application of particle size analysis*. Cambridge University Press, 1991.

- [26] Paul A. Gunning, Martin S.R. Hennock, Andrew M. Howe, Alan R. Mackie, Peter Richmond, and Margaret M. Robins. Stability of oil-in-water emulsions. the effect of dispersed phase and polysaccharide on creaming. *Colloids and Surfaces*, 20(1-2):65 – 80, 1986.
- [27] David J. Hibberd, Andrew M. Howe, and Margaret M. Robins. Use of concentration profiles in creaming emulsions to determine phase coexistence. *Colloids and Surfaces*, 31(0):347 – 353, 1988. Proceedings of an International Conference.
- [28] G.E. Mapstone. The Salting-out of Polyethylene Glycol Emulsifiers. *Journal of the society of cosmetic chemists*, pages 239 – 243, 1961.
- [29] W. Hartevelde. *Bubble Columns: structures or stability?* PhD thesis, Delft University of Technology, 2005.
- [30] H.-M. Prasser, A. Böttger, and J. Zschau. A new electrode-mesh tomograph for gas-liquid flows. *Flow Measurement and Instrumentation*, 9:111–119, 1996.
- [31] D. Ito, H.-M. Prasser, H. Kikura, and M. Aritomi. Uncertainty and intrusiveness of three-layer wire-mesh sensor. *Flow Measurement and Instrumentation*, 22: 249–256, 2011.
- [32] M.J. Da Silva and U. Hampel. Kapazitäts-Gittersensor: Prinzip und Anwendung. *Technisches Messen*, 77(4):209–214, 2010.
- [33] P.M.T. Smeets. Master’s thesis, Delft University of Technology, Faculty of Applied Sciences, Department of Multi-Scale Physics, 2007.
- [34] D.J. Griffiths. *Introduction to Electrodynamics*. Prentice-Hall International, 1999.
- [35] C.H.K. Williamson and G.L. Brown. A series in $1/\sqrt{re}$ to represent the Strouhal Reynolds number relationship of the cylinder wake. *Journal of Fluids and Structures*, 12(8):1073 – 1085, 1998.
- [36] Nikolay Ivanov Kolev. *Multiphase Flow Dynamics 2, thermal and mechanical interactions*. Springer-Verlag Berlin Heidelberg, 2007. ISBN 978-3-540-69834-0.
- [37] J.O. Hinze. Fundamentals of the Hydrodynamic Mechanism of Splitting in Dispersion Processes. *American Institute of Chemical Engineering Journal*, September 1955.
- [38] S. Galinat, O. Masbernat, P Guiraud, C Dalmazzone, and Noïk. Drop break-up in turbulent pipe flow downstream of a restriction. *Chemical Engineering Science*, 60:6511–6528, 2005.
- [39] C.T. Crowe, J.D. Schwarzkopf, M. Sommerfeld, and Y. Tsuji. *Multiphase Flows with Droplets and Particles, second edition*. CRC Press, Taylor & Francis Group, 2012.
- [40] Mamoru Ishii and Novak Zuber. Drag Coefficient and Relative Velocity in Bubbly, Droplet or Particulate Flows. *AIChE Journal*, 25(5):843–855, 1979.
- [41] I.H. Abbott. *Theory of wing sections*. McGraw-Hill, 1949.

- [42] S. V. Alekseenko, P. A. Kuibin, V. L. Okulov, and S. I. Shtork. Helical vortices in swirl flow. *Journal of Fluid Mechanics*, 382:195–243, 1999.
- [43] Piet M. T. Broersen. The Removal of Spurious Spectral Peaks From Autoregressive Models for Irregularly Sampled Data. *IEEE Transactions on instrumentation and measurement*, 59(1):205–214, January 2010.
- [44] H.E.A. van den Akker and R.F. Mudde. *Fysische Transportverschijnselen I*. VSSD, 2003.
- [45] Jaber Almedeij. Drag coefficient of flow around a sphere: Matching asymptotically the wide trend. *Powder Technology*, 186(3):218–223, 2008.
- [46] P.G. Saffman. The lift on a small sphere in a slow shear flow. *Journal of Fluid Mechanics*, 22:385–400, 1965.
- [47] H. Brauer. Umströmung beschleunigter und verzögerter Partikeln. *Wärme- und Stoffübertragung*, 27:321–329, 1992.
- [48] Yixiang Liao and Dirk Lucas. A literature review of theoretical models for drop and bubble breakup in turbulent dispersions. *Chemical Engineering Science*, 64:3389–3406, 2009. section 4.
- [49] C. Martínez-Bazán, J.L. Montañés, and J.C. Lasheras. On the breakup of an air bubble injected into a fully developed turbulent flow. Part 2. Size PDF of the resulting daughter bubbles. *Journal of Fluid Mechanics*, 401:183–207.
- [50] C.D. Eastwood, L. Armi, and J.C. Lasheras. The breakup of immiscible fluids in turbulent flows. *Journal of Fluid Mechanics*, 502:309–333, 2004.
- [51] G.K. Batchelor. Axial flow in trailing line vortices. *Journal of Fluid Mechanics*, 20:645–658, 1964.
- [52] Alan Reynolds. On the dynamics of turbulent vortical flow. *Zeitschrift für angewandte Mathematik und Physik ZAMP*, 12:149–158, 1961. ISSN 0044-2275.
- [53] O. Kitoh. Experimental study of turbulent swirling flow in a straight pipe. *Journal of Fluid Mechanics*, 225:445–479, April 1991.
- [54] T. O'Doherty, A. J. Griffiths, N. Syred, P. J. Bowen, and W. Fick. Experimental analysis of rotating instabilities in swirling and cyclonic flows. *Developments in Chemical Engineering and Mineral Processing*, 7(3-4):245–267, 1999.
- [55] H. Tennekes and J.L. Lumley. *A first course in turbulence*. The MIT Press, 1972.

APPENDIX A

Description of swirling flow

This appendix provides a theoretical basis to describe swirling flow. The presented theory is based on single phase flow. The Navier-Stokes equations are given in the first section. Then, we provide an empirical description of swirling flow, i.e. the swirl number. The final section discusses vortex breakdown and characterization of unsteady flow effects.

A.1 Governing equations

Conservation of momentum leads to the general description for fluid motion, the Navier-Stokes equations:

$$\rho \left(\frac{\partial \vec{v}}{\partial t} + \vec{v} \cdot \nabla \vec{v} \right) = -\nabla p + \nabla \cdot \vec{T} + \vec{f} \quad (\text{A.1})$$

here \vec{T} is the viscous stress tensor and \vec{f} are body forces.

Equation A.1 cannot be solved analytically. Assumptions or simplifications need to be made to solve the equation:

- incompressible flow; the swirling flow deals only with liquids
- constant viscosity μ ; the liquids used are all Newtonian at almost constant temperature
- conservation of mass, given by the continuity equation: $\frac{\partial \rho}{\partial t} + \vec{\nabla} \cdot (\rho \vec{v}) = 0$.

simplifies the Navier-Stokes equation to:

$$\rho \left(\frac{\partial \vec{v}}{\partial t} + \vec{v} \cdot \nabla \vec{v} \right) = -\nabla p + \mu \nabla^2 \vec{v} + \vec{f} \quad (\text{A.2})$$

For cylindrical coordinates, this works out to the general case:

$$\rho : \quad \frac{\partial u_z}{\partial z} + \frac{1}{r} \frac{\partial r u_r}{\partial r} + \frac{1}{r} \frac{\partial u_\phi}{\partial \phi} = 0 \quad (\text{A.3})$$

$$r : \quad \rho \left(\frac{\partial u_r}{\partial t} + u_r \frac{\partial u_r}{\partial r} + \frac{u_\phi}{r} \frac{\partial u_r}{\partial \phi} + u_z \frac{\partial u_r}{\partial z} - \frac{u_\phi^2}{r} \right) = -\frac{\partial p}{\partial r} + \mu \left(\frac{1}{r} \frac{\partial}{\partial r} \left(r \frac{\partial u_r}{\partial r} \right) + \frac{1}{r^2} \frac{\partial^2 u_r}{\partial \phi^2} + \frac{\partial^2 u_r}{\partial z^2} - \frac{u_r}{r^2} - \frac{2}{r^2} \frac{\partial u_\phi}{\partial \phi} \right) + \rho g_r \quad (\text{A.4})$$

$$\phi : \quad \rho \left(\frac{\partial u_\phi}{\partial t} + u_r \frac{\partial u_\phi}{\partial r} + \frac{u_\phi}{r} \frac{\partial u_\phi}{\partial \phi} + u_z \frac{\partial u_\phi}{\partial z} + \frac{u_r u_\phi}{r} \right) = -\frac{1}{r} \frac{\partial p}{\partial \phi} + \mu \left(\frac{1}{r} \frac{\partial}{\partial r} \left(r \frac{\partial u_\phi}{\partial r} \right) + \frac{1}{r^2} \frac{\partial^2 u_\phi}{\partial \phi^2} + \frac{\partial^2 u_\phi}{\partial z^2} + \frac{2}{r^2} \frac{\partial u_r}{\partial \phi} - \frac{u_\phi}{r^2} \right) + \rho g_\phi \quad (\text{A.5})$$

$$z : \quad \rho \left(\frac{\partial u_z}{\partial t} + u_r \frac{\partial u_z}{\partial r} + \frac{u_\phi}{r} \frac{\partial u_z}{\partial \phi} + u_z \frac{\partial u_z}{\partial z} \right) = -\frac{\partial p}{\partial z} + \mu \left(\frac{1}{r} \frac{\partial}{\partial r} \left(r \frac{\partial u_z}{\partial r} \right) + \frac{1}{r^2} \frac{\partial^2 u_z}{\partial \phi^2} + \frac{\partial^2 u_z}{\partial z^2} \right) + \rho g_z \quad (\text{A.6})$$

So far, no analytical solution has been found that solves the set of equations above. Computational calculations taking into account the full Navier-Stokes equations are known as Direct Navier-Stokes (DNS). For large systems, like the axial cyclone in this thesis, the large range of sizes (μm to m and μs to s), DNS requires more computational power than a university has available.

A.2 Empirical description of swirling flow

The following assumptions improve understanding of equations A.4-A.6:

- **Reynolds-Averaged Navier-Stokes:** time-averaged decomposition of the velocity in a mean part and a time-dependent part: $u_i(t) = U_i + u'_i(t)$
- **Steady-state:** $\partial u_i / \partial t = 0$ and $\partial p / \partial t = 0$
- **Axi-symmetry:** $\partial / \partial \phi = 0$
- **No net radial flow:** $U_r = 0$.

With these assumptions, the Navier-Stokes equations work out to:

$$\rho : \quad \frac{\partial U_z}{\partial z} + \frac{\partial u'_z}{\partial z} + \frac{1}{r} \frac{\partial r u'_r}{\partial r} = 0 \quad (\text{A.7})$$

$$r : \quad \rho \left(\frac{\partial \overline{u'_r u'_r}}{\partial z} - \frac{1}{r} \frac{\partial r \overline{u'_r u'_r}}{\partial r} \frac{U_\phi^2}{r} + \frac{\overline{u_\phi'^2}}{r} \right) = \frac{\partial P}{\partial r} \quad (\text{A.8})$$

$$\phi : \quad \rho \left(U_z \frac{\partial U_\phi}{\partial z} + U_r \frac{U_\phi}{\partial r} + \frac{U_r U_\phi}{r} + \frac{\partial \overline{u'_\phi u'_z}}{\partial z} + \frac{1}{r} \frac{\partial r \overline{u'_r u'_\phi}}{\partial r} + \frac{\overline{u'_r u'_\phi}}{r} \right) = \mu \left(\frac{\partial^2 U_\phi}{\partial z^2} + \frac{1}{r} \frac{\partial}{\partial r} \left(r \frac{\partial U_\phi}{\partial r} \right) - \frac{U_\phi}{r^2} \right) \quad (\text{A.9})$$

$$z : \quad \rho \left(U_z \frac{\partial U_z}{\partial z} + \frac{\partial \overline{u_z'^2}}{\partial z} - \frac{1}{r} \frac{\partial r \overline{u'_r u'_z}}{\partial r} \right) = \mu \left(\frac{\partial^2 U_z}{\partial z^2} + \frac{1}{r} \frac{\partial}{\partial r} \left(r \frac{\partial U_z}{\partial r} \right) \right) - \frac{\partial P}{\partial z} \quad (\text{A.10})$$

For the condition $\partial/\partial z \ll \partial/\partial r$ Batchelor [51] found an analytical solution:

$$U_r(r) = 0 \quad (\text{A.11})$$

$$U_\phi(r) = qW_0 \frac{r_0}{r} \left(1 - e^{-\left(\frac{r}{r_0}\right)^2} \right) \quad (\text{A.12})$$

$$U_z(r) = U_\infty - W_0 e^{-\left(\frac{r}{r_0}\right)^2} \quad (\text{A.13})$$

with q the balance between axial and azimuthal velocity, W_0 the axial vortex velocity, r_0 the characteristic vortex radius and U_∞ the maximum axial velocity (found at the upstream side). This approximation of the flow holds when viscous transport of momentum is dominant, which holds only for laminar flow. Reynolds [52] provides a more accurate derivation from a physics perspective. Results with the model of Batchelor [51], however, have a reasonable agreement with experimental data (see for example Dirkzwager [3]) and is practical in use. Even with current computing power and physical modelling, Slot [13] shows it is hard to provide an accurate model of the flow.

A.3 Swirl number

The swirl intensity in pipe flow can be expressed in terms of a non-dimensional number, this is the Swirl number Ω . There are various definitions for the swirl number [3], we use the formulation as provided by Kitoh [53]:

$$\Omega = \frac{2\pi\rho_c \int_0^R u_z u_\theta r'^2 dr'}{\rho_c \pi R^3 u_b^2} \quad (\text{A.14})$$

with ρ_c the liquid density, u_z the axial velocity, u_θ the azimuthal velocity, R the tube radius and u_b the liquid bulk velocity.

The interpretation of Ω is not straightforward. The integral in the numerator involves two parameters: (i) the angular momentum of a finite volume ($\vec{r} \times \vec{p} = \rho r u_\theta dV$) and (ii) the distribution of the mass flux over the radius (ru_z). These quantities are non-dimensionalized in the nominator with the mass flux ($\rho\pi R^2 u_b$) and the term Ru_b .

Due to friction at the wall, the swirl intensity Ω decreases in the downstream direction. The relation between the swirl intensity at distance z has been estimated by Dirkzwager [3]:

$$\Omega(z) = \Omega_0 e^{-C_d \frac{z-z_r}{D}}, \quad (\text{A.15})$$

with Ω_0 the swirl number at position z_r where it is generated and C_d a decay coefficient.

A.4 Advanced concepts

The preceding section provided us with empirical relations to understand the basics of swirling flow. The simplifications in the parametrization do not allow to account for time-dependent effects

A.4.1 Vortex Breakdown and flow reversal

A vortex is a fluid structure performing a helical motion, where both the axial and azimuthal velocity are over the complete cross section in the same direction. Vortex breakdown is the phenomenon that the vortex does not stretch across the complete tube diameter, but leaves a region around the centreline that has a velocity in the opposite direction. This looks like a helical flow around a virtual body, a body being fluid flow in the reversed direction.

The vortex breakdown in the axial cyclone is apparent as a region with reverse flow. Although the complete description of the flow would require the analytical solution of the Navier-Stokes equations (eq. A.4 to A.6, the driving force can be understood with a simpler concept. Consider four points in the tube: (i) close to the swirl element near the wall, (ii) far downstream, just before the end of the tube with the swirling flow, close to the wall, (iii) far downstream, just before the end of the tube with the swirling flow, in the center and (iv) close to the swirl element in the center. The pressure difference between the points at the same axial position (e.g. (i) vs. (iv) and (ii) vs. (iii)) are given by:

$$\Delta p = \int_{r_1}^{r_2} \frac{\rho v_\theta^2}{r} dr. \quad (\text{A.16})$$

Due to the decrease in swirl strength in the axial direction, Δp decreases for increasing axial distance to the swirl element. Therefore, the relation between the different pressures is as follows: $p_{(i)} > p_{(ii)} > p_{(iii)} > p_{(iv)}$. The pressure gradient on the centerline is opposite to the bulk flow direction, resulting in a reverse flow region. According to O'Doherty et al. [54] recirculation zones are formed for flows with a swirl number above 0.6.

A.4.2 Time-independent instabilities

The equations describing cyclonic fluid flow (eq. A.4-A.6) do not contain forces that can break symmetry from itself. Without any external disturbance, axi-symmetrical flow remains axi-symmetrical, almost all terms in A.4 are zero or counterbalancing. There are many sources that can contribute to a non-symmetric radial velocity: (i) non-symmetric inflow of liquid, caused by bends, (ii) lack of symmetry in the swirl generating device, (iii) lack of symmetry in the tube surrounding the vortex or (iv) non-orthogonal placement of the cyclone with respect to earth's gravity.

Equations A.8 - A.10 show that these effects also hold for the time-averaged case, which leads to a vortex spiralling around a helical core.

The vortex breakdown includes also the introduction of asymmetry - what does this

do for the flow. O'Doherty et al. [54] report axial-symmetric vortex-flow only exists for very low Re and Ω : $Re < 1000$ and $\Omega < 0.6$.

APPENDIX B

Estimation of turbulence parameters

Idea of this paragraph: (i) the system we look at is turbulent, (ii) the consequence of turbulence is the existence of turbulent eddies (iii) these eddies transfer momentum to other directions and to other scales (iv) dispersed droplets are sensitive to this momentum transfer.

B.1 Turbulence

The effect of turbulence of the flow is the existence of eddies at different sizes, ranging from the Kolmogorov microscale to the size scale of the flow (in our case: the diameter of the tube). The turbulent eddies are important, since they will exert a force on dispersed droplets. For droplets below a critical diameter D_{crit} the impulse by the turbulent eddies drag exceeds the momentum of the droplets - the dispersed droplets will act like flow tracers. On the bulk scale, this effect is known as turbulence dispersion.

Smallest length scale To quantify the effect of turbulent eddies in our swirling flow, the time-dependent velocity data obtained with LDA is used. Due to the irregular interarrival times of the tracer particles, a frequency analysis which ranges beyond the average sampling rate can be done. The average sampling frequency was 10 to 1000 Hz.

The irregular LDA data was examined with the ARMAseI (Auto Regressive Method for Spectral Analysis) as provided by Broersen [43]. It is very unlikely that the turbulence in our system is isotropic. It is however feasible to guess that the radial and axial direction contain the same amount of turbulence. We only have measurement data for the axial and azimuthal velocity. Figure B.1 shows a characteristic turbulent spectrum, where the frequency drops for frequencies beyond the integral time scale. The smallest scales are on the right size of this spectrum.

We conducted a procedure to estimate the scale of the smallest eddies in the flow based on the procedure described by Tennekes and Lumley [55]. The relevant quantities are (i), the turbulent dissipation rate:

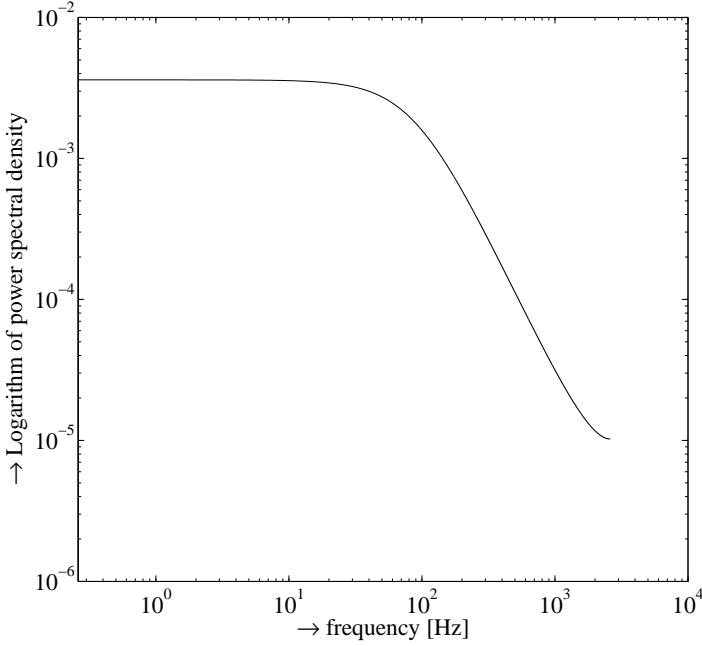


Figure B.1: Example of a time spectrum estimate with Armasel. Data for the strong swirl element, $56 \text{ m}^3/\text{h}$, $r = 12.5 \text{ mm}$, azimuthal velocity at 782 mm downstream.

$$\epsilon = 2\nu \overline{s_{ij}s_{ij}} = 15\nu \overline{\left(\frac{\partial u_1}{\partial x_1}\right)^2}, \quad (\text{B.1})$$

and (ii) the Kolmogorov microscale:

$$\eta = \left(\frac{\nu^3}{\epsilon}\right)^{1/4}. \quad (\text{B.2})$$

For each point of interest, the estimate of the turbulent time spectrum was calculated with ARMAseI like in figure B.1. According to Tennekes and Lumley [55] the integral scale is given by $\frac{\omega \ell}{u} = 2.4$. This is the point where the curve starts to bend. From that, we derive $\frac{\ell}{u}$. The end of this graph is marked by the position $\frac{\omega \eta}{v} = 0.74$ with ω the frequency, η the Kolmogorov length scale and v the Kolmogorov velocity scale. From this value the turbulent dissipation rate η is calculated and therewith the Kolmogorov length η .

B.2 Method

According to Tennekes and Lumley [55] (page 279), the integral scale is given by $\frac{\omega \ell}{u} = 2.4$; this is the point where the curve starts to bend from horizontal to the

descending slope. Based on this condition, for each velocity component (both azimuthal and axial), the value of $\frac{\ell}{u}$ can be approximated. From Tennekes and Lumley [55] it follows that the end of the frequency graph, where the power spectrum increases more rapidly, is marked by the position $\frac{\omega\eta}{v} = 0.74$ with ω the frequency, η the Kolmogorov length scale and v the Kolmogorov velocity scale. From the value for ω at the end of the curve, the turbulent dissipation rate η is calculated and therewith the Kolmogorov length η .

The procedure above is performed for the selected flow rate and measurement position, a part of 1000 time steps from each time series was obtained.

B.3 Result

The method mentioned above has been applied on a dataset of the strong and weak swirl element at a flow rate of 56 m³/h. Figure B.2 shows the estimates for the smallest scales at different radial positions and for the different velocity components.

The smallest eddies are found at $r = 40$ mm. Figure 4.6 shows the velocity profiles for the different swirl elements. The azimuthal velocity profile is rather flat at $r = 40$ mm, but the axial velocity has almost its maximum velocity over there. The high total velocity leads to high turbulence production and therewith small eddies.

Accuracy The results shown in figure B.2 should have a large uncertainty. Although the method makes it hard to quantify this, the laborious process to come to the results in combination with the required subjective data evaluation makes results not highly reproducible, as can be seen for the weak swirl element at $r = 20$ mm.

The method in chapter 5 proofed to be a more stable predictor of turbulent dispersion, than the estimate of the Kolmogorov scale provided in this appendix.

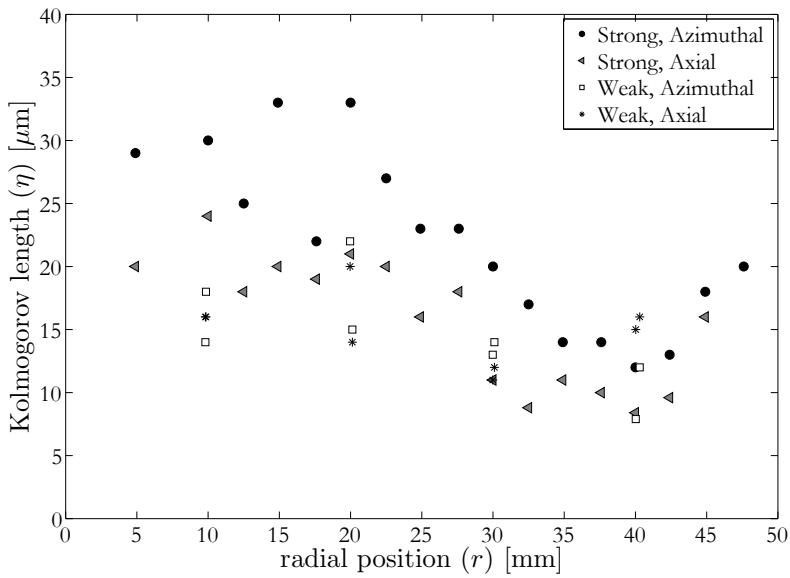


Figure B.2: Estimate for the Kolmogorov length scale based on the axial and azimuthal velocities. Flow rate: $56 \text{ m}^3/\text{h}$, flow split = 0.3 and measurement 782 mm downstream of the strong swirl element

APPENDIX C

Uncertainty analysis

The rig is equipped with fixed measurement devices for the flow rates, pressures, density and interface levels. Besides these devices, there is temporary measurement equipment, such as the Laser Doppler apparatus, the wire-mesh, endoscope, optical probes etc. This section deals with the measurement results of the fixed equipment.

C.1 Accuracy of the measurement equipment

Float flow meters The inflow of oil and brine is measured with float flow meters type Heinrichs BGN with a specified measurement error of 1.28 m³/h.

Coriolis flow meter The flow in the HPO is measured with a Coriolis flow meter of Emerson type MicroMotion Elite CMF300. The error in the mass flow is 0.10 %, for the density 0.5 kg/m³.

Oil cut in the HPO The oil cut in the HPO is derived according to the following equation:

$$c_{\text{HPO}} = \frac{\rho_{\text{HPO}} - \rho_{\text{brine}}}{\rho_{\text{oil}} - \rho_{\text{brine}}}. \quad (\text{C.1})$$

Temperature dependence The densities of oil and brine (in kg/m³) are calculated based on temperature T (in °C), according to the following relations:

$$\rho_{\text{brine}}(T) = -0.5202 \left[\frac{\text{kg}}{^\circ\text{Cm}^3} \right] T [^\circ\text{C}] + 1074.7 [\text{kg/m}^3], \quad (\text{C.2})$$

$$\rho_{\text{oil}}(T) = -0.7417 \left[\frac{\text{kg}}{^\circ\text{Cm}^3} \right] T [^\circ\text{C}] + 891.41 [\text{kg/m}^3], \quad (\text{C.3})$$

these relations are experimentally determined with the density measurements in the Coriolis flow meter present in the rig.

C.2 Oil Concentration in outputs

Oil cut in the HPO The error in the measured values results in an error in the calculated value for c_{HPO} . The uncertainty $u_{c_{\text{HPO}}}$ depends on the following components:

$$u_{c_{\text{HPO}}}(\rho_{\text{brine}}) = \left| \frac{\partial c_{\text{HPO}}}{\partial \rho_{\text{brine}}} u_{\rho_{\text{brine}}} \right| = \frac{\rho_{\text{HPO}} - \rho_{\text{oil}}}{(\rho_{\text{oil}} - \rho_{\text{brine}})^2} u_{\rho_{\text{brine}}} \quad (\text{C.4})$$

$$u_{c_{\text{HPO}}}(\rho_{\text{oil}}) = \left| \frac{\partial c_{\text{HPO}}}{\partial \rho_{\text{oil}}} u_{\rho_{\text{oil}}} \right| = \frac{\rho_{\text{brine}} - \rho_{\text{HPO}}}{(\rho_{\text{oil}} - \rho_{\text{brine}})^2} u_{\rho_{\text{brine}}} \quad (\text{C.5})$$

$$u_{c_{\text{HPO}}}(\rho_{\text{HPO}}) = \left| \frac{\partial c_{\text{HPO}}}{\partial \rho_{\text{HPO}}} u_{\rho_{\text{HPO}}} \right| = \frac{1}{\rho_{\text{oil}} - \rho_{\text{brine}}} u_{\rho_{\text{HPO}}} \quad (\text{C.6})$$

The total estimate of the error is given by:

$$u_{c_{\text{HPO}}} = \sqrt{(u_{c_{\text{HPO}}}(\rho_{\text{brine}}))^2 + (u_{c_{\text{HPO}}}(\rho_{\text{oil}}))^2 + (u_{c_{\text{HPO}}}(\rho_{\text{HPO}}))^2} \quad (\text{C.7})$$

The order of $u_{c_{\text{HPO}}}$ is $1 \cdot 10^{-3}$.

Oil cut in the LPO The oil concentration in the LPO is determined according to:

$$c_{\text{LPO}} = \frac{\Phi_{\text{oil}} - \Phi_{\text{HPO}} c_{\text{HPO}}}{\Phi_{\text{oil}} + \Phi_{\text{brine}} - \Phi_{\text{HPO}}}. \quad (\text{C.8})$$

Φ_{oil} and Φ_{brine} are measured with the float flow meters, Φ_{HPO} with the Coriolis flow meter and c_{HPO} follows from equation C.1.

The resulting error in c_{LPO} follows from the error in the variables in equation C.8

$$u_{c_{\text{LPO}}}(\Phi_{\text{oil}}) = \left| \frac{\Phi_{\text{brine}} + (c_{\text{HPO}} - 1)\Phi_{\text{HPO}}}{(\Phi_{\text{oil}} + \Phi_{\text{brine}} - \Phi_{\text{HPO}})^2} u_{\Phi_{\text{oil}}} \right| \quad (\text{C.9})$$

$$u_{c_{\text{LPO}}}(\Phi_{\text{brine}}) = \left| \frac{\Phi_{\text{HPO}} c_{\text{HPO}} - \Phi_{\text{oil}}}{(\Phi_{\text{oil}} + \Phi_{\text{brine}} - \Phi_{\text{HPO}})^2} u_{\Phi_{\text{brine}}} \right| \quad (\text{C.10})$$

$$u_{c_{\text{LPO}}}(\Phi_{\text{HPO}}) = \left| \frac{\phi_{\text{oil}} - c_{\text{HPO}}(\Phi_{\text{oil}} + \Phi_{\text{brine}})}{(\Phi_{\text{oil}} + \Phi_{\text{brine}} - \Phi_{\text{HPO}})^2} u_{\Phi_{\text{HPO}}} \right| \quad (\text{C.11})$$

$$u_{c_{\text{LPO}}}(c_{\text{HPO}}) = \left| \frac{-\Phi_{\text{HPO}}}{\Phi_{\text{oil}} + \Phi_{\text{brine}} - \Phi_{\text{HPO}}} u_{c_{\text{HPO}}} \right|. \quad (\text{C.12})$$

The values contribute to the error in the oil cut calculation for the LPO:

$$u_{c_{\text{LPO}}}^2 = (u_{c_{\text{LPO}}}(\Phi_{\text{oil}}))^2 + (u_{c_{\text{LPO}}}(\Phi_{\text{brine}}))^2 + (u_{c_{\text{LPO}}}(\Phi_{\text{HPO}}))^2 + (u_{c_{\text{LPO}}}(c_{\text{HPO}}))^2 \quad (\text{C.13})$$

The order of $u_{c_{\text{LPO}}}$ is 0.01.

Coriolis flow meter in the LPO In the last months of the project, a Coriolis flow meter was installed in the LPO. This flow meter was a Endress+Hauser Promass 83I with a nominal diameter of 50mm. This flow meter has a specified error for the mass flow of 0.10 % of the measured value and 0.5 kg/m³ for density. This brings the measurement error for the volumetric oil concentration in the LPO to the order of the error for the HPO: 10⁻³. The error is indicated in the graph with the respective results.

APPENDIX D

Drag relation for a sphere

In this work, we use the drag estimation for a sphere as provided by Almedeij [45] for all Reynolds numbers smaller than 10^6 .

The drag coefficient C_D is given by:

$$C_D = \left[\frac{1}{(\phi_1 + \phi_2)^{-1} + \phi_3^{-1}} + \phi_4 \right]^{1/10} \quad (\text{D.1})$$

where the different functions ϕ are given by:

$$\begin{aligned} \phi_1 &= \left(24\text{Re}^{-1}\right)^{10} + \left(21\text{Re}^{-0.67}\right)^{10} + \left(4\text{Re}^{-0.33}\right)^{10} + (0.4)^{10} \\ \phi_2 &= \frac{1}{\left(0.148\text{Re}^{0.11}\right)^{-10} + (0.5)^{-10}} \\ \phi_3 &= \left(1.57 \cdot 10^8 \text{Re}^{-1.625}\right)^{10} \\ \phi_4 &= \frac{1}{\left(6 \cdot 10^{-17} \text{Re}^{2.63}\right)^{-10} + (0.2)^{-10}}. \end{aligned}$$

Figure D.1 displays equation D.1.

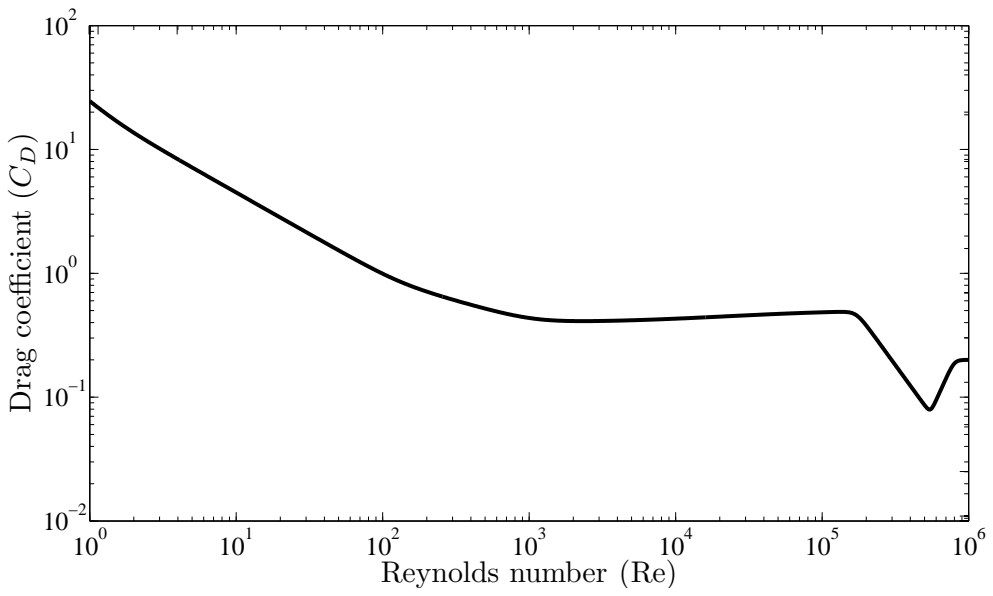


Figure D.1: Drag coefficient as function of the Reynolds number for the relation in equation D.1.

List of publications

Papers

1. L.J.A.M. van Campen and R.F. Mudde, *Droplet breakup in an Axial Cyclone*, paper and oral presentation for the International Conference on Multiphase Flow, Jeju (South Korea), May 2013.
2. L.J.A.M. van Campen, J.J. Slot, R.F. Mudde and H.W.M. Hoeijmakers, *A numerical and experimental survey of a liquid-liquid axial cyclone*, International Journal of Chemical Reaction Engineering, Volume 10, issue 1, June 2012.
3. L.J.A.M. van Campen, J.J. Slot, R.F. Mudde and H.W.M. Hoeijmakers, *An axial cyclone for oil/water separation*, conference paper for the 12th International Conference on Multiphase Flow in Industrial Plants, Ischia (Italy), September 2011.
4. L.J.A.M. van Campen and R.F. Mudde, *Direct droplet size measurements in an oil/water axial cyclone*, to be submitted to the International Journal of Multiphase Flow.

Patent

1. Eckhard Schleicher, Martin Löschau, Laurens van Campen, *Gittersensor für hochleitfähige Medien*, patent submitted to the Munich Patent office.

Acknowledgements

Wetenschappelijk onderzoek is niet iets wat je als kluizenaar tot een goed einde kan brengen. De interactie met collega's, stafleden, de industrie en de rest van de buitenwereld is essentieel: ik had niet zonder gekund. Deze drie pagina's geven mij de gelegenheid alle betrokkenen te benoemen die zeer hebben bijgedragen aan de totstandkoming van dit proefschrift.

Allereerst ben ik Rob erkentelijk dat hij me in de zomer van 2008 benaderde om dit project te doen. Waar ik aanvankelijk het doen van een promotieonderzoek niet als serieus vervolg van mijn carrière beschouwde, had dit project de juiste mix van wetenschap, industriële inmenging en experimenteel geknutsel om mij enthousiast te maken. De grote mate van verantwoordelijkheid die je aan me overliet, heeft me zeer gevormd en daar heb ik nog dagelijks profijt van.

Harry Hoeijmakers bevond zich als tweede promotor hemelsbreed op grote afstand, maar was altijd beschikbaar om binnen en buiten de geplande ISPT progress meetings mee te denken. Ook Karin Schroën (WUR) had een belangrijke rol, niet alleen vanwege de fysisch-chemische inzichten, maar ook vanwege de nimmer aflatende bemoedigende opmerkingen en recordsnelheid van het beantwoorden van e-mails! Jesse en Thomas, als collega-onderzoekers in ons ISPT project bedank ik jullie zeer voor alle discussies die we hebben gehad. Juist de verschillen in onze achtergronden maakten dat we veel verschillende aspecten van onze olie water axiaal cycloon goed hebben kunnen bekijken.

Het bijzondere van dit ISPT project was de grote interactie met "de industrie". Dit project had nooit bestaan zonder de drijvende kracht van Paul Verbeek, die in alle fases van het project nauw betrokken was. Ook al heb ik Wouter Harteveld (Shell) slechts enkele keren gesproken, zijn bevologenheid en ideeënrijkheid heeft me erg aangestoken. Frames heeft in de personen van Johanna en Martijn veel tijd en moeite in het project gestoken, uiteenlopend van nadenken over het ontwerp van een nieuw swirlelement, tot de technische aanbesteding van een nieuw scheidingsvat, alles werd snel en precies opgevolgd. Danny van der Krogt van Wintershall heeft veel bijgedragen aan mijn inzicht van de dagelijkse praktijk van *hydrocarbon recovery*, zodat ik ons eigen werk beter in een breed perspectief kon plaatsen. Tenslotte wil ik Arian Nijmeijer (squash!), Peter Veenstra en Remko Westra niet onbenoemd laten.

Tijdens mijn werkzaamheden maakte ik deel uit van de afdeling Multi-Scale Physics (tot 31-8-2012) en de sectie Transport Phenomena (vanaf 1-9-2012). Het meemaken van de herijking die aan deze naamswijziging ten grondslag lag en de weerslag die dat had op de (ondersteunende) staf, hebben op mij grote indruk gemaakt. Ik ben blij dat de groep als geheel er in mijn ogen hechter uit is gekomen.

Het bouwen van een grote experimentele opstelling zoals in dit onderzoek, is niet alleen mogelijk. Alle lof voor Jan en Jaap (K) die zo vlak voor hun pensioen nog dit fysiek zware werk zo netjes hebben uitgevoerd. Jaap (vR), Evert, Wouter, Lodi en Thea, bedankt voor alle kleine en grote klussen waar jullie me bij hebben geholpen. Nog een speciaal woord van dank voor Jaap Kamminga die me alle essentiële vaardigheden heeft bijgebracht om in het laatste jaar zonder technicus de opstelling zelf draaiende te kunnen houden.

Naast de ondersteuning in het lab, mag ik de secretariële ondersteuning niet vergeten: Amanda, Angela, Anita en Fiona, dankjewel! Typically, the office mates are those who you see most often (at least, when your lab is nearby). And whether it was W220, 34B-3C-1-160 of 0.519, I'd like to thank Annekatrien, Özgür, Adrian, Zaki, Anton, Michiel, Bernhard, Duong and Wenjie for the pleasant moments together, the patience with all my complaints and frustrations and last but not least, for keeping the pranks with my workspace within reasonable limits.

In de loop van de tijd hebben vijf studenten met mij gewerkt aan een gerelateerd project. Als eerste Wout aan een onderzoek om druppels te volgen met een hogesnelheidscamera. Vervolgens kwam Yoerik als MSc student om het werk van Wout voort te zetten (zowel experimenteel als numeriek). Bauke en Rik hebben gewerkt aan hun BEP bij mij. Matty heeft veel werk verzet aan de geometrievariaties die je vindt in hoofdstuk 7.

Ook met andere studenten en aio's was het prettig optrekken, van de koffiepauze tot op de curlingbaan of de grotten in Limburg: Rudi, Rick, Alexander, Niels, Koen, Cees, Matthijs, Maarten, Aljen, Gijs en Rosanne: 't was gezellig! En Dries, als 'vaste' reisgenoot hebben we toch aardig wat gezien van de wereld (in ieder geval Italië, Zuid-Korea en Japan - alleen jammer van de karaoke... ;)

Although Luis Portela was not formally involved in the work of this thesis, it is great to have an "encyclopedia on fluid dynamics" nearby. Where the conversations did not only turbulence and its measurements, but extended to the weal and woe of university life. Ook Stephanie Hessing heeft onbewust veel coaching verzorgd binnen het thema *how to manage your manager*, bedankt!

De boog kan niet altijd gespannen staan: veel zaken die op 't eerste gezicht niets met een olie/watercycloon te maken hebben, hebben zeker zowel afleiding als inspiratie gegeven.

In de loop van de tijd heb ik het genoeg gehad heel wat sportactiviteiten te mogen organiseren: de WinterWedstrijden (roeien), het Europees Universiteitskampioenschap roeien in 2010, de NSRF Slotwedstrijden van 2011 t/m 2013 en de wielerronde van Delft van 2011 t/m 2013. Het is mooi om te zien hoe je met een heel diverse groep, grote dingen kan opzetten, plus, je leert jezelf goed kennen. Alle betrokkenen, het was mooi met jullie samen te werken!

Als jury was ik bij menig roeiwedstrijd te vinden, op of aan het water. Naast

gezellige dagen is het leuk om je kennissenkring uit te breiden buiten de technische hoek, maar wel veilig met *Ons Soort Mensen*.

Mens sana in corpore sano: op de fiets en op de schaats! Waar de technische uitdaging van fietsen te vinden is in de nieuwste mechanische snufjes, is de schaatstechniek een uitdaging waar ik mijn tanden nog tot in het vrijwel oneindige op stuk kan bijten. In ieder geval, WTOS'ers en ELSjes, bedankt voor de mooie tijd!

Zelf had ik nooit zo ver kunnen komen zonder de liefdevolle en kansrijke opvoeding van mijn ouders en ondersteuning die er tot op de dag van vandaag is als het nodig is. Ook mijn broer, zus, zwager, neefje en nichtje, het is altijd goed om te zien dat er meer in het leven is dan promoveren. En *last but not least*, Ingeborg, ook al heb je alleen het laatste stukje van het werk van dichtbij meegemaakt, ik ben blij dat ik alle hoogte- en dieptepunten met jou heb kunnen delen!

Laurens van Campen

Delft, november 2013

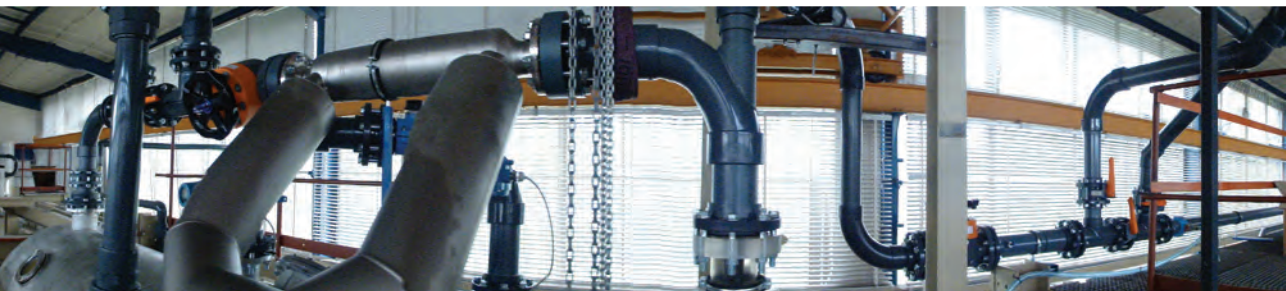
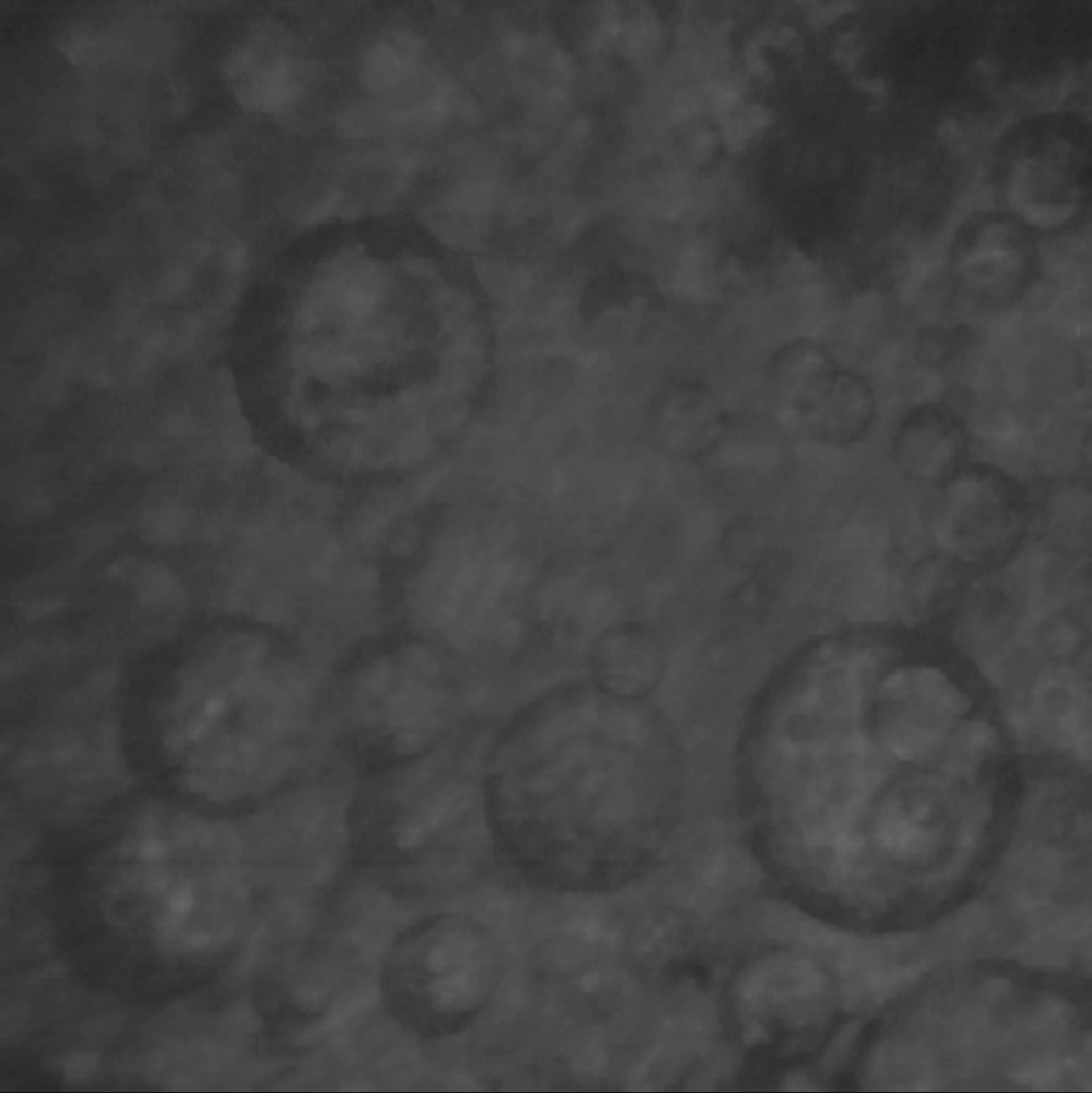
Curriculum Vitae



I was born on the 25th of May, 1984 in Nijmegen, The Netherlands. I grew up in Veghel, where I went to primary school, afterwards I joined Gymnasium Bernrode in Heeswijk as secondary school. After graduation at the gymnasium in 2002, my education continued at Delft University of Technology with the Bachelor and Master programme Applied Physics, completed in February 2009 at the Department Radiation, Radionuclides & Reactors Department. The title of my MSc thesis was “An experimental investigation on the use of FEP as refractive index matching material for LDA in rod bundle flow”.

Following my MSc thesis work, I started in 2009 the PhD programme of which this thesis is the result, with prof. dr. Rob Mudde as thesis advisor, first in the Department of Multi-Scale Physics, from September 2012 onwards in the section Transport Phenomena of the Department of Chemical Engineering.

I started October 7th, 2013 as Researcher Natural Gas Treating at Shell Global Solutions International in Amsterdam.



ISBN 978-90-6464-736-9



9 789064 647369 >

 **TU**Delft

